Towards reliable contacts of molecular electronic devices to gold electrodes

Peter F. Cafe

A Thesis submitted as required for the fulfilment of a

Doctorate of Philosophy at the University of Sydney

March 2008

Declaration

I declare that the work presented in this thesis is all my own (other than where figures, quotations, results and tables have been extracted from other publications or persons and have been expressly referenced as such in the narrative), with the following exceptions:

- The theoretical calculations of Chapter 2 were performed by Professor Jeffery R Reimers and Dr Ante Bilic of Sydney University, School of Chemistry.

- DFT calculations of conductance for pyrazine, 4,4′-bipyridine and TATPP were performed by Mr Sören Wolthat of Sydney University, School of Chemistry.

Peter Cafe

Acknowledgements

"A friend walks in when everyone else walks out"

- Unknown Source

Publications arising from this work

- **"Chemisorbed and Physisorbed Structures for 1,10-Phenanthroline and Dipyrido[3,2-a:2′,3′-c]phenazine on Au(111)"** Peter F. Cafe[a], Allan G. Larsen[a], Wenrong Yang[a], Ante Bilic[a], Iain M. Blake[a], Maxwell J. Crossley[a], Jingdong Zhang[b], Hainer Wackerbarth[b], Jens Ulstrup[b], and Jeffrey R. Reimers[a]*

The Journal of Physical Chemistry C, published by the American Chemical Society, publishes scientific articles reporting research on the following sub-disciplines of physical chemistry:

- Nanoparticles and nanostructures
- Surfaces, interfaces, and catalysis
- Electron transport, optical and electronic devices
- Energy conversion and storage

[a] School of Chemistry, The University of Sydney, NSW, 2006, Australia
[b] Department of Chemistry and NanoDTU, Technical University of Denmark, DK-2800 Lyngby, Denmark

SYNOPSIS OF THIS THESIS

The aim of this thesis is to more fully understand and explain the binding mechanism of organic molecules to the Au(111) surface and to explore the conduction of such molecules. It consists of five discreet chapters connected to each other by the central theme of "The Single Molecule Device: Conductance and Binding". There is a deliberate concentration on azine linkers, in particular those with a 1,10-phenanthroline-type bidentate configuration at each end. This linker unit is called a "molecular alligator clip" and is investigated as an alternative to the thiol linker unit more commonly used.

Chapter 1 places the work in the broad context of Molecular Electronics and establishes the need for this research.

In Chapter 2 the multiple break-junction technique (using a Scanning Tunnelling Microscope or similar device) was used to investigate the conductance of various molecules with azine linkers. A major finding of those experiments is that solvent interactions are a key factor in the conductance signal of particular molecules. Some solvents interfere with the molecule's interaction with and attachment to the gold electrodes. One indicator of the degree of this interference is the extent of the enhancement or otherwise of the gold quantized conduction peak at $1.0\ G_0$. Below $1.0\ G_0$ a broad range for which the molecule enhances conduction indicates that solvent interactions contribute to a variety of structures which could bridge the electrodes, each with their own specific conductance value. The use of histograms with a Log_{10} scale for conductance proved useful for observing broad range features.

Another factor which affects the conductance signal is the geometric alignment of the molecule (or the molecule-solvent structure) to the gold electrode, and the molecular alignment is explored in Chapters 3 for 1,10-phenanthroline (PHEN) and Chapter 4 for thiols.

In Chapter 3 STM images, electrochemistry, and Density Functional Theory (DFT) are used to determine 1,10-phenanthroline (PHEN) structures on the Au(111) surface. It is established that PHEN binds in two modes, a physisorbed state and a chemisorbed state. The chemisorbed state is more stable and involves the extraction of gold from the bulk to form adatom-PHEN entities which are highly mobile on the gold surface. Surface pitting is viewed as evidential of the formation of the adatom-molecule entities. DFT calculations in this chapter were performed by Ante Bilic and Jeffery Reimers.

The conclusions to Chapter 3 implicate the adatom as a binding mode of thiols to gold and this is explored in Chapter 4 by a timely review of nascent research in the field. The adatom motif is identified as the major binding structure for thiol terminated molecules to gold, using the explanation of surface pitting in Chapter 3 as major evidence and substantiated by emergent literature, both experimental and theoretical. Furthermore, the effect of this binding mode on conductance is explored and structures relevant to the break-junction experiment of Chapter 2 are identified and their conductance values compared. Finally, as a result of researching extensive reports of molecular conductance values, and having attempted the same, a simple method for predicting the conductance of single molecules is presented based upon the tunneling conductance formula.

Table of Contents

Chapter 2   Break-Junction Experiments. 2-1

Chapter 5   Simple Methods for Estimating Molecular Conductivity. 5-1

Chapter 6   Bibliography 6-1

Chapter 7   APPENDICES 7-1

Towards reliable contacts of molecular electronic devices to gold electrodes

University of Sydney

"After climbing a great hill, one only finds that there are many more hills to climb." (Nelson Mandella)

Chapter 1 General Introduction

1-0 Synopsis of Chapter 1: General Introduction

The general introduction explores the background of the field of Molecular Electronics, with reference to the last 50 years of technological advance in the semiconductor industry, and views Molecular Electronics as an inheritor of the mantle of Moore's Law. Molecular Electronics is defined as the control of individual molecules or particular groups of molecules such that we can make them do useful tasks and replace larger scale devices.

The Molecular Electronics Group within the School of Chemistry, Sydney University, is introduced.

Some constraints of Molecular Electronics are outlined and a number of basic tasks of research are identified, with the following two singled out for focus in this thesis:

- To measure single molecule conductance.

- To define the contact of molecules to other components.

The binding module of a molecule is introduced as a molecular "Alligator Clip", and self-assembly is identified as a critical process in device manufacture, however binding modes and self-assembly mechanisms are in need of further understanding.

A brief mention is made of five common types of molecular conduction experimental techniques, whilst this research has chosen the multiple break-junction technique with statistical analysis as the most suitable.

Three additional major research activities are described.

The Chapter concludes by connecting each of the subsequent research chapters (Chapters 2 to 5) to develop a general theme that can be briefly described as:

The Single Molecule Device: Conductance and Binding.

1-1 Background

1.1.1   The background and context of molecular electronics

"Molecular electronics is thus very much about contacts"[2].

The massive worldwide semiconductor industry drives the even more massive software and hardware development sector with its succession of breakthroughs in speed and miniaturisation. Expectations are generally high that the industry can deliver continuous advances in the basic building blocks which function in such things as mobile phones, computers, portable MP3 players, and even toasters and fluffy toys, and that the rate of advancement is predictable. This "axiom" is commonly referred to as "Moore's Law", being formally presented in 1965 by Gordon Moore, Director of Fairchild Semiconductor's Research and Development Laboratories, in the 35th anniversary issue of *Electronics* magazine[3]. He intonated that transistor density on a computer microchip will double, and costs will halve, each twelve months, and this has been (roughly) borne out by empirical observation to the present time. In the 1990s, it was generally accepted that Moore's Law implied that computing power at fixed cost would continue to double every 18 months. This periodic doubling means exponential growth, which has now placed current silicon-chip development "bang-up" against the fundamental physical limits of conventional microelectronics. Moore recently admitted that Moore's Law, in its current form, with CMOS silicon, will "run out of gas" in 2017.[4] Speculations on the continued application of Moore's Law therefore lean towards radical departures from silicon technology to such things as molecular electronics, quantum computing, spin devices, bio-computing, DNA computers, and other theoretically possible information processing mechanisms[5] (and their integration, as suggested in Figure 1-1).
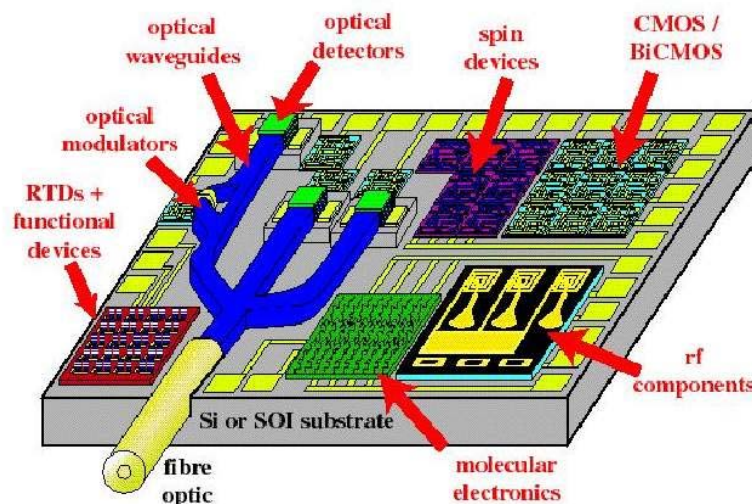
Figure 1-1 – Possible integration of various existing and future technologies, as suggested by Compañó *et al.* in 1999[6]. In this vision *molecular electronics* is an integral component in an array of novel technologies.

1.1.2   What is molecular electronics?

Molecular electronics is the branch of nanotechnology in which it is envisaged that integrated circuitry will be constructed from component molecules acting as capacitors, resistors, logic gateways, memory registers, *etc*, joined by molecular wires (such as carbon nanotubes). This notion was envisioned in 1974 by Aviram and Ratner[7] and further developed in 1982 by Carter[8]. With such high promise held before them, many teams of scientists have proceeded to create the science which would define this new future of molecular thinking machines. As Newton's theories of motion defined the physics of the few centuries that followed him, so will the emergent laws of nanotechnology help define the new electronics of the coming century, and the collaborative effort which will achieve this is of the same order as the human genome program, of which this dissertation is but one minute component.

We may view molecular electronics as the design, fabrication and assembly of molecules into functioning electronic circuits.

> *"Molecular electronics ... allows chemical engineering of organic molecules with their physical and electronic properties tailored by synthetic methods". [Reed 2003, p32]*[9]

In 2001 Carroll and Gorman asked the question "Can we control the position of individual molecules or particular groups of molecules such that we can make them do useful tasks?"; and furthermore "Can we use the intrinsic properties of these molecules to replace larger scale devices?"[10]. They define molecular electronics as the search for the answers to these questions.

1.1.3　Sydney University Molecular Electronics Group and the program of work which has led to this thesis.

The **Molecular Electronics Group** at Sydney University (officially since January 2002) has been one of the contributing research groups in this field. Their major contributions have been in the *theoretical modelling* of the forces which govern the behaviour of the basic components of matter – chemical binding and electron transport. However to expand on and verify their theoretical results, they have recently developed an *experimental research program*, commenced in 2003, which was pioneered by the present author as a research student (as expounded in subsequent chapters and supporting information).

The initial aim of this program was to *measure* experimentally the conductive properties of select molecules, and hence a large portion of this thesis is devoted to single molecule conduction and the experiments conducted are described in detail with

their results and implications (Chapter 2). However co-incident research at Sydney University and elsewhere highlighted the need for **more clearly defined contact geometries**[2, 11, 12]. Thus another important and basic result of this research examines the linker unit which joins component molecules to gold electrodes, and defines the possible geometries for the bonding of 1,10 phenanthroline to the gold(111) surface (Chapter 3), with implications for the very important thiol linkages also (which are further developed in Chapter 4). The determination of the binding geometries of 1,10 phenanthroline on gold (111) is supported by STM imaging and theoretical calculations using density functional theory.

The development of techniques to do this is in itself remarkable as we seek measurements of nanometers and nanoamps. At this realm of measurement we are close to the limits of observability as we attempt to distinguish between the effects of our observation tools and the quantities we seek to measure. However scanning probe microscopy (first reported by Binnig in 1982[13]) has given unprecedented access to the miniature world of molecules, particularly in imaging ordered monolayers to atomic resolution.

Here the use of the multiple STM Break-Junction technique has been used to perform measurements of single molecule conduction[14]. (Initially some molecular conduction experiments were tried using the conducting Atomic Force Microscope [cAFM], after Cui, *et al.* (2001)[15], however this method proved extremely difficult to reproduce and since it was first published in 2001 very little further research has occurred using this method: the original research group has since revised the method [and results] in 2007.[16])

1-2 Current factors in molecular electronics research

1.2.1   Constraints of research in molecular electronics

Scientific research aims to more fully explain the natural world and reconfigure it in novel (and beneficial) ways, and in so doing helps to define the future, and in a wide range of applications from biology to computing, this is certainly the case for molecular electronics and its umbrella discipline of nanotechnology. This exciting potential is one point even opposing visionaries K Eric Drexler and Rick Smalley agree upon:

> *"Like Drexler, Smalley believes that the potential of nanotechnology to benefit humanity is almost limitless"*[17].

Numerous candidate molecules have been proposed, probed and even proven (theoretically or experimentally) to be possible electronic components, however actual device fabrication (on a commercial level) has proven elusive, with formidable engineering and production barriers to be overcome – among them connectivity and the stochastic behaviour of individual molecules[18].

1.2.1.1   Making functioning molecular devices

It is generally accepted in molecular electronics that if the field is to reach its proposed potential (*i.e.*, to replace silicon technology in chip manufacture) then science not only needs to discover and define the molecules, and not only to develop ingenious methods to probe these molecules, *but also* to come upon a way to mass-produce the

devices which use them, and arms of nanotechnological research are reaching into areas of device fabrication, reproducibility, etc: *i.e.* cost-effective, consumer appropriate and marketable techniques. Thus the concept of "*Self-Assembly*" has become important, to which this thesis contributes a more complete understanding (Chapter 3).

In 1999 The *European Commission IST Programme Future and Emerging Technologies* identified four problems in the (then) state of research into molecular electronics:[6][*Section 2.2.4.5*]

> "*Intramolecular electronics are far behind other alternative concepts as none of the following issues have yet been demonstrated:*
>
> - *Self-assembly of single devices at reasonable (or small) integration densities, let alone integration with conducting molecular wires.*
>
> - *appropriate yield of devices from chemical or biological reactions for fabricating or manufacturing of circuits;*
>
> - *high data bandwidths for interconnects;*
>
> - *the potential for low cost per bit has not been demonstrated.*"

These issues certainly present challenges to researchers such as myself and the Molecular Electronics Group at Sydney University, however all indications are that the research will result in some remarkable breakthroughs. For example problems associated with high current flow and "band-width" through single molecules have already been addressed by the possibility of Quantum-dot Cellular Automata (QCA) [reported by Hush 2003[19]]:

> "*Craig Lent and colleagues have discussed the possibility of molecular-scale computing devices that operate without the flow of continuous current. This type of computation can, in principle, be achieved by quantum-dot cellular automata (QCA)*" [20]

1.2.1.2   Molecular self-assembly of devices

In 1999 it was noted that, despite the predictions, not a single transistor had been created on the basis of molecular electronics:

> *"... A number of proposals have appeared in the literature for molecular devices but few have been demonstrated. No real molecular three-terminal transistor device defined in this roadmap has yet been demonstrated"*[6]

Nevertheless just four years later Stan and Franzon (2003), *et al*, listed a number of molecular electronic devices which had been made, including resonant tunnelling diode devices, programmable molecular switches, carbon nanotube transistors, and diodes[21], and at the present time a Google® Patent search on "Molecular Electronic Device" returns over 800 registered USA patents, and include such "inventions" as nanowires, shift registers, wire transistors, amplifiers, memory, dielectrics, rectifiers, switches, as well as systems of manipulation, integration, orientation, testing, assembly and programming.

Yet a commercially proven device is yet to be engineered and a production-model molecular computer component is still some decades away. Presently researched methods or components are stepping stones to the future:

> *"Granted, they are not yet at the stage where these molecular devices are ready for production and can be incorporated into circuits. In fact, some may never directly see the actual light of commercialisation. They are enabling technologies — technologies on which commercialised versions will be developed. But the need is defined, the trend is clear, and the maturing process of refining and advancing these designs is moving forward."*[22]

At the very least, one result of this research is an increase in the understanding and specialized utilization of molecular bonds, which may be of particular use in drug discovery, synthesis and delivery, catalysts, and chemical storage[23, 24], as well as biological repair systems[25, 26]. However, even if complete molecular scale computer chips do not eventuate as a reality in our life-times, it is most likely that we will soon see the fabrication of molecular devices which will *integrate with* and *complement* other branches of technology[21, 27].

Molecular electronics is defining the science which will take us into that future.

1.2.2 Integration of molecular devices: the molecular *"Alligator Clip"*

When talking about circuitry, the current reference point is silicon wafer, with feature sizes of the order of 200 nm. For molecular electronics to deliver significant benefits (commensurate with the magnitude of the research), we should expect feature sizes at least 2 orders of magnitude smaller than this, with similar decreases in power consumption and heat loss, and increases in computational speed.

In both research and ultimate device manufacture, we need to interface with these systems.

> *"At the heart of the problem is the need to interface reliably with an individual molecule."* [28]

Molecular Electronics as it is envisaged involves the exact placement of individual molecules in relation to other molecules. It involves the precise joining of "function" molecules to "wire" molecules, function molecules being certain designer

molecules which will act as memory devices[29], diodes[30], logic gates[31], transistors[32], etc, *i.e.* the basic components of an electronic circuit, and some possibilities in such architectures and "bottom-up" fabrication (*i.e.* self-assembly) have been explored by Stan and Franzon, *et al.*[21].

This construction process works in the biological world by proteins, the machines which connect sites on molecules to sites on other molecules, and it happens in aqueous environments. However proteins are yet to be discovered which will operate in non-aqueous media or function with the types of molecules that traditionally define the chip industry, silicons, oxides, metals and semi-conductors. We are yet to discover all the ways of designing these specific placements, and ways of mass-manufacturing the process. The requirement of exact synthesis of molecular circuits is a challenge for the near future, however, organic-metal complexes and self-assembly techniques are being developed to meet these function and fabrication constraints[21]

A similar level of precision is required in the current state of play in the experimental research. Individual molecules need to be addressed experimentally and interrogated. Despite Smalley's "fat finger" and "sticky finger" descriptions of the problems of such precision[17], practical methods are currently being utilised to at least probe individual molecules. Common instruments used to investigate molecules are microscopes such as the STM and AFM.

However the *stochastic nature* of molecular co-ordination is to be addressed. It has become apparent through the research of this thesis and others that if molecular scale devices are to be testable at least and most probably useable at all, stable and predictable bonds to metal or semiconductor electrodes are a prerequisite[2, 12, 33].

In this thesis the functional group which tethers a molecule to a metallic surface (terminal) is dubbed an "***Alligator Clip***", after Tour[34, 35], Hush[36] and Crossley[37], and in the thesis of Anton Grigoriev[38]. Hermann *et al.* refer to a linking and self-organising motif as the "***universal adapter***"[39]; it's an "***anchor***" according to Tao[40], and is called "***solder***" by Devens Gust[41].

Seminario, Zacarias and Tour (1999)[35] first described these linking functional groups as "*molecular alligator clips*" and found by density functional theory calculations that the terminal groups of sulfur, selenium and tellurium bound well to gold, and of these sulfur has been used extensively in both theoretical and practical research. However he found that the isonitrile had limited use as an alligator clip, as it "*was only possible when the connection was made to one Au atom, and in this case the trend in the electron affinity, provided by the negative of the LUMO, dropped abruptly.*" (p. 758). However since then nitrile linkers to gold have been observed experimentally to form monolayers by both monodentate[42-47], bidentate[48-53], and even terdentate[54] nitrile ligands and to bridge break-junctions, as both amines[40, 43, 55] and azines[56], and several nitrile-type "alligator clips" have otherwise been proposed[37, 57].

This thesis establishes that the single Au atom binding for the bi-dentate ligand 1,10-phenanthroline is in fact *both* stable *and* predictable when that Au atom is an adatom on the Au(111) surface, and it's position on the surface is stabilised (i.e. locked-in) by the intermolecular interactions of the organic molecules.

1.2.3   Experimental techniques for molecular conduction experiments

With the conduction characteristics of single molecules being the most important aspect of current research into molecular electronics, five important methods have been developed to measure the current passing through a molecule. They are the use of Crossed-Wire Junctions, Break Junctions, Scanning Tunnelling Microscopy (STM), conducting Atomic Force Microscopy (cAFM), and in addition to the single break-junction experiment a recent technique involves the use of a modified STM to perform multiple break-junction experiments and perform statistical analysis on the hundreds of current traces produced[14]. All methods involve gold electrodes, high levels of purity, and tethering of an organic species to the gold electrode ("alligator clip"). The analysis of most methods require some speculation about the bond geometry between the molecule and the gold electrode and/or evidence of the formation of some sort of consistent monolayer.

1.2.3.1   Crossed wires junctions

A junction is formed between two thin wires. One wire passes over the other and oriented at right angles to it. The distance between the wires is controlled quite accurately down to sub-Angstrom units by a magnetic device. The wires typically are gold and are 10μm in diameter. One of the wires is covered in a monolayer of the molecule of interest. The wires are brought together until a current is detected. This method was pioneered by Kushmerick *et al.* in 2002[58] and has been used to study several different types of molecules.[59]

In this method, if the current remains stable during small movements of the crossed-wires it is assumed that the molecules have bonded stably to both wires. The

number of molecules forming the bridge between the two wires is unknown (but is typically less than ten), but the results are integer multiples of a "lowest curve" which is the current in a *single* molecular bridge.

1.2.3.2   Break-junctions

In this method, typically a gold wire is stretched until it breaks, and held near that break point. The gap spans two atomically fine tips of gold. The stretching and breaking of the wire are obtained by etching a thin gold line onto a substrate and then 3-point bending the substrate until the gold line breaks. The bending is controlled by a piezo-electric device and can control the movement to within an Angstrom. The point of breakage is determined by the moment the current through the wire ceases. The tips are then exposed to a solution containing the molecule of interest and a monolayer forms on the exposed tips of the gold. The gap is slowly brought back together again until a current forms (but not back to the point of breakage). (See Figure 2-2, page 2-5) The measurement of current follows the same methods as in Crossed-Wire Junctions[60-62]

However with break junctions the material characteristics of the metal at the point of breakage are difficult to determine. The metal is definitely stressed and deformed and so the geometric alignment of the molecules on the surface of the gold cannot be determined. It has been shown that bond geometry has a great effect on current flow[63], and so with this method it cannot be guaranteed that results are integer multiples of a single molecule.

1.2.3.3   Scanning tunnelling microscopy (STM)

In STM an "atomically fine" conducting tip is brought near a surface until a current is detected. That current is a tunnelling current theoretically flowing between one atom on the tip and one atom on the surface. The tip is rastered across the surface and most commonly a feedback-loop (with high gain) adjusts the height of the tip to maintain constant current (constant current mode). The height of the tip is presented as a topology image of the surface. Alternatively, with low gain, the height does not change dramatically and a current image is generated ("constant height mode").

The STM has enabled surface scanning to be conducted precisely to vertical resolutions of 0.01 Angstroms and horizontal resolutions of a few Angstroms. As well as being able to precisely map surfaces to extremely fine resolutions, it can perform tunnelling spectroscopy on the surface.[64, 65]

The tip must be close to the surface to allow tunnelling to occur but not touch the surface (shorting of the tip on the surface or "crashing"). The instrument is sensitive to both electrostatic and acoustic interference and needs to be isolated from these influences. The surface must allow tunnelling (i.e. be non-insulating).

The constant current mode "topology" image obtained from STM is not necessarily a true topology of the surface but rather a map of electronic density of states on the surface. Both topology and conduction affect the appearance of the image. Constant height mode can only be used to scan small flat regions, because with low gain the tip is more likely to crash into surface irregularities, however it is extremely sensitive to molecular features and slight changes in conductance across the surface.

STM has been used by many researchers to study the conduction of single molecules.[66, 67]

1.2.3.4   Multiple break junctions with statistical analysis

In 2003 Nongjian J. Tao[14] *et al*. first used a modified STM to hold stationary a gold tip at a point on the gold surface (in the presence of a dilute solution of a molecule of interest), then repeatedly crash the tip into the surface and withdraw. This would form a micro-thin gold wire then break it, with one or more molecules bridging the break for a brief moment as the tip withdraws. The technique can quickly perform thousands of break junction experiments on a specific molecule. The conductance traces are then screened and collated to produce a histogram showing peaks of conduction relating to multiples of the single molecule. This method has been reproduced by others using both STM[42] and custom made devices[43].

If one already has an STM, this is perhaps the easiest method to obtain reliable results because little additional equipment is required and it uses large numbers of individual break-junction experiments so that data can be analysed with some statistical certainty. However since the first reported results of this experiment by Tao, it has become apparent that the methods of data selection and collating of the conductance traces are critical in producing results which lead to meaningful conductance peaks in the histograms. Certain novel techniques of analysis have been published since, including tunnelling background subtraction and log scale graphing of conductance[68]; and "last step analysis"[69], which are each explored in Section 2.3.2. Although this method does not resolve this issue of bond geometry mentioned above, peak(s) in the histograms will appear at conductances indicating the *most likely* bond configuration(s) given the *specific experimental conditions*.

1.2.3.5   Conducting atomic force microscopy (cAFM)

In Atomic Force Microscopy (AFM) a tip of extremely fine sharpness is attached to a flexible cantilever and is brought into contact with a surface, and rastered across a surface. The vertical movements of the tip (in response to dispersion forces between the tip and the surface) are magnified some thousands of times by reflection of a laser off the back of the cantilever and detected by a four-quadrant photo-diode. This method can also detect twisting movements of the cantilever.

This device measures topology to horizontal and vertical resolutions using a feed-back loop to control the height of the tip, similar to the STM. However with AFM the surface need not be conductive. It also gives a greater idea of pure topology because it is not affected by conduction variations throughout the surface. However the resolution is generally not as high as STM and it is extremely difficult to obtain molecular recognition by AFM.

In *conducting* Atomic Force Microscopy (cAFM) the tip is coated with a conductive layer and a current can be passed through the tip to the surface and current image can be produced which is virtually independent of the topology. The measurement of conduction can be separated from the mechanism of the tip, which is not the case in STM.[70]

Once a feature is identified by the AFM, such as a molecule of interest, the tip can be positioned on that point and an I-V curve taken. In 2001 Cui, *et al.*[15] first used this method to identify gold nanoparticles attached to one end an 1,8-octanedithiol molecule whose other end was tethered to a gold(111) surface (the octanedithiol was sparsely inserted into an existing monolayer of "insulating" 1-octanemonothiols), and

then run an I-V sweep through the nanoparticle to obtain the I-V characteristics of the dithiol molecule.

Despite initial anticipation about the method, it proved more difficult than expected to reproduce and one of the original authors later conceded this and revised the method (and results)[16]. (For this current thesis the method was attempted for many months but was difficult to master and quite expensive.)

1-3 Research activities

The results which are reported in the following chapters have been supported by the major activities and collaborations which are listed below:

1.3.1   Overseas visits

Collaborative research secondments of the author were as follows:

- **To: Arizona State University (ASU), Tempe, Arizona USA: Department of Physics and Astronomy (3 months):**

From September to November 2003 work was done for three months with Professor Stuart M Lindsay and his team, who have pioneered major breakthroughs in the field of molecular electronics. The purpose of the visit was to learn the techniques of the conducting AFM method of single molecule conduction[15]. Although the method could not be successfully reproduced, the experimental experience allowed the *nanoPrep Lab* at Sydney University to be properly designed (see below). Also during this time valuable training was experienced at Molecular Imaging Inc, Ash Ave, Tempe, Arizona in use of the AFM, gold substrate preparation and H_2 flame annealing.

- **To: Technical University of Denmark, DK-2800 Lyngby, Denmark: Department of Chemistry and NanoDTU, (2 months)**

In September and October 2006 work was done with Professor Jens Ulstrup and his team. Their work has mainly been in high resolution STM images of molecular monolayers on gold surfaces. The purpose of the visit was to investigate 1,10-phenanthroline and DPPZ monolayers on Au(111) and to learn better STM techniques.

1.3.2   Design and fit of new laboratory at Sydney University

The experimental arm of the Sydney University molecular electronics group was completely new in 2003. Before any research could be carried out the proper facilities had to be established. Thus, initial research activities were centred around the design and furbishment of an appropriate laboratory, in conjunction with the Electron Microscope Unit at Sydney University (EMU). This presented an opportunity to get involved in the specification of the instrument and the design of the lab, which contained numerous challenges given the space and budget restrictions and the lack of prior experience in the field within the University.

Based upon the research papers, many discussions with Dr Jens Ulstrup[ℜ], and the secondment at ASU in the labs of Dr Stuart Lindsay, the *nanoPrep Lab*, situated in the basement of the EMU has been designed and completed. It includes the following major equipment procurements and positioning:

- Molecular Imaging Picoscan Plus combination AFM and STM.

- Large chemical fume hood with ducting to the roof and a scrubbing filter.

- Laminar flow cabinet with hepafilter.

- Millipore Water filtering system.

- Drying Oven

- Hydrogen Flame annealing apparatus.

[ℜ] Dr Jens Ulstrup was a visiting fellow at Sydney University during March to June 2003. He is from Technical University of Denmark and has pioneered much work on the formation of monolayers and the use of the STM in single molecule experiments.

- Provision of inert gas (argon and nitrogen)

- Acid storage cabinet.

- Flammables storage cabinet.

- Schröedinger Sharpener (for making fine STM tips)

In addition to the major equipment purchases and fittings, there were all the necessary tools, glassware, chemicals, protective devices and equipment. The area of the laboratory had to accommodate all these in a functional way, as well as include suitable storage areas, shelving, bench tops and work spaces. Services of water, power, lighting, positive flow of fresh air, supply of general consumables (paper towels, gloves, etc) waste disposal, contaminated waste disposal, and seating were all specified whilst considerations were given to all aspects of occupational health and safety.

Drawings of the *nanoPrep Lab* design in plan (Figure Appendix-1-67) and in sketches (Figure Appendix-1-68) are included in Supporting Information, Section 7-1.

1-4 Conclusions to Chapter 1

Molecular electronics is a natural inheritor of Moore's Law, whether the research results in "molecules which can perform useful tasks" or merely "enabling technologies". Self-assembly is a fundamental concept for mass production of devices.

Whilst the field of Molecular Electronics holds tremendous promise, clear definitions of molecular behaviour within electronic circuitry are needed.

The most obvious and critical of these definitions is the **conductance** of a molecule. Definitions of the mechanism of self-assembly and interface with electrodes are also required.

However the single molecule in this context does not exist: it is part of a circuit, bound to gold electrodes in one form or another, via a tethering device, and thus becomes part of an extended molecule which includes the electrodes. Solvent binding during break-junction experiments also contributes to a variety of possible structures. The long-range electron interactions between the electrodes, the tethering device, and the molecule, and the solvent interactions, play an important role. In this sense, there is no point where the molecule ends and the electrode begins: *i.e.* the molecule cannot be simply taken out of this context and its resistance calibrated like a light bulb.

The contextual nature of the molecule in its miniaturised circuit has to be classified. The "alligator clip" is itself a vital component of the circuit and the nature of the binding, its strength, orientation and geometry, are critical factors in the electronic behaviour of the circuit and need to be determined.

In Chapter 2 this thesis meets these challenges by providing experimental research into **conductance values for single molecules** using a modified STM to perform multiple break-junctions with statistical analysis.

In Chapter 3 it contributes by exploring one such tethering device in detail, the **1,10-phenanthroline "alligator clip"**, determining its binding modes, binding strength, and contact geometry. This is done by a combination of STM imaging, electrochemistry, and theoretical techniques using DFT and *a priori* calculations.

In Chapter 4 it extends findings on the binding modes of 1,10-phenanthroline to the **binding modes of thiols** in general, using surface pitting as the connecting evidence, and drawing upon extensive nascent research in support.

The research methods of theory and experiment move forward often hand-in-hand, each calibrating against the other. Both are tedious and time consuming, but theoretical calculations can often provide answers for experimental situations and give clues as to what may or may not be expected from a given experimental configuration, sometimes allowing the experimentalist to focus on more likely outcomes.

In Chapter 5 it presents **simple methods** of calculating the conductance of single molecules, which may assist both current experimental and theoretical methods.

(Blank Page)

Chapter 2 Break-Junction Experiments.

2-0 Synopsis for Chapter 2

This chapter focuses on the *break-junction* technique of determining single molecule conductance, and performs the experiment on five different molecules. Conductance can be expressed in units of the Conductance Quantum, G_0, which has a value of 7.7480917×10^{-5} Siemens♠.

The introduction in this chapter gives important background and includes a useful table outlining the reported conduction of various relevant molecules (from prior research), and introduces the tunnelling decay formula. (The values in this table and the tunnelling decay formula inspired the proposition outlined in Chapter 5.)

The general introductory comments on the experimental section include a discussion concerning various selection criteria and data analysis techniques for analysing the large amounts of data arising from hundreds of break-junction experiments (Section 2.3.2 below, page 2-40).

From the experimental work, generally, it was found that enhancement of the gold quantized conduction peak at $1.0\ G_0$ was a reliable indicator that the molecule was able to bind to the gold in the expected way (*i.e.* attached at one end by its "alligator clip"). The use of $\log_{10}$ scale histograms enabled long-range effects to be observed.

♠ The standard in this chapter expresses all molecular conductance values in units of **$10^{-4}\ G_0$** for easy comparison The exception is for bis-appended porphyrin where the conductance was expressed in units of G_0.

Solvent effects played an important role in the range of conductance values observed: this was established in pyrazine and extrapolated to the other molecules.
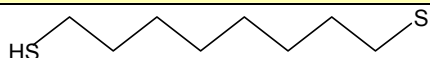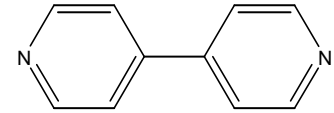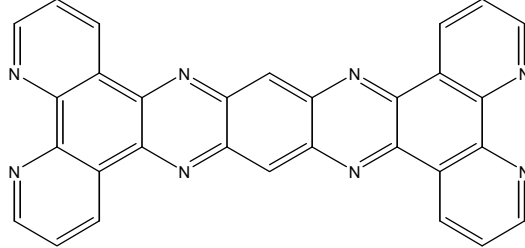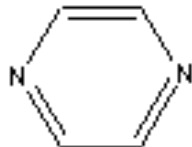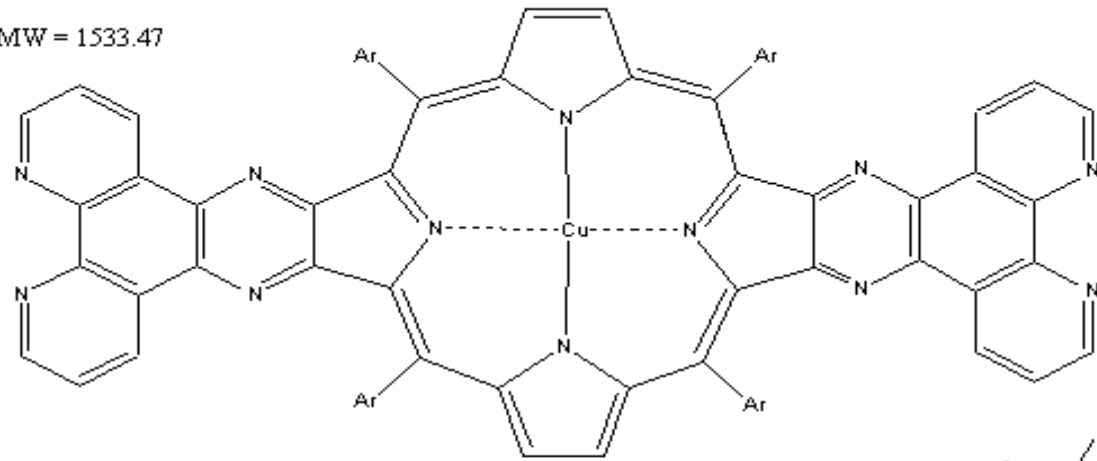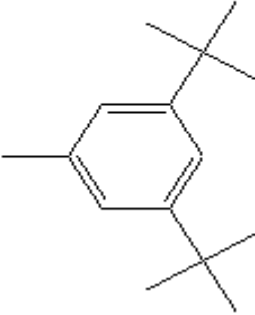
Brief results for the five molecules on which the STM Break-Junction experiments were conducted are as follows (the molecular structures are outlined in Table 2-1 below):

1. **1,8-octanedithiol** (Section 2-4): which, with a linear amplifier, has produced a single molecule conductance value of 2.5×10^{-4} G_0, agreeing with prior literature (which used a logarithmic amplifier). However the results are not as distinct. Nevertheless, it establishes that the methods and technical equipment are capable of measuring single molecule conduction.

2. **4,4′-bipyridine** (Section 2-5): Conduction of a single molecule was not established conclusively. Broad enhancement of conduction (over the solvent) was observed in the range from 10 to 150 $\times 10^{-4}$ G_0. Gold peaks were enhanced by the presence of 4,4′-bipyridine, indicating that the molecule interacts with the gold.

3. **TATPP**. (Section 2-6) In the solvents chosen (toluene and phenyloctane) TATPP showed no conductance peaks and did not indicate enhancement of the gold quantized conduction peak, most possibly due to its 4 middle nitrogen atoms and conjugated ring backbone being attracted to the gold surface. Considerations are given to redesigning the molecule to prevent adherence of its middle section to gold, and to make it more soluble.

4. **pyrazine** (Section 2-7): The "single value" of the conductance of pyrazine proved to be quite elusive, however through the application of $\log_{10}$ conductance scale histograms various long range features of pyrazine

conductance were uncovered. These proved to be solvent dependent. In most organic solvents the pyrazine could still interact with the gold and extend the gold quantized conduction peak, however this did not occur in the aqueous solvent. Of the organic solvents, carbontetrachloride provided the least solvent interactions and a peak was observed at 10×10^{-4} G_0: however, from these experiments alone, it cannot be ascribed to the conduction of a single pyrazine molecule. Aromatic solvents with delocalised π electron systems form strong interactions with pyrazine[71] and possibly prevent it from interacting with the gold electrodes. This is more pronounced in toluene, which is so similar to pyrazine in size and structure that it prevents all interactions with gold, showing no enhancement of the gold quantized conduction peak and no enhancement of conduction over the whole range of G_0 values investigated. However in phenyloctane the solvent interactions are not as strong and the gold quantized conduction peaks are enhanced, and there is a broad range in which conduction is enhanced also. The broad ranges of conductance are ascribed to alternative structures involving pyrazine and the solvent.

5. **bis-appended porphyrin** (Section 2-8): Results from various sets were inconsistent, highlighting the difficulties associated with this molecule. Even gold interactions (evidenced by enhancement of the gold peak) were inconsistent and underscore the subtle nature of solvent effects. Some sets of data indicated a peak at 0.1 G_0, with another at 0.2 G_0, but the structure(s) which caused the peaks cannot be determined.

Table 2-1: Molecular structure of molecules investigated experimentally in this chapter.

Molecule	Chemical formula	Structural diagram
1,8-octanedithiol	$C_8S_2H_2$	
4,4′-bipyridine	$C_{10}N_2H_8$	
TATPP Dipyrido[3′,2′:5,6;2″,3″:7,8]quinoxalino[2,3-i]dipyrido[3,2-a:2′,3′-c]phenazine Also called 9,11,20,22-tetraazatetrapyrido[3,2-a:2′3′-c:3″,2″-l:2‴,3‴]pentacene	$C_{26}N_8H_{10}$	
pyrazine	$C_4N_2H_4$	

bis-appended porphyrin

Short **Bi**-Phenanthroline-appended Porphyrin 32

MW = 1533.47

Where,   Ar =

2-1 Introduction to Chapter 2

> *"A basic task in molecular electronics is to understand electron transport through a single molecule bridged across two electrodes."[72]*

2.1.1 Description of the break-junction experiment

A break-junction is a nanoscale "gap" between two conducting electrodes into which is inserted a molecule whose conduction properties need to be investigated. Initially the two electrodes are touching or fused or even the one continuous piece of wire, which is stretched until the separation occurs, forming the minute gap between the broken ends of the electrodes. The molecule bridges the gap to complete an electric circuit. Initial break-junction experiments, like the one represented in Figure 2-2 below, allowed just one or a few measurement to be taken. The mechanical control of the break junction gap is by bending or pulling the electrodes and can be controlled to a level of angstroms by careful design of the equipment and/or the use of a piezoelectric device to control the necessary force.
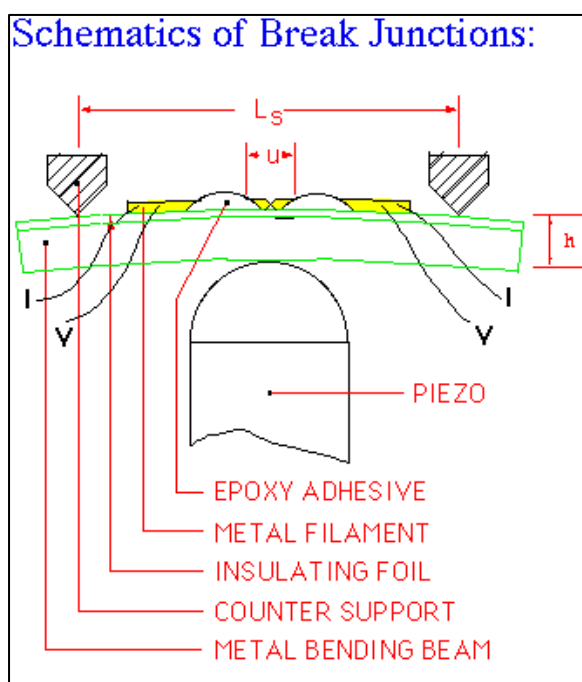
Figure 2-2: Schematic of one type of mechanically controllable Break Junction (courtesy of Chongwu Zhou[73]). (See also Section 1.2.3.2 above)

A piezoelectric tube is used in the mechanical control of the tips in STM and AFM scanning microscopy, where X,Y and Z displacement is controlled within a nanometer or less by application of potential to the sides of the tube. The STM scanner is easily adapted to perform break junction experiments provided the STM controller and the software have the necessary functionality.

A Scanning Tunnelling Microscope (STM) instrument was first reported by Xu and Tao in 2003[14] to perform multiple break-junction trials in a medium containing the molecule of interest, and the conduction of a single molecule was found by statistical analysis of the data from hundreds of conduction traces.

For the work expressed in this thesis, two different systems were available. The system used at Sydney University was a commercial STM (from Molecular Imaging). The system used at CSIRO (Lindfield) was a "home made" device. Relative advantages and disadvantages of the two different systems are discussed in Section 2.2.2 below.

2.1.2   Instrument provided at Sydney University – Molecular Imaging PicoPlus

The instrument used at Sydney University was a Molecular Imaging PicoPlus system with a Picoscan 2500 controller unit (see Figure 2-3 below), and using the Molecular Imaging's STM scanner (see Figure 2-4 below). (Note that since November 2005 Molecular Imaging products have been branded as Agilent products.)

The software loaded on the personal computer which drives the controller/instrument is called PicoScan 5.3.

Figure 2-3: The basic components of the Molecular Imaging scanning probe microscopy (SPM) system, which are attached to a personal computer. A number of different scanners can be placed in the PicoPlus unit (centre), including pure STM scanners and interchangeable AFM/STM scanners[74].

Figure 2-4: The Molecular Imaging's (Agilent's) STM scanner with two additional interchangeable pre-amplifier modules. One pre-amplifier module contains the logarithmic amplifier used to observe currents ranging from metallic conduction to molecular conduction observed during break-junction experiments (i.e. ranging from 10^3 to 10^{-5} G_0, depending on the applied bias.)[75]

2.1.3   Basic break-junction procedure on the Molecular Imaging system.

The procedure described below is a basic outline of the Molecular Imaging equipment at Sydney University and how the experiment functions. Further experimental details are outlined in the Experimental Section 2.2.2 below

A series of sweeps is usually collected using the solvent only, and then another series is collected after the molecule of interest is added to the solvent. Further series may be collected changing the bias and/or withdrawal speed. The sample/substrate is placed in a liquid cell.

Using a 0.25 mm gold wire in the STM scanner and placing the scanner over a gold substrate, the wire is brought to a distance of some nanometers from the gold substrate, a distance which is determined by the bias (typically 80 mV), STM scanning current (the "set point", say 0.4 nA), and electron tunnelling properties of the wire-substrate system. However, rather than raster the surface as in a normal STM, the instrument can then be configured to repeatably approach and withdraw from the gold surface, at different controllable speeds and distances (for example, approach at 200 nm s^{-1} for 40 nm and withdraw at 40 nm s^{-1} for 60 nm). After each withdrawal the instrument can return the to the set-point gap between the wire and the substrate, so it compensates for deformation of the wire tip or surface.

While the distance sweeps are occurring, the current flow (between the wire and the surface) is continually measured and current-distance data is collected (at a specified rate) and presented on the instrument's display as a graph of *current Vs distance*.

The approach speed is usually not important but the approach distance should be just sufficient to allow the tip to crash into the surface. This is observed by saturation current.

The withdrawal speed is typically from 1 nm s^{-1} to 40 nm s^{-1} and should be adjusted facilitate observations: that is, to observe gold conduction steps or molecular conduction steps in the *current Vs distance* graphs.

The number of data points is usually around 2000. At a known withdrawal speed the withdrawal distance from one data point to the next may be calculated (for example, 0.2 Angstroms per data point).

With the *linear amplifier* the current range is extremely limited and it is not possible to observe gold conduction steps with the linear amplifier available at Sydney University. The current values are converted directly to conductance values (in units of the conductance quantum), using the bias and the formula:

$$G = \frac{12,906 \times I}{V} \quad G_0 , \quad \text{where } I \text{ is in amps and } V \text{ in volts. (see Section 2.1.6}$$

below).

With the *logarithmic amplifier* the current values are actually a pseudo-log of the true current and have to be converted to true current values using a conversion table, which is constructed using a series of known resistors (see Section 2.2.3 below). Then the true current values are converted to conductance values using the same formula.

2.1.4   Basic break-junction procedure on CSIRO's "home made" system.

The system used at CSIRO (Lindfield) was a "home made" device. It consisted of a tip-holder mounted to a 1 dimensional piezo-electric device, a liquid-cell sample holder, a signal generator and oscilloscope, other electronics, and in-house developed software. It was quite functional for the break-junction experiment, being purpose-built by an expert in electronics and computer programming (Jan Herrmann).

The procedure for using it was basically similar to that for the Sydney University set-up, except that it could take thicker gold wires (up to 0.5 mm in diameter) and there was no "set-point" to control the initial distance between the wire and the substrate. Although the software had a complicated human interface, it had additional triggers to control the vertical motion of the wire and to assist in data collection and presentation. Further details of the system are expressed in Section 2.2.2.2 below and elsewhere[43].

2.1.5   Use of Gold substrates and wires.

The most common form of electrode used in molecular electronics is gold. Gold offers the advantages of remaining reasonably pure for the time of the experiment in the presence of both air, most solvents and even most electrolytes. However there is a limit to the type of molecules which will bind to gold and form the electrode-molecule-electrode linkage. The most common is the thiol linkage (which is considered to be a covalent bond), but alternatives are sought. This body of work is mainly concerned with the amine or azine linkage, which bind more weakly as a ligand to a metal atom (or ion) because of the electron affinity of the nitrogen atom. If the metal atom is part of the gold electrode surface then we have the connection through which conduction can take place.

A bidentate ligand such as 1,10-phenanthroline is a comparable alternative to the thiol linker (Chapter 3).

Gold also has the property that its surface is somewhat fluid. That is, atoms which are released from bulk may migrate over the surface quite freely, with a very small energy barrier to movement to neighbouring sites with local energy minima. This occurs even though the atom is still strongly bound to the surface (this is established in Chapter 3 and Chapter 4). It explains why, for example, it is impossible to maintain a thin gold wire during break-junction experiments. The atoms tend to migrate from the bulk back towards the thinnest part of the wire in order to reduce its surface-area to volume ratio (which reduces its overall energy). The speed of the break-junction experiment must be greater than the speed at which atoms can migrate back down the wire. But the speed must also be slow enough that the molecule has time to bridge the gap and that a number of data points (recording the current) may be recorded while it is there.

2.1.6   Quantum of Conductance (G_0) observed in Gold Wires

Current measurements during the separation of fused gold electrodes show that the current drops in a series of plateaus (see Figure 2-5 below). As the electrodes are separated (from a fused initial contact allowing a high level of metallic conduction) the gold thread which connects the two electrodes becomes increasingly thin. Its conductance is then roughly proportional to its cross-sectional area. With continued stretching, the diameter of the thinnest part of the wire decreases by discreet amounts of atoms related to the circumference at that point in time. This continues until the wire is a chain of single atoms, just before it breaks. Untiedt, *et al,* (2002) have established that the gold wire (consisting of a chain of single gold atoms) is most likely to be formed of a chain of one or 2 atoms, while forming chains of more than 3 gold atoms seems most

unlikely.[76] (Note: This applies only to un-stabilised gold chains, *i.e.* pure gold. In the

presence of attached molecules gold atoms may be quite mobile on the surface, their

mobility depending on the attached molecule. This may lead to stable single-atom chains

of more than 2 or 3 atoms in length. This is mentioned and established in various

sections below [e.g. Section 2.5.6] and in Chapter 4)

R. L. Whetten, B. E. Salisbury Georgia Institute of Technology, Atlanta, GA Quantum changes in conductance are observed at room temperature during the separation of two macroscopic contacts. In this case the separation is induced by vibrations in the experimental apparatus and the conductance is measured as a function of time by a digital oscilloscope. While in most cases this separation leads to a complete breaking of the electrical contact (inset) usually with a final conductance of a single quantum (2e^2/h), we also observe cases where the conductance changes reversibly (main plot) when the separation is not complete, but instead returns to full contact. The explanation of these observations lies in the creation of small nanometer-scale wires at the final stages of the contact separation.

Figure 2-5: Steps in the conductance curve during the formation of a gold wire by stretching. The left hand axis is in values of G_0. The inset shows the wire going to complete breakage, with the last step at about 1.0 G_0. The main graph shows the gold wire thinning in discreet steps, however it isn't allowed to break, and then the thinned gold wire spontaneously re-forms, illustrating the fluidity of gold atoms that they can migrate from the bulk back to the thinnest part of the wire. (From Whetten, *et al*, with their caption.[77])

The conductance of a chain of single gold atoms is closely equal to the unit of

conductance quantum, G_0, whose value is given by:

$$G_0 = \frac{2e^2}{h}$$
Equation 2-1

where h and e are the fundamental constants:

e = charge of an electron = 1.6021917 x 10^{-19} Coulomb, and

h = Planck Constant = 6.626196 x 10^{-34} Js

This gives a value of G_0 as **7.7480917 × 10^{-5}** Siemens.

This is analogous to a resistor with a value of 12,906.4 Ω (*i.e.* conductance is the reciprocal of resistance). Thus, from measurements of the observed current (*I*) under a fixed bias (*V*), the conductance (expressed in units of the conductance quantum) can be found simply using Ohms law (V=IR) and a constant, as follows:

Conductance (in units of the conductance quantum),

$$G = \frac{12,906 \times I}{V} \qquad G_0 \qquad \text{Equation 2-2}$$

2.1.7   Conductance observed in molecules.

When the break-junction experiment is conducted within a medium containing conducting molecules, further conductance steps are sometimes observed somewhat below the value of 1.0 G_0. This is understood to be instances when one or more of the conducting molecules bridge the gap between the electrodes after the last gold wire has snapped. The use of a Scanning Tunnelling Microscope to do this was first reported by Xu, *et al*, in 2003[14] (See Figure 2-6 below), using the Molecular Imaging Picoscan and additional software and hardware, with a logarithmic amplifier. They also analysed thousands of repeated break junction experiments by simply binning the data from conductance traces, which produced histograms with peaks representing conductance of one molecule or multiples thereof. Their results are included in the summary in Table 2-2 (page 2-15, below).
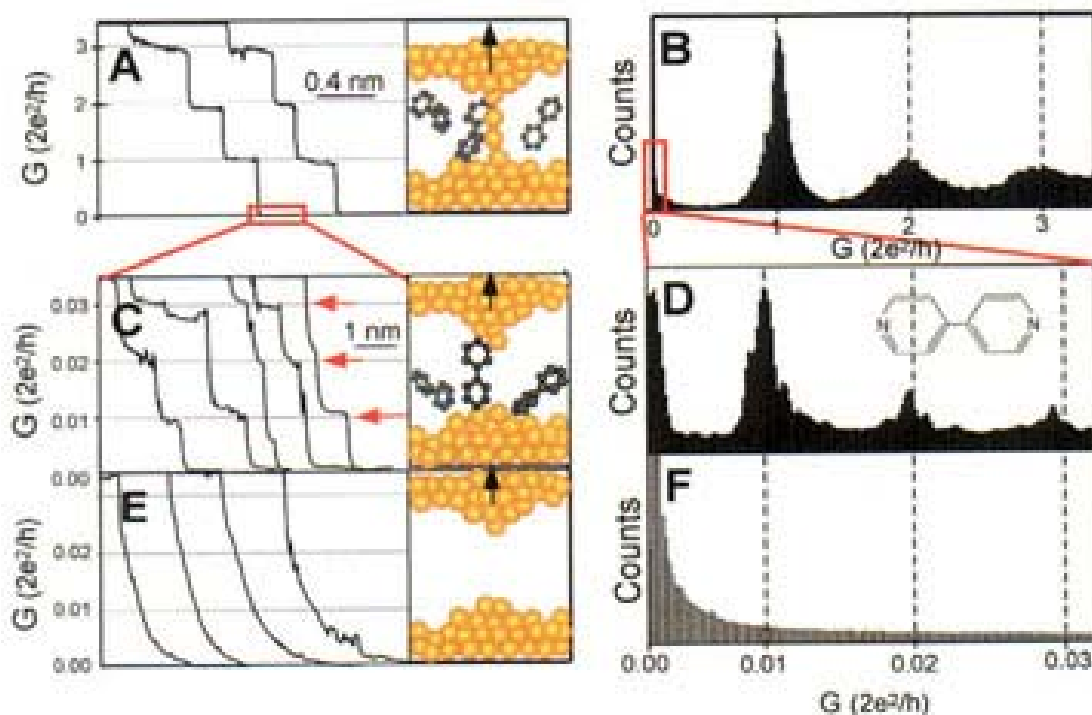
Fig. 1. (A) Conductance of a gold contact formed between a gold STM tip and a gold substrate decreases in quantum steps near multiples of G_o ($= 2e^2/h$) as the tip is pulled away from the substrate. (B) A corresponding conductance histogram constructed from 1000 conductance curves as shown in (A) shows well-defined peaks near 1 G_o, 2 G_o, and 3 G_o due to conductance quantization. (C) When the contact shown in (A) is completely broken, corresponding to the collapse of the last quantum step, a new series of conductance steps appears if molecules such as 4,4' bipyridine are present in the solution. These steps are due to the formation of the stable molecular junction between the tip and the substrate electrodes. (D) A conductance histogram obtained from 1000 measurements as shown in (C) shows peaks near 1 ×, 2 ×, and 3 × 0.01 G_o that are ascribed to one, two, and three molecules, respectively. (E and F) In the absence of molecules, no such steps or peaks are observed within the same conductance range.

Figure 2-6: This graphic and caption are taken from Xu and Tao's 2003 paper of Conductance in Single Molecules using STM tip with repeated break-junctions and statistical analysis[14]. **Graph B** shows conductance of gold atomic wires, with peaks at multiples of 1.0 G_0. **Graph D** shows conductance of the molecule (4,4'-bipyridine), with peaks at multiples of 0.01 G_0.[14]

2.1.8   Summary of conductance values of selected molecules

Table 2-2 (below) lists some relevant molecules studied recently and their

conductance values (at low or zero bias), as determined experimentally by break-junction

or other methods, or theoretically, and provides a useful handy reference for

interpretation of results in this chapter and for the application of the convenient

calculation methods of Chapter 5. (There are more examples in later sections, relevant to

TATPP (Table 2-9, page 2-62) and bis-appended porphyrin (Table 2-13, page 2-91)).

Table 2-2: Conductance Values for Selected Molecules (in 10^{-4} G_0)
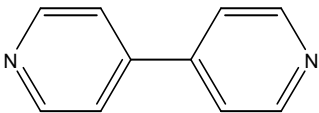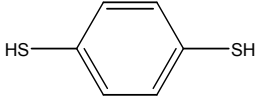
Table 2-2 Molecule and diagram	EXPERIMENTAL			THEORY	
	Experim'l Cond'ce. 10^{-4} G_0.	Year[Ref]	Exper'l. Method	Theo'cl Cond'ce 10^{-4} G_0.	Year[Ref]
4,4'-bipyridine	100	2003[14]	BJ	586 30	2005[78] 2008[79]
hexanedithiol	12.3 H=~11.0 L=~3.0 (L)=3.6	2003[14] 2006[40] 2006[40] 2006[69]	BJ BJ BJ BJ	20 23.9	2005[80] 2002[81]
octanedithiol	2.5 0.14 2.08 H=1.68 L=0.42 H=2.5 L=0.5 H=2.4 L=0.5 (L)=0.4 (L)=0.45	2003[14] 2001[15] 2007[16] 2006[11] 2006[11] 2007[72] 2007[72] 2006[40] 2006[40] 2006[69] 2006[68]	BJ cAFM cAFMrev BJ,multV BJ,multV BJ BJ BJ BJ BJ(LSA) BJ(slow)	0.86 3.2	2001[15] 2002[81]
decanedithiol	0.21 0.18 H=0.20 L=0.04 (L)=0.057	2003[14] 2007[16] 2006[40] 2006[40] 2006[69]	BJ cAFM BJ BJ BJ	0.44	2002[81]
dodecanedithiol	0.11	2007[16]	cAFMrev		
1,4-benzenedithiol	14.34 300 110 H=1000 L=100 5.8	2005[82] 2006[42] 2004[83] 2006[84] 2006[84] 1997[62]	nanoGap BJ BJ BJ BJ BJ (single)	6,063 top 645 hollow 2,100	2004[85] 2004[85] 2001[86]
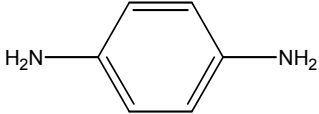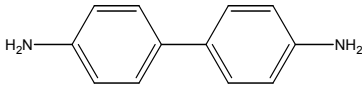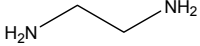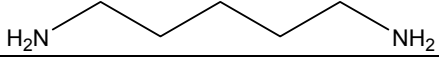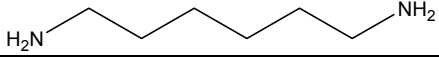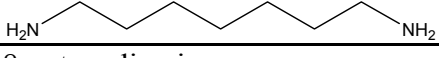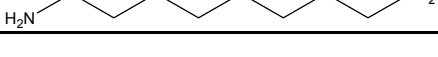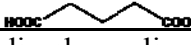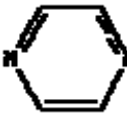
Table 2-2 Molecule and diagram	EXPERIMENTAL			THEORY	
	Experim'l Cond'ce. 10^{-4} G_0.	Year[Ref]	Exper'l. Method	Theo'cl Cond'ce 10^{-4} G_0.	Year[Ref]
1,4-bezenedimethanedithiol	4.9 6	2005[82] 2004[83]	nanoGap BJ		
1,4-diaminobenzene	64	2006[42]	BJ	460 64 28	2007[87] 2006[55] 2007[88]
4,4'-diaminobiphenyl	11.6	2006[55]	BJ	16	2006[55]
4,4'-diaminoterphenyl	1.8	2006[55]	BJ	3.5	2006[55]
1,2-ethanediamine	49 L=1.2	2006[42] 2006[40]	BJ BJ		
1,3-propanediamine	28	2006[42]	BJ		
1,4-butanediamine	10 10 H=14.5 L=0.95	2006[42] 2006[43] 2006[40] 2006[40]	BJ BJ BJ BJ		
1,5-pentanediamine	3.5	2006[42]	BJ	NH=4.46 NH_2=6.71	2007[89] 2007[89]
1,6-hexanediamine	1.5 H=2.7 L=0.06	2006[42] 2006[40] 2006[40]	BJ BJ BJ	NH=1.67 NH_2=3.95	2007[89] 2007[89]
1,7-heptanediamine	0.7	2006[42]	BJ	NH=0.55 NH_2=0.63	2007[89] 2007[89]
1,8-octanediamine	0.3 H=0.49 L=0.28	2006[42] 2006[40] 2006[40, 89]	BJ BJ BJ	NH=0.47 NH_2=0.56	2007[89] 2007[89]

Table 2-2 Molecule and diagram	EXPERIMENTAL			THEORY	
	Experim'l Cond'ce. $10^{-4} G_0$.	Year[Ref]	Exper'l. Method	Theo'cl Cond'ce $10^{-4} G_0$.	Year[Ref]
1,9-nonanediamine H_2N〜〜〜NH_2				NH_2=0.16	2007[89]
1,2-ethanedicarboxcylic acid HOOC〜COOH	H=12.0	2006[40]	BJ		
1,4-butanedicarboxcylic acid HOOC〜COOH	H=2.6 L=0.98	2006[40] 2006[40]	BJ BJ		
1,6-hexanedicarboxcylic acid HOOC〜〜COOH	H=0.52 L=0.18	2006[40] 2006[40]	BJ BJ		
1,8-octanedicarboxcylic acid HOOC〜〜COOH	H=0.10 L=0.029	2006[40] 2006[40]	BJ BJ		
pyrazine	nil			30 ~4.7(s)	2008[90] 2005[91]
Hydrogen atom in a gold chain `Au-H-Au`	1000 to 5000	2006[92]		5000	2006[93]
Carbon atom in a gold chain `Au-C-Au`	1000 to 2000	2003[94]		1000	2003[94]

Abbreviations used in Table 2-2:

H=   High Conductance regime
L=   Low conductance regime
(L)= Inferred (or assumed to be) Low conductance regime
BJ= Break Junction
cAFM=Conducting Atomic Force Microscopy
rev= revised method
LSA=Last Step Analysis used to analyse results
slow=withdrawal speed 1nm/s (usually around 40nm/s)
nanoGap=(method described in relevant paper)
multV=multiple values of bias were used to establish the conductance
BJ(single)=a single value was observed
NH= theoretical values calculated on amine NH anchoring group
NH₂=theoretical values calculated on amine NH_2 anchoring group
top and **hollow** refer to assumed sites for theoretical values (See Figure 11, below)
(s) – modelled by using sulfur atoms to bind to gold electrodes (substituting for 2 hydrogen atoms), so in effect it was something like 1,3-dithiol-2,5-pyrazine

2.1.9   Tunnelling Decay Constant

The conduction of similar alkanes whose difference is only in the number of carbons in the backbone has been observed so as to deduce the tunnelling conductance of one single carbon atom (*i.e.*, a –CH_2– unit as part of an alkane). This quantity is called the "tunnelling decay constant", ß, and is used in the following formula, which follows from McConnell (1961)[95]:

$$G_N = Ae^{-ß N},$$ Equation 2-3

Where G_N is the conductance of a chain containing N -CH_2- units. Occasionally the tunnelling decay constant is expressed in length (*i.e.* per Angstrom).

Use of this formula in is explored more in Chapter 5.

2-2 Particulars of the break-junction experimental work

2.2.1 Summary of molecules investigated

Below is a summary of the molecules examined using the break-junction method:
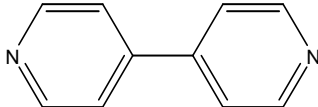
Name: **1,8 octanedithiol**

Molecular Structure:

Source: Aldrich (97+% purity, used as supplied).

Rationale: This molecule was explored initially to see whether the method was valid and to compare with prior research by using the linear amplifier.

Name: **4,4′-bipyridine**

Molecular Structure:

Source: Fluka (anhydrous, assay>98%, used as supplied).

Rationale: This molecule was examined also to see whether the method was valid on azines and to compare with prior research.

Name:

Dipyrido[3′,2′:5,6;2″,3″:7,8]quinoxalino[2,3-*i*]dipyrido[3,2-*a*:2′,3′-*c*]phenazine

Also known as: 9,11,20,22-tetraazatetrapyrido[3,2-a:2′3′-c:3″,2″-l:2‴,3‴]pentacene

Abbreviation: **TATPP**
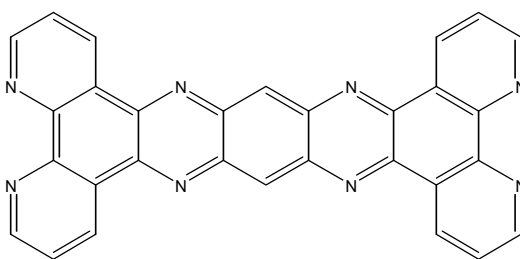
Molecular Structure:

Source: Prepared by the University of Sydney Organic Chemistry Department (by Dr. Iain M. Blake.) by a procedure involving the condensation of 1,2,4,5-benzenetetraamine with 1,10-phenanthroline-5,6-dione, outlined elsewhere.[96, 97]

Rationale: This molecule was synthesised for this experiment. It was considered to be likely to have good conduction because of its conjugation, to show consistent conduction plateaus because of its rigidity, and to bind well to gold because of the bidentate nature of the two phenanthroline-type ends.

Name: **pyrazine**

Molecular Structure:

Source: Fluka (assay >98% , used as supplied.)

Rationale: Pyrazine was considered to be a most likely molecule to use in the break-junction experiment because its conduction was expected to be high, as it was a small rigid molecule consisting of a π-conjugated ring. It also supported one theme of this thesis, that nitrogen groups could be used rather than thiols to attach molecules to the gold electrode. No prior publications were found to indicate an experimental value for the molecular conduction of pyrazine, however a theoretical value had been calculated.

Name: **bi-phenanthroline-appended porphyrin**

Abbreviation: bis-por

Molecular Structure:

Short **Bi**-Phenanthroline-appended Porphyrin 32

MW = 1533.47

Where, Ar =
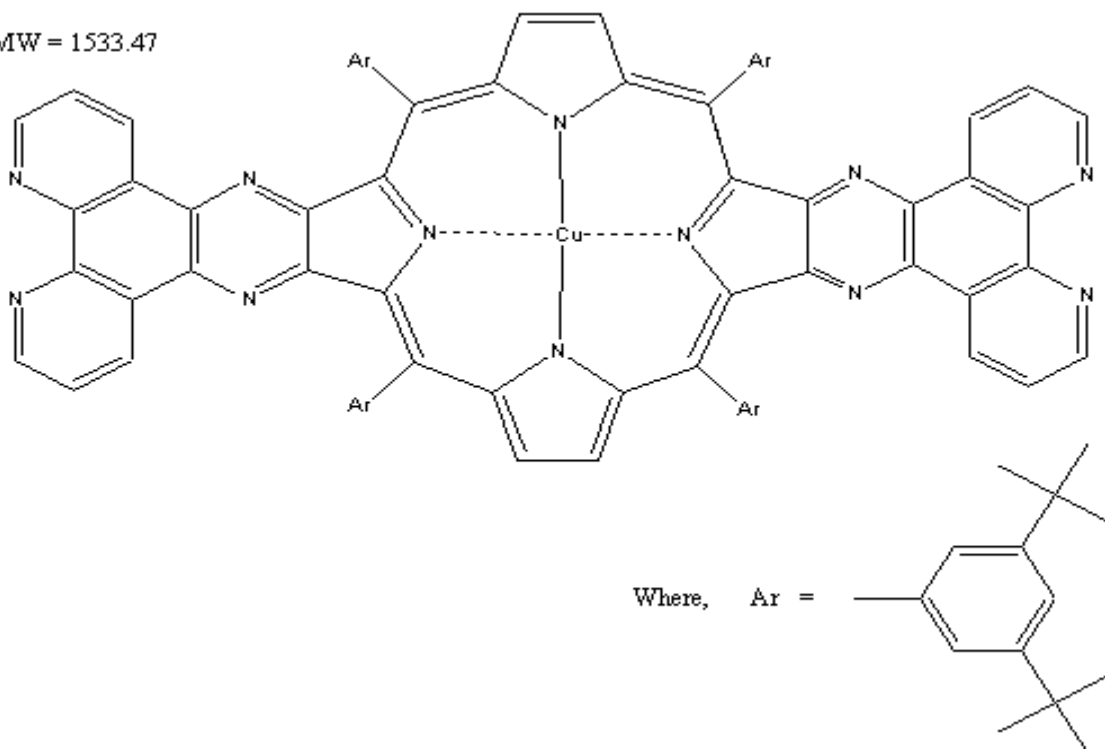
Source: The bis-phenanthroline-appended porphyrin was prepared by Dr Warren Hough at the University of Sydney Organic Chemistry Department, by condensing a porphyrin tetraone with 1,10-phenanthroline-5,6-diamine described elsewhere.[98]

Rationale: Porphyrins are of particular interest to organic chemists at Sydney University as possible candidates for molecular wires and devices[98, 99]. A likely method of securing such molecules to gold electrodes is via the phenanthroline "alligator clip"[36], hence this molecule has been synthesised. However very little experimental work has been done on it and on the conductance of porphyrins in general. This is the first attempt to obtain its molecular conduction.

2.2.2 Experimental procedure

The break junction experiments carried out in this thesis were either conducted at:

- Sydney University's Electron Microscope Unit (***USYD***)

or

- The Commonwealth Serum and Investigation Research Organisation laboratories located at Lindfield NSW (***CSIRO***),

with slight differences in the experimental procedure at the two sites, and with two very different instruments, for which there is more information in the next section.

Water: Throughout the experiment all water referred to, for both cleaning and experimentation, was rated 18.2 MΩ Millipore® water fed from the town water supply.

Glassware: Cleaning of all glassware and the liquid cell was done by simmering in ~15% nitric acid for more than 1 hour, after which they were rinsed copiously, left to soak for 30 minutes, and rinsed copiously again in water.

Gold: Gold tips were prepared by cutting 0.25 mm gold wire at USYD or 0.5 mm wire at CSIRO with snips. They were then H_2 flame purified, and at CSIRO they

were further treated by ultraviolet light. Gold tips for aqueous experiments were then coated in apiezon wax using a heating device with wax as supplied from Apiezon Products, M&I Materials, Manchester, UK. Gold substrates at USYD were made of evaporated gold on freshly cleaved mica and H_2 flame annealed as provided from Molecular Imaging Inc, and further H_2 flame purified just prior to use. Gold substrates at CSIRO were prepared in-house by vacuum evaporation on glass and H_2 flame purified. Prior to use they were treated with ultraviolet light.

Solvents: (molecular structures are shown in Figure 2-7)

- Toluene ($C_6H_5CH_3$, MW=92.14) was freshly distilled from sodium prior to use.

- Phenyloctane (synonym: octylbenzene) ($C_6H_5(CH_2)_7CH_3$, MW=190.33) was used as provided from Fluka (purum >98% gc; B.P. 264-268°).

- Carbontetrachloride (synonym: tetrachloromethane) (CCl_4, MW=153.82) was freshly distilled from calcium hydride.

- Aqueous: Sodium perchlorate monohydrate ($NaClO_4{:}H_2O$, MW=140.46) was used as provided form UNIVAR (99.5% purity) to prepare a solution in water (18.2 MΩ Millipore®).

(a)   Toluene

(b)   Phenyloctane

(c)   Carbontetrachloride

(d)   sodiumperchlorate
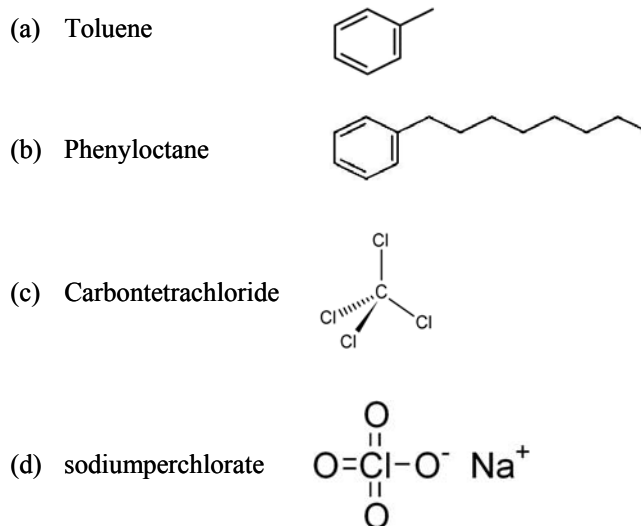
Figure 2-7: Solvents used for break-junction experiments.

Equipment: The instruments used have been previously described (Sections 2.1.2, 2.1.3 and 2.1.4). Additional equipment was as follows:

For USYD experiments the gold substrate was placed on the STM sample holder and a Teflon liquid cell placed over it and clamped into position (Figure 2-8).
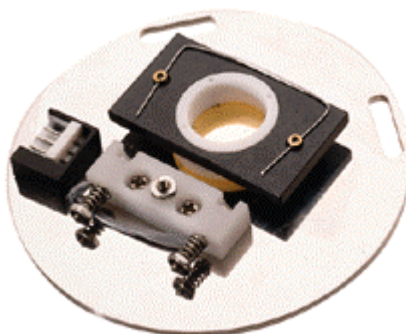
Figure 2-8: Agilent's (ex-Molecular Imaging) sample holder and liquid cell (white), with a gold substrate inserted between the liquid cell and the sample holder, used in experiments conducted at USYD (image courtesy of Agilent web site)[100].

For experiments conducted at CSIRO, a "home-made" Teflon liquid cell was used and when assembled with the gold substrate was functionally similar to Figure 2-8.

Procedure: For USYD, first the gold tip was placed in the head of the STM unit (Figure 2-4) and the unit placed in position in the PicoPlus II (Figure 2-3), and the height of the sample plate adjusted using a dummy sample plate. Then the solvent was placed in the liquid cell to about half-full and the sample plate inserted beneath the STM scanner unit. The STM was set to approach the sample. When it engaged (*i.e.* when it detected the "set point" current) the custom spectroscopy script ("current Vs distance") was opened and parameters entered which enabled the gold tip to approach the surface and crash into the gold substrate, and then withdraw at a specific speed, and it was also set to perform multiple sweeps. (If sets of sweeps were required in air, this was first done without the solvent, and then done again with the solvent.)

For the volatile solvents toluene and carbontetrachloride the experiment was conducted in a glass environmental chamber with a petri dish containing the solvent placed in the bottom of the chamber (to saturate the air in the chamber). The environmental chamber is shown in the PicoPlus II unit in Figure 2-3.

Various sets of sweeps were conducted in the solvent (or air) adjusting the parameters as necessary for each set (*e.g.* bias or withdrawal speed).

After all the sets for the solvent were done, a solution of the solvent and the molecule was prepared at double the required molarity. The sample plate was removed (or when the environmental chamber was used, the STM scanner was removed) and the liquid cell "topped-up" with the solution containing the molecule. The components were then reassembled and various sets of sweeps were conducted on the molecule.

For experiments conducted at CSIRO, the procedure was extremely similar, with the only difference being in the way the unit was assembled and in the operation of the

approach of the gold tip and how the software then controlled the instrument (described elsewhere[43]).

2.2.2.1   Instrument used at Sydney University, advantages and disadvantages.

The experiments conducted at Sydney University used a Molecular Imaging STM (Scanning Tunnelling Microscope: see Section 2.1.3 above) with parameters entered into its operating software to control the motion of the gold probe. The main *advantages* of using this system were:

1. The functionality already existed in the instrument and the only extra item required was the gold wire to make the tips.

2. The instrument could be configured to carry out multiple successive sweeps without user intervention.

3. By fine adjustment of the set-point current and switching *on* the option to "restore servo" after each sweep, the instrument was able to reset the initial distance for the start of the next sweep. This gave rise to greater consistency in the sweeps and allowed for smaller movement of the tip. (During each sweep there is an amount of distortion to the surface and the tip, changing the geometric alignment. This means that at the end of one sweep, the gap between the tip and surface may not be the same as it was at the beginning, even though the movement up was equal to the movement down. By using the set-point current, the gap between tip and surface can be restored prior to the next sweep.)

4.   It was contained within a vibrational isolation unit.

The main *disadvantages* of the using STM scanner were:

1.   The functionality of the software did not allow the option to trigger movement based upon current events. This means that there was no direct control over how much the tip crashed into the gold surface (it was controlled indirectly by resetting the height to the set-point current.) and at what points in withdrawal to start and stop data collection. This also meant that the user had to observe the current traces of each sweep continually to monitor for anomalies and to stop and reset the experiment as necessary.

2.   There was no functionality in the software to reject sweeps. Given that only 10 to 30% of sweeps show evidence of molecular conduction, the extraction of relevant data was quite difficult, given the amount of data that had to be analysed.

3.   The gold wire could be no more than 0.25 mm in diameter and, being gold, was often too soft and flexible to stay in position or remain straight. Short wires had to be used but sometimes they wouldn't reach the sample without the STM nose hitting the sides of the liquid cell.

4.   The instrument and the environment had a number of performance and operational shortcomings which added to the difficulties of the experiment, sometimes causing confusion trying to interpret what was being observed, and at other times causing significant delays.

5.   Experiments were initially done using the standard STM head (i.e. with a **linear amplifier**), which had a limited range. It could observe conduction in the molecular range (i.e. around 10^{-4} G_0), but not the metallic range (*i.e.* gold conduction, around 1.0 G_0.), so that it wasn't clear whether the break-junctions were being correctly formed each time.

6.   Later a **logarithmic amplifier** was obtained, which could observe conduction over a range from less than 10^{-5} up to 10^3 G_0, so that it was possible to observe both molecular and gold conduction in the one sweep. The logarithmic amplifier needed to be calibrated (by creating a calibration file using a number of known resistors: see Section 2.2.3 below for further details) and the data files created by the instrument's software had to be converted using the calibration file. Programs were written in FORTRAN to do the data manipulation.

7.   The PicoScan 5.3 software, which operated the controller and was the human interface, presented immediate graphs (traces) of each sweep on screen as Current Vs Distance curves. From these graphs it was possible to identify steps in the conduction curves which may indicate metallic or molecular conduction. However the graphs did not display results in conductance values. For the linear amplifier it was a simple piece of mathematics to determine the conductance value represented by a current step, and the step could then be identified. However for the logarithmic amplifier it was more difficult to evaluate apparent conduction steps. Furthermore, there was no functionality to present ongoing histograms of the accumulated data: final results of sets of sweeps could only be determined well after the experiment had finished.

2.2.2.2   Instrument used at CSIRO, advantages and disadvantages.

The experiments conducted at **CSIRO** used a "Home Made" instrument built by Jan Herrmann[43], which consisted of a mounting tube attached to a piezo device which in turn was attached to a stepper-motor. The whole device was placed over the sample, which was covered in a PTFE (Teflon) liquid cell. There were a number of different amplifiers available to explore different conduction ranges, as well as a logarithmic amplifier. The software which controlled the device was also written by Dr Jan Herrmann of CSIRO. The main *advantages* of this instrument were:

1. The mounting tube allowed thicker gold wire to be used (up to 0.5 mm diameter), providing greater rigidity to the system.

2. The software included functionality to control the break-junction depending on current triggers. This allowed placement of the tip to be reset automatically if gold conduction was not evidenced.

3. Data from each sweep was immediately presented on screen (in values of G_0) and the cumulative data from the set was displayed as a histogram, updated after each sweep. This enabled the experimenter to know immediately what kind of results were developing.

4. The software also enabled the device to reset its vertical position if there was too much or not enough conduction (and ignore the data), allowing sweeps to run without the need of user observation, and obtaining a higher percentage of data files with valid data.

5. It was possible to define many more data points in a given range with the CSIRO equipment, enabling even very small molecular conduction steps to be captured.

6. The computer was loaded with "PC Anywhere" and so effectively once the sample was set up, the experiment could be conducted from a remote site (*e.g.* from home), allowing large numbers of sweeps to be run with convenient observation, and also allowing some parameters to be changed remotely.

The main *disadvantages* of the *CSIRO* system were:

1. The instrument had no horizontal displacement. If, for some reason, the spot on the sample had become unsuitable for further sweeps, it had to be disengaged and moved manually.

2. It used a linear amplifier. It had a high range of about 3 or 4 orders of magnitude, and the range was extended by changing the gain setting, which enabled the operator to examine all possible conduction ranges from 13.0 G_0 to 10^{-7} G_0, however it was usually not possible to observe gold conduction and molecular conduction in the one sweep (see Section 2.3.1.2 below).

3. After each sweep it returned the tip to the original height (in absolute reckoning), which meant that if the surface or tip had deformed during the previous sweep, the next sweep started either too close or too far from the

surface (*i.e.* it did not rely upon tunnelling current to reset the actual gap between the tip and the sample).

4. The software had a complicated user interface.

However, since the software was written in-house, most of the disadvantages could possibly be addressed in some future re-write of the software.

2.2.3   Use of logarithmic amplifier

The logarithmic amplifier used at Sydney University enables current measurements to be taken over a range encompassing many orders of magnitude, and so it enables both gold steps and molecule steps to be observed in the one conduction sweep. However the amplifier is nominally logarithmic and the only way to convert to actual current is to construct a "calibration curve" using a series of known resistors and sweeping over a bias range for each resistor.

Various resistors were purchased from KA Electronics and Dick Smith Electronics and each was measured using a high quality multimeter (see Table 2-3 below). Each resistor in turn was bridged between the STM Scanner (with the logarithmic amplifier inserted) and the mounting plate, and was swept in the bias range – 10 to +10 volts and the output from the log amplifier (log current) tabled against the actual current (which is the input (bias) divided by the resistor value). The results are graphed in Figure 2-9 (low range) and Figure 2-10 (high range) below. From these sets of data a single conversion table was created which was used for the analysis in experimental sections to convert log-amp current to actual current.

Table of Resistor Values (kΩ)
5.65
50.8
100
510
996
10,020
103,600
737,000
1,265,000

Table 2-3: Resistors used in calibration of the logarithmic amplifier. Values were measured using an high-quality multimeter and are accurate to less than 1%.

Plot of output from Logaritnmic Amplifier (x axis) against true current in microAmps (calculated) (y-axis) --- Legend indicates the size of the resistor in kOhms ---

MAXIMUM SCALE 10 nanoAmps

Legend:
- 1265561
- 737240
- 103650
- 10025
- 996.15
- 510.25
- 100.02
- 50.834
- 5.6535

X-axis: Log Amp outputed value (nanoAmps)
Y-axis: True Current - microAmps
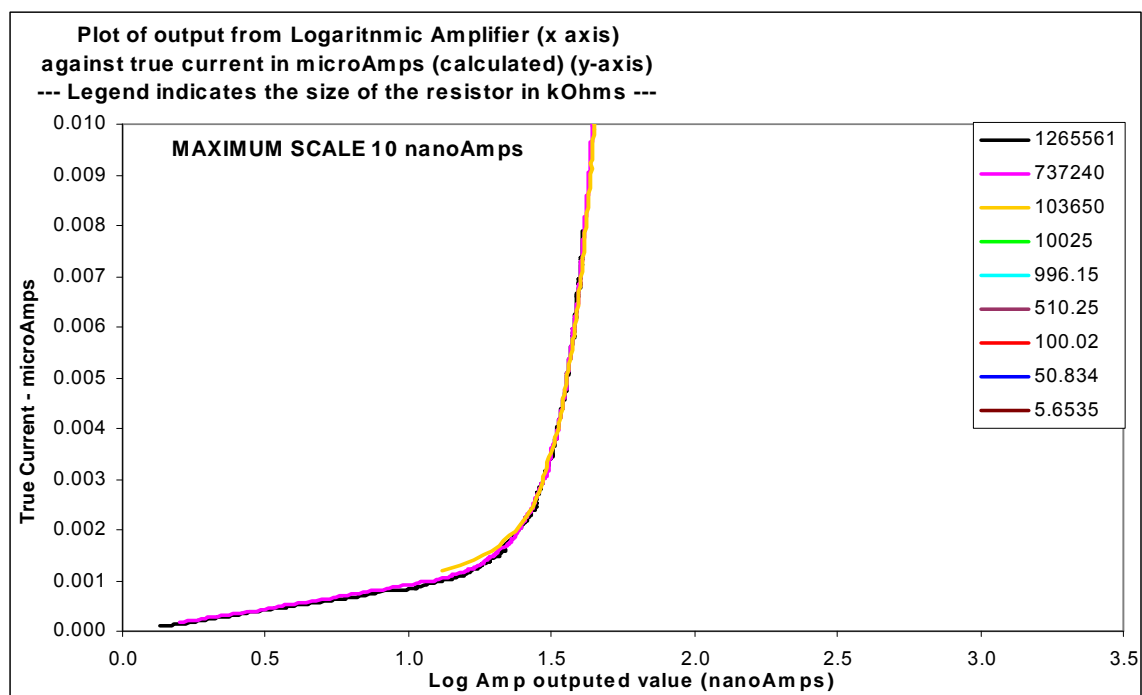
Figure 2-9: Construction of calibration curve: graph of True Current (**low range** – up to <u>10 nanoAmps</u>) against amplifier output ("Log-Current"). From zero to about 1.0 nanoAmp there is a linear relationship between the log-amp output and the true current. Only the two highest resistors give data in this range. From 1.0 nanoAmp to 3.0 nanoAmps the calibration curve swings upwards, and the third highest resistor (103650 kΩ) comes into effect at about 1.8 nanoAmps. There is an overlap of the ranges of first three resistors up to about 6.0 nanoAmps.

Plot of output from Logaritnmic Amplifier (x axis)
against true current in microAmps (calculated) (y-axis)
--- Legend indicates the size of the resistor in kOhms ---

MAXIMUM SCALE 10 microAmps

Legend:
- 1265561
- 737240
- 103650
- 10025
- 996.15
- 510.25
- 100.02
- 50.834
- 5.6535

True Current - microAmps

Log Amp outputed value (nanoAmps)
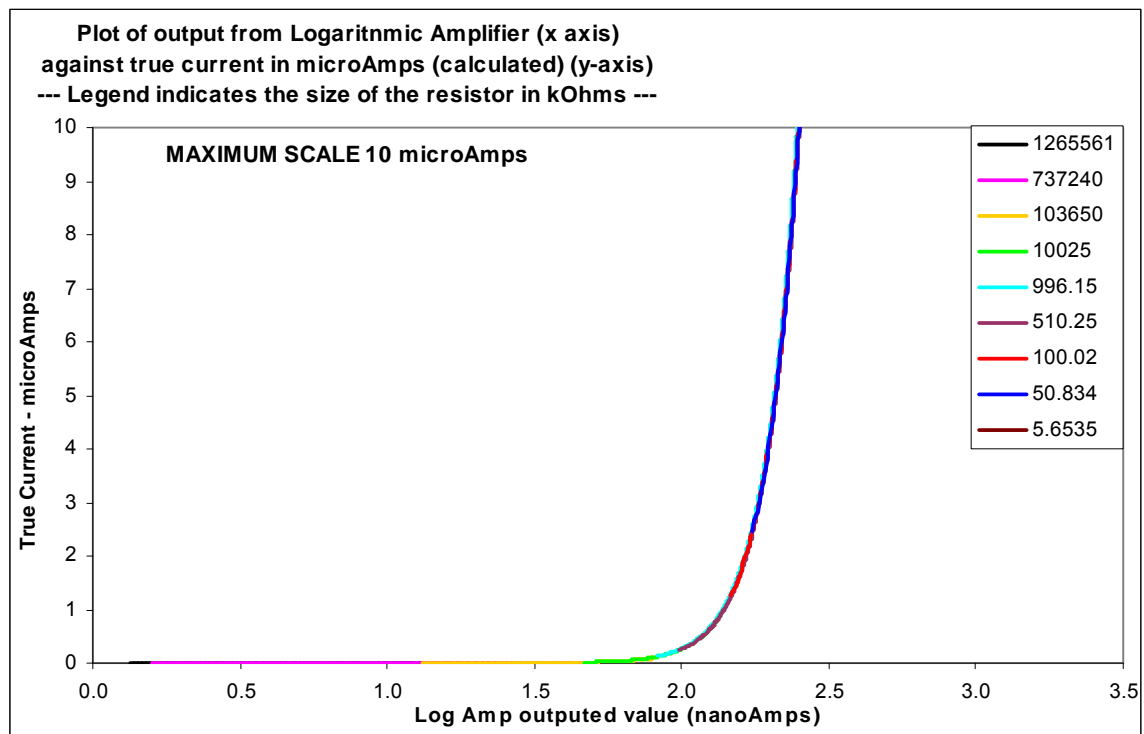
Figure 2-10: Construction of calibration curve: graph of True Current (**high range** – up to <u>10 microAmps</u>) against amplifier output ("Log-Current"). Following from the previous figure, the effective range of the various resistors continue in the calibration curve, with some overlap.

2-3 General comment on experiments and results

General details of the experimental preparation are given in Section 2.2.2 and include sources and purity of chemicals and solvents, and general sample preparation and experimental techniques which are not particular to individual molecules. Anything particular to a set of experiments or a molecule is described under the molecule's individual heading from Section 2-4 to 2-8 below.

2.3.1 Terminology and treatment of raw data.

Each withdrawal of the gold wire from the surface is called a "**sweep**". A group of sweeps with the same conditions done consecutively is called a "**set**", and a set may comprise hundreds of sweeps. For each of the five molecules investigated, a number of sets were collected, including solvent-only sets. If sets were collected consecutively as part of the one experiment they are called a **group**. A "**trace**" is the graph of data from a single sweep, and it may show a "**step**", which is a consecutive series of data points with roughly the same conduction value, which is generally considered to be a "**conduction event**": either the conduction of a single molecule, multiple molecules, or metallic gold wires of thickness one or more gold atoms. Some traces have multiple steps. Other traces may have no steps or ill-defined steps.

The raw data values for each set of sweeps were converted to values of conductance quantum, G_0, as follows:

- With the *linear amplifier* the raw data values were actual current (I in amps). The current values are converted directly to conductance values (G) using the bias (V in volts) and the formula $G = \dfrac{12{,}906 \times I}{V}$ G_0 (see Section 2.1.6 above).

- With the *logarithmic amplifier* the raw data values were a nominal log of the true current and had to be converted to true current values using the conversion table, which is constructed using a series of known resistors (see Section 2.2.3 above). Then the true current values are converted to conductance values using the same formula as above.

- With the data produced at CSIRO, the raw data values were true conductance values in G_0, so no further conversion was necessary.

The sets of data (in G_0 values) were analysed by two different methods. Both methods defined a certain **range** of G_0 values to which the analysis was limited. The difference in the two methods was in the way in which sweeps were rejected, leaving a number of **valid** sweeps.

Rejection *Method 1*: The only criterion by which a sweep was rejected was if the first data point did not reach a "saturation value" (this would indicate that metallic conduction was not achieved and the gold wire did not form). Thus all other sweeps were included[φ]. The reasoning behind this method was that sweeps may include instances of conduction events which may not be indicated by clear steps but which may be evidenced in the overall summation of data (following Quek, *et al.*, 2007[87], who found that most conduction steps were less than 1 Angstrom wide and used all 59,000 sweeps on benzenediamine without filtering).

Rejection *Method 2*: In addition to the rejection criterion of *Method 1*, individual sweeps were also rejected if there were not 200 or more data points in the defined analysis range. The reasoning behind this method was that most of the sweeps indicated

---

[φ] Where a linear amplifier was used saturation or gold conduction could not be established and so all sweeps were included in the analysis.

noise (erratic conduction signals) in the analysis range and that any true conduction event would be indicated by a *significant* step in the individual trace. This method resulted in very few individual sweeps being accepted. The range was determined by an arbitrarily chosen upper bound, and then both the lower bound and the bin size were 1% of the upper bound.

Both methods relied on "**binning**" of the data, in which the data from all *valid* sweeps in a given set was collated into **bins** using a defined range of G_0 values and a certain bin size, usually resulting in anywhere between 40 and 200 bins per range. Each bin would cover a small extent of the data range and would have a "**count**", which was the total number of data points from all valid sweeps of the given set which fell into that bin. Each bin also had a mid-point value.

In order to compare different data sets the count was divided by the number of valid sweeps, and histograms were drawn graphing "**Counts per Valid Sweep**" against conductance, $\mathbf{G_0}$ (where G_0 was the mid-point value of the bin). A peak in the histogram would indicate if a set showed a consistent conduction event (according to the reasoning of each method).

2.3.1.1   Special analysis techniques used.

Apart from the standard practise of binning the data to form histograms, the following techniques were applied:

(a)   Normalising data by dividing by the number of valid sweeps: (This technique was applied in all analyses). It was found that the most valid method for comparing different sets of data was to normalise each set by dividing by the number of

valid sweeps (previous paragraph). This gave a powerful tool for comparing molecule sets against solvent sets within the same group, and to some extent across groups provided the bin size was the same. This method has not been reported before.

(b)   **Rejection of sweeps without 200 data-points in the defined range**: As described above in *Rejection Method 2*, this was method applied to all molecules when binning was done on a linear scale within a defined range. This method has also not been reported before.

(c)   **Log G_0 scale graphs:** Where possible additional histograms were also constructed using a $\log_{10}$ scale for the horizontal axis (conductance). This was proven to be a useful technique to view the overall effect of the molecule to conductance over a wide range (i.e. over 6 orders of magnitude, from 10^{-5} G_0 to 10 G_0), which in some cases showed no peaks in linear scale histograms. This method was reported by Gonzalez, *et al*, (2006).[68]

(d)   **Gaussian smoothing**: In one group of data obtained from CSIRO it was useful to apply Gaussian smoothing to join different data sets. This is a common statistical analysis technique, and has been used in break-junction experiments before[43].

2.3.1.2   Various gain settings used at CSIRO

At CSIRO a linear amplifier was used. However it had a variable gain setting, so that even though the range of the amplifier was limited, it was possible to look at various conductance ranges by changing the gain setting. By this method each set of sweeps was done at a fixed gain setting and limited to a particular range (for example the "gold

conduction range", around 1.0 G_0). To examine other ranges, the gain setting was changed and another set of sweeps was conducted.

The range of conductance values depended upon the bias. Approximate ranges for each gain setting, at 100 mV and 50 mV, are shown in Table 2-4.

	Bias 100 mV		Bias 50 mV	
Gain Setting	max (G_0)	min (10^{-4} G_0)	max (G_0)	min (10^{-4} G_0)
5	13	10	26	20
6	1.3	1	2.6	2
7	0.13	0.1	0.26	0.2
8	0.013	0.01	0.026	0.02
9	0.0013	0.001	0.0026	0.002

Table 2-4: Approximate range of conductance values able to be observed for the amplifier on the CSIRO equipment, at various gain settings and at bias of 100 mV or 50 mV.

2.3.1.3   Gold quantized conduction peaks

For various reasons (which need not be mentioned here), the logarithmic amplifier was not used in all cases at Sydney University. However in the sets of data where it was used, the data sets were also "binned" in a range which included 1.0 G_0, to see if gold conduction steps were evident. Nearly all such sets of data, including solvent sets, showed very clear peaks at or near 1.0 G_0 and most showed at least one other peak at 2, 3 or 4 G_0. Samples of such histograms are produced in Figure 2-11 below. Generally these histograms are not shown in the results sections (long range $\log_{10}$ scale histograms are used to draw attention to the gold quantized conduction peaks where necessary). In this thesis, the enhancement of gold conduction steps after the molecule is added to the solution is viewed as evidence that the molecule is able to interact with the gold and this concept is explored in the various results sections.

This comment does not apply to experiments conducted at CSIRO, which used a series of linear amplifiers rather than a log amplifier. The set-up provided a cumulative histogram on screen at the end of each sweep, as the experiment was in progress. Gold conduction was established by first running a set of sweeps at low gain (gain=5), providing a range which included 1.0 G_0. In subsequent sets the gain was increased to examine lower ranges of possible molecular conduction gold conduction was assumed if current reached the maximum of the range.

Samples of histograms for each molecule in the gold conduction range.
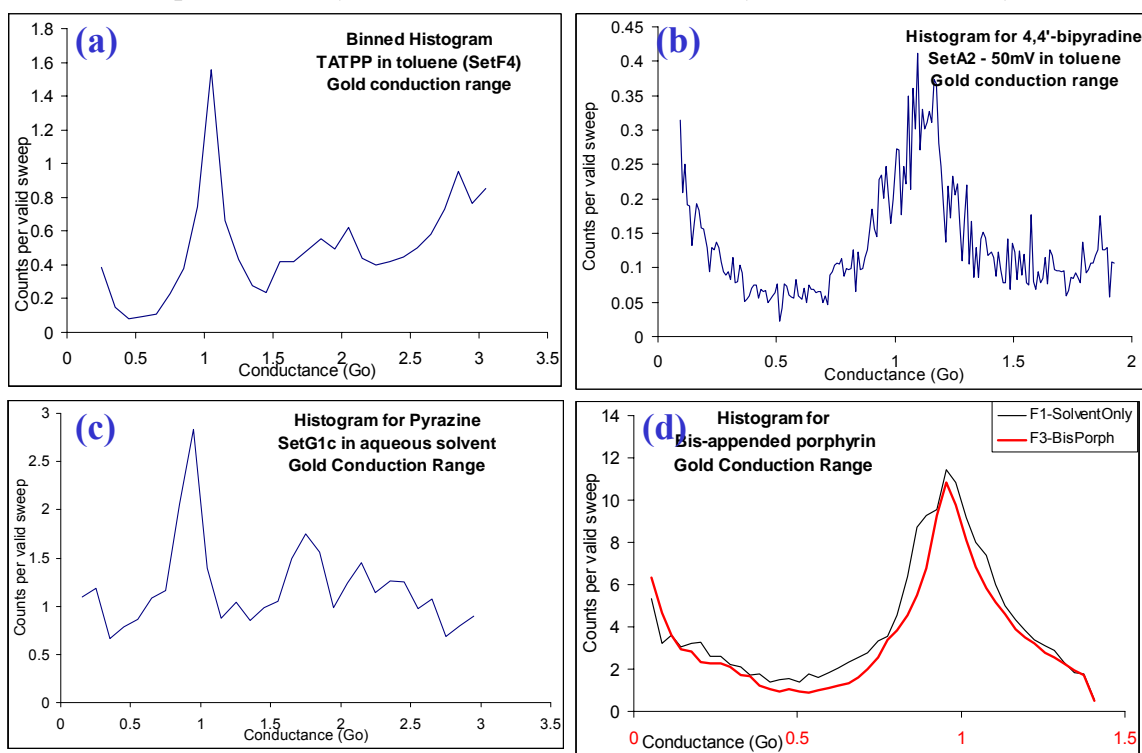
Figure 2-11: Sample of histograms from the various data sets in the gold conduction range. Graph (d) includes a solvent-only histogram. **(a)** TATPP in toluene, *Set F4*; **(b)** 4,4′-bipyridine in toluene *Set A2*; **(c)** Pyrazine in aqueous solution *Set G1c*; and **(d)** bis-phenanthroline-appended-porphyrin in phenyloctane (*Set F3*) and phenyloctane only (*Set F1*).

2.3.2   Other data selection and analysis techniques used in literature.

Usually with break-junction experiments there are four types of conduction traces which may be produced by a single sweep:

A.   Traces which show clear steps in the molecular conduction region (40-50%*),

B.   Traces which show noise in the same region (20%*),

C.   Traces which drop smoothly and steeply to very low conduction (tunnelling), which produce little data in the molecular conduction region (30%*), and

D.   Traces which do not commence from a saturation value, which indicate that an effective break-junction has not formed.

* The percentages of traces A, B and C are from Li, *et al*, (2006)[101] on 1,8-octanedithiol: See Chapter 4 Figure 4-57 on page 4-6 for examples of the three types of traces. Li avoids traces of type D by using interface software. For sets of solvent-only sweeps, the percentage of traces of type C is much greater, but solvent sets still occasionally show steps or noise in the molecular conduction area[87].

Type D are traces which are produced because the mechanical control of the tip does not create an effective break-junction. With overriding software to interface with the STM controls during the experiment one can gain more sophisticated control over the movement of the gold tip and greatly reduce the "bad data" and eliminate all type-D traces. Such software was not available in this work.

A narrower selection of data would selectively enhance the histograms produced in this thesis, but the underlying histogram peaks should appear to some extent, even with all the types of curves included, as noted by Gonzalez, *et al*, (2006)[68]:

"*Data selections do not help improve the result.*"

and

"*The situation is unsatisfactory, because there is at present no generally accepted objective selection criterion.*"

It is not always clear how prior researchers have selected their data (*i.e.* what criteria did they use for rejecting invalid sweeps): in some cases they have expressly stated that no data selection techniques were employed[43] (other than rejecting traces of type D based upon saturation, which seems to be a universal practise), and in others they probably used filters to reject a number of individual sweeps to improve the peaks in their histograms, however some leading researchers have been quite vague in the specific method of filtering (*i.e.* whether they manually trawled through the data to select desirable traces [subjective], or they used an algorithm built into their software [objective])[56, 101]. But data selection has been a common practise for enhancing results. The percentage of curves which produce "good" data varies considerably: from as much as 80%[11] to as little as 15%[72], and this is often dependent on the type of molecule being investigated. For 1,8-octanedithiol the percentage was typically 40%[101], 15% for perylene tetracarboxcylic[72], and 20 % for oligoaniline[11]. It is common to have 20 to 30% of sweeps producing noise in the molecular conduction region (*i.e.* no clear steps[40]). Even the solvent-only sets have a small percentages of traces with features which appear like molecular conduction steps[101].

Many research groups (including ours) have struggled with the concept and method of data selection. Perhaps because, as we found, it is often the case that individual traces have good steps but the binned histograms show no distinct peaks[42, 43].

Gonzalez, *et al*, (2006)[68] applied an algorithm to their data which extracted data from distinct plateaus (steps) only and then constructed the histogram from this selected data. With this method there was no need pre-select the "good" curves. They also used a method of plotting against log G rather than G, and also they subtracted the base-line, which was determined from solvent-only sweeps. With these methods their histograms became more distinct.

Jang, *et al*, (2006) used "last step analysis", where only the ***last*** plateau was used to construct a histogram. Their algorithm found the last step by first finding the last sudden drop and then looking at the data which appeared immediately before it. With this method there is no need for prior data selection.

In the work to prepare this thesis a number of different analysis techniques were investigated, including last step analysis, slope analysis, data smoothing, Fourier analysis, noise reduction, base-line subtraction and various sweep rejection criteria. However none of these techniques gave both significant and consistent improvements in results. Only the two different rejection methods described above have been included in the presentation.

2-4 Investigations of 1,8-octanedithiol

1,8-octanedithiol.

(For a comment about *thiol* and ***thiyl*** terminology see Section 4.1.3 below)

2.4.1 Rationalization:

As a preliminary series, the 1,8-octanedithiol was examined to establish "proof of concept". It is one of the most studied molecules in molecular electronics and its conduction has been measured in a variety of ways, both experimentally and theoretically. It was also one of the first to be used in the same type of break-junction experiment and clear results have been obtained by Tao[14].

The linear amplifier was used in these experiments.

2.4.2 Background research

Various experimental and theoretical values for the conductance of 1,8-octane dithiol are reported in Table 2-2 above, on page 2-15. A high-conductance regime and a low-conductance regime have been identified, corresponding to two different binding configurations of the molecule to the gold electrodes (these concepts are taken up more fully in Chapter 4). The generally accepted values for conductance of a single 1,8-octanedithiol molecule are 2.5×10^{-4} G_0 (high conductance) and 0.5×10^{-4} G_0 (low conductance).

2.4.3 Experimental set-up:

The break-junction experiments were carried out in approximately 1 mM of 1,8-octanedithiol in toluene.

2.4.4   The sets of sweeps for 1,8-octanedithiol

Three sets of sweeps were recorded, one solvent-only set labelled ***Set A0*** and two dithiol sets labelled ***Set A1*** and ***Set B2***. The parameters for these sets are listed in Table 2-5 below.

Set	item	bias	Solvent	Amp	number of sweeps	withdrawal speed ($nm \, s^{-1}$)
A0	solvent only	-50 mV	toluene	lin	296	12
A1	1,8-octanedithiol	-50 mV	toluene	lin	887	12
B2	1,8-octanedithiol	+50 mV	toluene	lin	824	12

Table 2-5: Parameters for the sets of sweeps relating to 1,8-octanedithiol

A selection of individual traces for *Set A1* is shown in Figure 2-13 below.

2.4.5   Results from all sets of data for 1,8-octanedithiol.

The data from the three sets of sweeps was analysed according to both *Method 1* and *Method 2* (Section 2.3.1 above) and the resultant histograms are shown in Figure 2-12 below. In units of 10^{-4} G_0, *Method 1* shows two possible peaks for *Set A1* at 2.4 and 5.9 (with 656 valid sweeps), and no definite peaks for *Set B2* (209 valid sweeps), whereas *Method 2* shows two strong peaks for *Set A1* at 2.2 and 5.8 (but with only 21 valid sweeps) and no peaks *for Set B2* (81 valid sweeps). Both methods show no peaks in the solvent-only set. (The steep rising parts of the graphs below 1.5 x 10^{-4} G_0 are due to the limitations of the instrument.)

These results are set out in Table 2-6, page 2-47 below and compared with standard results from Li, *et al*,[101].

Because the linear amplifier was used for 1,8-octanedithiol and thus the data covered a small range, there was no advantage to be gained by plotting against Log_{10} of conductance.

1,8-octanedithiyl – *Method 1* and *Method 2*.
All Sets and solvent only
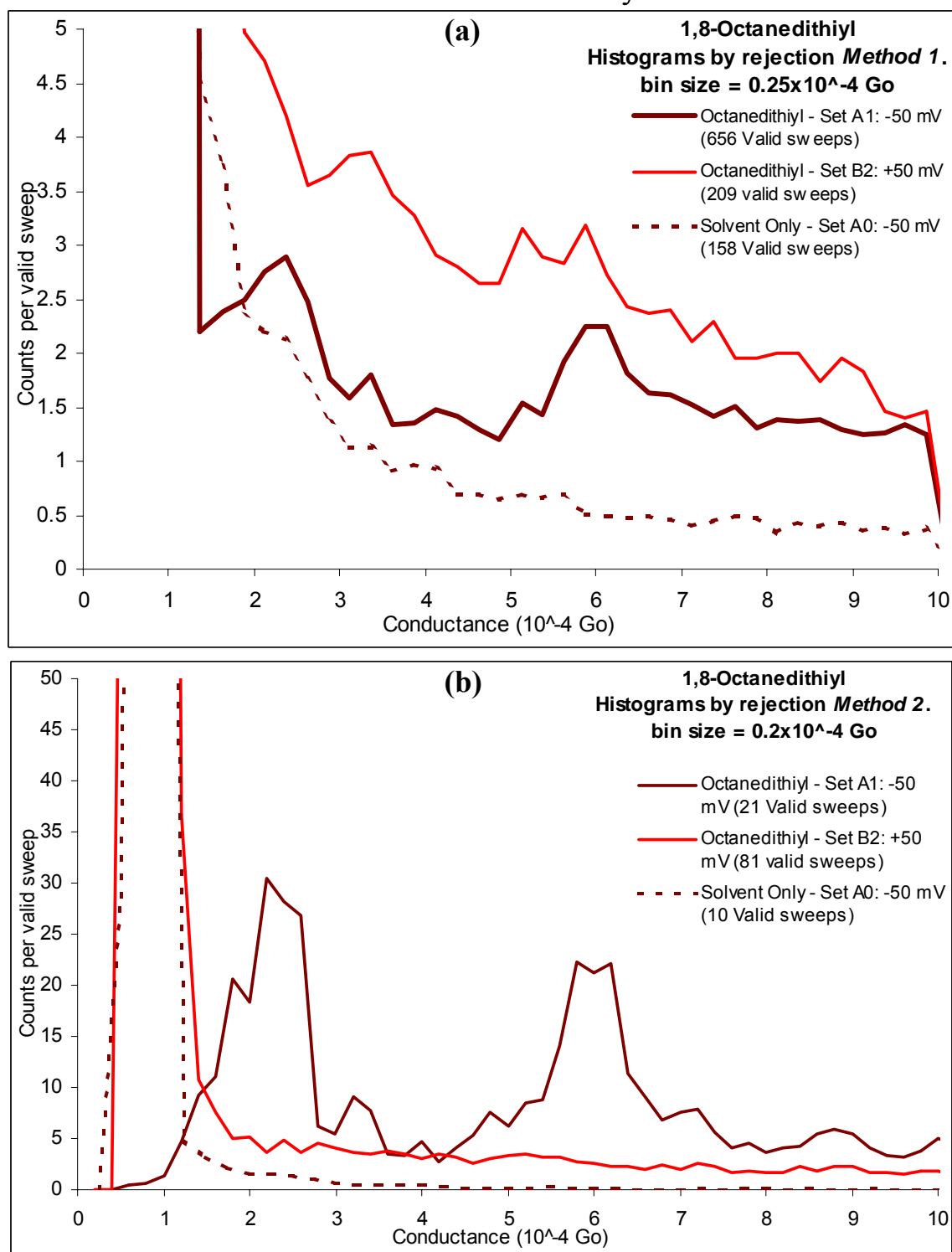
Figure 2-12: **(a)** *Method 1* and **(b)** *Method 2* histograms of the two sets of sweeps on 1,8-octanedithiol and the solvent set.

.

.

Series	Analysis *Method*	Peak Value (10^{-4} G_0)	Peak Quality	Interpretation
Set A1	*1*	2.4	poor	Conduction of a single thiol molecule.
Set A1	*1*	5.9	poor	Conduction of a two thiol molecules.
Set A1	*2*	2.2	strong	Conduction of a single thiol molecule.
Set A1	*2*	5.8	strong	Conduction of a two thiol molecules.
Set B1	*1*	nil	-	-
Set B1	*2*	nil	-	-
Li[101]	-	2.5	strong	Conduction of a single thiol molecule.
Li[101]	-	4.8	strong	Conduction of two thiol molecules.

Table 2-6: Summary of the results obtained for 1,8-octanedithiol. Included are standard results from Li, *et al*,[101] for comparison
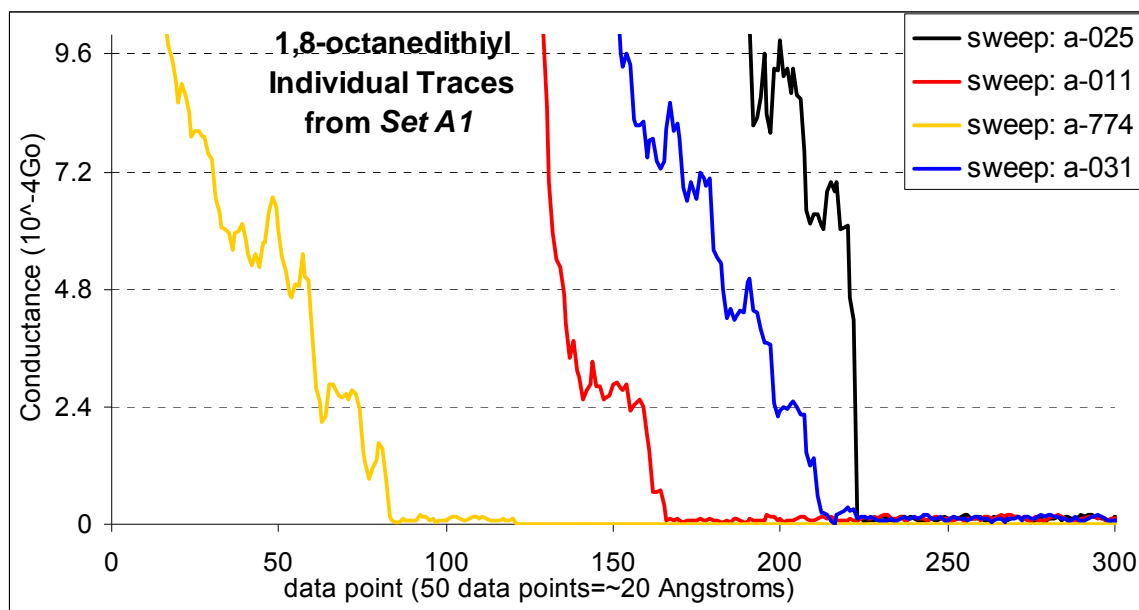
Figure 2-13: Sample of four individual traces of sweeps from *Set A1* for 1,8-octanedithiol. Horizontal dotted lines are drawn at intervals of 2.4×10^{-4} G_0, which is the conductance value determined for a single 1,8-octanedithiol molecule. 50 data points is approximately 20 Angstroms withdrawal distance.

2.4.6   Discussion of 1,8-octanedithiol results

Set A1 show similarity with prior research (*e.g.* Li, *et al,*[101] and Chen, *et al,*[40] – see Table 2-2, page 2-15 above) and establish that the procedure and the instrument are capable of performing single molecule conductance measurements, with the conductance of a single 1,8-octanedithiol molecule being 2.5×10^{-4} G_0. However *Set B2* does not show clear peaks (it has very weak broad peaks which differ slightly from *Set A1* and prior research, but are within the same order of magnitude). The explanation for the lack of clear peaks in *Set B2* may lie in the fact that the tip bias was positive rather than negative, though it is unclear exactly how this would affect the results in a non-electrochemical cell and an insulating solvent.

The use of the linear amplifier restricts the observable range such that it cannot be established that a gold bridge has been formed prior to creation of the break-junction, however the results from *Set A1* indicate that it is still possible to obtain reliable evidence of molecular conduction without this. Furthermore, with the linear amp, the window of current range is limited to a factor of 10, and to extend the results to explore a different G_0 range the bias must be modified (for example an increase in the bias from 5 mV to 50 mV (then to 500 mV) will decrease the mid-range from approximately 10^{-2} G_0 to 10^{-3} G_0 (then to 10^{-4} G_0), however such large bias changes cannot be considered an independent variable and Li, *et al,* report that histogram peaks broaden and decrease in height with higher voltages (over 80 mV, say), as well as shift slightly[101].

The results have established that the general methods of instrument usage and sample preparation techniques are adequate for detecting conductance in single molecules. Much greater sampling is required in order to obtain qualitative results however.

2.4.7   Conclusion of 1,8-octanedithiol Results

The conductance of a single **1,8-octanedithiol** molecule has been determined with a linear amplifier to be 2.5×10^{-4} G_0, agreeing with prior literature for the same break-junction but which used a logarithmic amplifier. However the results are not as distinct. Nevertheless, the aim was achieved, that is that the techniques and method were adequate for observation of single molecule conductance.

Chapter 4 gives a more thorough treatment of the general body of literature based upon the binding mode of thiol monolayers to gold, and the resulting implications for conductance measurements in break-junction experiments.

2-5 Investigations of 4,4′-bipyridine

4,4′-bipyridine.

2.5.1 Rationalization:

4,4′-bipyridine has previously been researched experimentally and theoretically. Experimentally, it has the highest *reliable* conductance value of the list of relevant molecules in Table 2-2 (page 2-15, above), and was the first molecule reported by Xu and Tao (2003) in their ground breaking paper which introduced the repeated break-junction method for determining molecular conductance[14]. It was considered important for this current thesis to reproduce these results and to draw conclusions, if possible, concerning the method. The logarithmic amplifier was used for this molecule.

2.5.2 Background research

Conductance of a single 4,4′-bipyridine molecule has been found to be:

- 100×10^{-4} G_0 by experimental methods, in an aqueous solvent[14].

- 30×10^{-4} G_0 by an unpublished theoretical calculation (provided by Mr Sören Wolthat in a personal communication).

- 586×10^{-4} G_0 by a published theoretical calculation.[78]

2.5.3 Experimental set-up:

The break-junction experiments involving 4,4′-bipyridine were carried out in a solution of approximately 10 mM of 4,4′-bipyridine in toluene.

2.5.4   The sets of sweeps for 4,4′-bipyridine

Five sets of sweeps were recorded, one solvent-only set labelled **Set B3** and four bipyridine sets labelled **Set A1, Set A2, Set B1** and **Set B2**. The parameters for these sets are listed in Table 2-7.

Set	item	bias	Solvent	Amp	number of sweeps	withdrawal speed (nm s^{-1})
B3	solvent only	50 mV	toluene	Log	297	12
A1	4,4′-bipyridine	20 mV	toluene	Log	157	12
A2	4,4′-bipyridine	50 mV	toluene	Log	730	12
B1	4,4′-bipyridine	30 mV	toluene	Log	212	12
B2	4,4′-bipyridine	60 mV	toluene	Log	1000	12

Table 2-7: Parameters for the sets of sweeps relating to 4,4′-bipyridine.

2.5.5   Results from 4,4′-bipyridine (all sets)

The data from the five sets of sweeps was analysed according to both *Method 1* and *Method 2* (Section 2.3.1 above).

Using *Method 1*, the conductance histograms from the four 4,4′-bipyridine sets are individually graphed with the solvent curve (Figure 2-14 below), and then graphed together on the one graph after baseline subtraction of the solvent curve (Figure 2-15 below). Using *Method 2*, all sweeps were rejected in all sets except for 2 sweeps in *Set A1*, and the resultant histogram for that set is shown (Figure 2-16 below).

Both *Method 1* and *Method 2* show possible peaks (which hardly rose above the noise level) for *Set A1* at around 110×10^{-4} G_0, with no clear peaks in any of the other sets, including the solvent only set.

These results are set out in Table 2-8, page 2-54 below, and compared with

standard results from Xu and Tao[14], whose histograms are also shown (Figure 2-17).

4,4'-bipyridine: *Method 1*
Individual graphs of each *Set*.
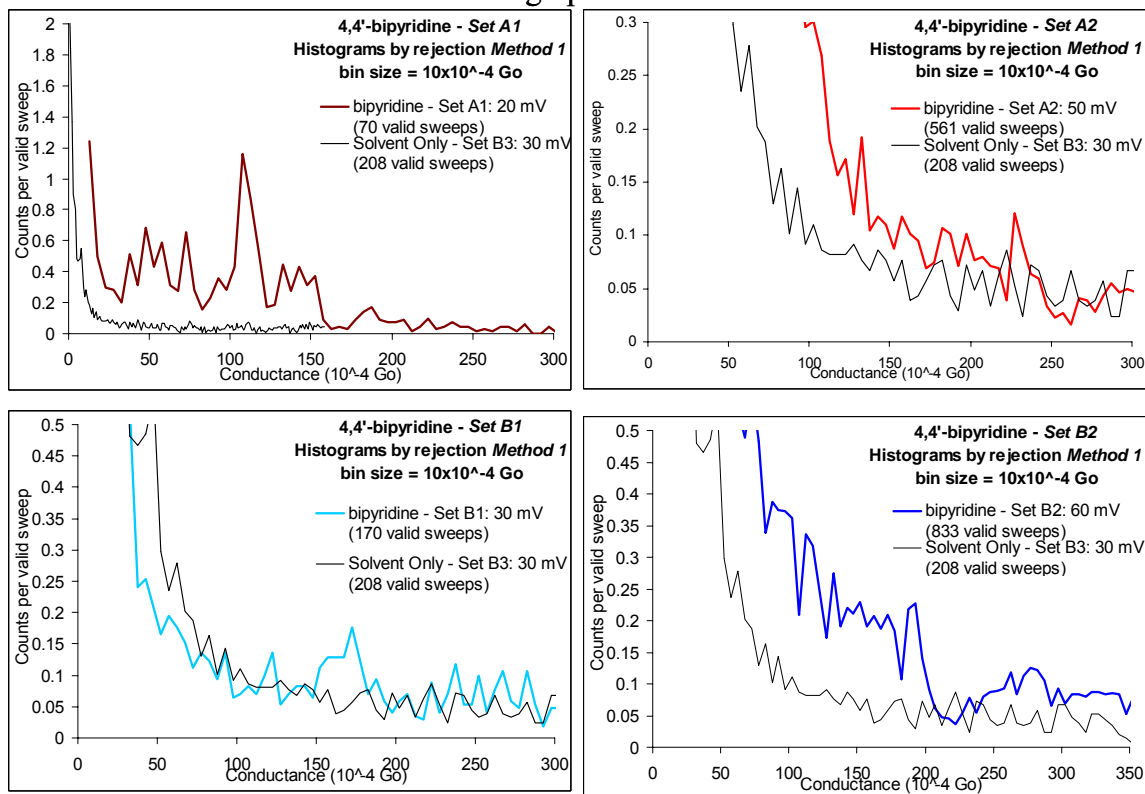
Figure 2-14: Binned histograms for 4,4′-bipyridine sets by *Method 1* analysis: Individual data sets are shown with the solvent curve (toluene) on each graph.

4,4'-bipyridine - *Method 1*

All *Sets* on a single graph after baseline subtraction (solvent *Set B3*).
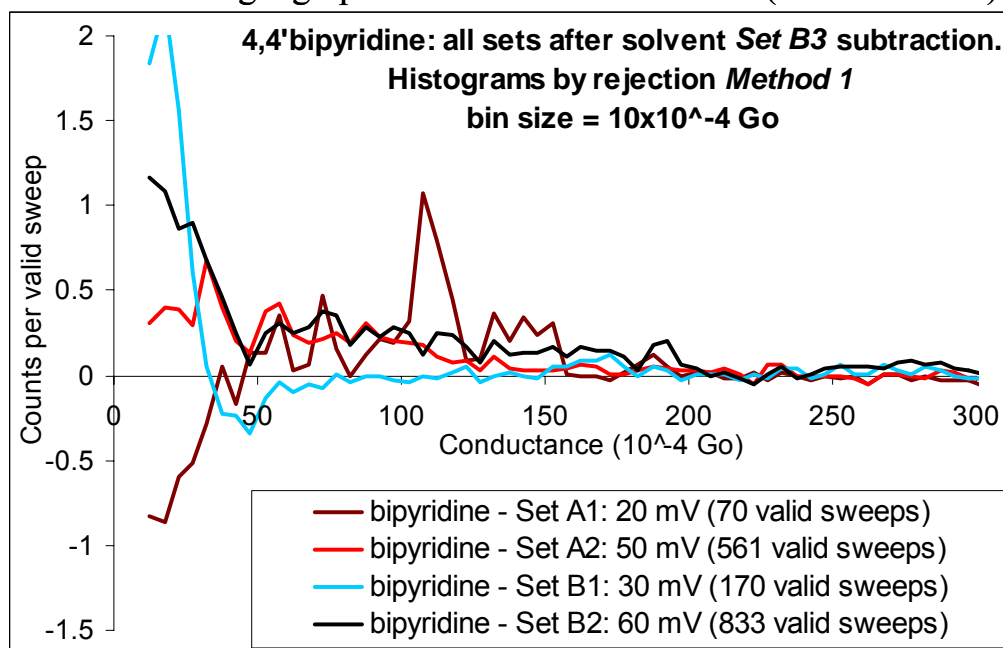
Figure 2-15: Binned histograms for 4,4′-bipyridine sets by *Method 1* analysis: All data sets are shown after baseline (solvent curve) subtraction.

4,4'-bipyridine - *Method 2*

Set A1 only.
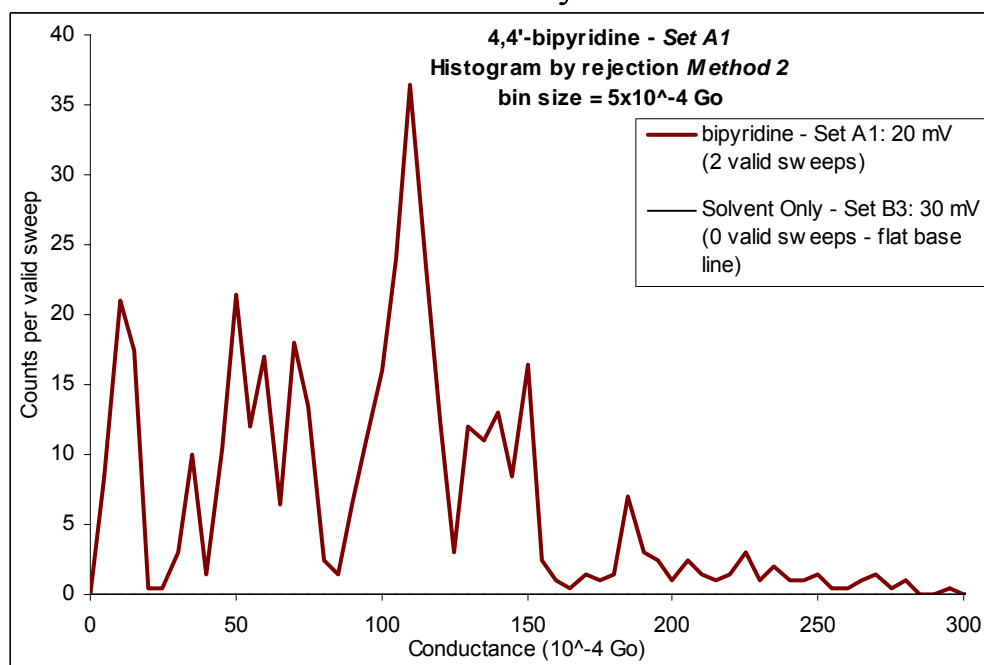
Figure 2-16: Binned histogram for 4,4′-bipyridine sets by *Method 2* analysis. Only *Set A1* had valid sweeps (2).

Series	Analysis *Method*	Peak Value (10^{-4} G_0)	Peak Quality	Interpretation
Set A1	*1*	107	poor	Indeterminate.
Set A1	*2*	110	poor	Indeterminate.
All other sets	*1 and 2*	nil	-	-
Xu and Tao[14]	-	100	strong	Conduction of a single bipyridine molecule.
Xu and Tao[14]	-	~198	medium	Conduction of two bipyridine molecules.
Xu and Tao[14]	-	~295	weak	Conduction of three bipyridine molecules.

Table 2-8: Summary of 4,4′ bipyridine results. Included are standard results from Xu and Tao[14] for comparison
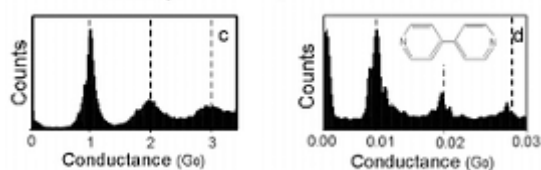
Figure 2-17: Histograms of Xu and Tao[14] for gold steps (**c**) and molecular conduction steps (**d**)

2.5.6   Log$_{10}$ histograms of 4,4′-bipyridine

Long-range comparison of the 4,4′-bipyridine and solvent results is shown in Figure 2-18 below. In **(a)** both curves are similar and differences between them generally do not rise beyond the level of noise.

Subtraction of the solvent from 4,4′-bipyridine (Figure 2-18 **(b)**) shows that 4,4′-bipyridine enhances the gold conductance peak (around 1.0 G_0), meaning that the steps for the last gold conduction plateau in the individual traces are generally longer than in the solvent only. This is a common observation of many break-junction

experiments and is believed to be due to the attachment of the molecule to the gold wire stabilising it during the thinning process. Surrounded by bound molecules, the wire of single atom thickness can extend beyond the two or three atom limit determined by Untiedt, *et al* (2002)[76], as the gold atom-molecule entity is more mobile than the gold atom alone (this is explored in Chapter 3 and Chapter 4). Also, there is an apparent enhancement of conduction over a broad range from 10 to 150 x 10^{-4} G_0, due to the presence of 4,4′-bipyridine.

4,4'-bipyridine – Log$_{10}$ histograms, all sets combined, and solvent set.
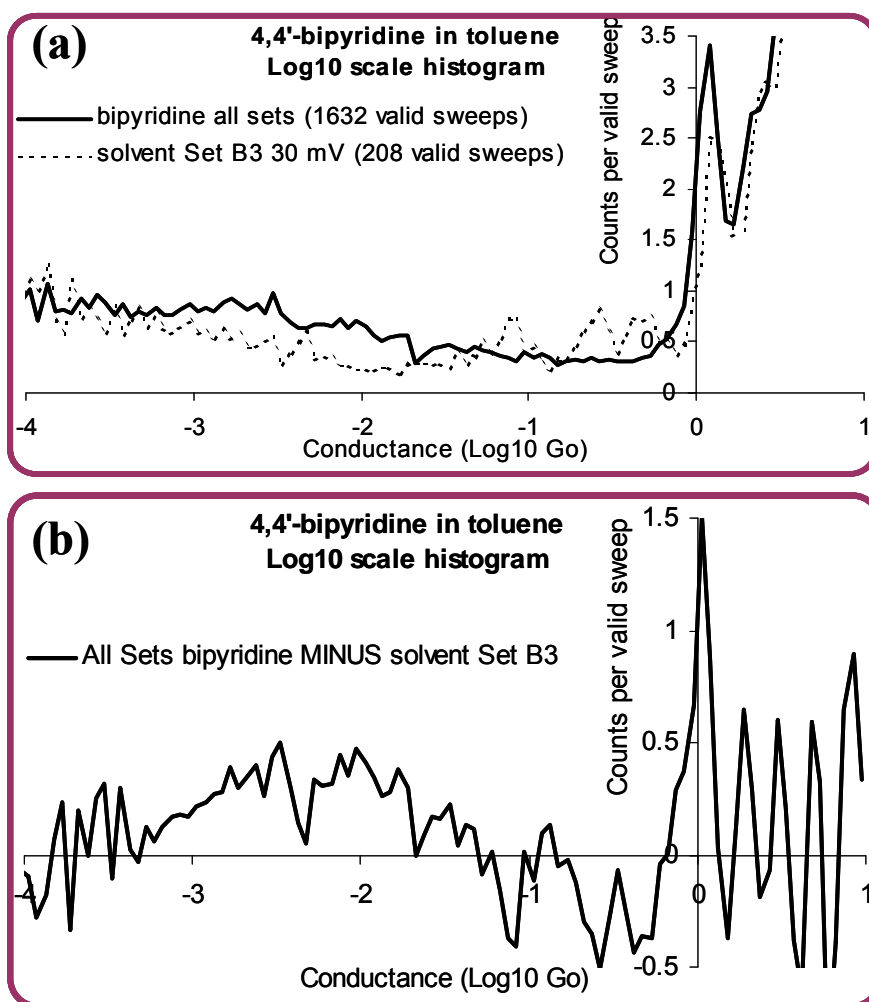
Figure 2-18: Histograms of all 4,4′-bipyridine and solvent (toluene, Set B3) against conductance in Log$_{10}$(G$_0$). **(a)** 4,4′-bipyridine (bold) and solvent (dotted). **(b)** 4,4′-bipyridine only after subtraction of the solvent curve.

2.5.7   Discussion and further analysis of 4,4′-bipyridine results

A weak peak appears in *Set A1* at around 110 x 10^{-4} G_0 by *both* methods and agrees well with prior literature (100 x 10^{-4} G_0[14]) but cannot be viewed as a conclusive result. By *Method 2* the peak has arisen from just two sweeps, and it would be of interest to determine if these were the *only* two sweeps that contributed to the peak obtained by *Method 1*. So those two individual sweeps were identified (Figure 2-19) and removed from data *Set A1*, and *Method 1* analysis was redone. The resultant histogram is shown below (Figure 2-20).

4,4'-bipyridine – Individual traces from *Set A1*
(Showing the 2 sweeps identified by *Method 2* and one other sweep)
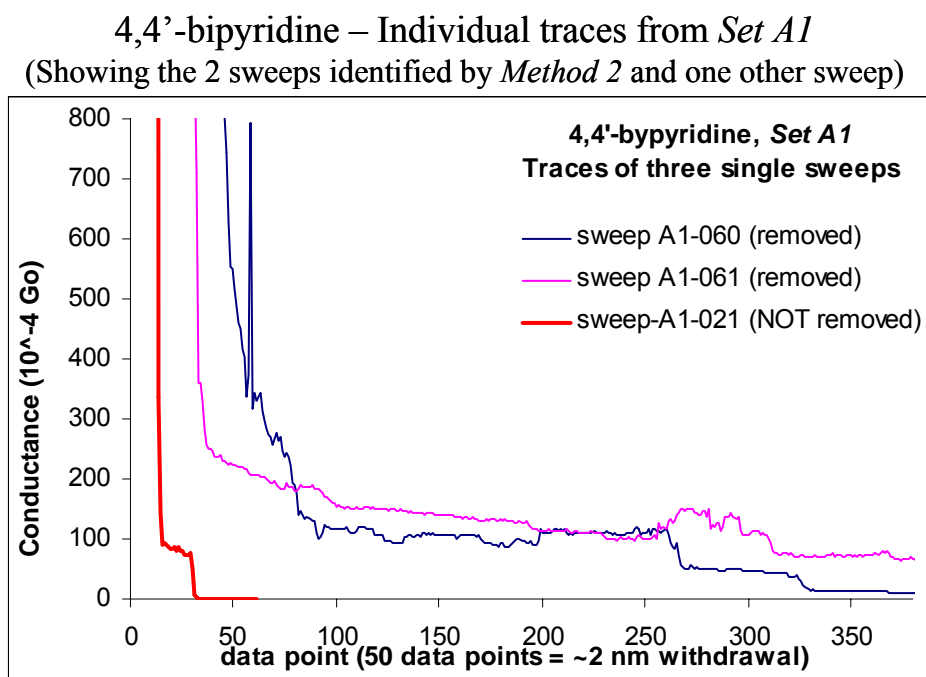
Figure 2-19: Individual traces of the two long-step sweeps identified in *Set A1* by *Method 2* (A1-060 and A1-061) on 4,4′-bipyridine. These were removed for a further analysis of *Set A1* by *Method 1*. Also graphed is the trace of a typical sweep which does not show the characteristics of the two that were removed (bold red). 50 data points is approximately 20 Angstroms withdrawal distance.

The resultant histogram has completely lost the peak that appeared at 107×10^{-4} G_0, which confirms that the peak arose from the data of just those two sweeps. However a weaker peak appears at 85×10^{-4} G_0. This value is still reasonably consistent with that of Xu and Tao[14], but again the peak is too weak to be conclusive.

4,4'-bipyridine - *Method 1*
Set A1 only, after two sweeps removed.
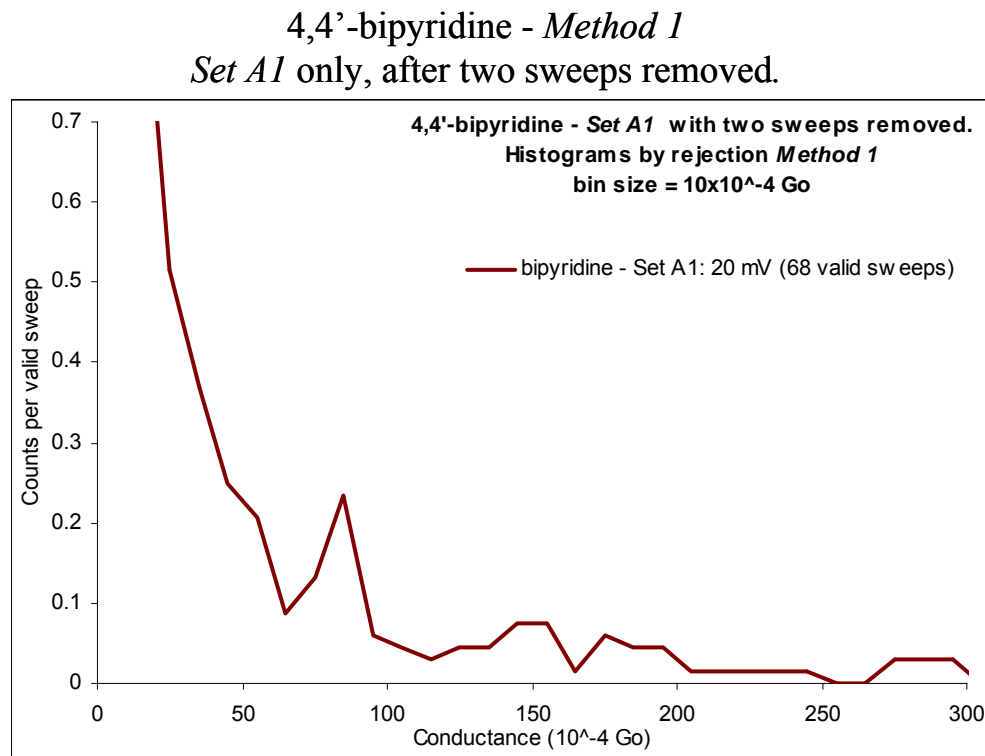
Figure 2-20: Binned histogram for 4,4′-bipyridine *Set A1* only by *Method 1* analysis. The two individual sweeps identified by *Method 2* have been removed from the data set prior to analysis.

The sharp peaks of Xu and Tao were not achieved (Figure 2-17). They sampled 1000 sweeps to obtain their histograms, whereas here more than 2000 sweeps were sampled in total, the largest single set being *Set B2* of 1000 sweeps, identical to theirs. It is not entirely clear what the reasons for the different peak clarities may be. In comparing these results with those of Xu and Tao three aspects are considered:

a) **Selection Criteria**: Xu and Tao give no indication what criteria they used to select (or reject) individual sweeps. Subsequent papers by the same research group indicate that as many as 85% of sweeps may be rejected because they did not show clear molecular conduction steps (see Section 2.3.2, Page 2-40, above, for a more complete discussion of data selection techniques), and it may be reasonable to assume that they were selective in the representation of their data for this paper also. Knowledge of and application of the same technique may have enhanced the results of this thesis. Their equipment was more sophisticated in that they had more direct control over the motion of the tip in relation to current triggers, and this would have produced more consistent data and enabled a better "fine-tuning" of the experiment *in process* to produce more traces with molecular conduction steps.

b) **Molecule concentration and solvent**: Xu and Tao used a concentration of 1 mM bipyridine in 0.1 M NaClO$_4$ aqueous solution, whereas in this research it was ~10 mM in toluene. It may be possible that the lower concentration is more amenable to a single molecule binding to the gold terminals of the break-junction. According to one report, the choice of solvent probably makes little difference,[101] however this is contradicted in the findings for pyrazine (Section 2-7 below). In the electrolyte it is possible to introduce *electrochemical control* (next point).

c) **Electrochemical Control**: Xu and Tao used a wax-coated gold tip in an electrolyte and charged the solution at a positive potential in relation to both gold tip and the gold substrate (at a positive bias the conduction steps would appear but at a negative bias the conduction steps would not appear). Such experiments require wax-insulated tips and an electrochemical cell and specialist techniques not available to this current research. Their *average* step width was 0.9 nm for the single molecule conduction step, whereas here (in toluene with no electrochemical control) one of the longest steps is only

0.6 nm (represented in Figure 2-19 above). As the binding strength of 4,4′-bipyridine to a gold electrode depends on the electrode potential[46], it is expected that should such technology become available it would greatly increase the quality of results with 4,4′-bipyridine and all amine or azine linker molecules.

2.5.8   Conclusion of 4,4′-bipyridine results

The conductance of a single 4,4′-bipyridine molecule (in toluene) has not been established. The weak peak between 85 and 110 x 10^{-4} G_0 agrees with prior research done in aqueous solution, but cannot be distinguished from noise conclusively. It is also reasonably close to theoretical values of 30 x 10^{-4} G_0[79] and 586 x 10^{-4} G_0[78].

An unambiguous result is that 4,4′-bipyridine produces higher gold quantized conduction peaks and thus longer gold conduction plateaus, suggesting that it stabilises the single-atom gold chain during the breaking of the junction and allows it to extend beyond the 2 or 3 atom limit determined by Untiedt[76], or at least allows it to stay at that length longer by providing highly mobile 4,4′-bipyridine-gold atom units which can rush to the narrowest parts of the wire to thicken it.

There is a broad enhancement of conduction (compared to toluene alone) over the range from 10 to 150 x 10^{-4} G_0.

Better results would possibly be obtained under electrochemical control with the solution charged at a positive bias in relation to both gold electrodes. Better software control during the experiment (*i.e.* appropriate triggers) would eliminate a number of unhelpful sweeps prior to data collection and allow greater consistency in results. Further technical resources are required to improve upon these results.

2-6 Investigations of TATPP

Dipyrido[3′,2′:5,6;2″,3″:7,8]quinoxalino[2,3-*i*]dipyrido[3,2-*a*:2′,3′-*c*]phenazine

Abbreviation: **TATPP**

Note: This molecule is called TATPP because it appears often in literature under the following name:

9,11,20,22-tetraazatetrapyrido[3,2-*a*:2′3′-*c*:3″,2″-l:2‴,3‴]pentacene.

2.6.1   Rationalization:

This molecule was synthesised for this experiment. It was considered to be likely to have good conduction because of its conjugation, to show consistent conduction plateaus because of its rigidity, and to bind well to gold because of the bidentate nature of the two phenanthroline-type ends. Determination of its conductance value was considered an important step in the process of creating molecular wires from fused porphyrins with phenanthroline-type "alligator clips" (See the rationalisation for bis-phenanthroline-appended-porphyrin in Section 2.8.1 below).

2.6.2   Background research

2.6.2.1   Similar molecules

Long, multiply-conjugated molecules have recently be subjected to break-junction experiments by Li, *et al,* (2007)[72] to determine their conductance values. These molecules and their different conduction results are reproduced in Table 2-9, below, along with TATPP. Although there are substantial differences to TATPP, an electron traversing each molecule would travel similar pathways (in terms of bonds and

conjugations traversed, as well as length), however there would be less conduction pathways available to an electron in TATPP.

Li attributes the differences in conduction of these molecules to different electronic couplings between the molecule and the electrodes, mainly caused by the different anchoring groups (*i.e.* the length of the anchoring group and whether it is conjugated or not; greater length = lesser conductance; more conjugations = more conductance).

Graphite is a conductor because of its multiple conjugations and multiple pathways.

In terms of Li's explanation, TATPP would have a better coupling to the gold electrode than the best conductor in his series. The number of conjugations and pathways is similar. However the four incorporated central nitrogen atoms may have a slightly decreasing effect on conductance.

The example of these molecules suggests that TATPP might have a similar conductance, say between 0.1 and 1.0 x$10^{-4}$$G_0$. (The side double bonded oxygen groups in Li's molecules may have a significant effect on conductance however it is unquantifiable and has to be ignored.)
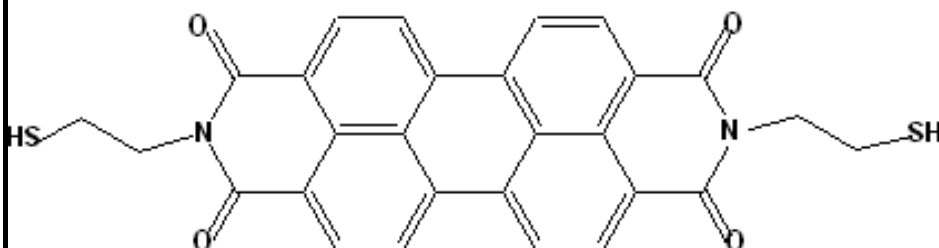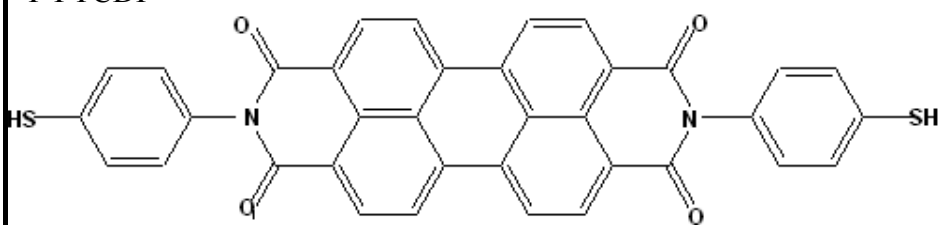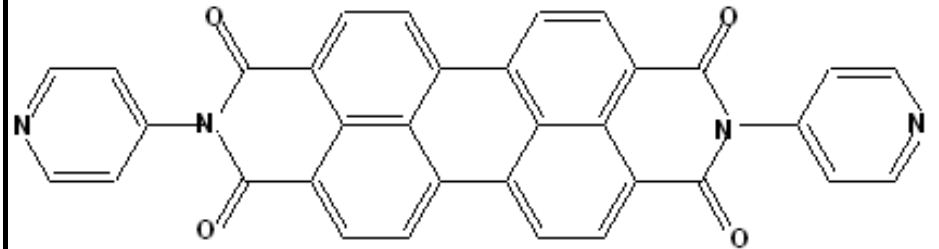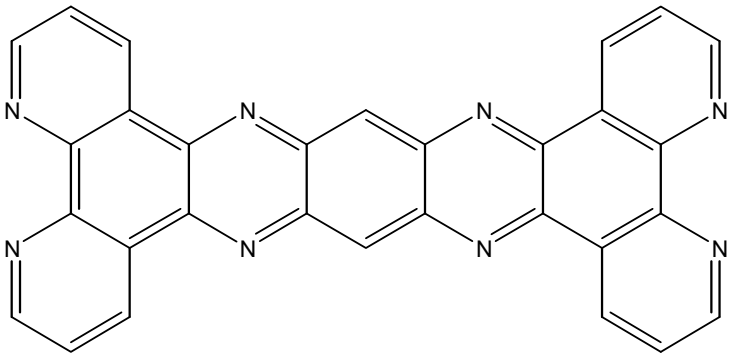
Name and Structure	conductance (10^{-4} G_0) Approx length (Å)
C-PTCDI	0.078 1650 Å
T-PTCDI	0.175 2156 Å
P-PTCDI	0.56 1988 Å
TATPP This molecule	estimated (from above values) to be between 0.1 and 1.0 1455 Å

Table 2-9: Conductance of multiply-conjugated molecules from Li, *et al,* (2007)[72]. TATPP is shown by comparison.

2.6.2.2   Theoretical value of conductance for TATPP

An unpublished theoretical value of conductance for TATPP is 0.01 x 10^{-4} G_o, provided by Mr Sören Wolthat in a personal communication (based upon the model shown in Figure 2-27).

2.6.3   Experimental set-up:

TATPP was dissolved in the solvent using a sonicator, then allowed to stand for more than one hour, and experimental samples were drawn from the middle of the solution so as to avoid both sedimentary and floating particles which may have been present.

For Group A the final experimental concentration was less than 1 mM in toluene; for Group F it was ~5 mM in toluene, and for Group G it was ~5 mM in phenyloctane.

2.6.4   The sets of sweeps for TATPP

Group A: Linear Amplifier: Three sets of sweeps were recorded with the linear amplifier, one solvent-only set labelled *Set A0* (toluene) and two TATPP sets labelled *Set A2* and *Set B1*. All used a bias of 50 mV.

Group F: Logarithmic Amplifier and toluene: Four sets of sweeps were recorded using the log amplifier and toluene as the solvent, two on the solvent only, labelled *Set F1* and *Set F2,* and two on TATPP labelled *Set F3* and *Set F4* (each at 40 mV and 80 mV).

Group G: Logarithmic Amplifier and phenyloctane: Four other sets also used the log amplifier but were done in a different solvent, phenyloctane. One set was the

solvent only at 40 mV (*Set G1*) and the others were TATPP at 40 mV (*Set G2*), and two

sets at 80 mV (*Set G3* and *Set G4*)

The parameters for these sets are listed in Table 2-10 in the three groups.

Group	Set	item	bias mV	Solvent	Amp	number of sweeps	withdrawal speed (nm s^{-1})
A	*A0*	solvent only	50	toluene	Linear	296	12
A	*A2*	TATPP	50	toluene	Linear	315	12
A	*B1*	TATPP	50	toluene	Linear	201	12
F	*F1*	solvent only	40	toluene	Log	212	12
F	*F2*	solvent only	80	toluene	Log	157	12
F	*F3*	TATPP	40	toluene	Log	730	12
F	*F4*	TATPP	80	toluene	Log	1000	12
G	*G1*	solvent only	40	phenyloctane	Log	286	12
G	*G2*	TATPP	40	phenyloctane	Log	479	12
G	*G3*	TATPP	80	phenyloctane	Log	454	12
G	*G4*	TATPP	80	phenyloctane	Log	570	12

Table 2-10: Parameters for the sets of sweeps relating to TATPP.

2.6.5   Results from TATPP (all sets)

In general TATPP was difficult to obtain results for molecular conduction. Individual traces showed little evidence of molecular conduction steps. TATPP was difficult to dissolve in the two solvents used (toluene and phenyloctane) and in many cases the binned results for TATPP looked similar to solvent only sets.

Using the *linear amplifier*, and toluene as the solvent, the Group **A** sets showed no molecular conduction peaks and little difference from the solvent only set (see Figure 2-21 below), however the range with the linear amplifier and a bias of 50 mV was limited to between 0.5 and 6.0 x 10^{-4} G_0 (approximately).

Groups **F** and **G** were analysed by *Methods 1* and *2* (Section 2.3.1 above), and were also binned using a $\log_{10} G_0$ scale for conductance to observe long range effects, if any.

Group **G**, in phenyloctane, showed no difference between the solvent and TATPP using any of the analysis methods or graphs (Figure 2-24 shows histograms for each set in **Group G**, by both analysis *Methods 1* and *2*, while Figure 2-26 shows a weighted average of all TATPP sets from group G and the solvent set on a $\log_{10} G_0$ scale.)

The various graphs for **Group F** are as follows:

- Figure 2-22 shows histograms for each TATPP set in **Group F** with the solvent set done at the same bias, by both analysis *Methods 1* and *2*.
- Figure 2-23 shows each TATPP set with its corresponding solvent set subtracted as a baseline, by both *Methods 1* and *2*.
- Figure 2-25 shows histograms for each TATPP set in **Group F** with the solvent set done at the same bias, graphed on a $\log_{10} G_0$ scale.

Generally there were no significant peaks in any of the histograms. Group **F** showed a poor peak at 1.7×10^{-4} G_0 by three different methods but it isn't distinguishable from the noise (By *Method 2* in Figure 2-22 (d); by *Method 2* with baseline subtraction in Figure 2-23 (b); and by the Log_{10}, histogram in Figure 2-25 (b).)

There was no consistent indication that the gold quantized conduction peak at 1.0 G_0 was enhanced by TATPP. Set *F3* (in toluene) shows a doubling of this peak by TATPP (which isn't significant), but in Set *F4* (in toluene) and Group **G** (in phenyloctane) the gold peak is identical in TATPP and the solvent.

(NOTE: There were extensive other sets in both toluene and phenyloctane, done both at Sydney University and CSIRO, which have not been included because they

merely repeated the phenomena of Groups **A** and **G**, where there was no difference

between the conduction of TATPP and the solvent.)
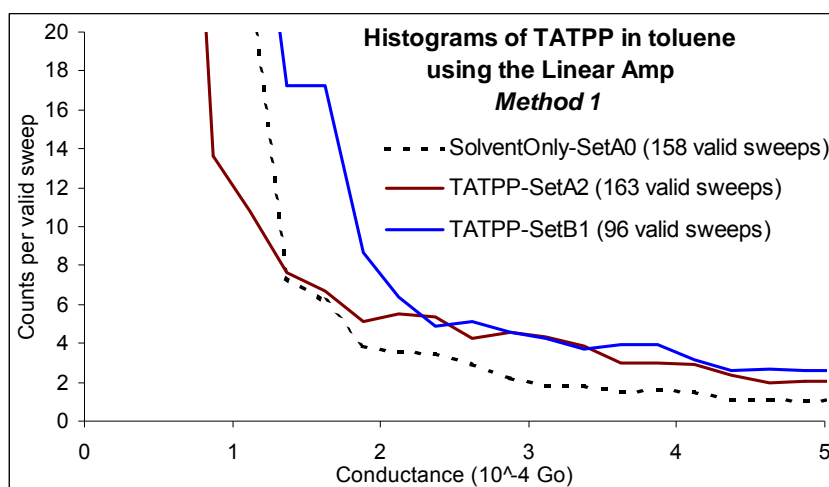
Figure 2-21: TATPP, Group **A** – Histograms of all sets done on the linear amplifier, in toluene, using rejection *Method 1*. No peaks appear. The bias was 50 mV for all sets: at this bias the useful range of the linear amplifier is limited to between 0.5 and 6.0 x 10^{-4} G_0. The solvent was toluene.
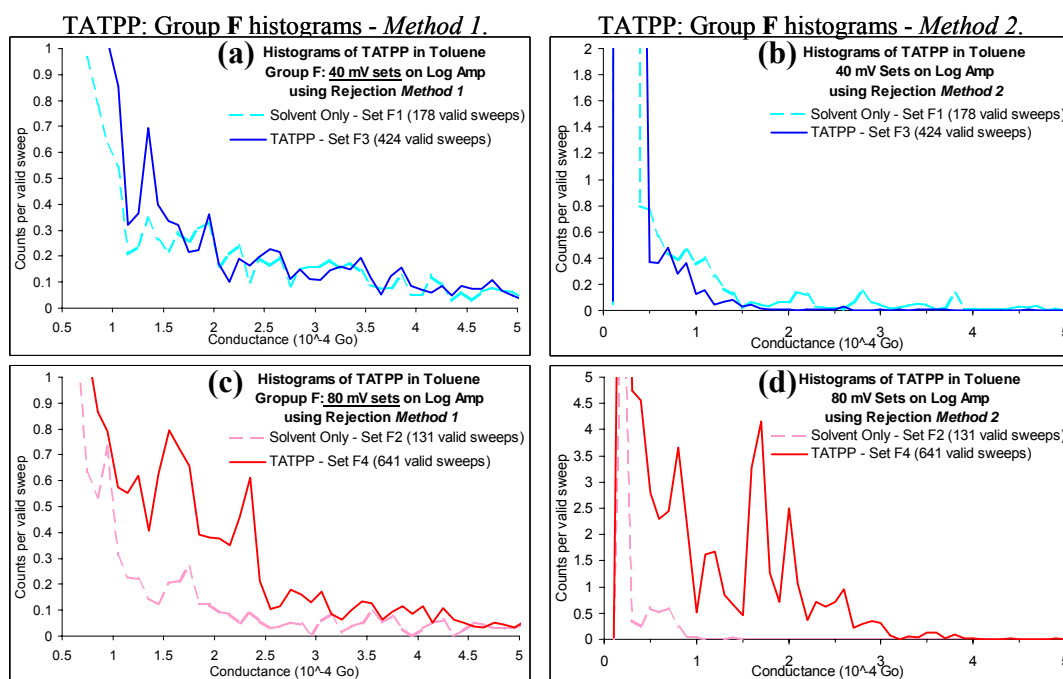
Figure 2-22: TATPP, Group **F** histograms with solvent curves. (**a**) 40 mV sets by *Method 1*. (**b**) 40 mV sets by *Method 2*. (**c**) 80 mV sets by *Method 1*. (**d**) 80 mV sets by *Method 2*. The log amplifier was used for all sets. The solvent was toluene.

TATPP: Group **F** histograms – Subtraction of the solvent curve.
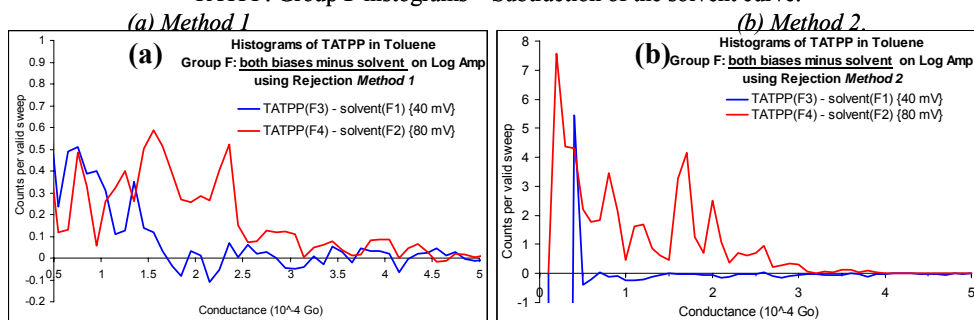
(a) Method 1   *(b) Method 2.*

Figure 2-23: TATPP, Group **F** histograms, TATPP with base-line subtraction (solvent). (**a**) 40 mV and 80 mV sets by *Method 1*. (**b**) 40 mV and 80 mV sets by *Method 2*. The log amplifier was used for all sets. The solvent was toluene.

TATPP: Group **G** histograms.
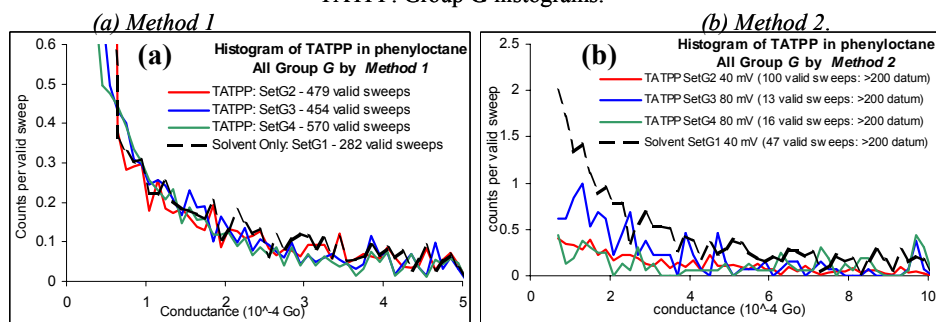
(a) Method 1   *(b) Method 2.*

Figure 2-24: TATPP, Group **G** histograms, each set (*G2*, *G3* and *G4*) graphed with solvent (*G1*). (**a**) by *Method 1*. (**b**) by *Method 2*. The log amplifier was used for all sets. The solvent was phenyloctane.

TATPP: Group **F** histogram – Log(10) conductance scale.

40 mV sets   80 mV sets
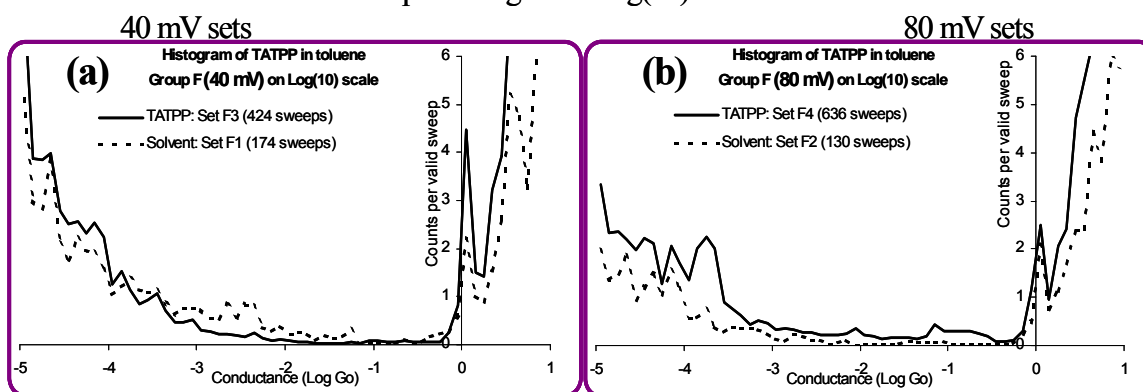
Figure 2-25: Histogram of Group **F** TATPP and solvent against conductance in $Log_{10}(G_0)$.   (**a**) 40 mV TATPP (*Set F3*) and 40 mV solvent (*Set F1*).   (**b**) 80 mV TATPP (*Set F4*) and 80 mV solvent (*Set F2*). The solvent is toluene.

TATPP: Group **G** histogram – Log(10) conductance scale.
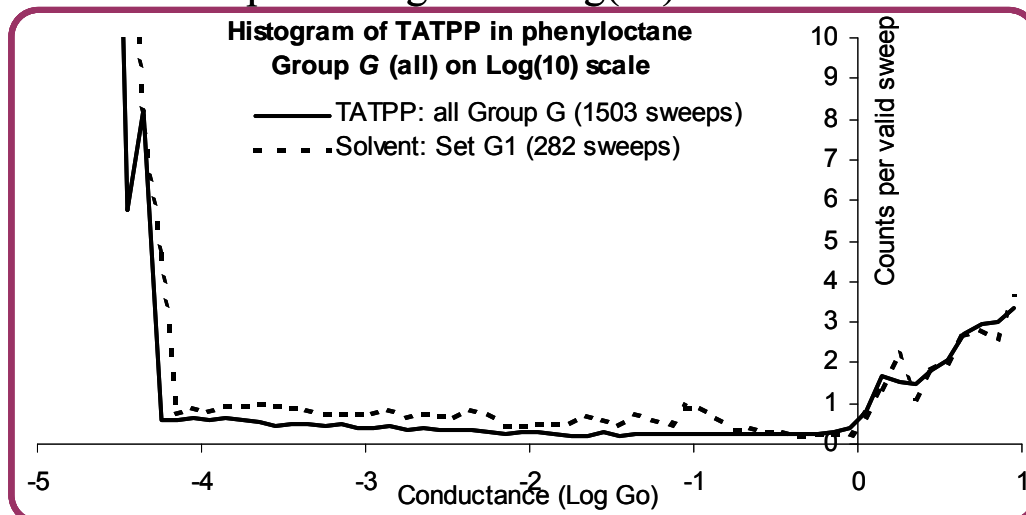
Figure 2-26: Histogram of all Group **G** TATPP (combined *Sets G2, G3* and *G4*) and solvent (phenyloctane, *Set G1*) against conductance in $Log_{10}(G_0)$. There is no long range effect of TATPP against the solvent only.

2.6.6   Discussion of TATPP results

TATPP was designed specifically for the break-junction experiment. Being bidentate on both ends and entirely conjugated it was considered to link well to gold and have a high and easily observable conductance value. However clear indications of conduction were somewhat elusive, and the poor peak in *Set F4* at 1.7×10^{-4} G_0 cannot be considered as evidence of a conduction event, even though it compares well with similar molecules (Table 2-9, page 2-62, above), yet is significantly higher than the theoretical value provided by Mr Sören Wolthat of 0.01×10^{-4} G_0 (based upon the model shown in Figure 2-27).

Gold conduction steps were not enhanced by the presence of TATPP in either solvent. This is a reliable indicator that the molecule was not interacting with the gold in a "proper" way: that is that it did not connect one of its phenanthroline-type ends to the gold to create a more mobile gold atom-TATPP entity. This occurred in both solvents. The two solvents are somewhat similar in that they both consist of a benzene ring with a

tail, with the tail being eight times longer in phenyloctane over toluene. It is most likely that it is the structure TATPP not the solvent interactions which is preventing "proper" attachment of the molecule to gold.
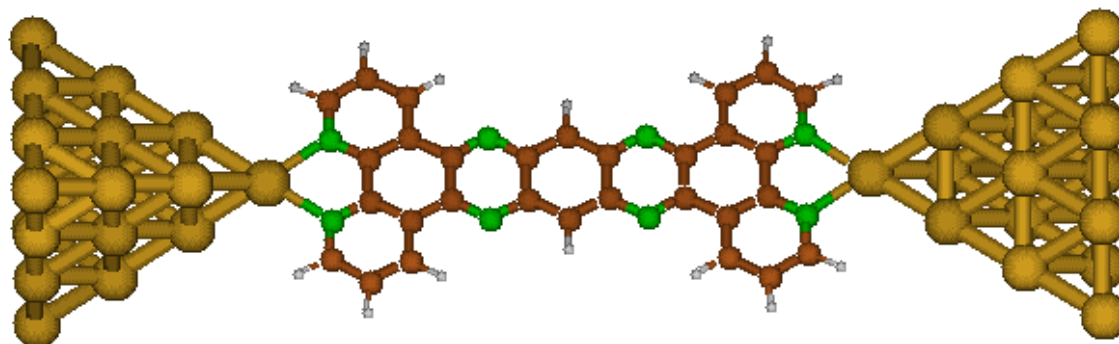
Figure 2-27: Theoretical model of TATPP geometry during break-junction experiments (graphic provided by Mr. Sören Wolthat).

2.6.6.1   Difficulty in observing conductance for TATPP

When individual traces of the *Set F4* are examined, they indicate noisy "conduction steps" for TATPP (see Figure 2-28, below). If this indicates a conduction event of TATPP, the signal is erratic and does not accumulate to show peaks in the binned histograms. A high number of traces dropped from 1.0 G_0 (gold conduction) to zero with almost no features in between, similar to the solvent curve.

It proved more difficult than expected to align the molecule in position between the gold wires when the break junction was formed (see the idealised model in Figure 2-27 above). The possible reasons for this were:

1)   The molecule had a number of nitrogen atoms and conjugated rings along its length. The dispersive forces of the multiply conjugated backbone can cause benzene rings to lay flat on a metallic surface[102], and it is possible that TATPP could lay flat on the gold surface rather than upright (as 1,10-phenanthroline

and DPPZ do – See Chapter 3). This would make it more difficult to form the correct alignment, as it would have a "sticky middle" as well as "sticky ends".

2)   The molecule was not very soluble in either toluene or phenyloctane. It may have not been very mobile in the solution.

3)   The bond between the azine linkers and gold atoms is weak and not highly directional, and so has much more angular freedom than, say, the thiol linker unit. This may give rise to a number of different molecular alignments to the gold ends during the break-junction experiment, which would explain why conduction could be indicated over a broad range rather than a single value.

TATPP – *Set F4* – Some individual traces.
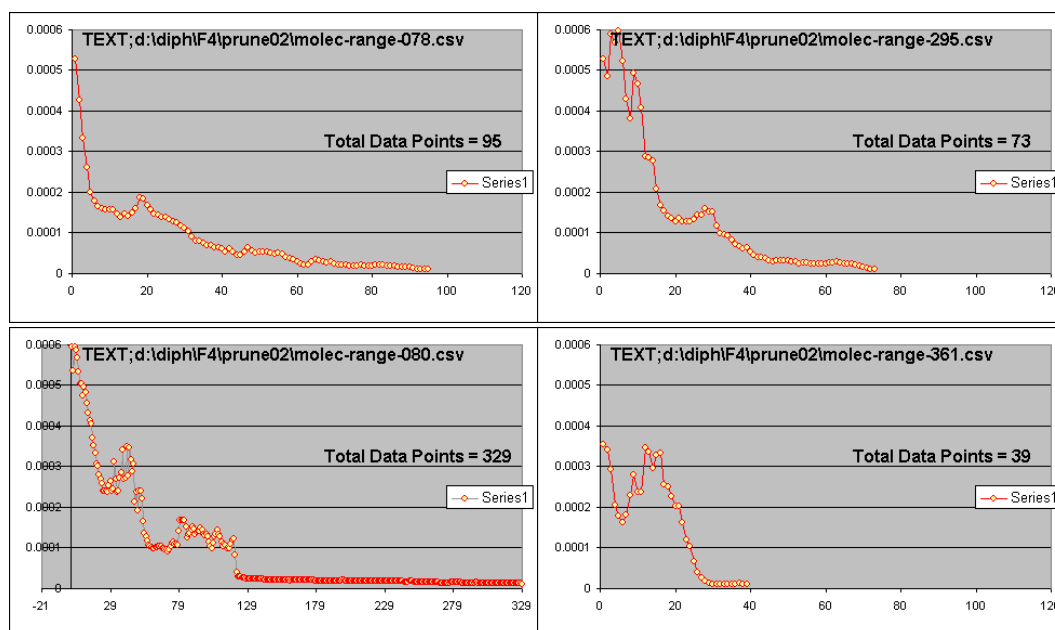
Figure 2-28 Four examples of individual sweeps from *Set F4* – The scale on the vertical axis is G_0. Steps possibly indicating molecular conduction are small and "noisy".

Possible approaches to solve these problems for future research would be:

a) Create another similar molecule with side groups in the middle (e.g. tetrabutyl) which would both offer steric hindrance to the molecule laying flat on gold, and provide greater solubility.

b) Perform the experiment in an electrochemical cell with a positive bias applied to the solution[14].

2.6.7   Conclusion of TATPP results

It is difficult to observe the conductance of TATPP in the break-junction experiment because of its low solubility and possible stickiness to gold in its middle, due to the centre nitrogen atoms in the conjugated π-bonded backbone. No conclusive conduction event was observed.

Most probably, TATPP did not adhere to the gold surface in a way that would facilitate observance of single molecule conduction – that is, it was not bound to the gold by its phenanthroline-type alligator clips: either because of solvent interactions or because it laid flat on the gold (being attracted by its central nitrogen atoms as well as its end ones). Further investigations which could determine this were hampered because it was difficult to find other solvents which could dissolve TATPP.

Better results may be obtained by performing the experiment under electrochemical control, or by redesigning the molecule to have better solubility and to be less prone to lay flat on the gold surface.

2-7 Investigation of pyrazine

pyrazine: $C_4H_4N_2$
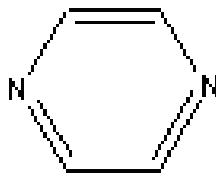
2.7.1   Rationalization:

Pyrazine, bipyridine, TATPP and DPPZ are typical ligands used to developing more complex devices containing ruthenium, osmium, or other metal atoms and/or ions and/or metallated porphyrins which are being considered as possible molecular electronic devices.[103-105] As far back as 1966 pyrazine was considered useful in vanadium superconductors[106].

Pyrazine was considered to be a most likely molecule to use in the break-junction experiment because its conduction was expected to be high, as it was a small rigid cyclic molecule consisting solely of π-bonds. It also supported the theme of this thesis, that nitrogen groups could be used rather than thiols to attach molecules to the gold electrode. No prior publications give an experimental value for the molecular conduction of pyrazine, however a theoretical value had been calculated. Pyrazine is also soluble in a number of solvents, both polar and non-polar.

2.7.2   Background research

Interestingly, there is no published background research (experimental). Given that pyrazine is a most likely candidate for molecular conduction experiments (previous

paragraph) it may not be through a lack of attempts. (As the results here show, the "single value" of the conductance of pyrazine is quite elusive. Insubstantial peaks appeared in most conductance histograms plotted on a short-range linear scale, and it was only through the $\log_{10}$ graphs of the conductance histograms that evidence of pyrazine's conduction becomes apparent.)

An unpublished theoretical value of conductance for pyrazine is 30×10^{-4} G_o (provided by Mr Sören Wolthat in a personal communication).

The other theoretical value of 4.7×10^{-4} G_o listed in Table 2-2 may not be very helpful as it was modelled by using sulfur atoms to bind to gold electrodes (substituting for 2 hydrogen atoms), so in effect it was something like 1,3-dithiol-2,5-pyrazine

2.7.3   Experimental set-up:

Pyrazine readily dissolved in all solvents. The final concentration (and solvent) used for each group was:

Group C: ~10mM in phenyloctane

Group D: ~5mM in toluene

Group E: ~30mM in toluene

Group G: ~20mM in 0.1 M sodium perchlorate (aqueous).

Group H: ~10mM in carbontetrachloride

Group K: ~10 mM in phenyloctane

Group L: ~10mM in carbontetrachloride

2.7.4   The sets of sweeps for pyrazine

In all, 45 sets of sweeps in 7 groups were recorded in different solvents and at varying biases, including solvent only and air only sets. All sets done at Sydney University used the logarithmic amplifier. (A further 17 sets recorded on the linear amplifier at Sydney University have not been included because they do not cover a sufficient range.) Group *K* comprises 9 sets recorded at CSIRO, using various gain settings. The parameters for these sets are listed in Table 2-11 below. The aqueous solvent was 0.1 M sodiumperchlorate. Withdrawal speeds were also varied.

Group (done at)	Set	item	bias mV	Solvent	No. of sweeps	Speed nm s^{-1}
C	C1a	solvent only	100	phenyloctane	161	4
(Usyd)	C1b	solvent only	100	phenyloctane	501	4
	C2	pyrazine	100	phenyloctane	701	4
	C3	pyrazine	100	phenyloctane	654	4
	C4	pyrazine	100	phenyloctane	634	4
D	D1a	air only	65	-	96	6
(Usyd)	D1b	air only	65	-	510	6
	D1c	air only	100	-	16	6
	D2a	solvent only	50	toluene	680	6
	D2b	solvent only	50	toluene	471	6
	D3a	pyrazine	50	toluene	1000	6
	D3b	pyrazine	30	toluene	1000	6
E	E1a	air only	65	-	171	2.6
(Usyd)	E1b	air only	100	-	116	2.6
	E1c	air only	50	-	167	2.9
	E2a	solvent only	50	toluene	857	2.6
	E3a	pyrazine	50	toluene	245	2.6
	E3b	pyrazine	50	toluene	402	2.6
	E3c	pyrazine	30	toluene	809	0.4
G	G1a	solvent only	100	electrolyte (Aq)	500	59
(Usyd)	G1b	solvent only	100	electrolyte (Aq)	609	24
	G1c	solvent only	100	electrolyte (Aq)	464	24
	G2a	pyrazine	60	electrolyte (Aq)	1000	24
	G2b	pyrazine	60	electrolyte (Aq)	723	24
H	H0	air only	60	-	270	15
(Usyd)	H1a	solvent only	60	carbontetrachloride	120	7
	H1b	solvent only	80	carbontetrachloride	201	7
	H2a	pyrazine	80	carbontetrachloride	501	4
	H2b	pyrazine	100	carbontetrachloride	512	4
	H2c	pyrazine	66	carbontetrachloride	430	4
K	K1a	solvent only	100	phenyloctane	301	40-5*

Group (done at)	Set	item	bias mV	Solvent	No. of sweeps	Speed nm s^{-1}
(CSIRO)	K1b	solvent only	100	phenyloctane	200	40-5*
	K1c	solvent only	100	phenyloctane	300	40-7*
	K1d	solvent only	100	phenyloctane	336	40-8*
	K2a	pyrazine	100	phenyloctane	238	40-5*
	K2b	pyrazine	100	phenyloctane	500	40-7*
	K2c	pyrazine	100	phenyloctane	501	40-8*
	K2d	pyrazine	50	phenyloctane	500	40-9*
	K2e	pyrazine	50	phenyloctane	52	40-8*
L (Usyd)	L0	air	80	-	219	4.8
	L1a	solvent only	80	carbontetrachloride	216	15.0
	L1b	solvent only	80	carbontetrachloride	454	3.0
	L2a	pyrazine	80	carbontetrachloride	392	3.0
	L2b	pyrazine	80	carbontetrachloride	469	3.0
	L2c	pyrazine	80	carbontetrachloride	51	3.0

Table 2-11: Parameters for the sets of sweeps relating to pyrazine. Groups B, C, D, E, G, H, and L were conducted at Sydney University, and group K at CSIRO.
* All sweeps at CSIRO (All Group **K**) were done at 40 nm/s, the extra number is the gain setting (see Section 2.3.1.2 above).

2.7.5   Results from all sets of data for pyrazine.

Linear scale histograms by methods *1* and *2*, and log$_{10}$ scale histograms, for all sets of data were prepared. Of the linear scale histograms, only Group **L** had an observable peak. All the others had broad features which are best observed in the log$_{10}$ scale histograms: none of the specific peaks that appeared in the linear scale histograms were significantly stronger than the noise and/or the data set was too small to be significant (other than Group L).

Except for Group L, all the linear scale histograms are included in APPENDIX 2 (Section 7.2.1) (by *Method 1* only: *Method 2* graphs showed no additional information to the *Method 1* histograms and so have not been included).

The Log$_{10}$ scale histograms (totals) are shown in Figure 2-29 below. They indicate broad ranges where pyrazine enhances conduction, which are solvent dependent. These ranges are summarised in Table 2-12 below.

Experiments in phenyloctane were conducted at both Sydney University (Group C) and CSIRO (Group K). The $\log_{10}$ scale histograms (totals) for each are shown in Figure 2-30 below with trend lines for both pyrazine and solvent.

The $\log_{10}$ scale (total) histogram for Group G (aqueous solvent - Figure 2-29 (d)) is reproduced with trend lines in Figure 2-32.

Solvent	Group	Figure	Conductance range which is enhanced by the presence of pyrazine (10^{-4} G_0)	Enhance gold conductance peak?
phenyloctane	C	Figure 2-30 (a)	very broad, from 1 to 1000 trend line peak at 4.0	No.
	K	Figure 2-30 (b)	broad, from 1.0 to 100, trend line peak at about 11.0	yes, x3
toluene	D	Figure 2-29 (b)	Nil.	very much, x 8
	E	Figure 2-29 (c)	Nil$^\chi$	Yes
aqueous 20 mM NaClO$_4$	G	Figure 2-29 (d) Figure 2-32	from about 300 to 3200 trend line peak at 1300	reversed
carbon-tetrachloride	H	Figure 2-29 (e)	generally lower than 25, with a peak at 10.	extremely, x12
	L	Figure 2-29 (f)	from 7.0 to 18.0, with a sharp peak at 12.0	extremely, x60

Table 2-12: Summary of all results from pyrazine $\log_{10}$ histograms, all solvents.

$^\chi$ In Figure 2-29 (c) (Set E in toluene) there is a strong peak for pyrazine around 1 x 10^{-4} G_0. However the same peak is also present in the solvent-only curve. The pyrazine curve is consistently a factor of 4 times the solvent curve for the entire data range, so there is no specific range for which pyrazine enhances conduction. This peak has to be ignored and there are no specific conductance features for pyrazine from this histogram.

Pyrazine break-junction experiments done at Sydney University
in various solvents. All sets on Log_{10} scale.
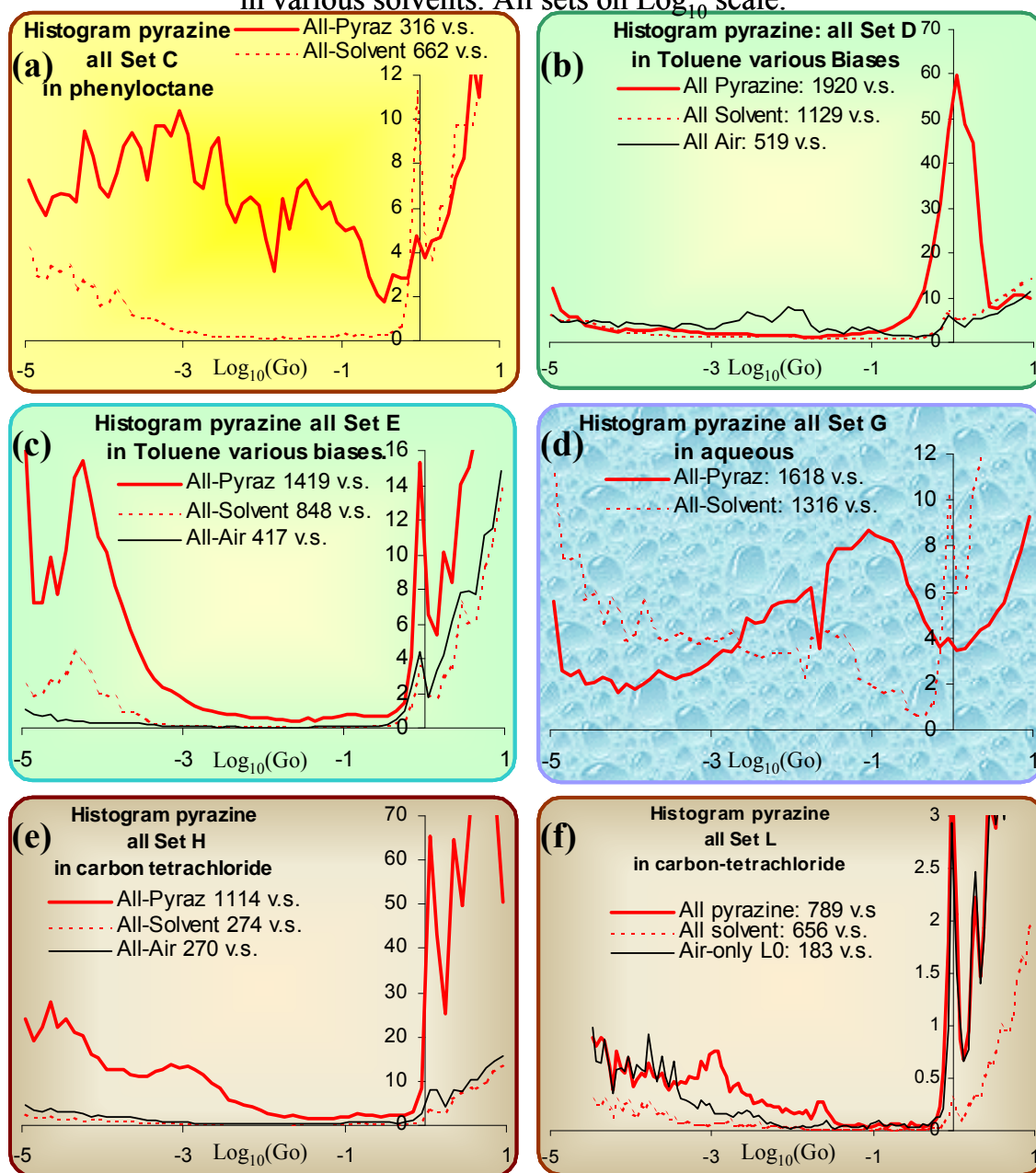
Figure 2-29: Log_{10} scale histograms of pyrazine in various solvents. Each graph shows a weighted total for pyrazine (bold red line), solvent only (dotted red line) and in some cases air (thin black line).

(a) Group C (in phenyloctane)   (b) Group D (in toluene)

(c) Group E (in toluene)   (d) Group G (in aqueous sol.)

(e) Group H (in carbontetrachloride)   (f) Group L (in carbontetrachloride)

The vertical axis is counts per valid sweep, the horizontal axis is conductance in $Log_{10}(G_0)$. v.s. = valid sweeps.

NOTE: The graph backgrounds are colour-coded according to *solvent*.
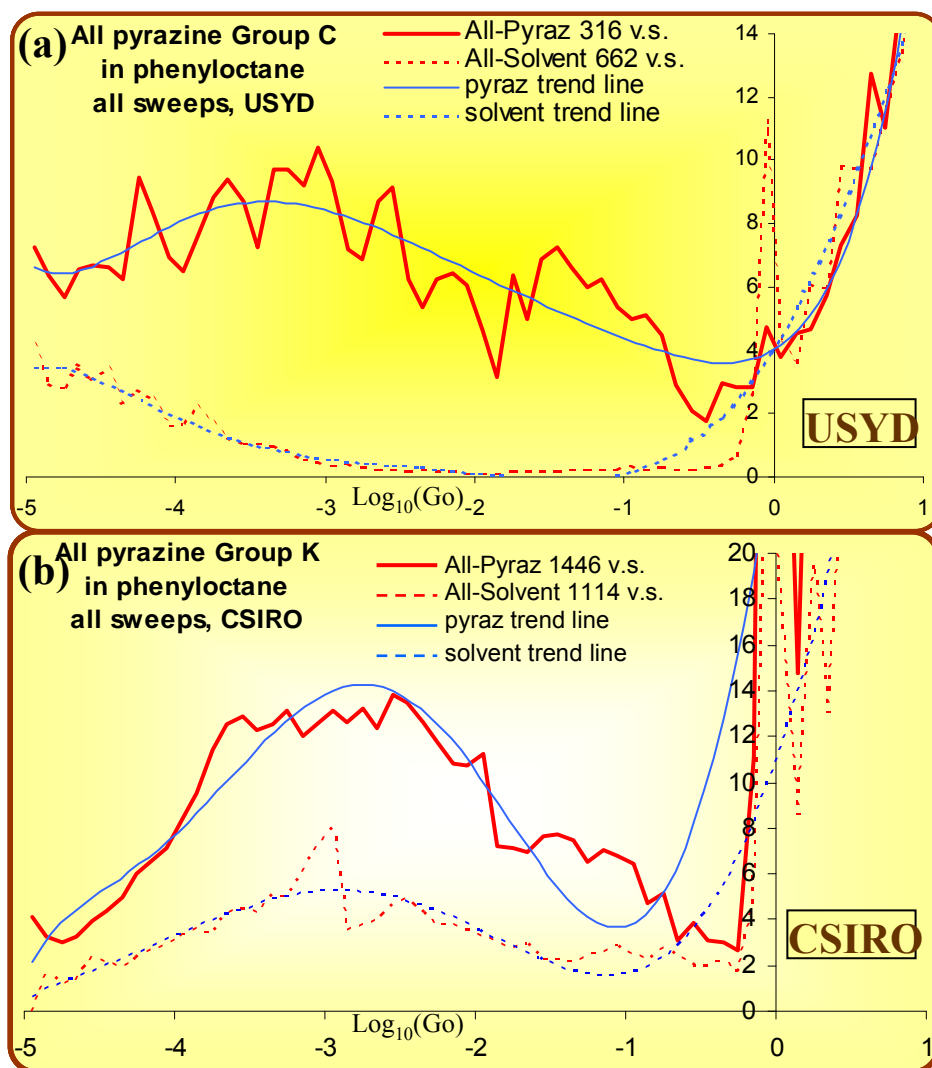
Figure 2-30: Log_{10} scale histograms of pyrazine in phenyloctane. Each graph shows a weighted total for pyrazine (bold red line) and solvent only (dotted red line). Trend lines by 6th order polynomial smoothing are also shown for pyrazine (thin blue line) and solvent (dotted blue line) (a) Group C done at Sydney University (in phenyloctane) (b) Group K done at CSIRO. (in phenyloctane) The vertical axis is counts per valid sweep, the horizontal axis is conductance in $Log_{10}(G_0)$.   v.s. = valid sweeps.

Pyrazine in carbon-tetrachloride – all Group L by *Methods 1* and *2*.
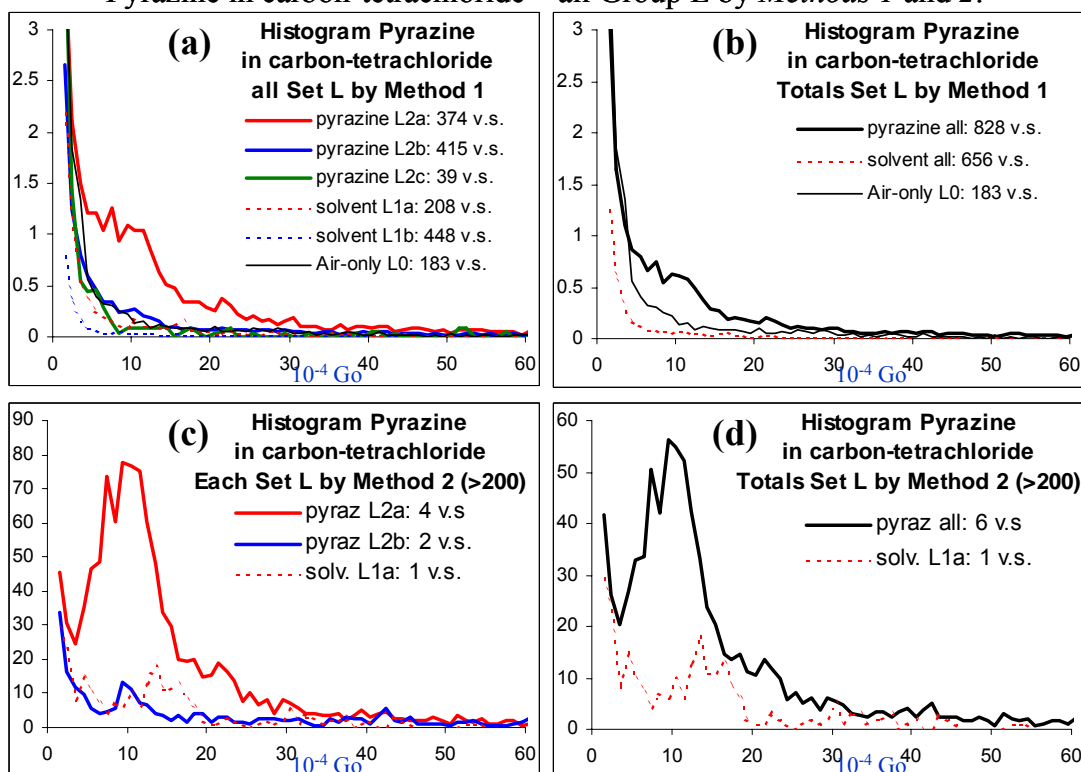
Figure 2-31: Linear scale histograms of pyrazine in carbontetrachloride (Group L) by *Method 1* (upper graphs) and *Method 2* (lower graphs), and showing individual sets (left) and weighted total of individual sets (right). Bold lines are pyrazine, dotted lines are solvent only, and the thin black line is air only (There were no valid sweeps for air by method *2*). Bias = 100 mV. The vertical axis is counts per valid sweep, the horizontal axis is conductance in 10^{-4} G_0.   v.s. = valid sweeps.

Pyrazine break-junction experiments.
Group G in aqueous solution.
Total on Log_{10} scale with trend line.
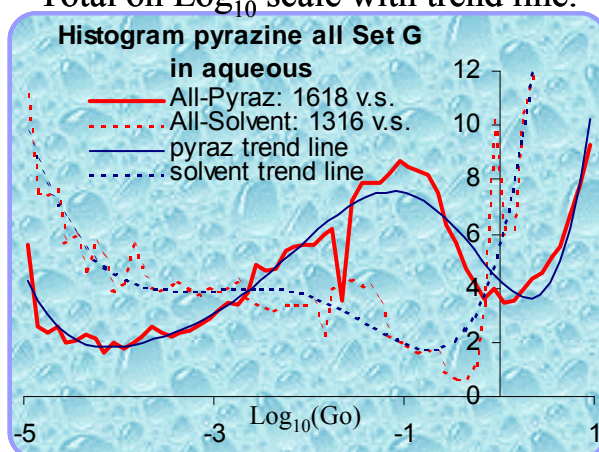
Figure 2-32: Pyrazine Group G log_{10} histogram, with trend lines by 6th order polynomial smoothing for pyrazine (thin blue line) and solvent (dotted blue line) (in aqueous sol.)

2.7.6 Discussion of pyrazine results:

2.7.6.1 General observations

Each solvent has broad ranges of conductance where pyrazine shows a conduction signal greater than solvent. Sharp peaks are elusive for pyrazine (except in the Group L in carbontetrachloride). The general explanations for the broad ranges are as follows:

1. The pyrazine molecule inserts itself into the break-junction in a variety of geometric configurations, each with its own characteristic conductance. This would account for a number of different conductance values, which may vary by as much as an order of magnitude or more.

2. Sometimes 2 or more pyrazine molecules are bridging the gap at the same time, however if there are different geometric configurations available to each molecule, then the conductance of two molecules will not necessarily be double the conductance of one molecule.

3. The pyrazine may somehow join as a multiple of more than one molecule in a line, stacked to each other by interactions between the conjugated rings.

4. The solvent may interact with the pyrazine forming complexes.

5. Variation of withdrawal speeds had no observable effect on conduction.

6. Finally, the configuration of the terminal gold atom(s) to which the pyrazine connects can contribute to a variation in conduction (this is shown for thiol conduction in Chapter 4).

All of these factors combined give rise to a very wide range of results which are indicated by the broad ranges in the histograms.

Interaction of pyrazine with the solvent molecule, particularly solvents with a conjugated ring (see Figure 2-34), is the most significant contributor to this broad range[71]. Pyrazine conduction in each solvent is considered separately below:

2.7.6.2   In phenyloctane

The results obtained at Sydney University (Group C) and CSIRO (Group K) show high similarity over the broad range (Figure 2-30), with 316 and 1446 valid sweeps respectively. With over a thousand individual traces, the CSIRO data should be taken as most reliable. However the Sydney University data, done on completely different equipment, is viewed as an independent verification of the CSIRO data. The peak of the fitted trend line is 11.0×10^{-4} G_0 (CSIRO) and this is confirmed with the USYD peak being quite close (4.0×10^{-4} G_0^{Σ}).

In the CSIRO data, the extensive broadness of the peak is over 2 orders of magnitude, from 1 to 100×10^{-4} G_0. (This is more or less confirmed by the USYD data, which is however much broader but with a smaller data set.) Such a range could encompass many different pyrazine configurations between the gold electrodes, including configurations involving solvent interactions. The peak at 11.0×10^{-4} G_0 represents the mid range and not necessarily the conduction of a single molecule. It could perhaps suggest the conductance of the most likely configuration of pyrazine molecule(s), but even this conclusion cannot be drawn with any certainty from this data alone.

Σ A sharp spike in the Group C data at about $10^{-4.2}$ G_0 has affected the trend line. This spike is most likely a noisy aberration, and if removed then one would expect the peak of the trend line to be closer to the Group K result (11×10^{-4} G_0).

Pyrazine enhanced the gold quantized conduction peak in the CSIRO sets, but decreased it in the USYD sets. This apparent contradiction is baffling, and perhaps the best explanation is that the small data set of the USYD group can be considered an anomaly around 1.0 G_0.

For the CSIRO group, when pyrazine is added the gold-conduction peak at 1.0 G_0 is 3 times the size of the solvent-only peak (Figure Appendix-2-75 **(a)** page 7-10 below). Samples of individual traces done at CSIRO (Figure 2-33 below) illustrate the enhancement of the gold conduction plateau at 1.0 G_0. This is a common observance during break-junction experiments and is interpreted here as evidence that the molecule is able to interact with gold and participate in the drawing-out of the thin gold wire of one-atom thickness (See Section 2.5.7 above).

Pyrazine in phenyloctane at 100 mV (CSIRO). Individual traces (Gain=5).
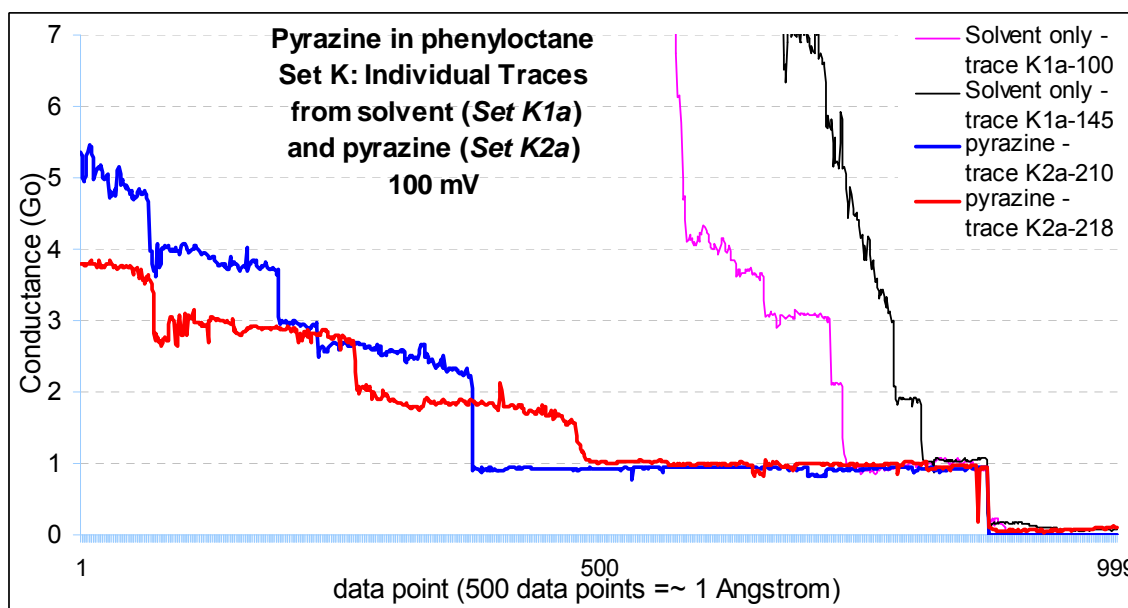
Figure 2-33: Pyrazine in phenyloctane – Typical individual traces, gold steps. Solvent traces (K1a-100 and K1a-145) have much smaller gold steps than the pyrazine traces (*K2a*-210 and *K2a*-218). This was typical of many traces in the two sets.

2.7.6.3   In toluene

There was virtually no evidence of pyrazine conduction over any range in toluene, other than to enhance the gold quantized conduction peak, which it did by 8 times in group D (Figure 2-29).

Toluene is the same basic size and shape as pyrazine (see Figure 2-34), it is not surprising that the interaction between the molecule and the solvent should be so strong as to completely prevent it forming a bridge between the gold electrodes. It doesn't completely prevent the pyrazine from adhering to the gold, because the gold peak is enhanced: this is evidence of an interaction of the gold with the pyrazine. But toluene's attraction to pyrazine is so strong that it does not allow the pyrazine to connect both ends to gold. During the break-junction experiment, as the gold wire snaps, although one end of a pyrazine molecule may be attached to one gold electrode, the other end cannot go to the other gold electrode because the pyrazine's is "piggy-backing" a toluene molecule. The attached toluene in insulative and has no "alligator clips" to join to the gold, so the bridge between the electrodes is not formed.
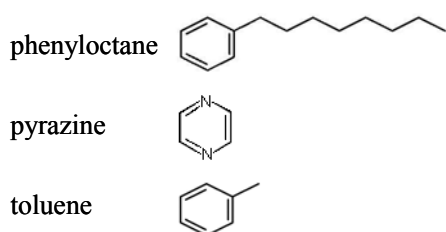
Figure 2-34: Comparison of pyrazine (middle) with the two similar solvent molecules, phenyloctane (top) and toluene (bottom).

2.7.6.4   In aqueous solvent

(The aqueous solvent was 0.1 M sodiumperchlorate.)

A large range of enhanced conduction was evident in the aqueous solvent but at much higher values than the organic solvents. Strong solvent-molecule interactions are a significant factor in the conduction histogram of pyrazine in the aqueous solvent. Unlike the solvents toluene and phenyloctane that bond with the pyrazine via π–stacking of the similar conjugated rings, the pyrazine-water complex is flat. The water molecule lies in the plane of the aromatic ring, and the lone pair of electrons on the nitrogen atom functions as the acceptor in the N─H-O hydrogen bond.[107] The species bridging the gold electrodes is most probably a complex with a variety of structures and geometries. However it does conduct better than the aqueous solvent alone over a high and broad range, from 300 to 3200 x 10^{-4} G_0.

At the lower conductance range, lower than 300 x 10^{-4} G_0, the addition of pyrazine lowers the conductance histogram peaks. *I.E.* there are less conduction events in the range where pyrazine indicated conduction in the organic solvents. This indicates that the components that conduct in the organic solvent (which are one or more pyrazine molecules in various configurations) are prevented from conducting when in the presence of water. In water conductance is dominated by water-pyrazine complexes that have a higher conductance than pyrazine alone.

The peak of the enhanced conduction range is 1300 x 10^{-4} G_0. This probably indicates the conductance of a preferred configuration of the pyrazine-water complex which dominates conduction, however it gives no indication of that structure.

It is interesting to note that in water alone the gold steps are quite high (~10 counts per valid sweep), much higher than in air or other solvents (~4 cpvs) (compare (d) with (b), (c), (d) and (f) in Figure 2-29). However when pyrazine is added the enhancement completely reverses.

2.7.6.5   In carbontetrachloride

When pyrazine is added to carbontetrachloride the conduction is enhanced over a small range (compared to the other solvents), and the enhancement is much lower.

There is a peak in the conduction curves for Group H at ~ 10×10^{-4} G_0: it is not a sharp peak but with over 1000 valid sweeps the curve has little noise and the peak is definite; nevertheless the peak in Group L (789 v.s.) is much sharper at 12×10^{-4} G_0 (Figure 2-29 (e) and (f)). The same peak is evidenced in the linear plots of Group L at ~11×10^{-4} G_0 (Figure 2-31).

The peak identified by group G is confirmed to be a single conduction event by the sharpness of the same peak in Group L. That is, this value *is* the conductance of a *specific* configuration of pyrazine between two gold electrodes, and that this is the *preferred* configuration of pyrazine between the electrodes when in the solvent carbontetrachloride.

Still, it does not prove conclusively that it is the conduction of a single molecule of pyrazine.

Carbontetrachloride is a smaller solvent molecule than toluene or phenyloctane, and most importantly it has no aromatic or π-system. Therefore its attraction to pyrazine is not through π–stacking of similar conjugated rings. There is less steric hindrance to

the motion of the pyrazine molecule(s) and it can couple between the gold electrodes more easily.

In carbontetrachloride the gold steps are dramatically enhanced by the addition of pyrazine. (The solvent alone does not enhance the gold steps.) Because of lower solvent-pyrazine interactions, the pyrazine is able to bind independently to the gold and participate in the drawing-out process during the creation of the gold wire of single-atom thickness (See Section 2.5.6 above where this is first mentioned).

2.7.7   Conclusion of pyrazine results

Pyrazine-solvent interactions play an important role in the conductance of pyrazine during break-junction experiments. A small, non-conjugated solvent such as carbontetrachloride allows the pyrazine to interact with the gold without solvent interference. This is evidenced by the extreme enhancement of the gold quantized conduction peaks.

Brolo (1998) noted that pyrazine is able to form a monolayer on Au(111)[45]. Thus there is an attraction and a co-ordination of geometry between pyrazine and the Au(111) surface. During the break-junction experiment this attraction is brought into play by stabilising the gold wire when it is one gold atom in diameter, and allowing it to stretch to lengths beyond the 2 or 3 atom limit determined by Untiedt, *et al*, (2002)[76].

Larger solvent molecules with conjugated rings interfere with the interaction between pyrazine and gold, but do not completely prevent it. One end of the pyrazine molecule may be free to attach to the gold surface (and enhance the gold quantized conduction peak, as in toluene and phenyloctane). But the other end may be hindered, and in the case of toluene with its close binding, completely prevented from attaching to

the other gold electrode. The effect is not so drastic in phenyloctane, where the solvent is not so similar to pyrazine, but it still gives rise to a number of alternative structures, making it difficult to observe a single value for the conduction of pyrazine.

In water the conduction is dominated by the polar solvent (giving a high but broad conductance range), with the hydrogen-bonded water molecules preventing the pyrazine's sticky ends (N atoms) from attaching to gold (evidenced by a decrease in the gold quantized conduction peak.). With electrochemical control (See Section 2.5.7 above and [14]) it may be possible to control the pyrazine-water interactions by providing a driving force to attract the pyrazine away from the water to the gold terminals.

In a sealed jar, unsolvated pyrazine is highly crystalline and sublimes at room temperature within the closed container, reforming pyrazine crystals at the neck of the jar. This implies that there is one mode of solidification with high order but weak intermolecular bonding. Individual molecules loosen easily from the end of pyrazine stacks and there is no other binding mode to facilitate a liquid phase. Toluene can substitute for pyrazine in π-stacking, creating short insulating "crystals" in solution (i.e., dimeric, trimeric and longer stacks of pyrazine and toluene). Phenyloctane also does to some extent, but it gives up its pyrazine attachment more easily.

A specific conductance peak for pyrazine is found at 10×10^{-4} G_0. It cannot be determined from these results that this is definitely a single pyrazine molecule standing upright between two gold electrodes with its nitrogen atoms attached to the gold terminals. Before that could be determined there would need to be more than one peak at multiples of this value. However it is quite close to the two theoretical values provided (which are 30×10^{-4} G_o and 4.7×10^{-4} G_o, see Section 2.7.2 above).

2-8 Investigation of bis-appended porphyrin

bis-phenanthroline-appended porphyrin.

2.8.1   Rationalization:

The basic form of a porphyrin (right) is a heterocyclic macro cycle derived from four pyrrole-like subunits interconnected via their α carbon atoms via methine bridges (=CH-). The macrocycle, therefore, is a highly conjugated system, and has 22 π electrons. Many porphyrins occur in nature, such as in green leaves and red blood cells, and in bio-inspired synthetic catalysts and devices.
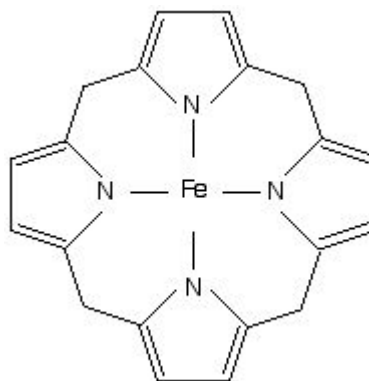
Chemical structure of ferroporphyrin, a porphyrin molecule that has an iron ion in the middle.

Heme, the iron complex of protoporphyrin IX, is the prosthetic group of a number of major proteins and enzymes that carry out diverse biological functions. These include binding, transport, and storage of oxygen (haemoglobin and myoglobin), electron-transfer processes (cytochromes), activation and transfer of oxygen to substrates (cytochromes P450), and managing and using hydrogen peroxide (peroxidases and catalases).

Molecular electronic scientists are interested in mimicking nature by using porphyrins as a framework for holding atoms or molecules in place during electron transfer reactions or as molecular wires in small devices (See Figure 2-35, below). Attachment of the wire to metallic electrodes could be effected by molecular "alligator clips"[36, 98] of extended 1,10'-phenanthroline linker units. The bis-appended porphyrin investigated here is an example of such a unit consisting of a single porphyrin.
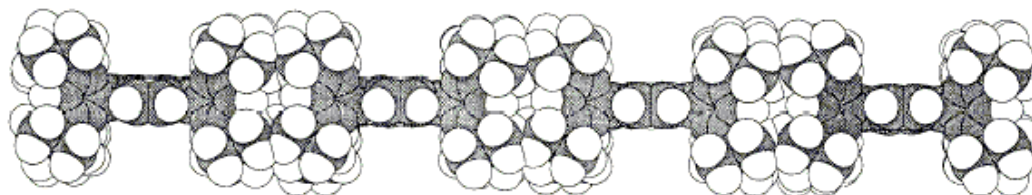
Figure 2-35: Proposed molecular wire (space filling model) consisting of 4 fused porphyrins (tetrakisporphyrin) from Reimers, *et al*, (1996)[37]. The core is conductive whilst the outer edges (bulky bits) are insulative and soluble in many organic solvents. Tethering of the ends to metallic electrodes by molecular "alligator clips" may be obtained by attachment of bidentate 1,10-phenanthroline end groups.

2.8.2   Background research

2.8.2.1   Similar molecules

Extended porphyrin wires have been investigated for their electrical conduction properties by from Kang, *et al,* (2005)[78] and Yoon, *et al*, (2003)[108]. Both groups used the same type of Zn(II) porphyrins with benzenethiol "alligator clips" on each end and performed the experiment using the electromigration-induced break-junction technique. Their findings are listed in Table 2-13 below. Also in a related paper using the same data, Kang, *et al*, (2005) have found that conductance was temperature-dependent and length-dependent as well and concluded:

> *"Length dependence measurements show that conductance decreases much more slowly with molecular length than the exponential dependence for a coherent tunnelling process. It suggests that the electrical conduction through porphyrin arrays is mainly due to the thermally activated hopping transport".*[109]

For such long molecules the conductance values they found were remarkably high, indicating the strong electronic coupling between metal sites available throughout the wire. They have calculated conductance of a single porphyrin unit as **71.7×10^{-4} G_0** for the fused porphyrin chain and **8.60×10^{-4} G_0** for the orthogonal porphyrin chain[109], however this was crudely done by simply dividing the resistance by the number of porphyrin units, with no regard to the resistance of the two benzenethiol "alligator clips".

An analysis of their data by extrapolation of linear resistance shows that resistance could not be linearly-length dependent as the line crosses the zero point at n=4 (implying that the Z4-porphyrin would be a superconductor).

In this thesis their data has been used to construct new graphs of <u>conductance Vs N</u> (number of porphyrin units) (Figure 2-36, page 2-92, below), for both T-type (fused) and Z-type (orthogonal), on both a linear scale and log scale. A linear equation and the exponential equation were determined. Values of conductance have been then calculated both ways for single-porphyrin T1 and Z1 molecules, as well as the benzenethiol alligator clips, and are set out in Table 2-14, page 2-92 below.
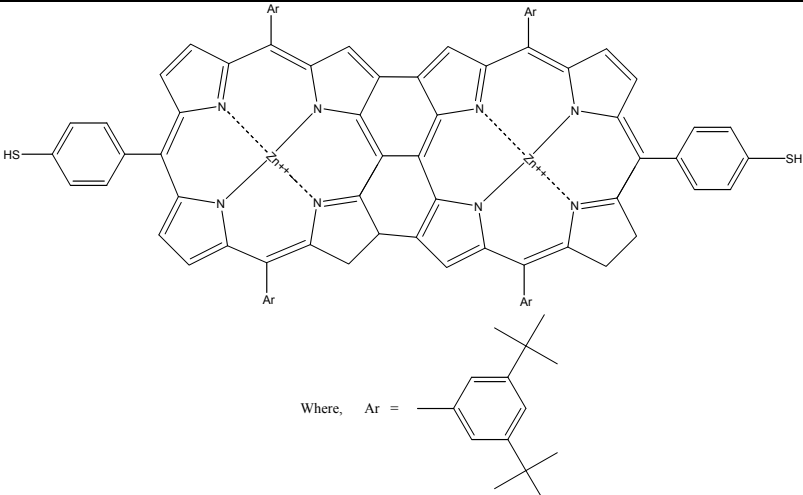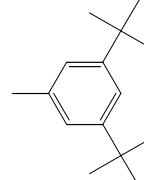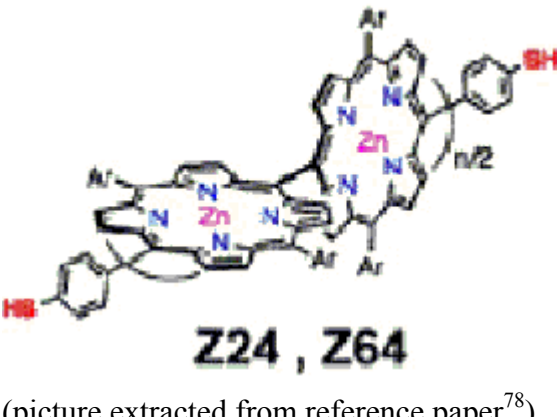
.Name	Structure	Cond'nce $10^{-4} G_0$
T6: six fused (ZnII) porphyrins with benzene-thiol alligator clips. (NOTE: T2 is shown in the diagram)	Where, Ar =	11.7^{78}
T8	as above	2.58^{108}
Z24 – 24 orthogonally-linked (ZnII) porphyrin with benzene-thiol alligator clips (NOTE: Z2 is shown)	**Z24 , Z64** (picture extracted from reference paper[78])	0.38^{78}
Z48	as above	0.193^{108}
Z64	as above	0.125^{78}

Table 2-13: Room temperature conductance at or near zero bias of multiple porphyrins with benzene-dithiol "alligator clips" from Kang, *et al,* (2005)[78] and Yoon, *et al,* (2003)[108].

Conductance values plotted against number of porphyrin units.
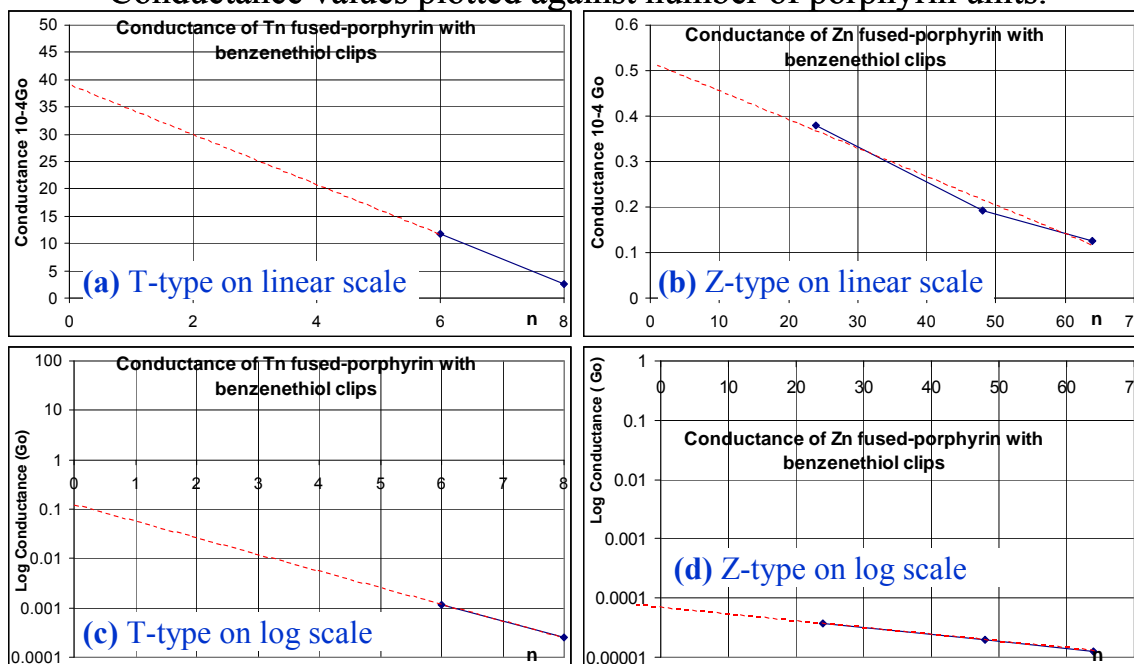
Figure 2-36: Conductance values of Kang, et al, (2005)[109] plotted against number of porphyrin units. Where C = conductance and n = the number of repeat units:

(**a**) and (**b**) are plotted on a linear scale for the vertical axis (rather than a log scale) based upon their theory that conduction is not due to tunnelling but hopping transport. Lines of best-fit (dotted) are extended to the axis and are of the form $C_n = A - Bn$ (x$10^{-4}G_0$) :

(**a**) is for T (fused) porphyrins: A=39.06 ;   B=4.56
(**b**) is for Z (orthogonal) porphyrins: A=0.522 ;   B=0.00638

(**c**) and (**d**) are plotted on a log scale for the vertical axis, conforming with tunnelling theory $C_n = Ae^{-\beta n}$ where β is per porphyrin unit (in G_0):
(**c**) is for T (fused) porphyrins: β=0.769 ;   A=0.1194 G_0
(**d**) is for T (orthogonal) porphyrins: β=0.0273 ;   A=0.0000726G_0.

Molecule	Conductance (if linear relationship) (x10^{-4} G_0)	Conductance (if exponential relationship) (x10^{-4} G_0)
clip-T1-clip	34.5	553
clip-Z1-clip	0.52	0.71
clip-clip only (using T data)	39.06	1194
clip-clip only (using Z data)	0.522	0.726

Table 2-14: calculated conductance of 1 porphyrin unit (T1 or Z1) using linear extrapolation or exponential extrapolation. Also, the calculation of the conductance of the benzenethiol clips only, using both methods for both the T and Z sets of data.

2.8.2.2   Theoretical value of conductance for bis-appended porphyrin

Various length T-type porphyrins (free-based) have been modelled by Tagami, *et al*, (2003)[110] using self-consistent tight-binding calculations. An exponential conductance curve was created (similar to that for the same molecule in Figure 2-36 (c) above) and is reproduced in Figure 2-37, below. (It should be noted that they modelled Aluminium contacts rather than gold and "held" the edge of the untethered porphyrin wire at 2.2 Å from the flat Al electrodes.) By their formula, the conductance of a single porphyrin (without the two phenanthroline appendages) would be 0.997 G_0.
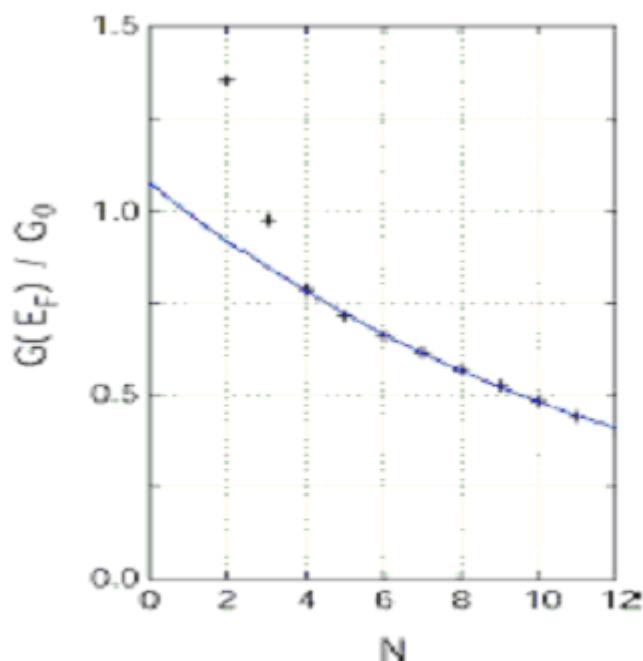
Relation between zero-bias conductance $G(E_F)$ and molecular length N. The cross marks denote the values obtained in the calculations. The solid curve corresponds to the exponential decaying function of $G(E_F) = G_m \exp(-\beta L)$

Figure 2-37: Tagami, et al, (2003)[110] exponential conductance curve for T (fused) porphyrins (free-based). N is the number of porphyrin units. Their caption is reproduced also. In terms of the formula A=1.082 G_0, and β= 0.0095 Å⁻¹. alternatively, β=0.0817 <u>per porphyrin unit</u>

2.8.3   Experimental set-up:

All experiments were conducted at CSIRO and done in phenyloctane at 100 mV.

Break-junction experiments done on the bis-porphyrin were at a concentration of

~ 5 mM in phenyloctane.

2.8.4   The sets of sweeps for bis-porphyrin

In all, 22 sets of sweeps in 7 groups were recorded. All break-junction sets of bis-

appended porphyrin were done at CSIRO with a bias of 100 mV and a withdrawal speed

of ~40 nm/s, and used phenyloctane as the solvent. The parameters for these sets are

listed in Table 2-15.

Set	Amp GAIN	item	Solvent	number of sweeps
A1	5	solvent only	phenyloctane	200
A2	8	solvent only	phenyloctane	888
A3	9	solvent only	phenyloctane	573
A4	7	solvent only	phenyloctane	500
A5	6	solvent only	phenyloctane	653
B1	5	bis-por	phenyloctane	850
B2	8	bis-por	phenyloctane	400
B3	9	bis-por	phenyloctane	564
B4	5	bis-por	phenyloctane	200
B5	6	bis-por	phenyloctane	1394
B6	7	bis-por	phenyloctane	550
B7	8	bis-por	phenyloctane	519
C1	9	bis-por	phenyloctane	850
C2	8	bis-por	phenyloctane	659
C3	9	bis-por	phenyloctane	444
C4	9	bis-por	phenyloctane	1417
D1	6	bis-por	phenyloctane	435
D2	5	bis-por	phenyloctane	198
D3	7	bis-por	phenyloctane	1091
D4	7	bis-por	phenyloctane	651
E1	5	bis-por	phenyloctane	229

Set	Amp GAIN	item	Solvent	number of sweeps
E2	6	bis-por	phenyloctane	444
E3	6	bis-por	phenyloctane	700
F0		bis-por	phenyloctane	
F1	5	solvent only	phenyloctane	371
F2	9	solvent only	phenyloctane	642
F3	5	bis-por	phenyloctane	1000
G1	9	bis-por	phenyloctane	1033
G2	6	bis-por	phenyloctane	1285
G3	6	bis-por	phenyloctane	1332

Table 2-15: Summary of sets of sweeps on bis-appended

2.8.5 Results from bis-por (all sets)

Equipment at CSIRO has a linear amplifier with a set-able gain to probe different conduction ranges (see Section 2.3.1.2). Prior to each set of sweeps a certain gain setting is selected, which gives results lying in a certain conductance range. Results have been grouped according to the gain setting.

Some conductance features of bis-por were evident in the histograms using a $\log_{10}$ conductance scale. These histograms are reproduced on the following six pages, one for each of the gain settings (5, 6, 7, 8 and 9), and a composite histogram of all data sets over all ranges (Figure 2-38 to Figure 2-43).

Using *Methods 1* and *2* there are some peaks in the gain = 6 sets, and these histograms are shown in Figure 2-44. Method *1* and *2* histograms for all the other gain settings show no peaks and are included in APPENDIX 2, page 7-12.

Bis-appended porphyrin in phenyloctane.
All Sets with GAIN=5: Histograms on log(10) scale.
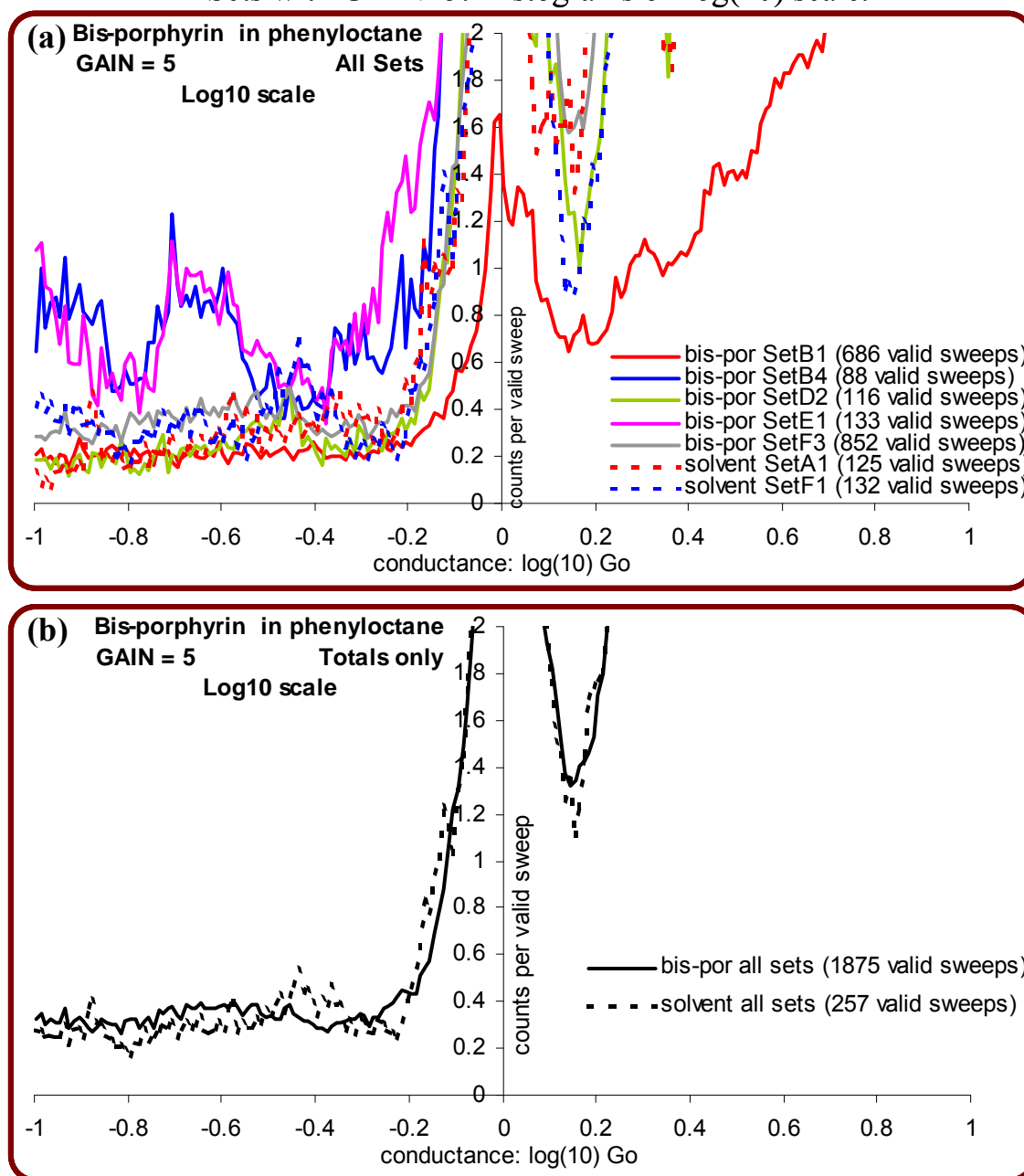
Figure 2-38: Histograms of bis-appended porphyrin in phenyloctane sets with gain=5 against $\log_{10}$ scale for conductance, and showing individual sets (upper) and weighted total of individual sets (lower). Full lines are bis-por and dotted lines are solvent only. Bias = 100 mV. The vertical axis is counts per valid sweep, the horizontal axis is conductance in $\log_{10}(G_0)$.

Bis-appended porphyrin in phenyloctane.

All Sets with GAIN=6: Histograms on log(10) scale.
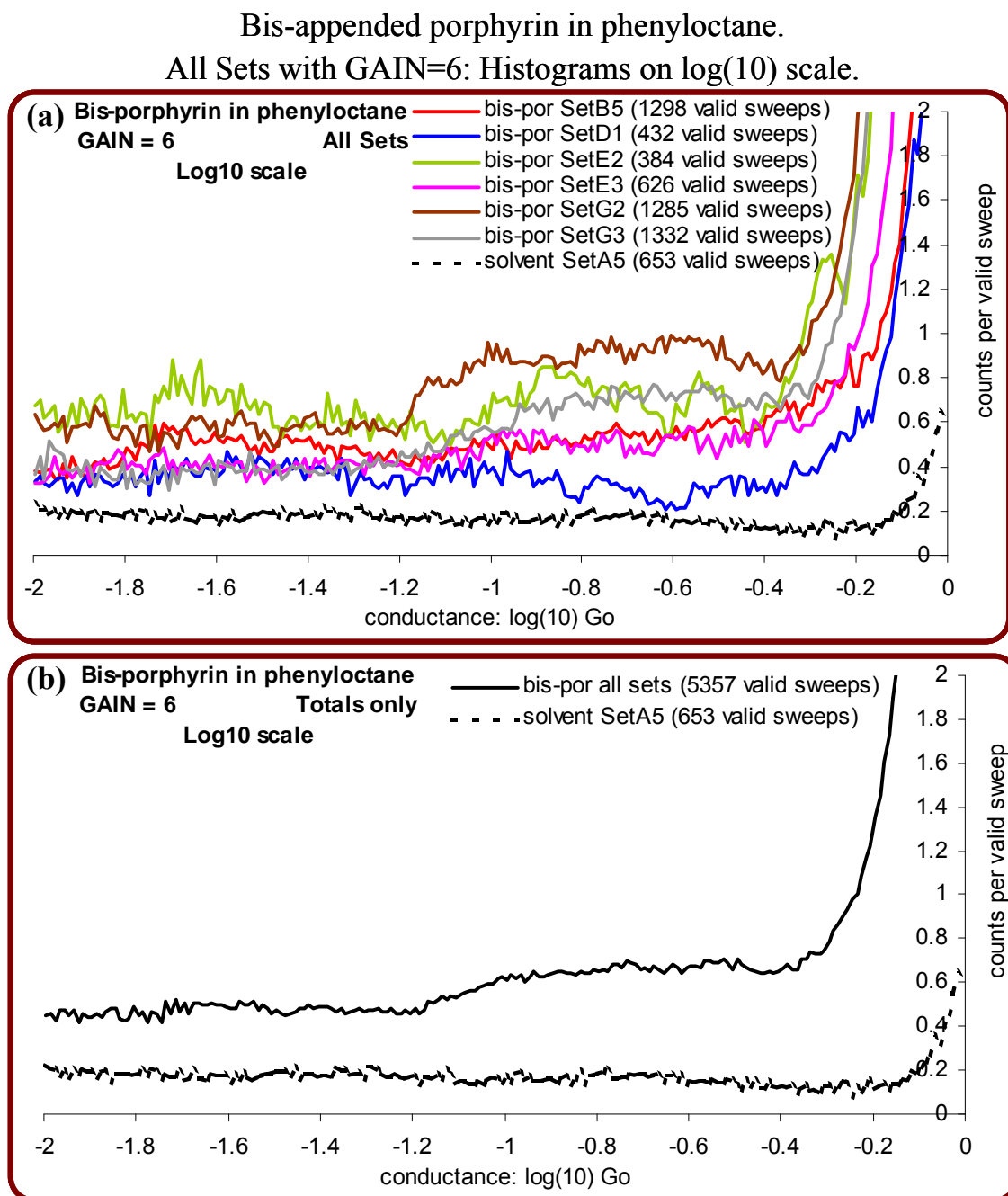
Figure 2-39: Histograms of bis-appended porphyrin in phenyloctane sets with gain=6 against $\log_{10}$ scale for conductance, and showing individual sets (upper) and weighted total of individual sets (lower). Full lines are bis-por and dotted lines are solvent only. Bias = 100 mV. The vertical axis is counts per valid sweep, the horizontal axis is conductance in $\log_{10}(G_0)$.

Bis-appended porphyrin in phenyloctane.
All Sets with GAIN=7: Histograms on log(10) scale.
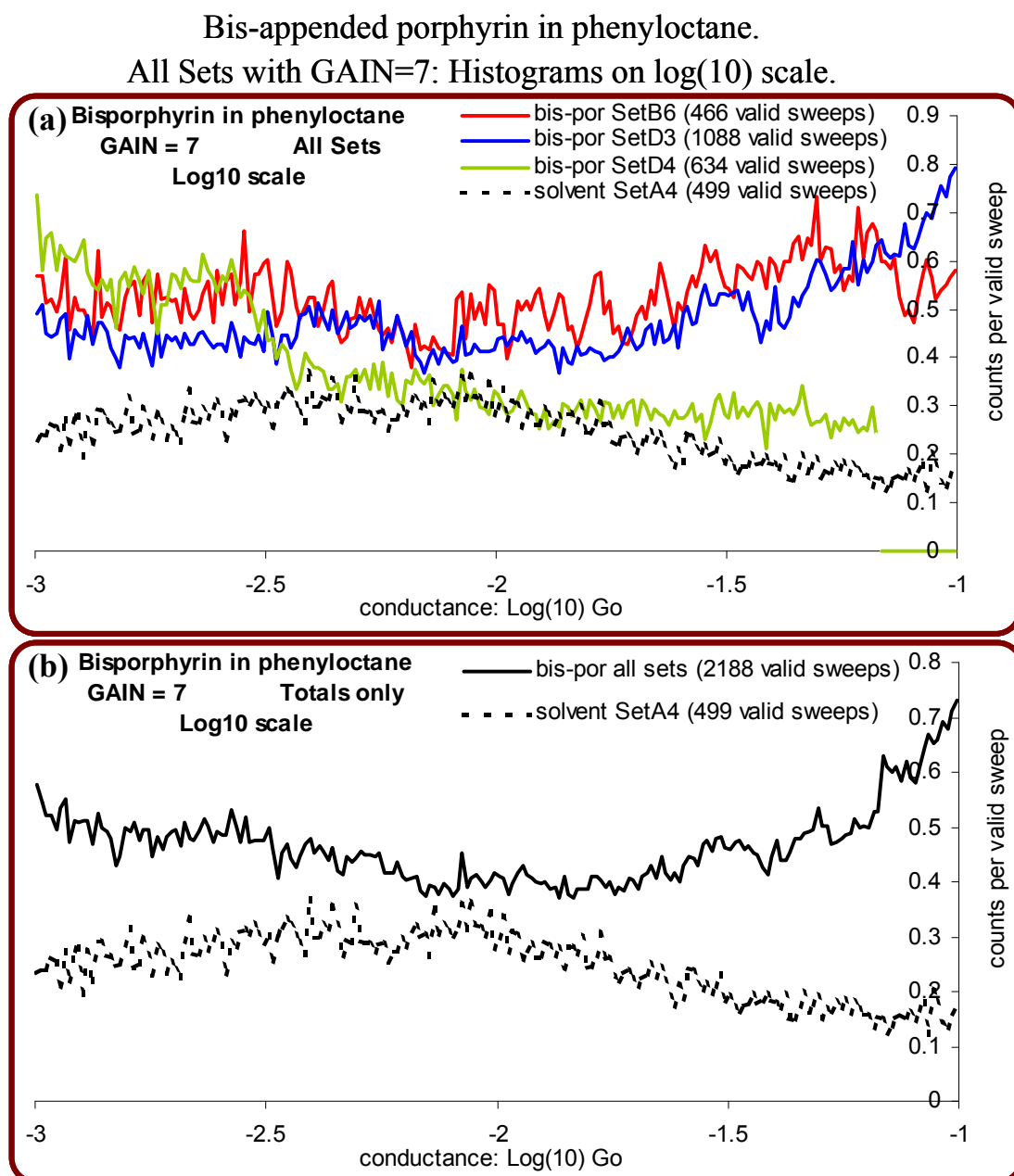
Figure 2-40: Histograms of bis-appended porphyrin in phenyloctane sets with gain=7 against $\log_{10}$ scale for conductance, and showing individual sets (upper) and weighted total of individual sets (lower). Full lines are bis-por and dotted lines are solvent only. Bias = 100 mV. The vertical axis is counts per valid sweep, the horizontal axis is conductance in $\log_{10}(G_0)$.

Bis-appended porphyrin in phenyloctane.
All Sets with GAIN=8: Histograms on log(10) scale.
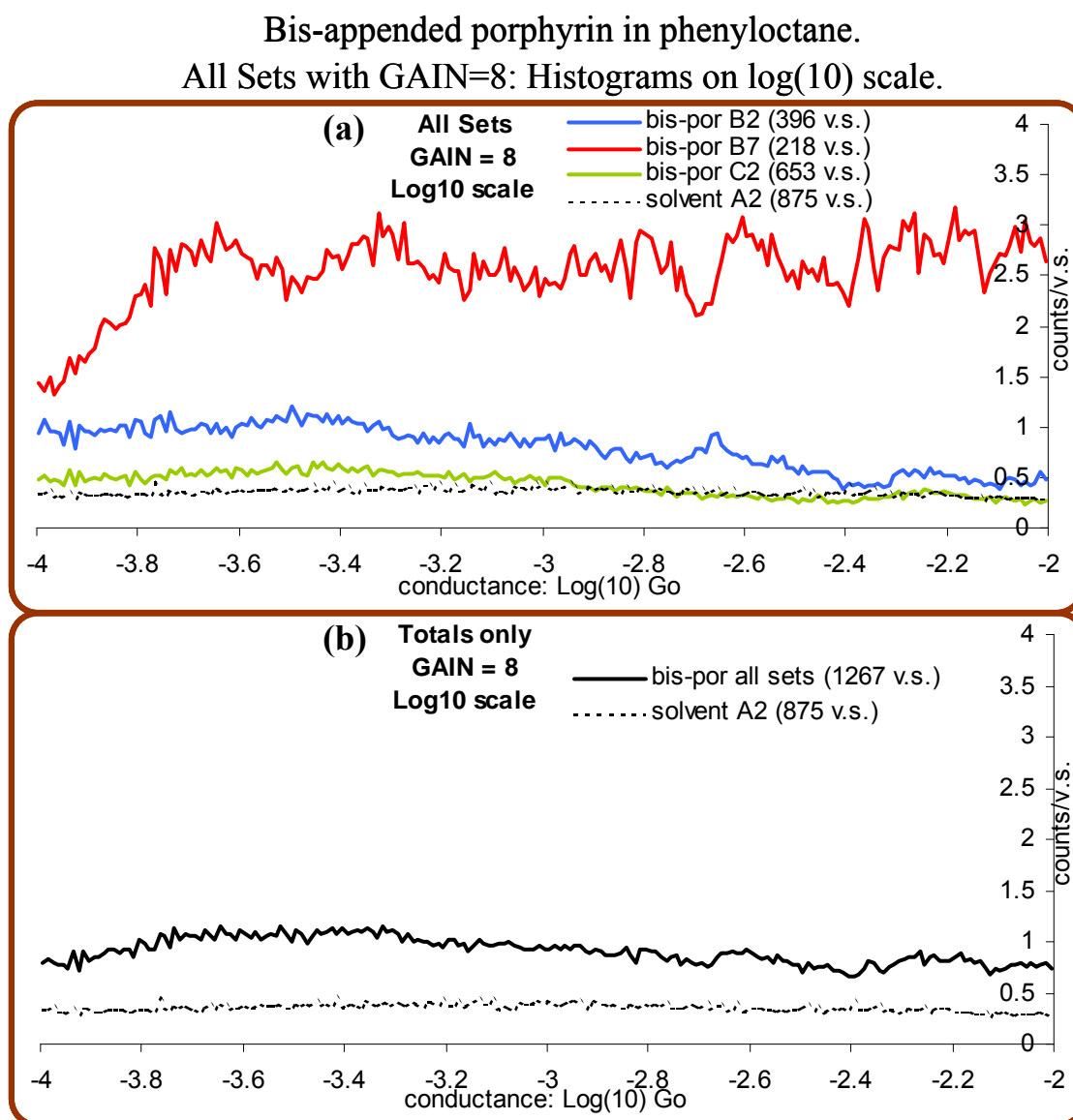
Figure 2-41: Histograms of bis-appended porphyrin in phenyloctane sets with gain=8 against $\log_{10}$ scale for conductance, and showing individual sets (upper) and weighted total of individual sets (lower). Full lines are bis-por and dotted lines are solvent only. Bias = 100 mV. The vertical axis is counts per valid sweep, the horizontal axis is conductance in $\log_{10}(G_0)$.

Bis-appended porphyrin in phenyloctane.
All Sets with GAIN=9: Histograms on log(10) scale.
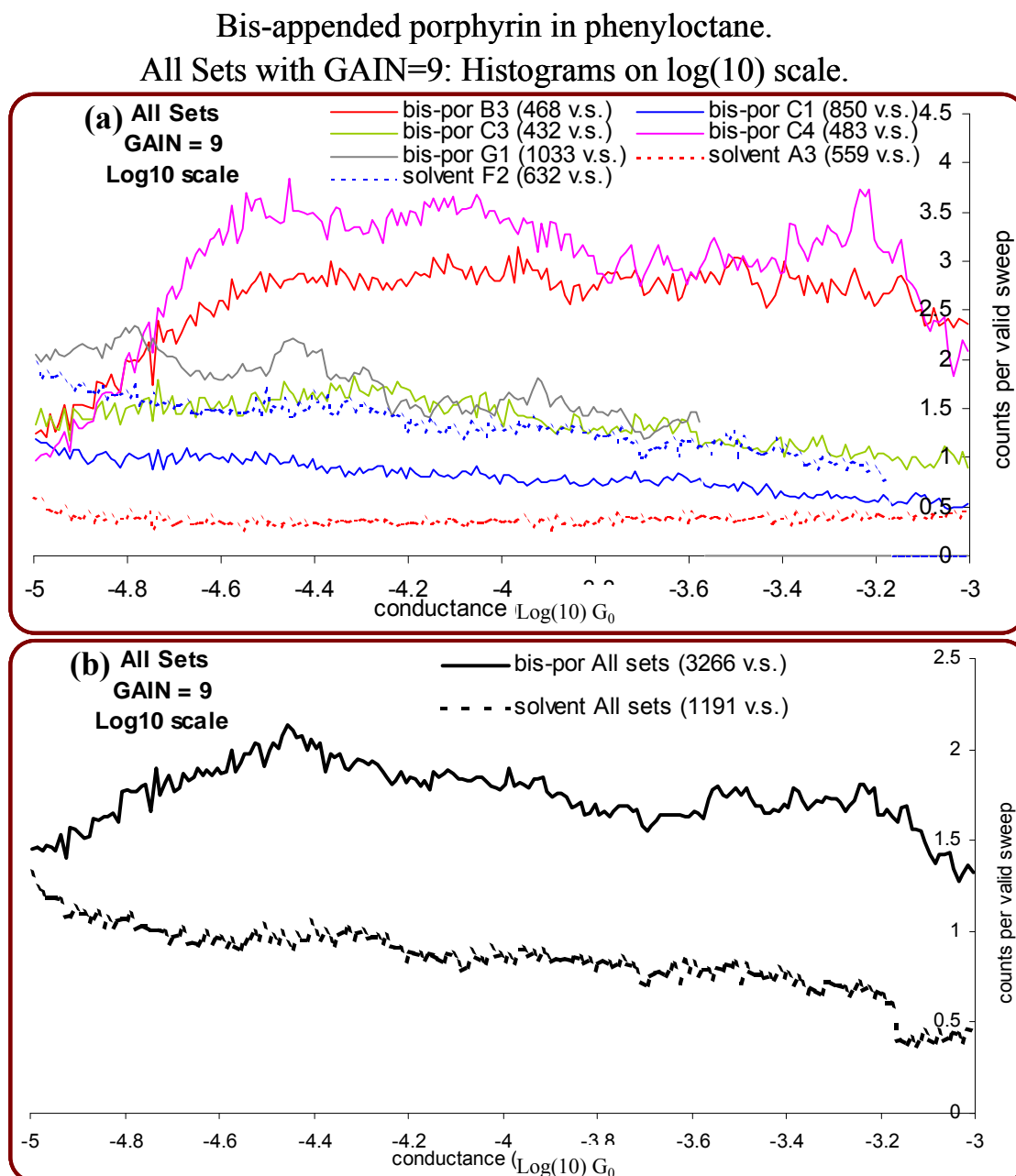
Figure 2-42: Histograms of bis-appended porphyrin in phenyloctane sets with gain=9 against $\log_{10}$ scale for conductance, and showing individual sets (upper) and weighted total of individual sets (lower). Full lines are bis-por and dotted lines are solvent only. Bias = 100 mV. The vertical axis is counts per valid sweep, the horizontal axis is conductance in $\log_{10}(G_0)$.
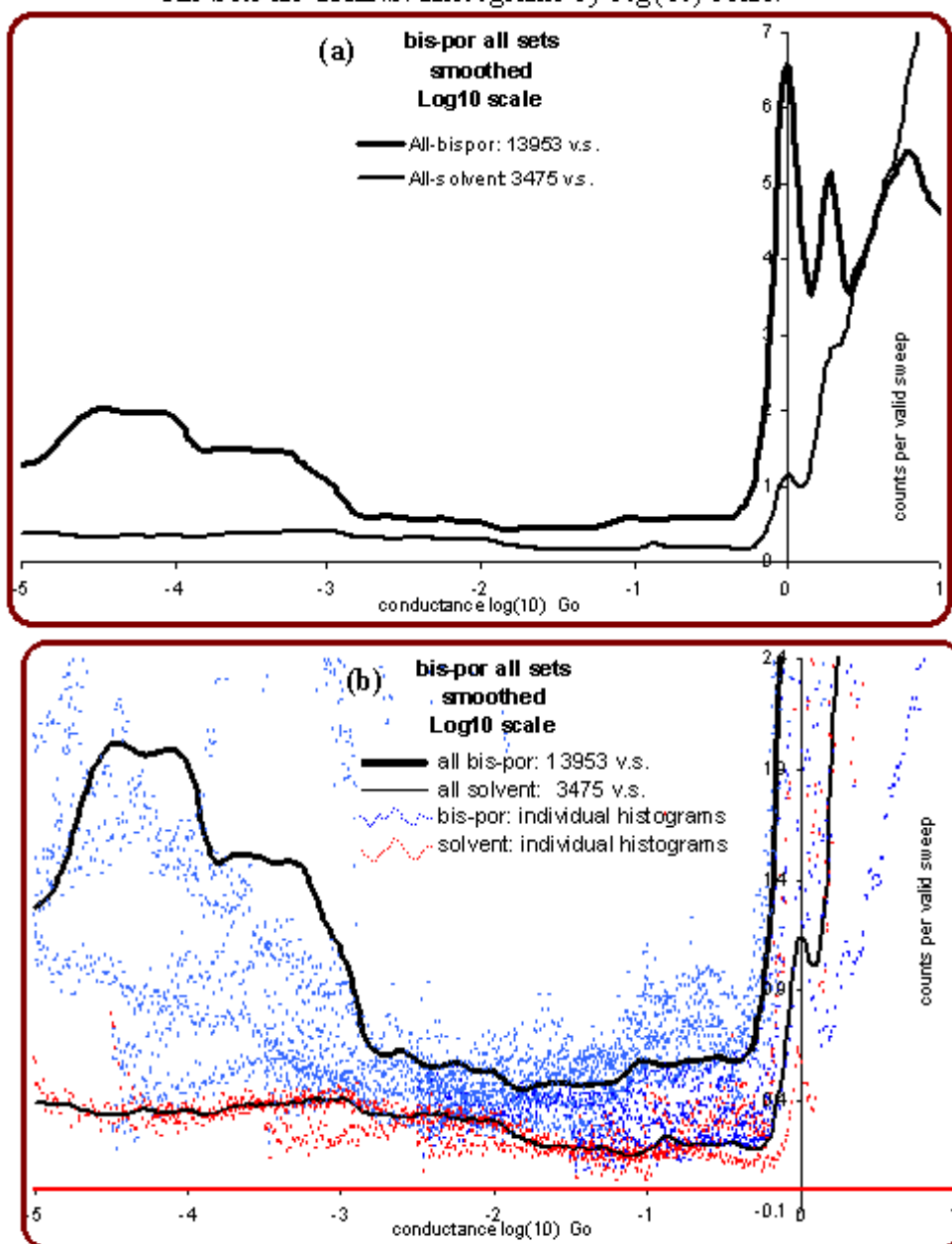
Figure 2-43: Histograms of bis-appended porphyrin in phenyloctane: <u>All sets at all gains</u>, against $\log_{10}$ scale for conductance. The upper graph shows weighted total of all sets (bold line = bis-porphyrin and light line = solvent only). The lower graph shows the same with a reduced vertical scale to show more detail at lower conductances, and the blue dots are the un-joined histograms from each of the bis-porphyrin sets, and the red dots are the un-joined histograms from each of the solvent sets. Bias = 100 mV. The vertical axis is counts per valid sweep, the horizontal axis is conductance in $\log_{10}(G_0)$. Sudden drops in the "bis-porphyrin all sets" curve are due to anomalies in joining different data sets together. Gaussian smoothing has been applied to the data.

Bis-appended porphyrin in phenyloctane.
All Sets with GAIN=6.
Histograms by rejection *Methods 1 and 2*.
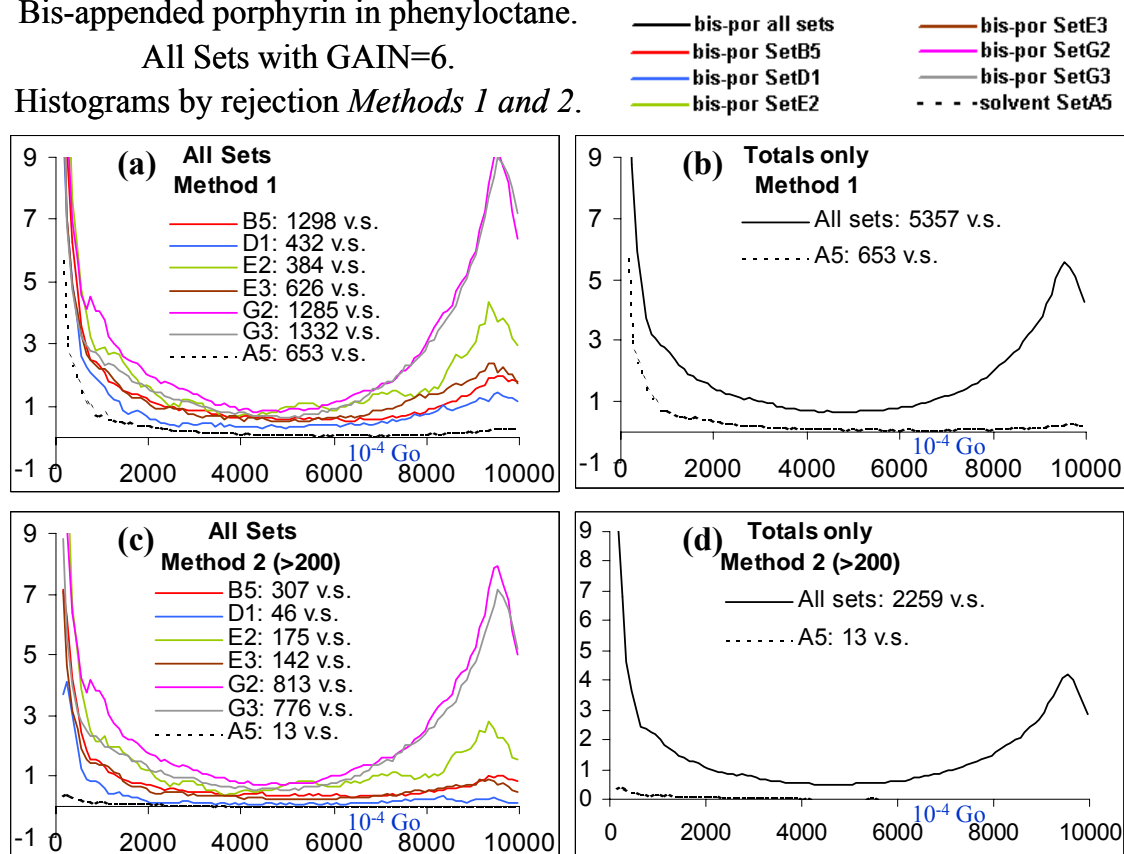
Figure 2-44: Histograms of bis-appended porphyrin in phenyloctane sets with gain=6 by *Method 1* (upper graphs) and *Method 2* (lower graphs), and showing individual sets (left) and weighted total of individual sets (right). Full lines are bis-por and dotted lines are solvent only. Bias = 100 mV. The vertical axis is counts per valid sweep, the horizontal axis is conductance in 10^{-4} G_0. v.s. = valid sweeps.

Conductance[⊗] peaks are evidenced at around 0.2 G_0 in sets *E1* and *B4* (Figure 2-38, $\log_{10}$ scale, gain=5). Both have low sweep count (~100 v.s. each) and the peaks do not occur in other sets at the same gain. There also appears to be peaks in both sets at 0.1 G_0 in the same histogram, however they are at the edge of the range.

A further analysis of the lower range of sets *E1* and *B4* by *Method 1* is shown in Figure 2-45 below. Both peaks 0.1 and 0.2 G_0 appear quite distinct. The total of the two sets has 221 valid sweeps so the two distinct peaks become a little more credible.

These conductance peaks are supported by broad peaks around the same value in sets *G2* and *E2* (Figure 2-39 (a), $\log_{10}$ scale, gain=6). The peak for *G2* is from 0.1 to 0.3 G_0 (1285 v.s.) while for *E2* the peak is centred around 0.15 G_0 (384 v.s.). The total for all gain=6 sets (Figure 2-39 (b)) shows a broad peak from 0.1 to 0.3 G_0 (5357 v.s.).

In the linear graphs (Figure 2-44), set *G2* has a peak at 0.1 G_0 by both methods *1* and *2* (with large data sets, 1285 and 813 v.s. respectively). Features from other sets at the same gain range do not generally rise above noise levels. However the histogram for the total of all sets, by *Method 2* (Figure 2-44 (d), 2259 v.s.) has virtually no noise and departure from curvature is suggestive of a conduction signal at 0.1 G_0.

Individual traces from *Set G2* are shown in Figure 2-46 below. Gold conduction steps are evident at 1.0 G_0. Molecular conduction plateaus are around $1/10^{th}$ of this value, with two distinct steps in traces 0621 and 0281 at 0.1 to 0.2 G_0 (these are not unique in the set).

[⊗] (Note: because the most significant results for bispor were quite high, conductance here is expressed in terms of G_0, not 10^{-4} G_0 as elsewhere.)

Bis-appended porphyrin in phenyloctane.
Sets E1 and *B4* only, and solvent *Set A1*: with GAIN=5.
Histograms by rejection *Method 1*.
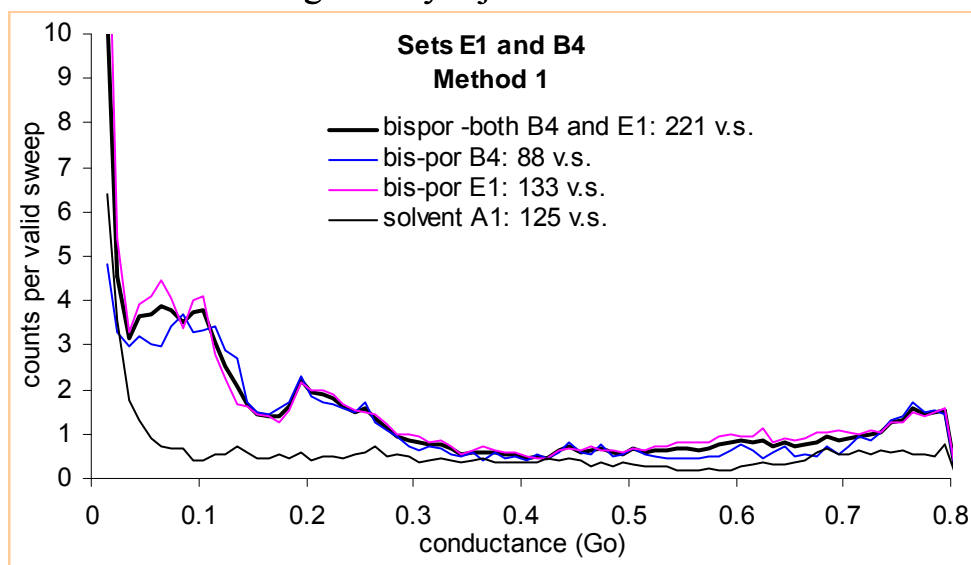
Figure 2-45: Histograms of bis-appended porphyrin in phenyloctane Sets *E1* and *B4* and solvent *A1*, with gain=5 by *Method 1*. Bias = 100 mV. v.s. = valid sweeps.

Bis-appended porphyrin in phenyloctane.
Sample of individual traces from Set G2
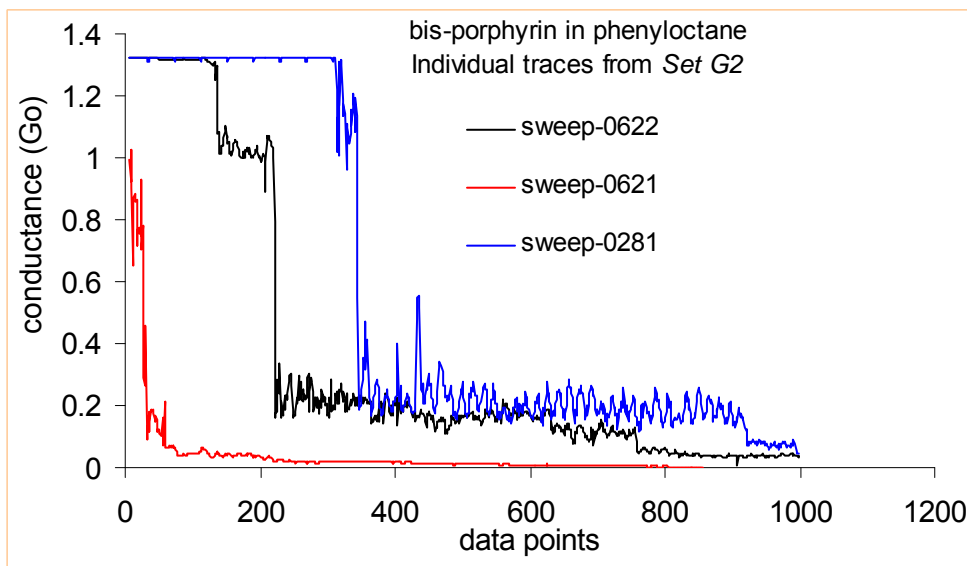
Figure 2-46: Sample of three individual traces from Set G2. Steps at 1.0 G0 indicate gold conduction. Steps at 0.1 to 0.2 G0 indicate molecular conduction. Bias = 100 mV.

Other $\log_{10}$ graphs (Figure 2-40 to Figure 2-43) do not show distinct peaks but a general enhancement in conduction over the whole range, particularly in the range from 0.1 to 0.6 G_0, and lower than 0.001 G_0.

The gold quantized conduction peak (in total) is significantly enhanced (Figure 2-43 (a)), however this is mainly due to Sets *G2* and *G3* (Figure 2-44 (a)). Other sets show much smaller or no enhancement of the gold peak.

2.8.6   Discussion of bisporph results

A conduction event (or series of events) of bis-appended porphyrin is evidenced at between 0.1 and 0.3 G_0. There are two distinct peaks at 0.1 G_0 and 0.2 G_0. From the available data it cannot be determined what configurations of the molecule are involved.

This is a much higher value than expected. Although theoretically the conductance of a single porphyrin (freebased, without the two phenanthroline appendages) has been calculated to be 0.997 G_0 (Section 2.8.2.2), an experimental value for a Zn based porphyrin is between 0.0001 and 0.05 G_0 (Section 2.8.2.1). There are few results to compare with and the variation in past research is quite high. The result here does not necessarily contradict prior research.

One possible geometry is that the porphyrin is laying flat between the two tips of the break-junction terminals, and that the conduction is primarily via the central copper atom, which, because of the metallic throughway, would be expected to have high conduction, near or just below 1.0 G_0. The broad value of the present result is not inconsistent with this scenario. However it is difficult under this scenario to explain the presence of two conductance peaks at 0.1 and 0.2 G_0.

Another possible geometry is that the porphyrin is standing lengthwise between the two break-junction terminals with its phenanthroline ends joining the two gold terminals. The individual traces, 0622 and 0281 (Figure 2-46) indicate two steps, one at 0.2 G_0 and another at 0.1 G_0. These may indicate the conductance of two and one bis-por molecules respectively. If they do, then the porphyrin could not be lying flat between the two electrodes. Two molecules can bridge the gap simultaneously only if they are positioned lengthwise.

Bispor enhances conduction over a broad range (Figure 2-43), but not consistently, suggesting that the mechanism is not a general mechanism but specific to the conduction of bispor given the experimental parameters (gold terminals, solvent interactions, etc). In general it was quite difficult to obtain consistent data for the bis-porphyrin with many sets appearing little different to the solvent-only sets or having no distinct features other than a broad enhancement of conduction.

Prior research has ascribed a peak at 0.2 G_0 to a carbon atom in the gold chain ("*After several hours of experiment 500 curves gave a peak at about 0.2 G_0, whose occurrence increases with time*".[94]), however in that work there is no mention of a peak at 0.1 G_0 or of two peaks. Here such peaks do not appear in the solvent only histograms. So this explanation is dismissed.

In only two sets was the gold conduction step significantly enhanced by the addition of bispor. This indicates that the molecule has difficulty attaching "properly" to the gold and this was only significantly achieved in those two sets. By "properly" it is meant that the molecule attaches by one of its phenanthroline-type alligator clips.

2.8.7 Conclusion of bispor results

Some results show a conduction event for bisappended porphyrin in phenyloctane at 0.1 G_0, with a second conduction event at 0.2 G_0. The presence of two peaks, one a multiple of the other, may lead to speculation that it is the conduction of one and two bispor molecules standing vertically between the gold terminals with the phenanthroline "alligator clips" joining the electrodes. However it is an extremely high value which has no support from other sources, and so it is sagacious to avoid such a rash conclusion. It may simply be due to the bispor molecule laying flat between the gold electrodes, or it may be a solvent effect. However the peak should be noted even though it cannot be conclusively explained.

Bispor can interact with the gold at one end, which is evidenced by the increase in the gold conduction steps, however this wasn't always achieved, most likely due to solvent interactions. The gold-bispor attachment may be susceptible to subtle changes in the concentration (which would vary over time due to solvent evaporation) or other experimental factors.

2-9 General conclusion to Chapter 2: break-junction experiments

Conclusions relating to the specific molecules are outlined in the relevant sections above and need not be repeated here. General conclusions from the whole series of experiments are expressed below.

Experiments on 1,8-octanedithiol have established that the method and equipment are adequate.

The observation of the enhancement of the gold conduction step at 1.0 G_0 has emerged as an indicator that the molecule can interact with gold. That is, it attaches to the gold by its azine or thiol "alligator clip". Drawing upon results of Chapters 3 and 4, the molecule is bound to a gold adatom and the adatom-molecule unit is highly mobile and can extend the time for which a single-atom gold chain exists during the break-junction experiment.

Should this enhancement of the gold peak *not* occur, it is unlikely that the experiment will go on to produce signals for the conduction of a single molecule. That is, if one end cannot attach, it is unlikely that two ends will attach in a specific geometric alignment.

For this reason the general increase in conduction of pyrazine in aqueous solution at a high range can be dismissed as a solvent dominated phenomenon, as there was no prior indication that the pyrazine attached independently to the gold (*i.e.* the gold peak was not enhanced by the addition of pyrazine).

Despite prior research to the contrary,[101] the solvent was observed to play an important role in the conduction behaviour of many molecules. The difference here is

that the molecules in which this observation was made all relied on azine linkers to the gold electrode (the prior research looked at 1,8-octanedithiol in toluene, dodecane, water, and 0.1M NaClO$_4$). Future break-junction experiments on molecules with conjugated rings and/or azine linkers will require a careful selection of solvent(s) and experimental conditions (such as electrochemical control) to isolate these effects.

The use of log$_{10}$ scale histograms has surfaced as a powerful tool for observing long range enhancement of conduction of the molecule over the solvent alone, which has received little attention until now. It identifies the fact that multiple configurations of the molecule are possible between the break-junction electrodes to produce this broad range, and these configurations include solvent effects. With many configurations possible it is quite difficult to isolate the configuration that indicates the conduction of a single molecule (if such a single configuration exists within the experimental parameters).

All the experiments on molecules with azine alligator clips would be enhanced by a tool that enabled electrochemical control of the liquid cell to break to solvent dominated effects and drive the molecule to attach to the gold terminals.

(blank page)

Chapter 3 Chemisorbed and Physisorbed Structures for 1,10-Phenanthroline and Dipyrido[3,2-a:2′,3′-c]phenazine on Au(111)

3-0 Synopsis for Chapter 3

Scanning tunnelling microscopy (STM) images of 1,10-phenanthroline (PHEN) and dipyrido[3,2-*a*:2′,3′-*c*]phenazine (DPPZ) on Au(111) are recorded using both *in situ* and *ex situ* techniques. The images of PHEN depict regimes of physisorption (relatively weak bonding) and chemisorption (relatively strong bonding with rearrangement of covalent bonds or structure) whilst DPPZ is only physisorbed. All physisorbed structures are not pitted and fluctuate dynamically, involving aligned (4 × 4) surface domains with short-range (ca. 20 molecules) order for PHEN but unaligned chains with medium-range (ca. 100 molecules) order for DPPZ. In contrast, the chemisorbed PHEN monolayers remain stable for days, are associated with surface pitting, and form a (4 × √13)R46° lattice with long-range order. The density of pitted atoms on large gold terraces is shown to match the density of chemisorbed molecules, suggesting that gold adatoms link PHEN to the surface. For PHEN, chemisorbed and physisorbed adsorbate structures are optimised using plane-wave density-functional theory (DFT) calculations

for the surface structure. Realistic binding energies are then obtained adding dispersive corrections determined using complete-active-space self-consistent field calculations using 2nd-order perturbation theory (CASPT2) applied to cluster-interaction models. A fine balance between the large adsorbate-adsorbate dispersive forces, adsorbate-surface dispersive forces, gold ligation energy, and surface mining energy is shown to dictate the observed phenomena, leading to high surface mobility and substrate/surface lattice incommensurability. Increasing the magnitude of the dispersive forces through use of DPPZ rather than PHEN to disturb this balance produced physisorbed monolayers without pits and/or surface registration but with much longer-range order. Analogies are drawn with similar but poorly understood processes involved in the binding of thiols to Au(111).

Theoretical calculations in this chapter were performed by Ante Bilic and Jeffery Reimers.

3-1 Introduction to Chapter 3

"Science must have originated in the feeling that something was wrong." (Thomas Carlyle, 1795-1881 British historian and essayist)

3.1.1 Established research – 1,10-phenanthroline monolayers

Molecular electronic devices typically are coupled with their ends tethered to electrodes. In experimental studies these electrodes are, in turn, connected to some instrumentation. One of the most common surfaces used for this purpose is Au(111), because of the relative ease of preparation of a clean, reproducible surface and the geometric reliability of monolayer formation based upon the expected chemical bonding of the molecule. Precise and predictable surface-adsorbate bonding and geometries are elusive, however, and inconsistent contact geometries have given rise to large discrepancies in experimental results.[43, 111] This report proposes geometries for the binding of 1,10-phenanthroline (PHEN) on the Au(111) surface, confirming its possible use as a molecular "alligator clip".[37, 57] The study also demonstrates enhanced properties for the binding of a laterally extended PHEN molecule, dipyrido[3,2-a:2′,3′-c]phenazine (DPPZ); both molecules are shown in Figure 3-47 below.
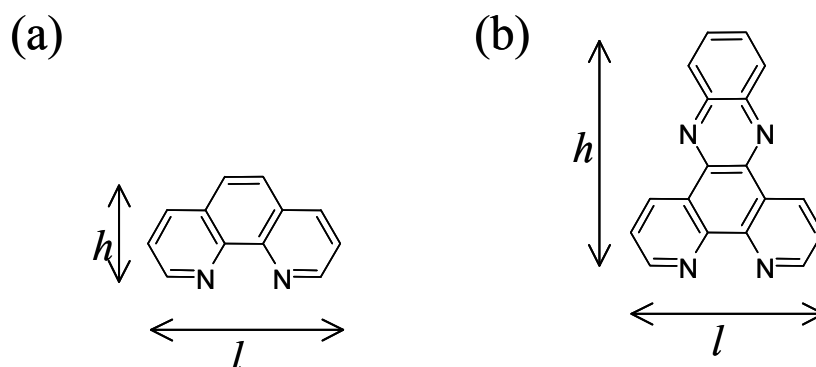
Figure 3-47: **(a)** 1,10-phenanthroline (PHEN): $C_{12}N_2H_8$. h=8.0 Å, l=11.1 Å; **(b)** Dipyrido [3,2-*a*:2′,3′-*c*]phenazine (DPPZ): $C_{18}N_4H_{10}$. h=12.9 Å, l=11.1 Å

3.1.1.1   1,10-phenanthroline on Au(111)

1,10-Phenanthroline monolayers from aqueous solution on Au(111) were first observed by Cunha, Jin and Tao by means of electrochemical Scanning Tunnelling Microscopy (*in-situ* STM) and shown to form locally ordered, complex and variable structures (1997).[48]   Important features of the monolayer noted in that study include:

1. The monolayer forms spontaneously.

2. The molecules stand with their axes vertical to the substrate surface and the nitrogen atoms facing the surface.

3. They form long chains of stacked molecules (like rolls of coins).

4. The PHEN molecules in each chain are aligned at 60° to the chain, with each molecule stacked slightly off-centre to its neighbours.

5. Stacking faults may occur along the chain, commonly forming groups of only 3, 6 or 9 fully aligned PHEN molecules.

6. Reversible phase transitions in the monolayer (order to disorder to order, etc.) occur with variations in the electrochemical potential of the substrate working electrode, attributed[112] to the large molecular dipole moment.

7. The monolayers can produce pits in the surface with a depth of typically one gold layer.

8. The pit sizes increase with increasing gold-substrate potential and decrease (and/or "islands" are formed) when this potential is then decreased.

9. Each PHEN molecule is observed in "high-resolution" (topology differential) images as two small bright features 3 Å apart indicating the alignment of the aromatic plane with respect to the chain propagation direction. The most intense signal in regular topology images has recently been attributed to the hydrogen atoms opposite the nitrogen head group.[112]

In order to analyse the PHEN structure for its possible use as an "alligator clip" linking covalently attached functional molecular units to the gold surface, enhanced regularity in its monolayers must be obtained, and possible effects due to interactions between attached groups on neighbouring molecules must be anticipated. For example, if strong surface – head group interactions control the monolayer structure, then the structure should be insensitive to the properties of attached entities other than, say, strong steric repulsions that they may induce.　 If the inter-PHEN interactions are significant, however, then the nature of the interactions between the attached units would always be critical.　 The net effect for PHEN-based systems is that means must be obtained for either eliminating or controlling the inherent PHEN stacking faults, phase transitions, pit formation, and long to medium range monolayer irregularity; understanding the basic nature of the surface – head group and intra-monolayer interactions are critical to this process.

3.1.1.2　　　1,10-phenanthroline on Cu(111)

The structure of PHEN on Cu(111) has also been observed[113] and has many features in common with that on Au(111) including the presence of ordered regions with very similar structure. As the lattice vectors for Cu(111) are 12% shorter than those for Au(111), this implies that the surface and substrate lattices are unrelated and hence the metal to head group interaction is of secondary importance.　 However there are also important differences such as increased long range order on Cu(111), no pitting on Cu(111), and a most significant change in the alignment of adlayer domains: these are only found at 120° orientations on Au(111) but occur at all angles on Cu(111).　 The nature of the interaction between PHEN and Au(111) thus remains an open question.

3.1.1.3   Surface pitting in monolayers on Au

Of the issues raised for PHEN monolayers on Au(111), the one that is most general is that of surface pitting. Cunha *et al.*[48] attributed the surface pitting to surface stress induced by the strong adsorption of the PHEN molecules on the surface, following the explanation expounded earlier by McDermott *et al.*[114] for pitting during thiol-based Au(111) monolayer formation. Thiols are known to form strong covalent chemisorptive bonds with gold,[115] in contrast to the weaker interactions expected for the binding of nitrogen-based electron donors including bidentate ligands such as PHEN[48] and 2,3′-bipyridine[49, 116] as well as monodentate ligands such as pyridine,[117-119] ammonia,[118, 120] and amines.[42] Nevertheless, pitting is observed in monolayers of all of these classes of bindings, making this phenomenon of general interest. The observed structure of PHEN on Cu(111) which is clearly due to physisorption and involves no pitting provides a useful reference system.[113]

3.1.2   Experimental presentments of this chapter –STM images

This chapter presents STM images of PHEN on Au(111). These images are obtained by varying the type of substrate used, the conditions of monolayer formation, including the degree and nature of electrochemical control, the solvents used in monolayer formation and in monolayer imaging (aqueous and non-aqueous), the size of the terraces on the Au(111) surface, and the monolayer maturation time. The motivation for this work is to find motifs from amongst the demonstrated[48] wide range available that enhance regularity, enable monolayer control, and reveal the nature of the forces that control the monolayer structure. Some images, recorded as a function of time during

monolayer formation using in situ STM techniques,[115, 121] show evidence for an initial scenario in which there is no pitting and the monolayer changes dynamically between structures with fixed surface registration. Other images recorded after pre-preparation of the monolayer, show a stable pitted phase. The density of the pits, and the nature of the structure observed in high-resolution images are determined. Also presented are the first STM images of dipyrido [3,2-a:2′,3′-c]phenazine (DPPZ) on Au(111), a laterally extended PHEN derivative that shows the type of extended conjugation that may be useful in a molecular device attached to a PHEN–type alligator clip.[37, 57] This part of the study allows the monolayer formation conditions to be varied through changes to the intermolecular interactions between adsorbate molecules.

3.1.3   **Theoretical presentments of this chapter – DFT etc**

The observed PHEN and DPPZ surface patterns are then interpreted using plane-wave Density-Functional Theory (DFT) to simulate the structure of physisorbed and chemisorbed monolayers, with chemisorption predicted to involve the formation of gold adatoms above the (111) surface that chelate the adsorbed molecules. These calculations are supported by 2nd-order Møller-Plesset perturbation theory (MP2) and Complete-Active-Space Self-Consistent-Field (CASSCF) combined with MP2 calculations[122] (CASPT2), of the dispersive intermolecular and physisorptive forces. These forces are not included in modern DFT functionals and do not account for the strong attraction that occurs between PHEN (and DPPZ) molecules[112] and between gold and aromatic molecules.[102] The combination of CASPT2 with DFT provides a comprehensive description of phenanthroline-based binding to gold, exposing many issues of direct relevance to the chemisorption of thiols and amines to gold.

3-2 Methods of Chapter 3

3.2.1   Chemicals.

1,10-Phenanthroline was purchased from Aldrich and used as received. Dipyrido[3,2-*a*:2′,3′-*c*]phenazine was synthesized from 1,10-phenanthroline-5,6-dione using the method of Amoouyal et al.[123] with 98% yield. It was purified using silica chromatography followed by recrystallisation from chloroform/pentane. Phenyloctane was used as supplied from Fluka (Purum Grade; > 98% purity with boiling point 264-268 °C). Millipore water from a Milli-Q 18.2 mΩ cm filter was used throughout.

3.2.2   Ex situ STM of pre-assembled PHEN monolayers.

Glassware was cleaned in Piranha solution and rinsed copiously in water. Gold on mica substrates were purchased from Molecular Imaging and annealed by a hydrogen flame for a few minutes prior to use. PHEN was dissolved in water by ultrasonication for 30 min at ~ 50 ºC and a 30 mM PHEN solution in 0.1 M NaClO$_4$ was prepared. The monolayer was formed from the aqueous solution with an applied potential of +0.7 V vs. SCE to the gold working electrode for an hour using a potentiostat with a calibrated 0.25 mm platinum wire as the reference and counter electrodes. The sample was then gently rinsed several times with water and three times with ethanol (99.9% decanted from bulk as received from Redox Pty Ltd) and left standing (in air) for at least a day. The pre-assembled monolayers remained stable for at least several days under ambient conditions as well as throughout STM imaging.

The STM images were obtained by a Molecular Imaging Picoscan II instrument; the STM tips were made from Pt$_{0.8}$/Ir$_{0.2}$ wire cut using precision wire snips. A PTFE (poly-tetra-fluoro-ethylene) liquid cell was used with phenyloctane as the imaging medium.

3.2.3   In situ STM of PHEN and DPPZ monolayers on single-crystal gold electrodes.

Glassware was cleaned by boiling in 15% nitric acid solution and rinsed copiously in Millipore water. Gold substrates were electropolished in 0.1 M H_2SO_4 at ~20 V DC bias, then rinsed successively in 1.0 M HCl and water, and annealed at 850 ºC for 6 hours. Before use, the Au(111) was further freshly annealed by a hydrogen flame and quenched in Millipore water which was saturated with H_2. The STM images were recorded using a Molecular Imaging Picoscan (USA) instrument using tips cut from 0.25 mm tungsten wire, sharpened by electrochemical etching (approx 15 V AC in approx 1.0 M KOH), and insulated by coating with Apiezon wax. Potential measurements were made using a platinum reference electrode that was calibrated against a SCE electrode after each measurement.

For the experiments on PHEN monolayers, a home-made Au(111)-electrode was used.[124-126] Single crystal beads were prepared by melting gold wire (99.999%, Ø 1.0 mm), with the (111) surface selected using a laser and fixed in position using a polymer adhesive before polishing. A solution of 0.36 mM PHEN and 50 mM $KClO_4$ (Sigma-Aldrich 99.99%) in water pH 6.5 ($HClO_4$, Fluka, Ultrapure) was freshly prepared and added to the STM cell to form the monolayers.

For the experiments on DPPZ, the adsorbate was dissolved in Analytical Grade ethanol using a sonicator. The Au(111)-substrate was a disk 12 mm in diameter and ~1 mm thick (Surface Preparation Laboratories, The Netherlands). The substrate was exposed to the solution for 24 hours with no potential control, rinsed with Millipore

water, and mounted in the microscope. Imaging was conducted under potential control in a 0.1 M phosphate buffer at pH 6.9.

3.2.4   Electrochemistry.

Reductive desorption experiments were conducted in a standard electrochemical cell using the CH Instrument 900B potentiostat. The reductive desorption experiments were carried out in either 0.1M KOH/water or 0.1M KClO$_4$/water solution. In both cases the solution had been de-aerated with nitrogen for 30 min. Recorded voltammograms showed clear indication of a reductive desorption current present in the first scan, which disappeared in subsequent scans. The current caused by the reductive desorption was determined as the difference between the first and second scan. Integration of this curve gave a precise measure of the average density of the monolayer. More details are provided in Appendix 7-3.

3.2.5   Calculations of adsorbates on gold surfaces.

All computations involving surfaces were carried out using the Vienna Ab initio Simulation Package (VASP),[127, 128] A plane-wave basis set was employed to expand the electronic wave functions using ultrasoft pseudopotentials,[129, 130] which allows the use of a low energy cut-off for the plane-wave basis set. The functional of Perdew and Wang (PW91),[131] a form of the generalized gradient approximation (GGA), was used throughout to model the electron-electron exchange and correlation interactions. The relaxation of atom positions was performed using a conjugate-gradient optimisation procedure.

The gold surface was modelled using supercells consisting of gold slabs three atomic layers thick separated by a vacuum region of 10-layer equivalent thickness; periodic boundary conditions were applied in all three Cartesian directions. While

improved convergence of the results could have been obtained by expanding the lattice to four layers thick, the improvements produced would be much less than other shortcomings of the calculations and so are not warranted. The interlayer spacing was taken from the analogously computed[132] value of the gold bulk lattice parameter, 4.2 Å, giving bulk Au-Au bond lengths of 2.970 Å, 3% longer than the observed value of 2.885 Å. All calculations included 16 gold atoms per layer. In low-coverage calculations, a single molecule was placed in the vacuum region on the upper side of the slab. This represents 1/16 ML coverage relative to surface atoms, sufficiently low that the molecules in adjacent cells are well separated. In high-coverage calculations, three PHEN molecules were included per unit cell, giving a density in accord with the high-density phase observed experimentally. Mostly, a (4 × 4) supersurface cell was used, resulting in the PHEN molecules being ordered into linear chains. To examine the observed stacking faults in linear chains, some calculations were also performed using a (4 × √13)R46º supersurface lattice. Wood's notation[133] is used to name the surface lattices. For both lattices, Brillouin-zone integrations were conducted on a 3 × 3 × 1 k-point Monkhorst-Pack grid with a Methfessel-Paxton smearing[134] of 0.2 eV. VASP calculations pertinent to gas-phase molecules employed cells of the same size as the supercells, an integration using the k-point only and a Gaussian smearing of only 0.01 eV. An energy of 348 eV, dictated by the pseudopotential of nitrogen, was set for the plane-wave basis-set cut-off in all computations. All calculations were performed spin unpolarised without correction for the dipole moment[135] of the sample as test calculations indicated that these effects were insignificant in the present context.

3.2.6 Calculations on models used to investigate dispersive interactions.

Calculations were performed for both PHEN dimers at their surface-optimised geometries and for PHEN above either a sheet of 16 gold atoms representing the surface or this sheet with an additional adatom above it. The calculations on the PHEN dimers were performed using GAUSSIAN-03[136] for the PW91 density functionals and using TURBOMOLE[137] for the MP2 methodology; these employed the extensive 6-31++G** basis set,[138] required by the close spacing found between the molecules in the monolayer. The PW91 calculations on the PHEN-sheet systems were performed by GAUSSIAN-03 whilst the CASPT2 calculations were performed using MOLCAS-5.2,[139] all with the 6-31G basis set[138] for C, N, and H and LANL2DZ[140] for Au. The CASPT2 calculations included either 10 (for the flat Au sheet) or 11 (for the sheet with the adatom) electrons in 13 active orbitals. All energies were corrected for basis-set superposition error.[141]

3-3 Results of Chapter 3

3.3.1   *In situ* STM studies of PHEN monolayer formation.

To calibrate the STM instrument, the single-crystal gold substrates were scanned and results showing the gold (22 × √3) reconstruction lines are provided in Supporting Information Figure Appendix-3-82. Also provided therein are images of poorly ordered monolayers taken during the early stages of monolayer formation (Figure Appendix-3-83), images of an atypical highly ordered domain (Figure Appendix-3-82), images of overlapping regions (Figure Appendix-3-85 and Figure Appendix-3-86), and experimental details describing how sub-molecular resolution is obtained. From these figures it is clear that uncontrolled drift of the STM tip across the surface is negligible throughout the experiment.

A revealing high-resolution *in situ* STM image of the surface is shown in Figure 3-48 below. It was obtained in the constant-current mode with the height of the tip constantly adjusted by a feedback loop to maintain the tunnelling current at a set-point value. While it is usual to show the height of the tip as a function of the scan (a topography image), Figure 3-48 shows instead the deviation of the current from the set-point value, presenting for this system higher-resolution information than that found in the topology image.   In the limit of large STM feedback, the current-deviation is small and the image formally depicts the first derivative of the topology with respect to the (left to right) scan direction. Further discussion of the nature of the imaging process is referred to Section 7.3.2 wherein topology (STM tip height) and derivative (set-point current deviation) images are compared.
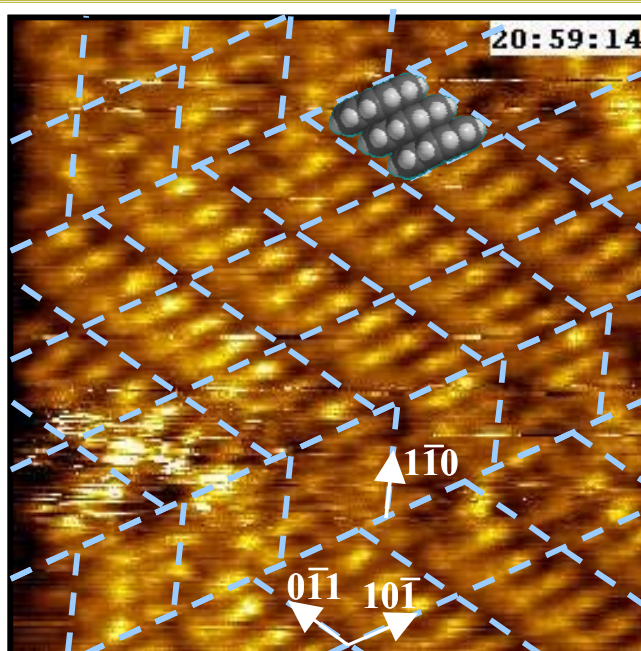
Figure 3-48: A 6 nm × 6 nm in-situ STM current-image scan of PHEN monolayer on Au(111) imaged in aqueous 0.05 M $KClO_4$ solution obtained using tip bias = -0.60 V (vs. the Au(111) substrate), set-point current = 0.85 nA (maximum deviation ± 10%), and sample potential = 0.08 V vs. SCE. Superimposed are arrows showing the observed substrate alignment, lines depicting (4 × 4) surface cells, and one image of the DFT-calculated surface cell containing three vertically aligned PHEN molecules.

The images obtained of PHEN on Au(111) have many qualitative features in common with those previously found[48] for this system. No pitting of the surface is obtained, the PHEN molecules appear vertically aligned in chains with two bright spots per molecule separated by ca. 4.0 Å, and irregularities occur after chains segments of 3, 6, or 9 PHEN molecules. The spacing between the bright spots is very sensitive to the measurement conditions including sample preparation, instrument feedback, orientation of the molecules with respect to the scan direction, etc., but this observation is significant as it directly indicates the orientation $\theta = 60°$ of the molecular plane about the vertically aligned molecular axis of symmetry of PHEN with respect to the chain propagation direction.

The STM image shown in Figure 3-48 is regular throughout domains but three domain boundaries are evident within the image. The smallest reproducible unit of the surface structure has cell vectors of length 11.1 Å at an internal angle of 122°, consistent with a (4 × 4) supersurface layer. On this single-crystal gold substrate, the adlayer surface-cell vectors all align to within 2° to the substrate $[1\bar{1}0]$, $[10\bar{1}]$, and $[0\bar{1}1]$ crystallographic directions. In Table 3-16 below the observed surface cell properties are compared to those of the Au(111) surface and those from DFT simulations (see Section 3.3.5); the observed substrate dimensions are in excellent agreement (5%) with those expected for an ordered (4 × 4) layer. Alternation between two of the three possible orientations of the cell vectors on the surface gives rise to the domain boundaries seen in the figure, as indicated by the superimposed lines. Each cell contains three pairs of bright spots indicating that three PHEN molecules comprise this repeat unit. Indeed, the observed surface coverage of density of $\Theta = 0.18$ PHEN molecules per surface Au atom is consistent with this implied 3:16 ratio. Note that while the observed substrate surface-cell dimensions for PHEN on Au(111) are very similar to those observed[113] on Cu(111), the observation of strict alignment of the adsorbate lattice with the substrate indicates that these systems are qualitatively different in nature.

Molecule Phase	PHEN Physisorbed		PHEN Chemisorbed		DPPZ Physisorbed
Source	STM images Figure 3-48 Figure Appendix-3- 85	DFT (4×4) lattice	STM image Figure 3-51	DFT $(4 \times \sqrt{13})R46°$ lattice	STM image Figure 3-53
Perpendicular distance between chains (Å)	9.7	9.98	10.0	9.98	10.5[a]
cell vector lengths (Å)	11.1, 11.1	11.52, 11.52	10.6, 9.4	11.52, 11.06	
angle between cell vectors	122°	120°	106°	104°	
angle between cell vector and Au $[10\bar{1}]$ vector	0°	0°		0°	unaligned
Separation between molecular π-planes (Å)	3.2	3.33	3.3	3.33	3.3[b]
Density (molecules nm^{-2})	2.5	2.61	2.5	2.61	2.5[b]
Coverage Θ (molecules per surface gold atom)	0.18	0.188	0.18	0.188	0.18[b]
Molecular orientation to the chain direction, θ	60º	60°	60º	60°	~60º[b]
Stacking faults along chains	after 3rd, 6th, or 9th PHEN	-	every 3rd PHEN	-	none[b]
Pitting extent	none		14-18%		none

Table 3-16: Structural properties from STM images and DFT calculations of PHEN and DPZ monolayers on Au(111).
Abbreviations: **a**: in tightly packed regions, typically 11.0 Å average.
b: tentative, from high-resolution regions such as Figure 3-53, f and g.

The observed domain boundaries for PHEN on Au(111) are associated with stacking-fault dislocations of the chains by one Au-Au bond vector (one quarter of a unit cell vector) in the $[10\bar{1}]$ direction. An image of three stacked molecules in a (4×4) surface cell taken from DFT calculations (see Section 3.3.5) is superimposed on Figure 3-48 above. Its properties are consistent with all of the STM observations. Further, this structural motif can account for the myriad of patterns[48] observed for PHEN monolayers simply by changing the pattern of the stacking faults. A longer-range perception of the structure imaged in Figure 3-48 is provided in Figure Appendix-3-85 where the STM scans of overlapping regions are provided. Figure Appendix-3-86 also provides images of an extended surface region containing just one domain.

The images shown in Figure Appendix-3-83 indicate that after initial exposure of the Au(111) to PHEN, long chains of PHEN molecules form but these chains are not ordered with respect to either each other or the substrate. With time ordered structures such as those in Figure 3-48 appear but these continue to fluctuate, as indicated in Figure Appendix-3-85. The monolayer is thus one reflecting dynamic equilibrium between a large number of structures each typically with good short-range order, i.e. order within the (4×4) cells, but poor medium-range order, i.e., only 6 to 20 of these cells form together into ordered domains.

3.3.2   Electrochemistry of PHEN monolayers.

The difference between the first and second sweeps obtained using cyclic voltammetry for PHEN monolayers on Au(111), highlighting the electrochemical signal

associated with desorptive reduction of the monolayer, are shown in Figure 3-49 below; the raw voltammograms and details of the analysis are provided in Supporting Information Figure Appendix-3-87.   The monolayer desorption has a broad and asymmetric character, as is often found when monolayers form in a mixture of surface environments. Integration of the signal indicates a surface coverage of $\Theta = 0.15$, close to the coverage of $\Theta = 0.18$ observed using STM (see Table 3-16 above) in ordered regions of the monolayer.   As the STM images indicate that the monolayer is incompletely formed and contains small low-density disordered regions, the average coverage is expected to be somewhat less than the fully-packed coverage.
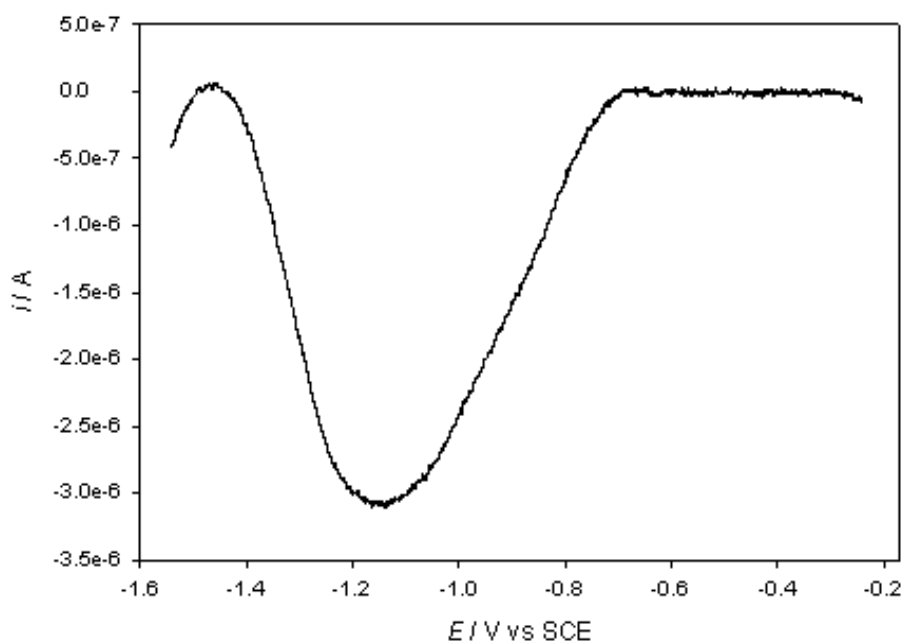
Figure 3-49: The isolated reductive desorption current *i* obtained as the difference between first and second scan on a 1,10-phenanthroline-coated gold electrode in 0.1 M KClO$_4$/water solution: Sweep rate, 5000 mV/s; electrode diameter, 1.0 mm.
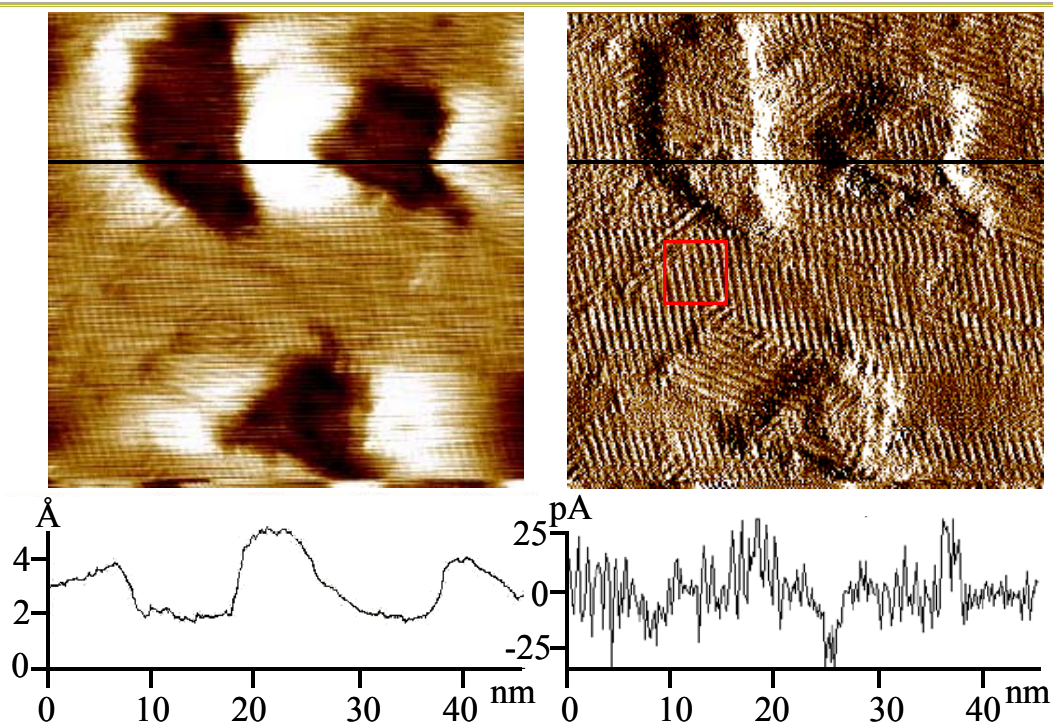
Figure 3-50: Results from STM imaging of a ca. 46 × 46 nm ex-situ produced monolayer of PHEN on Au(111) imaged in phenyloctane without potential control at a set-point current of 0.22 nA and tip bias (vs. the substrate) of 0.16 V. The left-hand figure shows the height (topology) image while the right-hand figure shows the deviation of the current from the set-point value; the upper images show the full scan while the lower graphs show the data along the marked scan line; the region of the red rectangle is shown amplified in Figure 3-51.
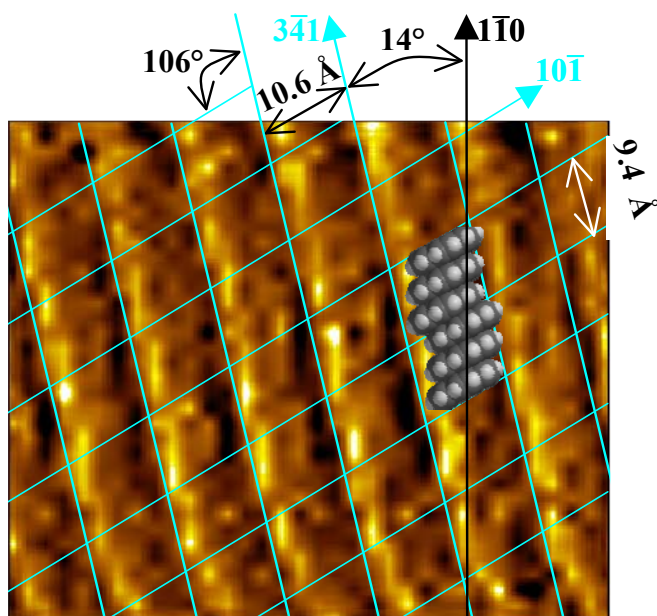
Figure 3-51: Zoom-in of the indicated ca. 6 nm × 7 nm section of the STM current image shown in Figure 3-50. Superimposed is the proposed (4 × √13)R46° supersurface lattice and two images of the DFT-calculated surface cell each containing three PHEN molecules, all scaled by 91% so as to fit the STM image.

3.3.3   STM of PHEN monolayers after electrochemical preparation.

The STM image shown in Figure 3-50 above is an example of that obtained after preparation of the monolayer on large-area gold terraces using an applied potential with respect to SCE of 0.7 V in 0.1 M NaClO$_4$, removing the potential and allowing the sample to stand (in air) for at least one day. This potential was chosen so as to possibly activate the monolayer rearrangement process whilst being below the potential at which gold is oxidized and the surface damaged (see Supporting Information Figure Appendix-3-88). The most significant differences between the images of this sample and those from the monolayers formed in situ are that the STM images no longer fluctuate with time and that pits now form on the surface. These changes are suggestive of a change in bonding, for example from physisorption to chemisorption.

Figure 3-50 shows both the usual STM height (topology) image and the simultaneously obtained current image (shown as the deviation of the current from the set-point value during scanning in constant-height mode), while a region of the current image is expanded in Figure 3-51. The height and current profiles across one of the scan lines are also shown in Figure 3-50, while the major results obtained from this and related images are summarized in Table 3-16 above.

The pits formed in the surface are one gold layer deep, similar to those found previously for PHEN monolayers under electrochemical potentials;[5] these are most clearly seen in the topology image. In the current image, the left edge of each pit appears dark as the STM tip descends into the pit while the right edge appears white as the tip ascends back out. As the observed deviations of the current are less than 10% of the set-point value, the current image reflects the first derivative of the topology image

with respect to the (horizontal) scan direction. The current images on the pit floor and on the surrounding plateau of Figure 3-51 are thus very similar whilst the contrast seen in Figure 3-50 changes significantly for adsorbate regions on the same plateau but with different molecular alignment.

The height profile in Figure 3-50 indicates that the pits are one atomic layer deep, and the pits are found to cover between 14% and 18% of the surface, as shown in Figure 3-50 and quantified in Table 3-16. Note that these measurements are made on large flat terraces that are well removed from gold lattice step edges, minimizing the contributions of these features to the monolayer structure. As the observed pit density is close to the surface density, it appears that the number of atoms mined from the surface is equal to the number of PHEN molecules that coordinate to it, suggesting that 1:1 chemisorbed coordination complexes of PHENs to gold adatoms form and dominate the binding in this regime. Lifting of the gold reconstruction lines (to recreate a bulk-like surface) from these large flat terraces alone will result in islands of gold covering ~4% of the Au(111) surface,[142] and it is quite possible that a combination of atoms liberated by this process and those from surface mining comprise the above-surface gold adatoms to which the PHEN molecules ligate. Assuming that the liberated gold atoms are available and used for PHEN chemisorption, the extra gold adatoms required (amid wide gold terraces) would leave pits covering approximately 14% of the surface, still consistent with the ratio observed on the large terraces. For small terraces and regions near step edges, the additional gold atoms can also be mined from the existing steps and hence the pitting density would be somewhat less than 14%, explaining the variable nature of pitting seen on different examples of the Au(111) surface. This effect has also been suggested in regard to thiol chemisorption on Au(111) adatoms.[143]

The enlarged image shown in Figure 3-51 is quite regular and appears to conform to the $(4 \times \sqrt{13})R46°$ supercell lattice superimposed on the figure. Within each unit cell there appears four streaks oriented in the $[1\overline{1}0]$ direction comprising adjacent intense black and white streaks separated by a less intense pair. At first appearance, this image looks quite different to the high-resolution images shown in Figure 3-48, but a mapping between the observed features may easily be constructed. This mapping is based on the DFT-optimised monolayer structure (see Section 3.3.5 below and Figure 3-55) that is also superimposed on Figure 3-51 depicting three PHEN molecules per unit cell in a lattice dominated by a single regular stacking fault. It is the only feasible molecular orientation that is consistent with the observed lattice parameters and image properties. Based on this model, the streaks apparent in Figure 3-51 depict not single PHEN molecules on the surface but rather result from blurring in the direction of stacking of similar features on adjacent molecules. The relative intensities of the two bright spots per PHEN molecule shown previously in Figure 3-48 vary with the feedback settings, scanning direction, and the sample orientation, each spot indicating that the STM tip is rising as the result of the motion of the tip over some region of the molecule. It is hence feasible that the image of the monolayer could appear as seen in Figure 3-51. Indeed, a small increase in the intermolecular space between two PHEN molecules stacked side by side in Figure 3-48 would naively be expected to make one of the white dots brighter and its neighbouring region darker as the tip can presumably descend further into the intermolecular space. The alignment of the 3 PHEN molecules in the surface cell is in Figure 3-51 shown to reflect this interpretation of the image.

Quantitative measurements of the observed lattice properties are compared to properties calculated using DFT for the (4 × √13)R46º supercell lattice in Table 3-16. The observed angle between the cell vectors of 106° is very close to the anticipated value of 104°, but the observed unit cell vectors are on average too small by 9%. As the method of sample preparation used prevents the calibration of the STM scanner to the gold reconstruction lines, errors of this magnitude are feasible. Also, the preparation method prevents the experimental confirmation of the registry between the surface and substrate lattice vectors. Not only is the (4 × √13)R46º supercell lattice envisioned in Figure 3-51 consistent with the quantitative results from the simulations but also it arises simply by *regular* application of an observed dislocation process to an observed substrate registry, see Figure 3-48.

3.3.4   *In situ* STM of DPPZ monolayers.

DPPZ readily formed monolayers of long chains of molecules standing vertically on the surface when prepared in ethanol and imaged by *in situ* STM in aqueous solution, as shown in Figure 3-52 and Figure 3-53. In Figure 3-52, six consecutive height (topology) images of the same region are shown (a to f). The first image (Figure 3-52 a) shows a highly ordered region near the top left-hand corner, a central region containing defect areas, and a more ordered bottom right-hand corner. Over the course of the scans, the disordered region gains order and Figure 3-52 d shows most molecules forming in oriented chains but the spacing between the chains is not regular and hence some disorder remains. However, in the frame Figure 3-52 e, the defect region again becomes more pronounced, evolving slightly in Figure 3-52 f; the differences between Figure 3-

52, e and f are small but may indicate the presence of a slight amount of downward drift

in the scanned region during these experiments.
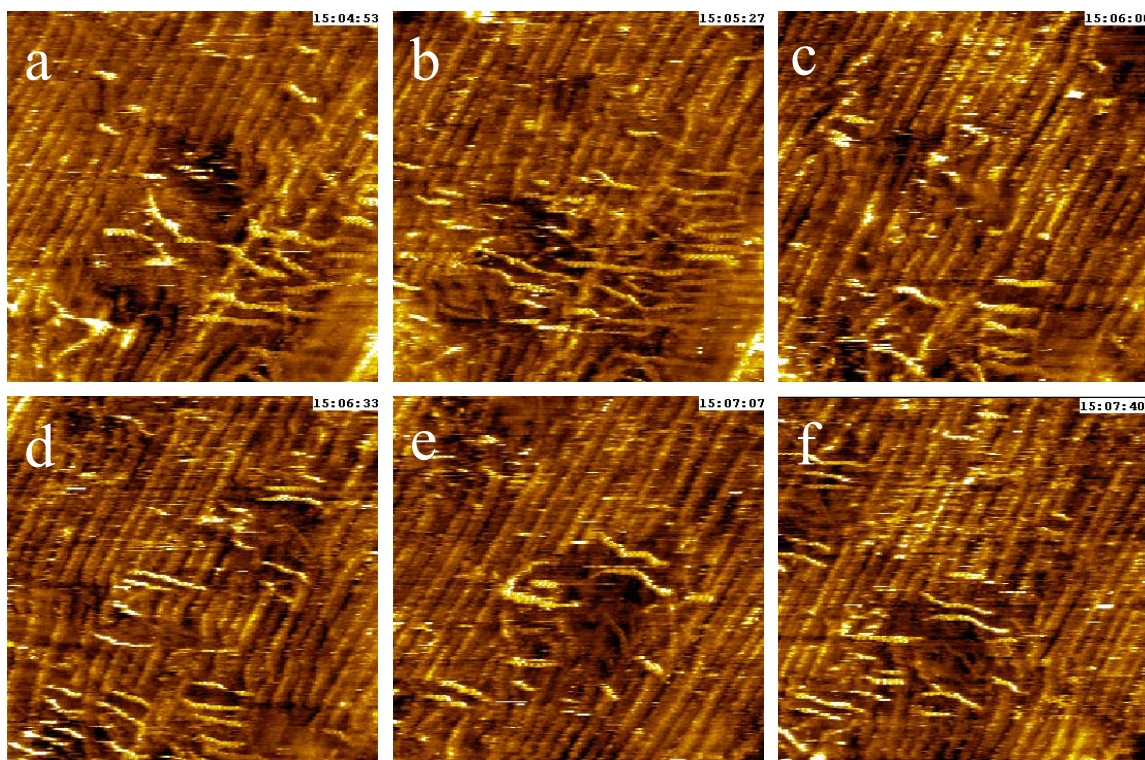
Figure 3-52: Six ca. 20×20 nm in-situ STM height (topology) images a-f, each taking 33 s to complete, taken over a 3 min period, of a DPPZ monolayer on Au(111) imaged in aqueous 0.1 M phosphate buffer at pH 6.9 obtained using tip bias = -0.40 V (vs. the gold substrate), set-point current = 0.16 nA, and sample potential = -0.12 V vs. SCE.
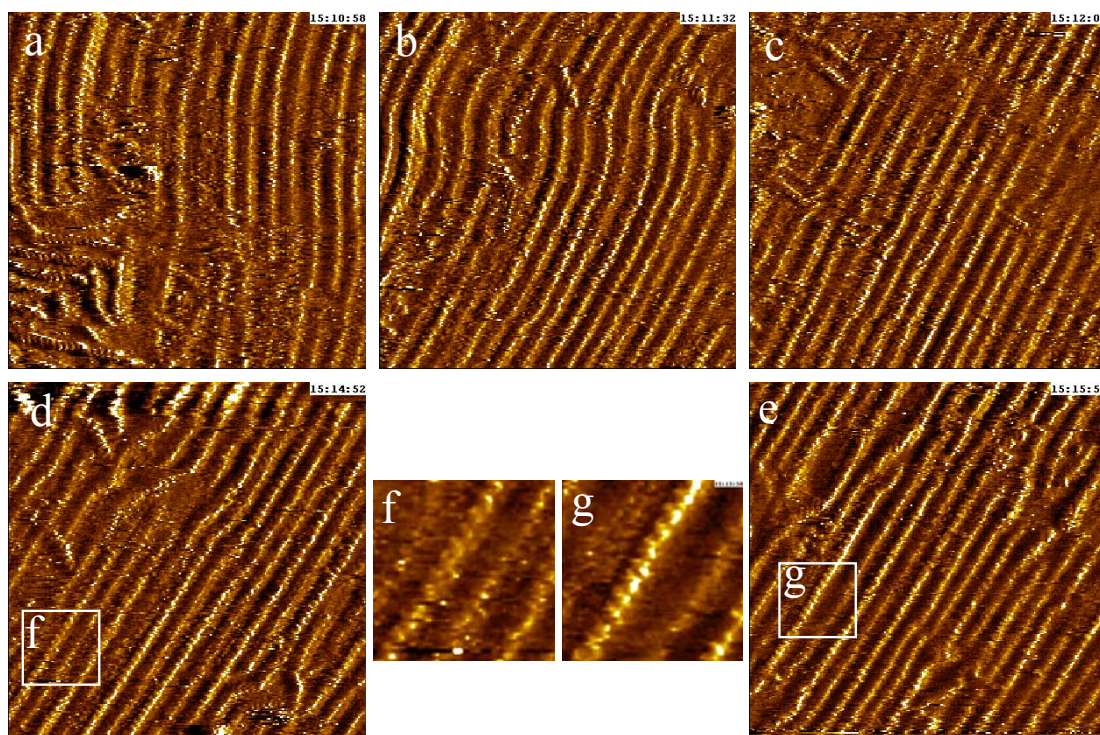
Figure 3-53: Five ca. 20 × 20 nm in-situ STM images a-e, each taking 33 s to complete, taken over a 5 min period, showing the deviation from the set-point current (maximum ca. ±10%) of a DPPZ monolayer on Au(111) imaged in aqueous 0.1 M phosphate buffer at pH 6.9 obtained using tip bias = -0.40 V (vs. the gold substrate), set-point current = 0.16 nA, and sample potential = -0.12 V vs. SCE. Frames f and g highlight 4 ´ 4 nm regions of long-lived local structure that produce higher-resolution images.

Shown in Figure 3-53 are five images taken over a 5 min period of another region on the surface. While Figure 3-52 displays a topology image of the apparent height of the monolayer, Figure 3-53 instead shows the higher-resolution current image akin to those shown in Figure 3-48 and Figure 3-50. This region shows medium range order with a regular lattice persisting over regions of up to 100 nm^2. However, the monolayer structure still changes on the timescale of the experiment. Similar to the results shown in Figure 3-52, the first frame scanned showed a significant region of disorder as well as an ordered region whilst the second and subsequent frames showed enhanced order. This suggests that the signal is enhanced and order increased whilst scanning. This basic

quality of the surface did not change after two hours, and the domains with and without long-range order are persistent at room temperature.

While the observed long-range order of the monolayer is poor, the short to medium range order for these DPPZ monolayers is significantly enhanced compared to the ca. maximum 20 nm^2 fully-ordered regions evident in Figure 3-48 and Figure 3-50 for PHEN monolayers. Long range order does not form as the spacing between the long DPPZ chains varies. In Figure 3-53 a, the chains are separated by 12-13 Å, but as order increases in the subsequent frames the average perpendicular distance between the chains decreased to 11 Å. High-resolution images of the large sample were difficult to obtain. The apparent pixelation along the chains evident in Figure 3-53 is in general not believed to be indicative of resolved structural features and this would imply unrealistic intermolecular spacings of 1.5 – 2.5 Å. However, in certain regions of the images such as those highlighted in Figure 3-53, f and g, the slightly more closely packed monolayer structure appeared robust over many scans and closely resembles that of PHEN in its physisorbed phase shown in Figure 3-48. The structural properties tentatively assigned to these DPPZ monolayers in Table 3-16 are based on these more highly resolved sections of the images.

An important feature of the observed STM images of DPPZ is the absence of surface pitting, suggesting that the monolayer is physisorbed. No evidence for stacking faults in the chain structure is found in the higher resolution regions of the images. However, all images show the chains meandering over the surface, indicating that precise surface registration is not required for monolayer production. This also suggests a physisorbed structure. The DPPZ monolayer on Au(111) appears to have more in

common with the monolayer of PHEN on Cu(111)[113] than it does with PHEN on Au(111).

3.3.5   DFT-Calculated structures of PHEN monolayers.

DFT calculations for the binding of benzene and nitrogen-bound molecules to Au(111) and related surfaces typically produce realistic structures but do not include the important dispersive contribution to the binding energy and hence considerably underestimate the strength of the interaction. The effect is more profound for aromatic-surface type interactions that favour horizontal alignment of molecules such as benzene[102] and PHEN than it is for the nitrogen-binding interactions that favour vertical alignment. Hence it is anticipated that the DFT calculations cannot reproduce the observed energetics of PHEN binding in these configurations; however, the structures produced in each case should be realistic, making these results a useful starting point for enhanced descriptions of the energetics. (The dispersive forces are weakly directional and so do not change the structure as much as the energetics. i.e. the results are qualatively reliable.) First the structures were determined, and then by using ab initio methods in the following subsection the relative strengths of the omitted dispersive interactions were estimated. Initial studies are performed using the (4 × 4) supercell found for physisorbed PHEN and the (4 × √13)R46° lattice found for the chemisorbed phase.

Firstly, calculations are performed placing just one PHEN molecule in the (4 × 4) supercell, a low coverage of just one PHEN per 16 gold surface atoms. The PW91 density-functional predicts vertical PHEN attachment above the surface at the structure shown in Figure 3-54 below with an energy of $\Delta E = -3.4$ kcal mol^{-1}. The potential energy surface shows only minor variation as the molecule is tilted parallel with the

surface, however, and the associated forces are so small that the geometry optimiser in VASP fails to adjust this variable from its initially chosen value. As a result, partially optimised interaction energies of –3.2 kcal mol^{-1} at a tilt of 45°, and –2.4 kcal mol^{-1} for the horizontal configuration, are obtained. These calculations thus anticipate large-amplitude motions of the physisorbed molecules at low coverage. The barrier for translation of a PHEN molecule across the surface tilted at 45° was evaluated to be just 0.4 kcal mol^{-1}, again indicating very flexible surface interactions. The effect of the neglected dispersion terms on these calculated energies will be considered later; the differences found by VASP are so small that the dispersion terms should actually dominate the shape of the potential energy surface. Key optimised structures are provided in full elsewhere.[1]
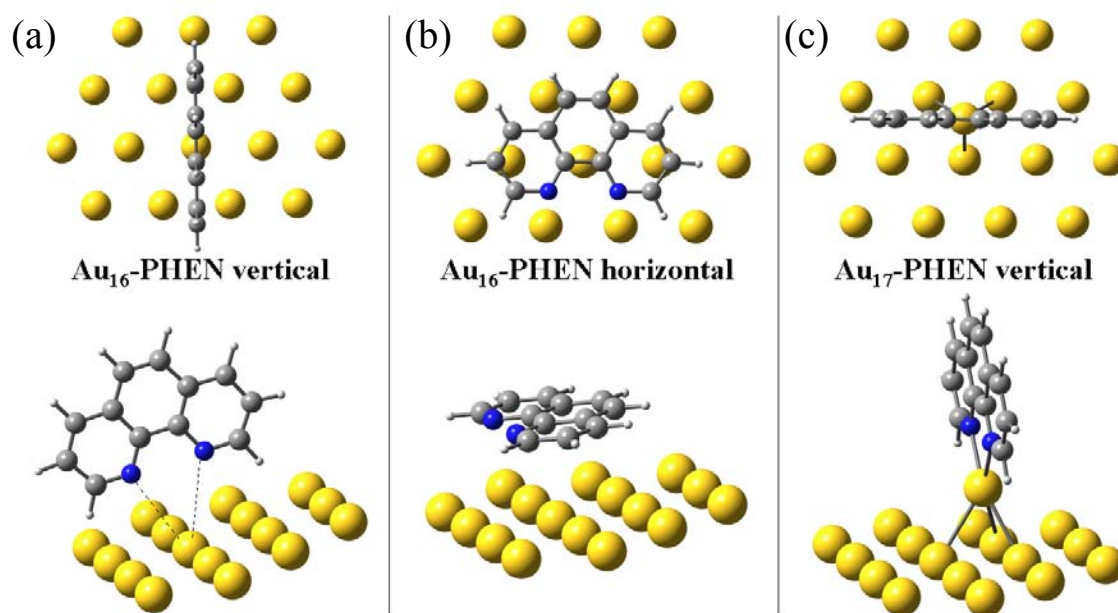
Figure 3-54: Two views of the PW91 optimised structures of PHEN on Au(111) in both **(a)** vertical and **(b)** horizontal configurations physisorbed on Au(111), as represented in the sheet models of the surface, as well as the corresponding views **(c)** of the model used when a gold adatom chemisorptively binds the adsorbate.

Next, calculations relevant to the observed physisorbed phase were performed placing three PHEN molecules into the (4 × 4) supersurface cell, a density of three molecules per 16 surface gold atoms. Only vertically stacked molecules are feasible at this density and PW91 predicts an interaction energy of $\Delta E = -1.1$ kcal mol^{-1}, expressed per mol of PHEN adsorbate. The observed spacing between equivalent atoms in the PHEN molecules apparent in Figure 3-48 and Figure 3-50 is 3.8 Å, a value incommensurate with the substrate lattice (the intermolecular spacing between the PHEN π-planes is thus 3.8 × sin θ = 3.2 Å, as indicated in Table 3-16). The incommensurability arises as three PHEN molecules span four Au-Au surface bonds providing a theoretical spacing of 2.88*4/3 = 3.84 Å. Clearly the three PHEN molecules per unit cell must reside in different registrations with respect to the surface layer, and this effect contributes to the calculated reduced binding of the PHEN molecules as the density increases. However, PW91 calculations for the periodic array of PHEN molecules in the absence of the gold substrate indicate a repulsive energy of 1.6 kcal mol^{-1}, accounting for most of the decreased stability. It is hence again clear that minimal energy costs are predicted by PW91 to be associated with translation of PHEN molecules across the surface. The dispersive contribution not withstanding, this accounts for the observed high mobility in physisorbed PHEN monolayers.

Finally, as the experimental results depicted in Figure 3-50 suggest that the stable monolayer found for PHEN on Au(111) contains gold adatoms above the surface chemisorbing each PHEN, two possible chemisorbed structures were optimised using PW91, one in the (4 × 4) supersurface cell supporting linear chains and the other one in the (4 × √13)R46º cell supporting regular stacking faults at every third PHEN. The resulting structures are shown in Figure 3-55 below and given in detail in the Appendix

(Section 7.3.2). Images of the (4 × √13)R46º structure were also previously superimposed on the experimental STM image in Figure 3-51. Note that four copies of the supersurface cells are displayed in Figure 3-55 to emphasize the relationships between adjoining cells. In each cell, one of the three PHENs per unit cell binds vertically above its gold adatom whilst the other two distort somewhat so as to produce a regular spacing between the molecules. One in three of the PHEN-PHEN interactions is clearly seen to be strained and the stacking faults in the (4 × √13)R46º structure are set to locate at this juncture. As indicated in Figure 3-55, these stacking faults are associated with single dislocations of the adsorbate in the [10$\bar{1}$] crystallographic direction; displacements of ca. half of the lattice spacing also appear feasible from inspection of Figure 3-55, but these would involve unfavourable location of the adatom on a HCP site (see below). Similar dislocations are also apparent in the physisorbed structure shown in Figure 3-48 but the dislocations therein have no regular pattern.

(4 × 4)
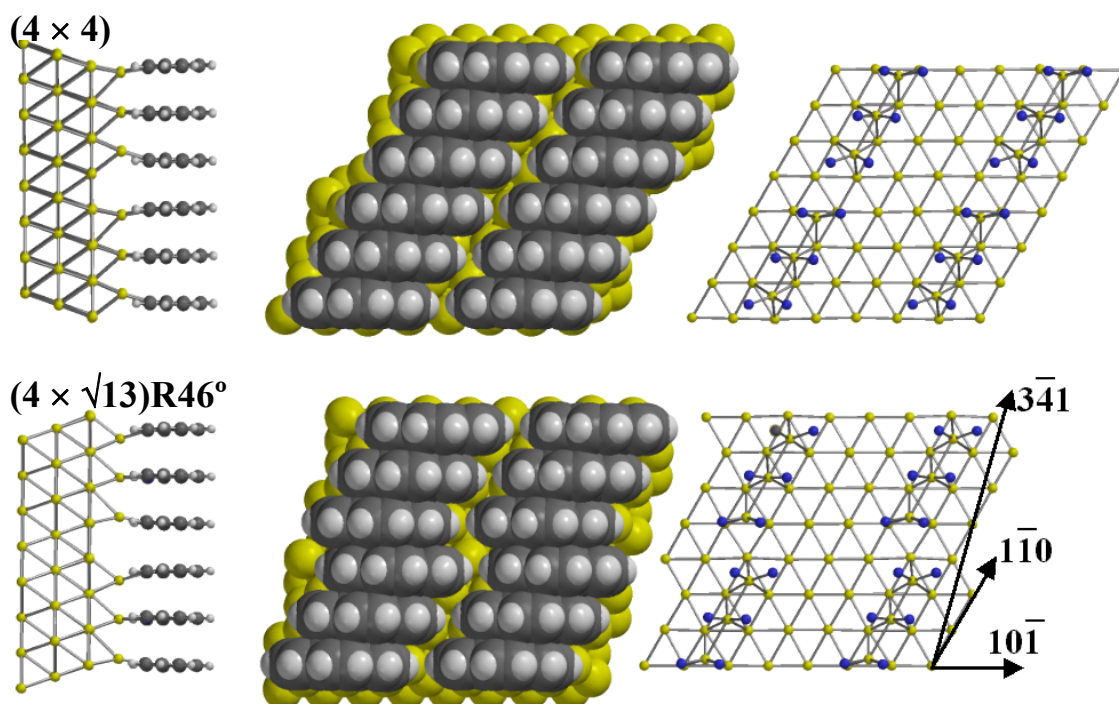
(4 × √13)R46º

Figure 3-55: PW91 optimised structure of PHEN on Au(111) chemisorbed via gold adatoms on three-layer (4 × 4) and (4 × √13)R46º supersurface unit cells. The images each show four copies of the optimised unit cell, viewed from left to right in side elevation, space-filling plan, and plan showing only the gold surface and adatoms as well as the nitrogen atoms.

The calculated average interaction energy of the PHENs with the adatom containing gold surface is −17.4 kcal mol^{-1} on the (4 × 4) supersurface cell and −15.0 kcal mol^{-1} on (4 × √13)R46º. These are both much larger than the binding to the flat surface due to the chemisorptive nature of the ligation of the adatoms by the PHENs, combined with the reduced steric repulsion of the lower PHEN hydrogens with the surface. However, the average energy required to take a gold atom from the bulk and place it above the surface on an adatom site is calculated to be 9.9 and 9.0 kcal mol^{-1} for the (4 × 4) and (4 × √13)R46º supersurface cells, respectively, reducing the total

chemisorption energy to –7.5 kcal mol^{-1} and –6.0 kcal.mol^{-1}, respectively. While these

values are much larger than the weak physisorptive interaction of –1.1 kcal mol^{-1}

calculated previously, proper treatment of the omitted dispersive interactions is required

before conclusions can be reached concerning the relative stabilities of the different

types of physisorptive and chemisorptive binding considered.   However, as another

check on the reliability of the approach, the energies of mining atoms from the surface

has also been calculated, obtaining energies within ± 2 kcal mol^{-1} from the bulk-atom

results used in the above calculation. These values differ depending on the nature of the

step edges before and after the mining process. As there appears to be only a very small

energy difference between surface and bulk gold atoms, and as the precise nature of the

pits produced is highly variable, use of the bulk values appears to be most appropriate.

The optimised structures shown in Figure 3-55 have the gold adatoms located on

FCC sites of the surface. Structures for the (4 × 4) supersurface lattice with these atoms

located above HCP and top sites were calculated to be higher in energy by 3.0 and 13.4

kcal mol^{-1}, respectively, while similar structures above bridge sites were found to be of

high energy and unstable. Calculations at low coverage (1 PHEN per 16 surface gold

atoms) indicated that the chemisorption energy of a single adatom to PHEN is –15.4 kcal

mol^{-1} at the FCC site and –14.8 kcal mol^{-1} at the HCP site. These energies are both much

lower than the average binding energy of –7.5 kcal mol^{-1} at high coverage**.** A variety of

different approaches was considered to interpret this effect, all leading to the conclusion

that it costs 2.5 to 3 kcal mol^{-1} to assemble two gold adatoms on adjacent FCC sites. The

barrier to translation of a single adatom/PHEN complex across the surface at low

coverage was evaluated to be less than 4 kcal mol^{-1}, similar to the barrier for translating a

PHEN molecule between two adjacent adatoms. Hence even the chemisorbed structure

is predicted to be quite mobile on the surface, explaining how it is that the geometrical distortions shown in Figure 3-55 that arise due to the incommensurate adsorbate and substrate lattices do not lead to significant energy penalties. Similar mobility has also been calculated for thiol chemisorption to adatoms on Au(111).[144]

3.3.6   MP2 and CASPT2 calculations on the role of dispersive interactions in monolayer production.

The coordinates of the three pairs of nearest-neighbour PHEN molecules were extracted from the (4×4) optimised structure shown in Figure 3-55 and used in gas-phase calculations of the adsorbate-adsorbate interaction energy by PW91 and MP2. The MP2 calculations include the dispersive contributions that are not included in current DFT functionals such as PW91.   The MP2 interaction energies, after basis-set superposition-error correction, are -10.3 kcal mol^{-1} between the strained PHENs (see Figure 3-55) and -10.6 kcal mol^{-1} between the others, averaging -10.5 kcal mol^{-1}. However, the corresponding PW91 average interaction energy is 2.2 kcal mol^{-1}, slightly more repulsive than the average energy of 1.5 kcal mol^{-1} from VASP PW91 calculations of the entire PHEN monolayer. These results indicate that the calculated VASP PW91 energies for high-density monolayers should be corrected by -13 kcal mol^{-1} in order to account for the dispersive interaction between the adsorbate molecules. Key results are summarized in Table 3-17 below.

Cluster	PW91	SCF/CASSCF	MP2/CASPT2	PW91 correction
PHEN – PHEN average	2.2	8.7	-10.5	-13
Au_{16} – PHEN vertical	-1.4	8.3	-7.5	-6
Au_{16} – PHEN horizontal	-1.6	12.0	-14.6	-13
Au_{17} – PHEN	-47.4	-29.0	-48.3	-1

Table 3-17: Calculated interaction energies, in kcal mol^{-1}, after basis-set superposition error correction, for the average of the three PHEN-PHEN cluster interactions apparent in Figure 3-55 and for the three gold – PHEN clusters shown in Figure 3-54, obtained using various computational methods, and the correction thus determined for PW91 calculations on surfaces.

Similar calculations were performed for PHEN interacting with cluster models for Au(111), at the extracted slab-optimised geometries shown in Figure 3-54 (and given in full elsewhere[1]), and the results are also given in Table 3-17 above. These clusters contain 16 gold atoms in a surface-layer sheet and optionally one additional adatom. MP2 calculations for this system are inappropriate due to the low band gaps of the gold clusters, so instead generalized CASPT2 calculations are performed. These involve explicit inclusion of the full electron correlation involving all electrons and orbitals close to the Fermi level of the metallic clusters, allowing all other electron correlations to be treated using a multi-reference generalization of the MP2 method.

Three established scenarios provide paradigms for the interactions considered: the interaction of ammonia with a single gold atom,[145] the interaction of ammonia with a gold surface,[118] and the interaction of benzene with copper[102] surfaces. For ammonia interacting with a single gold atom,[145] GGA-type density functions predict binding energies varying by over a factor of two, but PW91 is one of the most reliable of these methods, overestimating the binding by just 10%. As a result, we would expect that PW91 adequately describes the chemisorption process of PHEN binding to a gold adatom. PW91 also provides a realistic description of the energetics of ammonia sticking to Au(111),[118] despite it being clear that the dispersive interaction between the ammonia lone-pair and the filled gold d_{z^2} orbital is important to the interaction. This scenario is similar to PHEN binding vertically to a flat gold surface, though the interactions of nitrogen lone pairs with gold decrease in hybridisation order $sp^3 > sp^2 > sp$, and in addition the lower PHEN hydrogen atoms prevent proper access of the adsorbate to the surface. Hence the relative importance of the dispersive interactions is expected to be larger for PHEN binding and thus reduced accuracy is expected for PW91 in the description of this binding. Finally, PW91 predicts negligible binding for benzene to Au(111), Cu(111), and Cu(110), similar to the results described earlier for PHEN adsorbing horizontally on Au(111), while the observed interactions are quite substantial and 12-17 kcal mol^{-1} more attractive.[102, 146-148] CASPT2 is the only available computational method that includes the key dispersive terms in a realistic way. CASPT2 predicts a correction of 24 kcal mol^{-1} for benzene on Cu(110) for which the deficiency in the PW91 adsorption energy is 17 kcal mol^{-1}, in reasonable agreement with the experimental data. As CASPT2 also provides an excellent description of chemisorptive interactions, it is expected to provide a realistic description of the shortcomings of the

full-surface VASP DFT PW91 calculations for all the physisorption and chemisorption scenarios considered herein.

The energies calculated using PW91, CASSCF (the intermediate stage in the CASPT2 calculations that does not include dispersion), and CASPT2 are shown in Table 3-17 for the three clusters from Figure 3-54. PW91 again predicts negligible binding for the physisorbed clusters (ca. –1 kcal mol^{-1}), while CASSCF predicts significant repulsion (8 to 12 kcal mol^{-1}), and CASPT2 predicts strong binding: –7.5 kcal mol^{-1} for the vertical structure and –14.6 kcal mol^{-1} for the horizontal one. All methods predict strong binding for the chemisorbed structure involving a gold adatom. The results lead to energy corrections for the VASP surface PW91 calculations of –6, –13, and –1 kcal mol^{-1} for the physisorbed vertical, physisorbed horizontal, and (4 × 4)-lattice chemisorbed scenarios, respectively, in qualitative agreement with expectations based on known scenarios for binding in similar environments.[102, 118, 145]

3-4 Discussion: how PHEN and DPPZ molecules and monolayers bind to the Au(111) surface

The final estimated interactions for PHEN with Au(111) in some critical configurations are given in Table 3-18 below, obtained by combination of the PW91 calculated energies for the periodic adsorbate (also shown in the table) with the dispersion correction energies taken from Table 3-18. DFT calculations for the physisorption of PHEN on Au(111) predict weak binding that marginally prefers vertical alignment of the adsorbate, but the magnitude of the binding is far too small to account for the experimental observation that stable monolayers do form at room temperature. However, the corrected energies of -9 kcal mol^{-1} vertical and -15 kcal mol^{-1} horizontal provide estimates of plausible magnitude that clearly favour horizontal binding at low coverage. The orientation will be sensitive to applied bias, however, owing to the large dipole moment of the PHEN which drives vertical alignment under positive applied voltages,[112] as has been directly observed in related systems.[49, 116]

At intermediate coverage, PHEN dimers may start to form on the surface. The corrected interaction energy for a vertically oriented dimer from Table 3-18 is -15 kcal mol^{-1}, the same value as obtained for the horizontal single molecule. While the calculations are not capable of discerning the fine differences in relative energy that control actual monolayer production and dynamics, they clearly indicate a scenario in which molecules agglomerate to form a structured layer at higher adsorbate exposures.

Binding	Lattice	Orientation	Coverage	PW91	PW91 corrected
physisorbed	-	horizontal	low	-2	-15
physisorbed	-	vertical	low	-3	-9
physisorbed	-	vertical	dimers, chain ends	-2	-15
physisorbed	(4 × 4)	vertical	high	-1	-22
chemisorbed	(4 × 4)	vertical	high	-8	-22
chemisorbed	(4× √13)R46º	vertical	high	-6	-20[a]

Table 3-18: Calculated interactions of PHEN with Au(111), in kcal mol^{-1}, in some critical configurations, obtained directly from VASP PW91 calculations for the periodic surface and with correction (see Table 3-17) for dispersive interactions.
Abbreviation: [a] crude approximation using the same PHEN –PHEN dispersion contribution as calculated for the (4 × 4) supersurface cell.

This result also has implications for the PHEN molecules that form at the ends of the stacked chains apparent in Figure 3-48, Figure 3-50 and Figure 3-51: each terminal PHEN is akin to a PHEN in a dimer and so the energy required for it to fall off the chain must be quite minimal. Imperfectly formed monolayers are thus susceptible to dynamical processes that continually reshape their appearance, and as observed may be reshaped and even undergo large density fluctuations induced by the STM tip, a general process that is now attracting considerable attention.[39]

At high coverage, the stable structure of the physisorbed monolayer is both observed and predicted to involve vertically oriented stacked chains, but the calculated

interaction energies after correction are –22 kcal mol^{-1} for both the physisorbed and chemisorbed (4 × 4) structures; crudely assuming that the same PHEN-PHEN dispersive contribution applied to the (4 × √13)R46º chemisorbed one, its corrected interaction energy would be 1.5 kcal mol^{-1} less bound than this. Again, while these calculations cannot predict the small differences in these energies with accuracy, they indicate that the various types of binding should be comparable in energy. The experimental results indicate that once the chemisorbed structure forms, attaining high regularity with a minimum number of chain ends, the monolayer structure becomes stable over long periods of time. Also, as the ligation process directs vertical rather than horizontal alignment, the conformational flexibility of the chemisorbed structures are greatly reduced so that the PHEN molecules at the ends of chains become stable to rearrangement, locking in the overall structure. In addition to these stabilizing effects, the calculations also suggest that the barriers to rearrangement of the chemisorbed structures are at least 3 kcal mol^{-1} more than those for rearranging the physisorbed structures, slowing rates by an order of magnitude.

The purpose for measuring the structure of DPPZ on Au(111) was to induce a small but significant perturbation to the energy balance depicted above for PHEN. Due to the additional rings (see Figure 3-47), the dispersive interactions favouring vertical stacking are increased whilst the vertically oriented head-group to surface interactions and the steric packing interactions are less affected. The result is that the driving force for the molecules that terminate a surface chain to fall off the chain are reduced, manifested experimentally through the production of long stable chains and much more regular monolayers. Also, the apparent absence of stacking faults in the DPPZ chains indicates that the dispersive interaction favours linear chains while, as revealed from the

PW91 calculations, the substrate lattice effects drive the dislocation. The observed meandering of the chains in Figure 3-53 also indicates that the increased inter-adsorbate interaction, which is sufficiently soft to permit meandering, now dominates the adsorbate to head group interactions, which acts to register the adsorbate into discrete sites above the surface.

Nucleation of ordered PHEN monolayers on Au(111) is known to occur along the gold reconstruction lines.[48] This may occur because of an increased physisorptive interaction arising from the altered gold surface structure, or may arise as it is energetically easier to mine the additional gold surface atom from the reconstruction than it is to mine either the unreconstructed (111) surface or bulk gold atoms.[149] If the reconstruction is indeed lifted by this process, then the adatom could either be transported and deposited at a step edge or other irregularity, facilitating growth of a physisorbed layer, or additional atoms could be extracted from step edges or the top surface layer (thus forming pits), facilitating growth of a chemisorbed layer. The degree of pitting produced by PHEN on Au(111) can be reversibly controlled through the application of a surface potential,[48] an observation that is understood in terms of a scenario in which physisorbed and chemisorbed structures have very similar energies. As the dispersive interaction between two PHENs on adjacent sites in which one is chemisorbed and the other is physisorbed will be small, the lack of observation of mixed chemisorbed and physisorbed layers can readily be understood: interconversion requires a phase change from one form to the other.

3-5 Conclusions to Chapter 3: PHEN binding to gold and relevance to thiol binding

Two distinct states of adhesion of PHEN to Au(111) are found, a physisorbed state in which the PHEN molecules interact with the normal gold surface, and a chemisorbed state involving gold adatoms chelating the molecules to the surface. Energetic calculations indicate that these adsorbates are both strongly bound to the surface and of similar energy. While the chemisorbed state (at full monolayer coverage) is stable for extended periods of time, the physisorbed state is dynamically fluctuating at room temperature. Such fluctuations are possible owing to unstable chain ends and small barriers for diffusion of the physisorbed molecules across the surface and their reorientation. Changing between aqueous and non-aqueous solvents (without applied electrochemical potentials) had little effect on the qualitative nature of the monolayer, suggesting that solvent interactions are not critical. However, dispersive forces acting both between the adsorbate molecules and between the molecules and the surface are shown to be very important, controlling the energetics and dynamics of the system; for chemisorption, the relative strengths of the ligand bond and the energy required to produce the gold adatoms also contribute to this fine balance. Modulation of the intermolecular dispersive forces through extension of the aromatic ring system from PHEN to DPPZ is shown to change the balance of the forces realizing a reduced chain-end effect, fewer stacking faults, and much longer chains. For PHEN on Au(111), after initial adsorption, the molecular chains are disordered with respect to both themselves and the substrate lattice, but full registration with the substrate occurs as the monolayer matures. No such maturation is observed for DPPZ on Au(111), however. Indeed, the structure of DPPZ on Au(111) is very similar to that of PHEN on Cu(111), a structure

for which the substrate lattice spacings are too small to allow for proper registration of a high-density monolayer.[113] The substitution of DPPZ for PHEN and the substitution of Cu for Au thus both have similar effects on the structure of PHEN on Au(111).

In the chemisorbed state, prior to full surface monolayer coverage, the PHEN-adatom entity has little barrier to translation across the surface and so even though still strongly bound to the surface remaining upright, it has high mobility (see Figure 3-56 below). Thus whilst the monolayer is forming the PHEN-adatom units simply stack in long chains in a structure that is determined not so much by the gold substrate as by the dispersive forces between the molecules as they stack against each other standing upright upon the gold surface, with the gold adatoms registering above hollow sites in the (111) surface. However the stacking of the PHEN molecules and the registration of the gold adatoms with the surface are incommensurable. Whilst the PHEN-adatom bond is both strong and flexible enough to accommodate this incommensurability, the dispersive forces holding the PHEN molecules together in long chains are neither strong nor flexible enough to accommodate it. At full monolayer coverage pressure from tightly packed neighbouring chains, together with the incommensurability of the chain with the surface, results in a slip in the chains, and the dimensions of the incommensurability dictate that this slip will most likely occur at each third molecule in the chain.

Experimentally, a connection between pitting of the gold surface and chemisorption was established through examination of the pits formed on very large flat gold terraces, structures in which the number of atoms taken from the pitted volume matched the PHEN surface coverage. Pitting observed around step edges and other defects is much more difficult to quantify due to the complex interplay in these dynamically changing structures.

Significant surface pitting also appears consistently when molecular monolayers are formed on gold using thiol or other ligand tethers. McDermott *et al*. have examined the phenomenon of surface pitting[114] in alkanethiol monolayers based on supposed[150] correlations of the pitting with alkane chain length. Their suggestion is that the driving force of the pitting is the shrinkage of the uppermost layer of gold atoms due to electron sharing between the sulfur and gold atoms, adding electron density to the attractive mantle for the electrons between the gold atoms at a three-fold hollow binding site and thus increasing the attractive force between the three-fold hollow atoms. This interpretation has also been adopted by Cunha *et al*.[48] in relation to pits formed in phenanthroline monolayers. However, while substantial charge transfer is associated with thiol monolayer formation,[151] very little is involved in PHEN binding, questioning the general applicability of the mechanism.

Here the cause of the pitting is attributed to the PHEN molecules mining gold atoms from the surface to bind with as they move from the physisorbed state to the chemisorbed state. These adatoms can be taken from terrace edges, however on large flat (111) terraces these atoms are initially mined from lifting of the gold reconstruction lines or spot defects in the (111) surface, initiating a pit with step edges from which subsequent adatoms are mined, continuing until enough atoms are taken from the surface to accommodate each PHEN in a 1:1 ratio. Cunha *et al*.[48] found that the pitting both increased and decreased via electrochemical control, complementing this theory, as the two states are energetically close to each other and the movement from one to the other can be driven by electrochemical control. As the PHEN molecule moves back to the physisorbed state it donates its adatom back to the gold surface, reducing the pit size or forming islands.

The pitting effects depicted in the McDermott *et al.* model are realistic but do not account for the complex balance of forces associated with the mining of surface atoms in order to maximize the surface to head group and inter-adsorbate interactions. As the McDermott model is generally inadequate for PHEN and perhaps thiol monolayers and this research has established that pitting is caused by adatom formation, so that pitting, when it appears, is the most direct evidence available that the monolayer has formed via adatoms. It is thus likely that there exists a close analogy between the processes depicted herein for PHEN and those operative for thiols, and indeed quantitative calculations have explored this possibility in detail.[43, 152]

Thiol monolayer formation on gold can be associated with a large number of motifs depicting the formation of surface pits and vacancy islands.[150, 153, 154] It is this complexity that makes difficult isolation of the key effects controlling the process. However, for PHEN monolayers on gold, the results show that stable chemisorbed phases are intrinsically associated with gold adatom binding, while a range of alternate structures at comparable energies are also isolated. Adatoms have also been implicated in the binding of amines to gold,[42] and it is thus not unreasonable to suggest that such structures are also important for thiol binding. Indeed, the only available experimental information on the gold-sulfur geometry in thiol monolayers indicates that the sulfur sits vertically above a gold atom,[155, 156] as is expected only when adatoms are involved,[157] and DFT[149, 158] simulations indicate that thiol monolayers can extract gold from the reconstruction lines to produce adatom-bound adsorbates.[158] The results thus strengthen the case for significant adatom involvement in thiol monolayers.
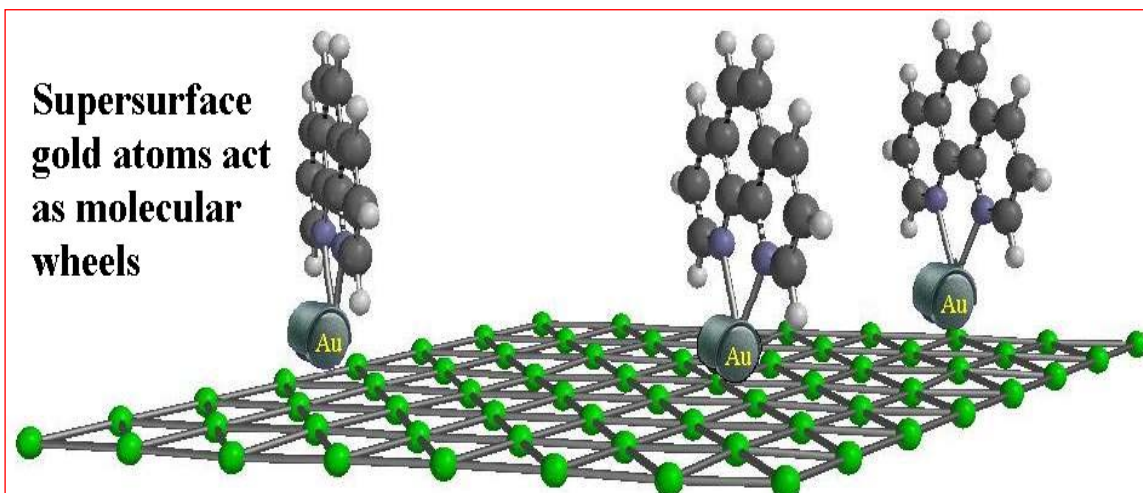
Figure 3-56: Cartoon of the chemisorbed PHEN-gold adatom entity. Prior to full monolayer surface coverage the entity has high surface mobility, whilst remaining bound and upright on the surface. Positioning will be dictated by surrounding PHEN-gold atom entities. By this mechanism the monolayer self-assembles.

(blank Page)

Chapter 4 The Nature and Conduction of

Thiols Chemisorbed to Gold.

4-0 Synopsis for Chapter 4

This chapter examines various research publications in the area of *thiol binding to gold* and makes natural extensions to the body of literature using conclusions drawn from Chapters 2 and 3. Through a thorough examination of the binding mode of the thiol (*i.e.* the deprotonated thiol) linker to gold with the help of extensive literature reports, it concludes that the gold adatom is implicated as a primary binding mechanism of thiols to the Au(111) surface (similar to the 1,10-phenanthroline linker studied in Chapter 3).

The adatom configuration is extended to dithiol binding to two gold terminals during the break-junction experiment, and it is determined that thiols are connected to the gold terminals via adatoms at *one* or *both* ends, with a fourfold decrease in conductivity respectively, giving rise to distinct peaks (or sets of peaks) in break-junction histograms.

Broadness of peaks observed in the histograms of break-junction experiments is mainly due to angular distortion of the molecule in relation to the gold electrode.

4-1 Introduction to Chapter 4

"Great things are not done by impulse, but by a series of

small things brought together." (Vincent Van Gough)

4.1.1   Importance of determining the binding mode

"At the heart of the problem is the need to interface

reliably with an individual molecule."[28]

At the Faraday Discussions #133, "*Molecular Wires And Nanoscale Conductors*" Manchester, September 2003, a world leader in experimental research into single molecule conduction, Professor Stuart Lindsay (Arizona State University), expressed a view that further research into molecular conductance, particularly theoretically, was being hampered by a limited understanding of the contact geometry (of the molecule with the metal electrode)[33].

At that same conference this author presented a poster titled "*Electrical conduction through single molecules: the nature of self-assembled monolayers: the bonding of nitrogen to the surface in 1,10-phenanthroline*". The theme of the poster was on the binding geometry of a molecule to gold, determining that 1,10-phenanthroline could bind to the Au(111) surface via a gold adatom (this poster was a preliminary delivery of the work which forms the basis of Chapter 3 of this thesis).

In most experimental work involving monolayer formation on gold, great care is taken to produce flat terraces of Au(111) surface upon which the monolayer can form and be characterised. The immediate assumption was that the molecules of the monolayer bound

directly to the Au(111) surface, and for a number of years the assumption was followed axiomatically in subsequent theoretical modelling.

However a common feature of many, but not all, monolayers was surface pitting, at a depth equal to one gold lattice parameter (*i.e.* the pitting was in the Au(111) surface, not the monolayer). Until the explanation of the adatom mode of binding of molecules to gold[1], the cause of the surface pitting was never adequately explained.

Since 2003 a number of publications have addressed the issue of contact geometry, yet by 2007 "*detailed understanding of the role of contact geometry is still required*"[111], and the weight of those publications is yet to be brought to bear upon a conclusion, particularly for thiol-based monolayers. The implications for molecular conduction, and in particular conduction observed in break-junction experiments, have received little attention.

4.1.2   Work of this chapter - adatom configuration in the thiol binding to gold

The results section (Section 4-2) presents a dissertation on the method of binding of the thiol radical to gold using a body of nascent research, both experimental and theoretical. It then explores how this impinges on break-junction experiments and the measured conductance values. It resumes a theme from Chapter 3 which implicates the adatom in the binding of 1,10-phenanthroline to gold, and develops this with the theme of Chapter 2, molecular conductance.

4.1.3   NOTE concerning *thiol* and *thiyl* terminology:

When a thiol binds to gold it does so covalently with the loss of a hydrogen atom. The resultant linking unit is termed a ***thiyl (or thiyl** radical).* However it is very common to

see in literature the resultant bound species described as a "thiol", perhaps because the name is more familiar, or perhaps because it refers to the source molecule, even though it is technically incorrect. Because this thesis draws upon many sources which use the term "thiol" instead of "**thiyl**", it has become necessary to follow that convention, particularly when citing or referring to another author's work. The reader must understand that where the term "thiol" is used to describe a molecule covalently bound to gold, it means "**thiyl**". UUPAC advises that **thiyl** is synonymous with sulfenyl radicals, and due to inconsistencies in use the term is not recommended.[159]

Occasionally the term "*thiolate*" is also seen in literature to (mistakenly) describe the chemisorbed deprotonated thiol. It is incorrect because a thiolate species is an ionic entity which would bond ionically to gold, which is not the case.

4-2 The adatom configuration of thiols bound to gold and its implications regarding molecular conduction.

This section outlines the result of literature research which arose due to the nature of experimental results presented in Chapter 2, that is that molecular conduction was not always a single value quantity, and also from the work presented in Chapter 3, which drew analogies with "*similar but poorly understood processes involved in the binding of thiols to Au(111)*."

It falls into two sub-sections, the first examines the binding mode(s) of thiols to gold and the second examines how the binding geometry affects molecular conductance.

4.2.1   Bond geometry: analysis of the dithiol results of Chapter 2

One would perhaps expect that if a molecule had a single value of conductance when trapped within a gold break-junction then its conductance value would be highly consistent and the resultant binned histogram would show extremely clear peaks at the conductance values: indeed there would be no need to construct histograms. However the position of specific steps from trace to trace vary, and the histogram peaks are broad, both here (Chapter 2) and in Li, *et al*,[101] (reproduced in Figure 4-57 below), and generally all similar experiments on all molecules. Furthermore, Li's work particularises two sets of conduction regimes, which they have labelled High and Low (Table 4-19 below).

Octanedithiol conductance by Li, *et al*, (2006)

(a) Three types of transient conductance traces recorded during separation of the STM tip from the substrate in toluene containing 1 mM octanedithiol. The percentage frequency with which each occurs is marked on the graph. (b) Conductance histogram constructed from the conductance traces that show steps (486 out of 1193 curves). Peaks located near integer multiples are marked by arrows and referred to as H peaks. The region that shows spikes is marked by a rectangular box. (c) Conductance histogram of the rectangular box region reveals a new set of peaks (referred to as L peaks). Bias was 0.1 V in measurements. See text for details of the analysis.
Copyright © 2007 American Chemical Society

Figure 4-57 Extract from Figure from paper by Li, *et al*, (2006)[101] with their caption. They have determined that 1,8-octanedithiol has two conduction regimes labelled H (High Conduction) and L (Low Conduction) and they have ascribed the different regimes to different binding geometries of the thiol linker to the gold.

Table 4-19: Conduction regimes of Li, *et al*, (2006)[101]

Regime	Conduction of 1 molecule (1,8-octanedithiol)
High Conduction	$1.68 \times 10^{-4} G_0$
Low Conduction	$0.42 \times 10^{-4} G_0$

Both regimes are well established and consist of a series of peaks corresponding to 1, 2 or 3 molecules. Furthermore, by testing a series of alkanedithiols, they found that the tunnelling decay constant, ß (from the conductivity equation $G_N = Ae^{-\beta N}$), is the same for each regime, the only difference being the pre-factor, A (by a factor of 4.0). Reasons for these variations have been postulated and have implications for this current research, and are related to geometry. Two effects are noted:

1. **Molecular distortion**: The molecule may stretch, twist, or otherwise distort due to shear, tension or applied bias during the experiment.

2. **Binding geometry**: The sulfur atom of the thiol may bind to the gold surface in a number of different geometries concerning its binding site on the gold surface *and* the angle at which it binds.

The **binding geometry** is the main effect and is explored under the next heading.

The **molecular distortion** is responsible for smaller variations. Bond twisting and molecular stretching *(i.e.* within the molecule) are considered to contribute little to the variation[56, 160],). The twist of the sulfur-carbon bond has very little effect[12, 161]. The weak dependence of conduction with elongation is probably due to the relaxation of the electrode geometry near the contact region[160]. Conduction is not strongly dependant on bias (within a range close to zero, say –0.8 to +0.8 V)[162].

NOTE on Solvent Effects: Solvent effects are not included in this consideration. It has been reported that temperature and solvent have little effect on conduction[101] (although temperature may affect conductance in polar solvents[72]) however this work has found that, for some conductive molecules, there are quite different conductive behaviours in different solvents when considering broad conductance ranges (See Chapter 2).

4.2.1.1   Analysis of the binding geometry of thiol linker to the Au(111) surface

The main contributor to variations in observed conductances for thiol-bound molecules is the binding geometry of the thiol to the gold surface. There are two

considerations here, the position and geometry of the gold atoms under the thiol, and the angle at which the thiol sits upon that gold geometry (which will be explored first).

4.2.1.1.1 Binding angle

The angle of binding has been identified as responsible for the broadness of histogram peaks:

> *"...broad transmission peaks are related to large angle transverse motion across the junction.*" Grigoriev (2006)[161]

It is commonly observed that the histograms peaks broaden as the applied bias is increased (for example He, *et al,* (2006), from 100 to 400 mV)[11], most likely due to an increase in the likelihood and range of the distortion of the bond angle.

Herrmann, *et al*, (2006)[43] found that with a <u>dithiolated alkane</u> (1,6-hexanedithiol), whilst there were often steps in the conductance traces, the binned histograms showed no clear peaks, however using a <u>diamine alkane</u> (1,4-butanediamine), the steps pointed to clear conductance peaks (see Figure 4-58, below), a phenomena also found by Venkataraman, *et al*, (2006)[42]. This suggests that the amine linkage is *more consistent* than the thiol linkage for producing reliable conductance values.

The reason may be in the possible bond geometries and angles at which the two molecules bind to gold.

Romaner, *et al*, (2006, with theoretical calculations on 1,8-octanedithiol)[163] find that the thiol link to gold is highly angle-dependent, whilst Venkataraman, *et al*, (2006 experiments on various diamines) find that the Au-amine bond is not strongly directional[42].

Xu, *et al*, (2003)[56] observe experimentally saw-tooth shapes in the conductance traces of octanedithiol which are less pronounced in **4,4′**-bipyridine, with the variation being 14% for the dithiol and 9% for the bipyridine. These saw-tooth shapes are most likely due to bond angle distortion whilst the break-junction terminals are being separated.

Further research is required into the effects of bond angle. Most recently, Quek, et al, (2007)[87] find that broadness of peaks is related to variations in bond structure, including incidence angle. It has been considered that what we see as a broad peak may clarify into a series of narrow peaks under certain conditions and with sufficient number of sweeps. The narrow peaks would relate to discreet preferred incident angles (of the molecule to the gold surface – proposed by Grigorev[161]). See Figure 4-58 below for an example which indicates a broad peak consisting of multiple peaks bunched together.

Figure 4-58: Histogram of Herrmann, *et al*, (2006) with their caption for the conductance of 1,4-butanediamine. A large number of sweeps (1388) shows a broad peak in the histogram: the broad peak appears to be composed of smaller narrow peaks. Grigoriev (2006)[161] suggests such peaks may arise because of discreet incident angles of the molecule on the gold surface. (Note that this is not suggested by the authors who produced the graph).

Figure 5 Conductance histogram generated from 1388 consecutive traces measured in the presence of a 2 mM solution of 1,4-butanediamine in 1,2,4-trichlorobenzene at a bias voltage of 0.25 V (solid line). The thin dotted lines represent fits to Gaussian peaks and to a residual tunneling background. The position of the peak maxima is indicated by the arrows. The thick dotted line is the sum of the individual fits. A histogram obtained from a measurement on the solvent without the molecules was subtracted prior to the fitting.

4.2.1.1.2 Underlying Geometry of the gold atoms involved in the thiol bond.

The atomic geometry of the gold atom(s) to which the thiol binds appears to be the most critical factor in conductance. This argument is developed in the following paragraphs.

Traditional thiol binding to Au(111)

Thiol-gold monolayers are usually prepared on the Au(111) surface, and so from the beginning (mid 1990's) theoretical models assumed that the sulfur head group was bound directly to a site on the (111) surface. Three primary binding sites were normally identified, being Hollow, Bridge or Top (Figure 4-59, below):

Hollow site   Bridge Site   Top site
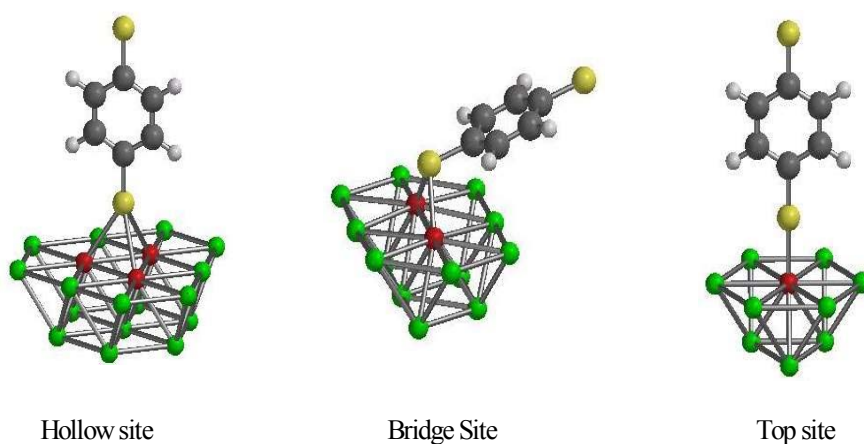
Figure 4-59: Three primary binding sites of a thiolated organic molecule to the Au(111) surface, using benzenedithiol as an example. (The hollow site actually has two forms, hcp or fcc: the difference between the two hollow sites is whether or not there is a gold atom in the second layer directly under the sulfur.) (Pictures courtesy of Gemma Solomon, personal communication).

As far as conductance is concerned, theoretical calculations show that for geometries of similar energies the conductivity may vary by less than an order of magnitude (*i.e.* for binding to "hollow" sites fcc or hcp, or to a bridge site), and that twist of the sulfur-carbon

bond has very little effect[12, 161]. However when the thiol atom binds to a top site conductivity increases by either 30%[161], a factor of 9.4 according to another calculation[11] and by 42 times according to a more rigorous calculation[12], however the top site is not favourable energetically, even though the only available experimental information on the gold-sulfur geometry in thiol monolayers indicates that the sulfur sits vertically above a gold atom.[155, 156] The effects of these different geometries on conductance are explored greater detail in Section 4.2.2 below.

Thiol bound to a gold adatom

More recently a gold-adatom geometry has been considered. The adatom may occupy a position above the Au(111) surface such as hollow, bridge or top, and the sulfur atom is bound to it (Figure 4-60, below).

This explains why, despite theoretical calculations to the contrary, experimental studies have indicated that the sulfur sits atop a gold atom: the gold atom is not *in* the (111) surface, but *above* it, as is expected only when adatoms are involved,[157] and DFT[149, 158] simulations indicate that thiol monolayers can extract gold from the reconstruction lines to produce adatom-bound adsorbates.[158]

Figure 4-60: Thiol bound to an adatom which occupies a hollow site above the Au(111) surface. (The Au(111) surface is represented here by the 3 lower gold atoms.) (Figure adapted from Li, et al[101])

This binding site has received little attention until very recently. (Even an extremely thorough analysis of thiol-gold binding as recently as September 2006 by Vericat, *et al,*[164] did not consider it, even though they highlighted surface pitting of Au(111), which is evidence of the formation of gold adatoms – see Chapter 3.)

This thesis has shown that the adatom is the binding mode of chemisorbed <u>1,10-phenanthroline</u> to Au(111) (Chapter 3), and it was recently found to be the preferred binding mode for <u>isocyanides</u> onto the Au(111) surface (Gilman, 2006)[165]. Venkataraman, *et al,* (2006) recently proposed that binding of <u>amine</u> to gold was via an adatom...

> "*... with sufficient angular flexibility for easy junction formation but well-defined electronic coupling of the N lone pair to the Au.*"[42].....

... and even more recently they identified it as the *most likely* binding mode[87] (using theoretical calculations).

For thiol binding to Au(111) there are a large number of recent helpful publications:

An insightful theoretical analysis of the formation of methanethiol monolayers has recently been prepared by Wang, *et al, (2007)*[166], modelling the system that appears in experimental research in STM images. They have determined that a methanethiol monolayer may form (from the dissociation of dimethyldisulfide), and that at a low surface coverage the monolayer is formed onto gold adatoms which are produced on the (111) surface via the lifting of the reconstruction, and that above a surface coverage of 7.8% (thiol head groups to gold surface atoms) the adatoms are drawn from the (111) surface leaving behind vacancy islands (pits) in the (111) surface. The adatom is implicated in thiol binding to the gold surface, and the formation of the thiol-gold adatom entity is endothermic.

Batista, *et al.*, (2006)[160] find theoretically that the thiol link may draw gold atoms towards it from the bulk, implying that the terminal of the thiol with the gold may include an adatom. Yu, *et al.*, (2006)[167] have established through X-ray standing wave experiments that the thiol absorption to gold is via thiol-adatom units which are mobile on the gold surface. Cometto, *et al.*, (2005)[144] highlight the mobility of thiols on gold with the adatom implicated also. Maksymovych, *et al*, (2006)[168] establish the adatom-thiol unit as responsible for the binding of the methanethiol to the gold and the formation of pits. Romaner, *et al*, (2006)[163] finds that the sulfur combines more strongly to an adatom than a perfectly planar surface (referring to theoretical calculations done on 1,4-benzenedithiol sandwiched between 2 gold electrodes). In a thorough approach including STM scans during *in situ* electrochemistry and extensive theoretical modelling, Esplandiu, *et al*, (2005)[143] conclude that thiols bind to a "defect layer" of gold atoms above the gold surface *(i.e.* adatoms), and determine that the thiol-adatom entity forms on step edges then and has little barrier to translation across the surface.

What has become evident from various research papers in the last two or three years and from the work of Chapter 3 is that pit formation alone is strong evidence of the formation of gold adatom-thiol entities that are the anchors of the molecule to the gold surface. Furthermore, these molecule-adatom units are *mobile* and intermolecular forces (of the absorbed molecule) then dictate the most energetically favourable structuring of these units on the surface (See the cartoon in Figure 4-61 below.)
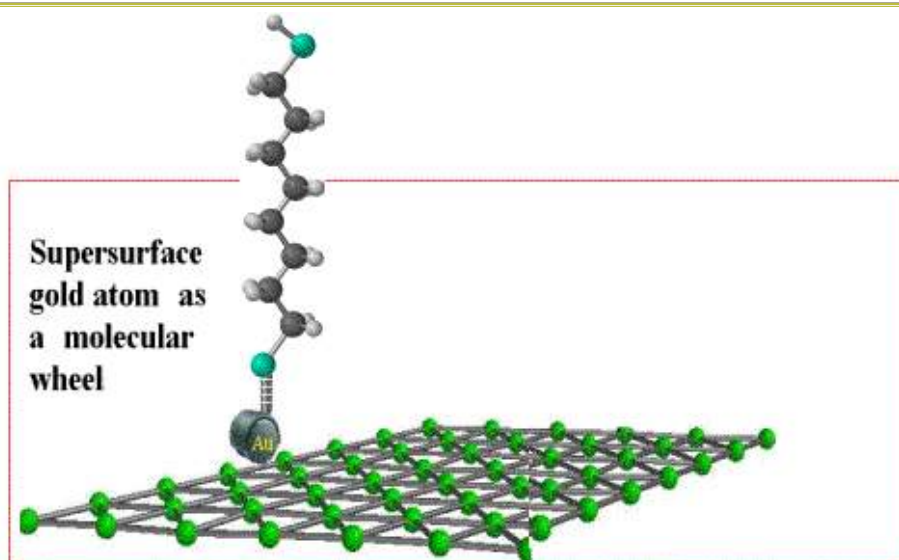
Figure 4-61: Cartoon of 1,8-octanedithiol bound (as a thiol) via a gold adatom. The low barrier to translation of the unit implies that it is mobile on the Au(111) surface, and it may be considered as a wheeled unit. Its position on the surface will be dictated by intermolecular forces between itself and other octanethiols *(i.e.* the monolayer will self-assemble)

4.2.1.2   Thiol binding during a break-junction experiment.

During the break junction experiment it is even *less* likely that an organic thiol would be bound to a site in the flat Au(111) surface.

The adatom model may be far more realistic for break-junctions when we consider that during the experiment the ends of the wire upon breaking are more likely to be conical or chain-like[169] rather than taking on the form of two gold (111) surfaces facing each other. An STM image of the gold surface after a number of break-junction sweeps (Figure 4-62 below, from He, *et al*, 2006[11]) shows that the surface is unlikely to retain its (111) facet at the point of the junction (the figure caption includes a quote from that paper concerning the inappropriateness of the use of the bi-planar model bridged by a dithiol molecule).
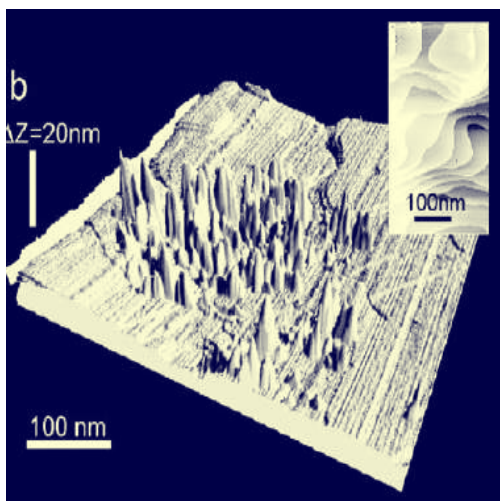
Figure 4-62: STM Image of the gold surface after a number of break-junction sweeps, from He, *et al*, 2006[11]. they quote:

"*One important factor may be the use of a planar Au(111) model for the contact; a glance at Fig 1b* (left) *shows how inappropriate this is. More realistic models of the contact geometry will require simulations of much greater complexity.*"[11]

In a similar thiol break-junction paper, Li, *et al,* (2006)[101] identify that it is unlikely that during a break junction experiment the dithiol molecule will be bound to two opposing flat Au(111) surfaces. They isolate two binding modes for consideration at *each* end of the molecule:

- The thiol binds to a hollow site in the Au(111) surface,

  and

- The thiol binds to a gold adatom which sits upon the Au(111) surface.

When the dithiol molecule is sandwiched between 2 gold electrodes, the most likely configurations of the two bonds are:

Hollow-Molecule-Adatom

and

Adatom-Molecule-Adatom

These configurations are reproduced from their paper in Figure 4-63 below. (Note: they call the adatom site "***top***"). They state a *Hollow-Molecule-Hollow* geometry does not occur because when the gold wire breaks there WILL be at least one pointy end.
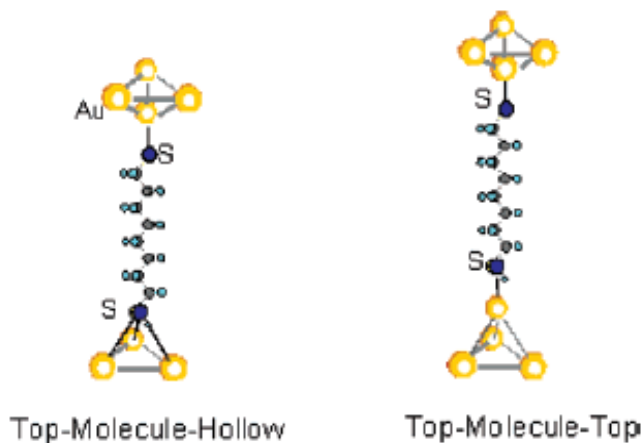
Figure 7. Models of two different molecule–electrode contact geometries.

Figure 4-63: Binding sequences of 1,8-octanedithiol during the break-junction experiment, proposed by Li, *et al*[101], where: "*Hollow*" means S binds to a hcp site, and "*Top*" means S binds to a gold atom atop a pyramid. *i.e.* The "***Top***" site here is analogous to an adatom

These two binding sequences were postulated as being responsible for the two conduction regimes observed in their experiments, with the **H**igh conductive regime associated with Top-Molecule-Hollow and being 4 times more conductive than the **L**ow conductive regime, being associated with Top-Molecule-Top (See Table 4-19, above)$^\Sigma$.

Interestingly, Gonzalez, *et al*, (2006)[68] found only the **L**ow conductance regime (~4.5 x 10^{-5} G_0) and no evidence of the **H**igh conductance regime, using a much slower withdrawal speed of 1nm/s (Li used 40nm/s). The inference here is that the slower speed allows time for both junctions to relax to the Top (adatom) configuration.

$^\Sigma$ Li says that "simulations" indicate that the top *(i.e.* adatom) site is less conductive than a hollow site, and cites support from an unpublished work by O. F. Sankey, with the expression "a 4-fold decrease in conductance" for the pyramidical site, consistent with this discussion. This ratio is confirmed by Müller (2006) (see the following Section).

4.2.2   Conductivity of thiols bound on an adatom

It has been established that the thiol is most probably bound to an **adatom** in a thiol monolayer on the Au(111) surface, with pitting being the most observable STM evidence of adatom binding. It has also been established that during break-junction experiments (on dithiols) one or both ends of the dithiol bind to an adatom rather than on a flat Au(111) surface.

But whilst these adatom configurations are *energetically* more favourable, are they better at **conduction**?

The answer is *no*. Li's paper (cited above)[101] speculatively estimated a four-fold decrease in conduction for a geometry which includes the additional adatom bond at one end. This and other geometries are explored thoroughly by Müller with their conductances compared (2006[169]). He examined 16 possible binding geometries for 1,6-hexanedithiol which might occur during a break-junction experiment and calculated the conductivity of each. His results are reproduced in detail in Figure 4-64 and Figure 4-65 below.
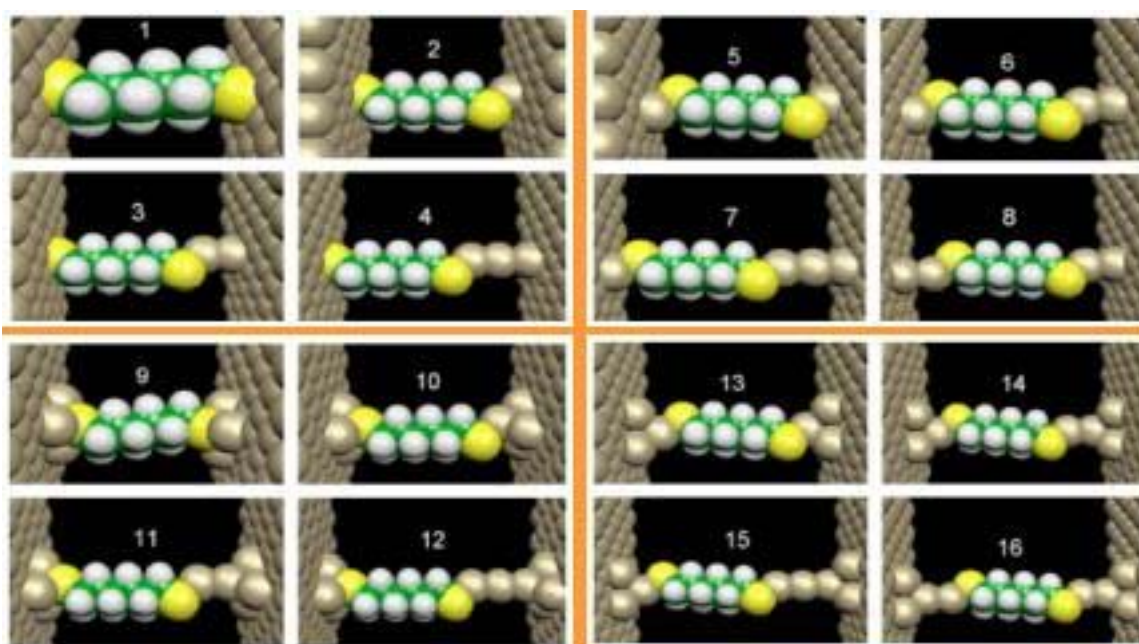

Figure 4-64 (reproduced from Müller, Phys Rev B 2006[169].) The 16 geometries considered by Müller. He used these to calculate the electrical

conductance values of a single 1,6-hexanedithiol molecule for the different electrode-molecule-electrode configurations. Note that Li's two models (Figure 4-63) would correspond approximately to numbers 2 and 5 (or 2 and 13).
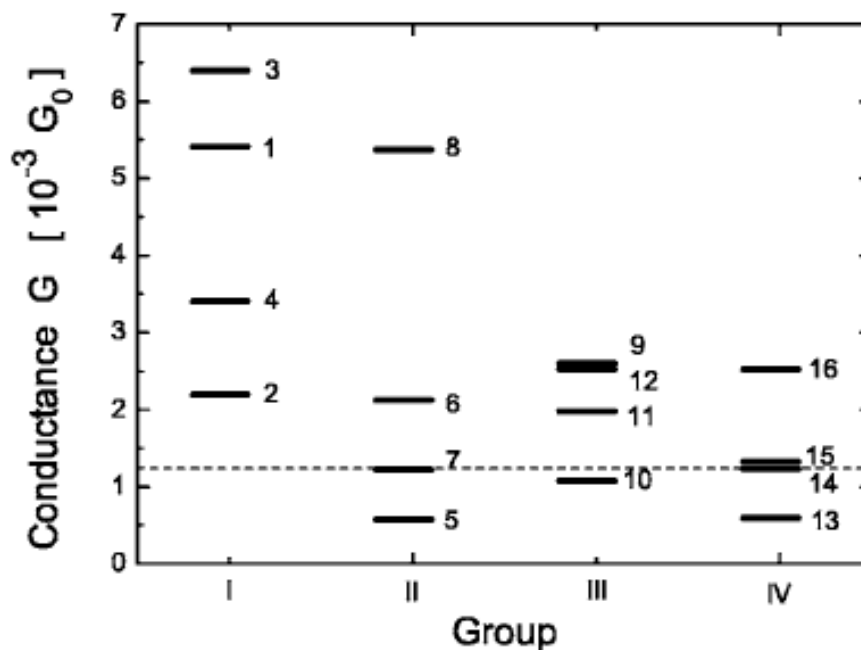
Figure 4-65: (reproduced from Müller, Phys Rev B 2006[169].) The **conductances** of the 16 geometries considered by Müller for a single 1,6-hexanedithyol molecule sandwiched between two gold electrodes. The dashed line indicates conductance value found experimentally by Xu and Tao[14] for the same molecule using the break-junction technique.

Müller calculates conductance using 16 different models of binding (using 1,6-hexanedithiol). Assuming the gold wire is no more than 3 atoms long[76,Γ], he has 0-0, 0-1, 0-2, 0-3, 1-1, 1-2, 1-3, 2-2 configurations, using a bulk of Au(111) surface (represented by semi-infinite electrodes). He has also included the truncated pyramid and the full pyramid in his models. Li's 2 models would correspond approximately to numbers 2 and 5 (or 2 and 13). Notably 5 and 13 give the smallest conductance values. The ratio between 2 and 5 (or 13) is

---

Γ The Untiedt model determined that the 1-atom-diameter gold wire is unlikely to be more than 2 or 3 units long, however in the presence of bound molecules this may not be the case. During break-junction experiments it is often observed that gold steps in conductance traces are much longer after the molecule has been added to the experimental liquid cell. Refer to Chapter 2 at various places where it refers to gold conduction steps.

4.4 to 1, agreeing remarkably with the experimentally-determined ratio between the **H** and **L** for Li, 1.68:0.42 (*i.e.* **4.0 to 1**).

There is also good convergence with the work of Batista, *et al*, (2006)[160], who found that the inclusion of a single gold atom between the thiol and the gold electrode (at one end only) decreases the conduction by a factor of three (performing theoretical calculations on octanedithiol).

In Gonzales[68], slower tip withdrawal (one 40th of the speed of Li) only the Low conduction regime is observed, which could be interpreted in this way: in the slower withdrawal there is sufficient time for the gold to arrange in pyramidical shapes at *both* ends, so the configuration ***top-molecule-top*** (using Li's terminology) would prevail, which gives the **Low** conduction. Li himself observed that ***top-molecule-top*** often followed ***top-molecule-hollow***, but never the other way around. This implies that at slow enough speeds pyramidical shapes would eventually form on both ends.

Jang, *et al*, (2006)[69] find only the **Low** conductance regime (0.44 x 10^{-4} G_0) for 1,8-octanedithiol using "last step analysis", and also finds **Low** conductance values for 1,6-hexanedithiol (3.6 x 10^{-4} G_0) and decanedithiol (0.057 x 10^{-4} G_0) which are the same fraction (¼) of the corresponding **High** conductance values found by Xu, et al (2003)[14] (being 12.3 x 10^{-4} G_0 and 0.021.0 x 10^{-4} G_0 respectively). The implication is that the same dependence of conduction on binding geometry is similar for all alkanedithiols (and possibly by extension to all organic thiols).

Similar reports on **H** and **L** for the anchoring groups of diamines and dicarboxylic acids show the factor is not ¼ but 1/15th and 1/10th respectively[40] (See Table 4-19, page 4-6, above,).

A corollary of Müller's work is that he found that certain theoretical configurations agreed better than others with the experimental results of Xu and Tao[14]. It has long been observed that theoretical approaches to conductance of molecules usually give conductances of at least an order of magnitude greater than experimentally observed values[161, 165]. However Müller *does* have theoretical conductances which agree with the work of Xu and Tao. Müller's finding suggests that more careful selection of binding geometries may lead to greater convergence of theoretically and experimentally observed conductances.

Other papers add somewhat to the discussion:

- Grigoriev, *et al,* (2006) found theoretically if the sulfur atom binds to a 3-atom gold island there is an order of magnitude decrease in conductivity[161].

- Batista, *et al,* (2006) determined theoretically that the main contribution to variation in conduction is the number of gold atoms between the molecule and the gold "slab"[160].

- Basch, *et al,* (2005) observed that small changes which break the symmetry can have a tremendous effect[152].

4-3 Conclusion to Chapter 4: dithiol binding and conductance.

Having performed break-junction experiments on 1,8-octanedithiol (Chapter 2), and established surface pitting as direct evidence adatom binding of 1,10-phenanthroline to the Au(111) surface (Chapter 3), and considering the all publications cited above, and in particular contrasting the papers of Müller and Li, *et al*, it is a conclusion of this thesis that during the break-junction experiment only certain electrode tip configurations prevail, the two most likely having adatoms involved in binding at one or both ends.

Different conduction regimes are related to the different binding modes. An adatom-molecule-hollow configuration will show as a High conduction regime. An adatom-molecule-adatom configuration will show as a Low conduction regime. In dithiols the ratio between High and Low regimes is 4:1, and this ratio is different for other linker units.

In slower withdrawals only the Low conductance regime is observed.

Broadness of histogram peaks (in break-junction experiments) is mainly due to variations in the angle at which the molecule binds to the gold, and to a lesser degree to other distortions. In most thiol monolayers on gold, the thiol preferentially binds to an adatom upon the Au(111) surface and the entity is mobile; the adatoms are extracted from the bulk leaving pits. In break-junction experiments these adatoms are expressed as the points of small pyramids. It is determined that during the break-junction experiment the main binding modes of thiol to the gold electrodes involve a gold adatom at one or both ends.

4-3 Conclusion to Chapter 4: dithiol binding and conductance.

(blank page)

Chapter 5 Simple Methods for Estimating Molecular Conductivity.

5-0 Synopsis for Chapter 5

This chapter examines publications in the use of the *tunnelling conduction formula*

$G_N = Ae^{-\beta N}$, (Section 5-2) where:

G_N is the conductance of N "simple" repeat units.

ß is the tunnelling decay constant per unit, and

A is the constant pre-factor, which is largely related to the type of linker units at the ends of the molecule (e.g. thiols, amines, etc).

By natural extension to the body of literature two methods are developed which exploit the tunnelling conduction formula, as follows:

Method (a):   To extend a known series of molecules (such as alkanedithiols) – this involves manipulation of the tunnelling decay constant, ß.

Method (b):   To impute from one series of molecules (such as alkanedithiols) to another series of molecules (such as alkanediamines) whose difference is solely in the linker units at each end. This involves manipulation of the pre-factor, A.

By the two different extrapolations of the tunnelling conduction formula, new theoretical conductance values were found for two molecules as set out in Table 5-20 below.

Molecule and structure	conductance x 10^{-4} G_0	Method	Section
1,12-dodecanedithiol	0.048	(a)	Section 5.2.4
1,4-bezenedimethanediamine	1.3	(b)	Section 5.2.5

Table 5-20 Molecular conduction values found by exploitation of the tunnelling conduction formula.

5-1 Introduction to Chapter 5

"Everything should be made as simple as possible,

but not simpler." (Albert Einstein)

5.1.1   Need for a simpler method for determining molecular conductance.

Both experimental and theoretical methods for determining single molecule conductance are quite difficult and expensive.

Experimental work requires a functioning preparation laboratory with clean areas and pure water supply, as well as an instrument capable of probing a single molecule (such as an STM), and each experiment requires components of pure gold. Equipment and sample preparation may take a full day or more and requires a high level of expertise, as does the operation of the instrument. Furthermore, the number of failures, for various reasons, is very high. Post experimental analysis of results is also quite time-consuming.

Theoretical calculations of molecular conductance are also laborious, and are still expensive in computer resources and require a high level of expertise. Traditional density functional theory (DFT) calculations are insufficient and lead to large discrepancies with experimental values[19]. Sophisticated methods required to obtain more accurate conduction values are only just emerging[170], and yet still results often vary from established experimental results by an order of magnitude or more[78, 87, 161].

A number of reliable conductance values of simple molecules are coming to light through various research groups around the world (See Chapter 2, Table 2-2, page 2-15

above). By comparing similar molecules patterns may appear which can be defined and extrapolated to other molecules.

If these patterns do appear, they offer a much simpler method of calculating the conductance of single molecules, and may improve on the accuracy of complicated DFT calculations. At the very least, they will provide a "ball-park" figure, which may give some assurance or guidance to a researcher, or may help the experimentalist in his search for evidence of conduction contained within thousands of data files.

5.1.2   The work of this chapter: exploiting the tunnelling conductance formula

This chapter presents determinations resulting from applying and extending the reports of prior literature in the area of molecular electronics. The results section (Section 5-2) presents the tunnelling conductance formula and uses it with prior experimental results to calculate conductance values for other molecules. Although this may seem an obvious thing to do, no published research has yet appeared which has done so. This is most probably because the reliability of the formula is only just coming to the fore, as it depends on a reliable body of prior results for individual molecules, which is only just emerging, and which, for a number of relevant molecules, has been conveniently collated in Chapter 2 (Table 2-2).

5-2 Tunneling conductance formula and its use to determine the conduction of single molecules.

5.2.1   The unit of the conductance quantum, G_0.

The conductance quantum is the quantised unit of conductance. It appears when measuring the conductance of a quantum point contact. It is a fundamental physical constant.

The value of the quantum of conductance, G_0, is given by:

$$G_0 = \frac{2e^2}{h}$$ Equation 5-1

where h and e are the fundamental constants:

e = charge of an electron = 1.6021917 x 10^{-19} Coulomb, and

h = Planck Constant = 6.626196 x 10^{-34} Js

This gives a value of G_0 as **7.7480917 × 10^{-5}** Siemens.

The conductance of chain of single gold atoms is close to 1.0 G_0, whilst the conductance of many of the single organic molecule studied in literature is generally around 10^{-4} G_0 (±2 orders of magnitude).

5.2.2   The tunnelling conduction formula

The conduction of similar alkanes whose difference is only in the number of carbons in the backbone has been observed so as to deduce the tunnelling conductance of one single carbon atom (*i.e.*, a –CH_2– unit as part of an alkane). This quantity is called the "tunnelling decay constant", ß, and is used in the following formula, which follows from McConnell (1961)[95]:

$$G_N = Ae^{-\beta N}, \hspace{3cm} \text{Equation 5-2}$$

Where G_N is the conductance of a chain containing N -CH_2- units. Occasionally the tunnelling decay constant is expressed in length (*i.e.* per Angstrom).

A is the pre-factor and is found to relate to the linker units at each end of the molecule.

If this formula holds consistently then it obviously can be used to predict the conduction of other molecules.

5.2.3   Values determined from prior research

Various research groups have tried to quantify the parameters in the tunnelling conductance formula, and their findings show a high consistency, as set out below.

5.2.3.1   Thiols

For alkanes with chemisorbed *thiol* end groups, the value of ß has been calculated as **1.07±0.05** per -CH_2- unit and **A=1.3** G_0, using experimental data by Xu, *et al,* (2003)[14].

Jang, *et al,* (2006)[69] confirm a value of **ß=1.0** per -CH_2- unit for alkanedithiols, and **A=0.22** G_0, using a break-junction with various withdrawal speeds (4 to 40 nm/s).

Similar work by Li, *et al,* (2006)[101] found experimentally (on various chemisorbed alkanedithiols) that the dithiols regularly produced two series histograms for each molecule, which they labelled high (H) and low (L). They determined that the tunnelling decay

constant was the same for both series *(i.e.* both $ß_H$ and $ß_L$ = 1.07), but the difference in the regimes was in the pre-factor, A. They determined that A_H=**0.70** G_0, whereas A_L=**0.14** G_0. The pre-factor relates to the conductance at the terminals, and the difference between the two regimes is ascribed to two different contact geometries of the thiol to the gold electrodes. This could imply that Xu's work quoted above, with **A=1.3** G_0, may have been observing the high conductance regime, whilst Jang's work cited above, with **A=0.22** G_0, may have been observing the low conductance regime.

5.2.3.2   Amines

For alkanes with *amine* end groups, the value of ß has been calculated as **0.91±0.03** per $-CH_2-$ unit by Venkataraman, *et al*, (2006), using *experimental* data[42], with **A=0.030** G_0. This value of ß is quite similar to that found for chemisorbed thiols, however the pre-factor **A** is very different, underscoring its dependence on the anchoring unit.

Fagas and Greer (2007)[89] *theoretically* calculate the tunnelling decay constant ß (per $-CH_2-$ unit) and the pre-factor, A, on a series of diamines to be as set out in **Table 5-21**, below. Here the values of ß are very similar (and also similar to that for chemisorbed thiols), but the pre-factor is quite different for the two different anchoring units.

Various ß and A values for amine anchoring groups[89]		
	NH junctions	NH_2 junctions
ß	0.98	0.79
A (G_0)	0.92	0.02

Table 5-21: Theoretically calculated Values of ß and A from Fagan and Greer (2007)[89] for diamines.

5.2.3.3　Thiols, amines and acids

Finally, Chen, *et al*, (2006)[40] have examined the effect of different anchoring groups by looking at alkanedithiols, alkanediamines and alkanedicarboxylic acids of length N for N=2, 4, 6, 8 or 10. In a thorough approach, they found both **H**igh and **L**ow conduction regimes for most molecules. A summary of their results is reproduced in **Table 5-22**, below. Again the values of ß were reasonably consistent; however the values of A depended strongly on the type of anchoring unit and on the different conduction regimes, which again are ascribed to differing contact geometries.

Various ß and A values for different anchoring groups, both High and Low regimes[40]		
	thiol junctions	amine junctions	acid junctions
β_H	1.02	0.81	0.81
A_H (G$_0$)	0.66	0.037	0.007
β_L	1.08	0.88	0.77
A_L (G$_0$)	0.22	0.0032	0.0006

Table 5-22: Values of ß and A from Chen, *et al,* (2006).

In summary, there is remarkable consistency in these observations and calculations. There is the inference that the conductance of other molecules may be calculated using this formula alone (rather than from first principle calculations or experimentally), provided values for the component units were known.

5.2.4　*Method (a)*: **Simple use of the conduction formula – determining the conductance of 1,12-dodecanedithiol**

As a first example, using the values of Chen, *et al*, in Table 5-22, above, one could predict a conductance for dodecanedithiol, using the formula as follows (from the high conductance regime):

$$G_N \quad = A e^{-\beta N},$$

and, by substituting 12 for the number of molecules and using Chen's values ß=1.02 and A =0.66,

$$=0.66 \text{xe}^{-1.02 \text{x} 12}$$

$$=0.048 \text{x} 10^{-4} \ G_0.$$

As expected (with 12 –CH_2– units) it gives an extremely low value. This compares very well with an experimental result of $0.11 \text{x} 10^{-4} \ G_0$ (Morita and Lindsay, 2007[16]).

5.2.5   *Method (b)*: **Further use of the conduction formula – determining the conduction of 1,4-bezenedimethanediamine.**

Is it possible to calculate a molecule's conductance if we simply change its anchoring groups? The conductance formula determines that the pre-factor, A, is primarily a function of the anchoring group, and the remainder of the formula, $e^{-ßN}$, is primarily a function of the rest of the molecule. (ß is mainly dependent on the length of the molecule, but also depends slightly on the metals involved and the nature of the interfaces. It is also expected to be slightly voltage dependent.[152])
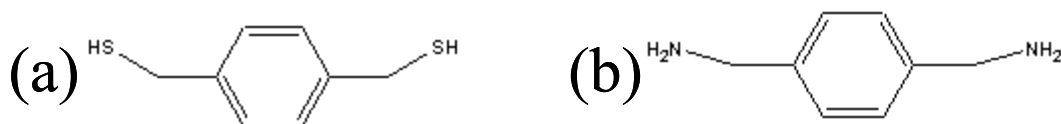
Figure 5.66:   (a) 1,4-bezenedimethane*dithiol* , and
(b) 1,4-bezenedimethane*diamine.*

A comparison of dithiol and similar diamine molecules is set out in Table 5-23 below. The comparison shows that the ratio of between conductances is constant, at around **4.7** (thiol/amine). It follows that if the conductance of any chemisorbed thiol-terminated molecule is known, the conductance of the corresponding amine-terminated molecule could

be calculated by dividing by 4.7. By this method, the conduction of 1,4-bezenedimethane*diamine* would be found by dividing that of 1,4-bezenedimethane*dithiol* by 4.7 (See the molecular structures in Figure 5.66 above). With the conductance of the dithiol as 6.0×10^{-4} G_0[83] the diamine is:

1,4-bezenedimethanediamine (calculated) = $6.0 \div 4.7$ = **1.3 $\times 10^{-4}$ G_0,**

This value is yet to be verified by any means, theoretical or experimental, but which we must consider to be reasonably accurate.

dithiol Molecule	Conductance $(10^{-4}G_0)$ ref	diamine Molecule	Conductance $(10^{-4}G_0)$ ref	Ratio thiol/amine
hexanedithiol	11 [40]	hexanediamine	2.7 [40]	**4.1**
octanedithiol	2.4 [40]	octanediamine	0.49 [40]	**4.9**
benzenedithiol	300 [42]	benzenediamine	64 [42]	**4.7**

Table 5-23: Comparison of dithiol and diamine conductances (where they exist in the same paper)

5-3 Conclusion to Chapter 5: the use of the tunneling conductance formula to determine the conduction of single molecules.

In the first example, with the most basic application of the tunnelling conductance formula, 1,12-dodecanedithiol was predicted to have a conductance of 0.048 x 10^{-4} G_0, comparing well with an experimental result. This type of application of the formula is obvious, and is secure and has a strong theoretical basis, established in Section 5.2.3. But it has limited application in that it can only be applied to longer or shorter versions of molecules which have already been investigated, three or four of which are needed to establish the parameters ß and A. As symmetry has an effect also, there might be slight variations for odd and even members of the series.

In the second example 1,4-bezenedimethanediamine was predicted to have a conductance of 0.048 x 10^{-4} G_0. There were no comparisons available in the literature. The method relied on the assumption that the pre-factor, A, was a function solely of the anchoring unit. The examples used showed a very consistent ratio between the thiol and the corresponding amine. Given that the ratio can be systematically established, the method is sound and reliable. It offers a very convenient and powerful method for estimating the conductance of whole families of molecules based upon known conductance of another family of molecules, the difference in the two families being in the anchoring units.

Current theoretical methods for determining single molecule conductance involve first principle calculations and the best methods consider large amounts of atomic data and include a number of user-defined parametric adjustments – that is, they are computationally laborious and somewhat subjective. Even so, calculated results can differ from well-

established experimental results by an order of magnitude or more[78, 161] (see also Table 2-2), and whilst there may be some understanding of the reasons for this, it remains elusively unquantifiable. In theoretical calculations a variety of realistic computational approaches are available, resulting in predictions that can vary by an order of magnitude or more. Larger uncertainties can arise in worst-case scenarios involving physisorbed molecules such as the azines studied in this thesis. In general, Density-Functional Theory is inaccurate for calculations of conductance because of its inability to treat long range electron correlation effects, the asymptotic potential error and the band-gap error.[19]

DFT calculations also require an initial "guess" of geometry, which may in itself be inappropriate, as developed in Chapter 4. These methods do not require such a guess.

The methods (a) and (b) presented here are extraordinarily simple and are reliable if based upon established experimental values and used with molecules whose conduction is primarily via a tunnelling mechanism. They will prove more useful as further *reliable* experimental data reaches the pool of public knowledge.

Highly conjugated molecules and in particular polymeric porphyrin chains or carbon nanotubes may conduct metallically (thermally activated hopping process)[109] or even ballistically[171], and in addition to the exponential term of the conduction formula there would be other terms, such as a linear component which would be simply related to Ohm's Law.

Chapter 6 Bibliography

1.   Cafe, P.F., Larsen, A.G., Yang, W., Bilic, A., Blake, I.M., Crossley, M.J., Zhang, J., Wackerbarth, H., Ulstrup, J., and Reimers, J.R., *Chemisorbed and Physisorbed Structures for 1,10-Phenanthroline and Dipyrido[3,2-a:2',3'-c]phenazine on Au(111)*. J. Phys. Chem. C, 2007. **111**(46): p. 17285-17296.

2.   Hipps, K.W., *It's all about contacts. (Perspective: Molecular Electronics)*. Science, 2001. **294**(5542): p. 536.

3.   Moore, G.E., *Cramming more Components onto Integrated Circuits*. Electronics, 1965: p. 114-117.

4.   Jurvetson, S.T., *Transcending Moore's Law with Molecular Electronics and Nanotechnology*. Nanotechnology Law and Business, 2004. **1**(1): p. 70 - 90.

5.   Tuomi, I., *The Lives and Death of Moore's Law*. First Monday (http://www.firstmonday.org/issues/issue7_11/tuomi/#author), 2002. **7**(11).

6.   Compañó, R., Molenkamp, L., and Paul, D., *Technology Roadmap for Nanoelectronics*, R. Compañó, L. Molenkamp, and P. DJ, Editors. 1999, European Commission IST Programme Future and Emerging Technologies.

7.   Aviram, A. and Ratner, M.A., *Molecular Rectifiers*. Chemical Physics Letters, 1974. **29**: p. 277.

8.   Carter, F.L., *Progress in concepts of conformational switching and molecular electronic devices*. 1982: Nav. Res. Lab., Washington DC. 24.

9.   Reed, M.A. and Lee, T., *Molecular Nanoelectronics* 2003: Stevenson Ranch, CA : American Scientific Publishers.

10.   Carroll, R.L. and Gorman, C.B., *The Genesis of Molecular Electronics*. Angewandte Chemie International Edition, 2002. **41**(73): p. 4378.

11.   He, J., Sankey, O.F., Lee, M., Tao, N.J., Li, X., and Lindsay, S.M. *Measuring single molecule conductance with break junctions*. in *Faraday Discussions 131 - Molecular Wires and Conductors*. 2006.

12.   Solomon, G.C., Riemers, J.R., and Hush, N.S., *Overcoming computational uncertainties to reveal chemical sensitivity in single molecule conduction calculations*. J Chemical Physics, 2005. **122**(224502): p. 1 - 7.

13.   Binnig, G. and Rohrer, H., *Scanning tunneling microscopy*. Applied Physics Letters, 1982. **40**: p. 178-180.

14.   Xu, B. and Tao, N.J., *Measurement of Single-Molecule Resistance by Repeated Formation of Molecular Junctions*. Science, 2003. **301**(5637): p. 1221 - 1224.

15.   Cui, X.D., Primak, A., Zarate, X., Tomfohr, J., Sankey, O.F., Moore, A.L., Moore, T.A., Gust, D., Harris, G., and Lindsay, *Reproducible Measurement of Single-Molecule Conductivity*. Science, 2001. **294**(5542): p. 571 - 574.

16.   Morita, T. and Lindsay, S.M., *Determination of Single Molecule Conductances of Alkanedithiols by Conducting-Atomic Force Microscopy with Large Gold Nanoparticles*. J American Chemical Society, 2007. **129**(23): p. 7262 -7263.

17. Smalley, R. and Drexler, K., *Open Debate: "NANOTECHNOLOGY": Drexler and Smalley make the case for and against 'molecular assemblers'*. Chemical and Engineering News, 2003. **81**(48): p. 37-42.

18. McGimpsey, W.G. *Molecular Electronics - Past, Present, Future?* in *Molecular Engineering - The next five years*. 2002. Worcester, Mass, USA: Second International Corporate/Academic Roundtable on Emerging Technologies.

19. Reimers, J.R., Cai, Z.-L., Bilic, A., and Hush, N.S., *Molecular Electronics III - Chapter "The appropriateness of Density Functional Theory for the Calculation of Molecular Electronics Properties"*. Vol. 1006. 2003, New York: New York Academy of Sciences.

20. Lent, C.S. and Timler, J., *Power gain and dissipation in quantum-dot cellular automata.* J Applied Physics, 2002. **91**(2): p. 823-831.

21. Stan, M.R., Franzon, P.D., Goldstein, S.C., Lach, J.C., and Ziegler, M.M., *Molecular Electronics: From Devices and Interconnects to Circuits and Architecture.* Proceedings of the IEEE, 2003. **91**(11): p. 1940 - 1957.

22. Smith, E.M. *Nano panelist sees molecular devices as next step toward smaller, cheaper, faster devices (James J. Marek, Jr.)*. ASME NEWS. 27 Apr 2007; http://www.asmenews.org/archives/backissues/aug01/features/nanopan.html.

23. Shi, N., Yim, G., Han, M., Xu, Z., Fan, X., Li, H., and Hong, J., *Coordination driving self-assembly of gold nanoparticles and tetrapyridylporphine into hollow spheres.* Chemistry Letters, 2005. **34**(11): p. 1468 - 1469.

24. Caruso, F., Caruso, R.A., and Mohwald, H., *Nanoengineering of Inorganic and Hybrid Hollow Spheres by Colloidal Templating.* Science, 1998. **282**: p. 1111-4

25. Greco, R.S., *Nanoscale Technology in Biological Systems*. 2005: CRC Press.

26. Wowk, B., *Cell Repair Technology.* Cryonics, 1988. **9(7)**(96): p. 21 - 32.

27. Stan, M.R., Rose, G.S., Ziegler, M.M., and Brown, C.L. *Hybrid CMOS/Molecular Electronics Circuits*. in *19th International Conference on VLSI Design - IEEE*. 2006: IEEE.

28. Allen, T.E.G., *The Conduction of Selected Platinum and Nickel Acetylides* 2003, University of Sydney, Honours thesis in School of Chemistry

29. Li, C., Fan, W., Lei, B., Zhang, D., Han, S., Tang, T., Liu, X., Liu, Z., Asano, S., Meyyappan, M., Han, J., and Zhou, C., *Multilevel memory based on molecular devices.* Applied Physics Letters, 2004. **84**(11): p. 1949-1951.

30. Ashwell, G.J., Urasinska, B., and Tyrrell, W.D., *Molecules that mimic Schottky diodes.* Phys. Chem. Chem. Phys, 2006. **8**(28): p. 3314 - 3319.

31. Huang, Y., Duan, X., Cui, Y., Lauhon, L.J., Kim, K.-H., and Lieber, C.M., *Logic Circuits with Carbon Nanotube Transistors.* Science, 2001. **294**(5545): p. 1313 - 1317.

32. Bachtold, A., Hadley, P., Nakanishi, T., and Dekker, C., *Logic Circuits with Carbon Nanotube Transistors.* Science, 2001. **294**(5545): p. 1317-1320.

33. Lindsay, S.M. *Closing Remarks*. in *Faraday Discussions 131 - Molecular Wires and Conductors*. 2006. Manchester.

34. Tour, J.M., *Molecular Electronics: Commercial Insights, Chemistry, Devices. Architecture and Programming*. 2003: World Scientific. 600.

35. Seminario, J.M., Zacarias, A.G., and M, T.J., *Molecular Alligator Clips for Single Molecule Electronics. Studies of Group 16 and Isonitriles Interfaced with Au Contacts.* J American Chemical Society, 1999. **121**(2): p. 411 - 416.

36. Bilic, A., Reimers, J.R., and Hush, N.S., *Adsorption of pyridine on the gold(111) surface: implications for molecular "alligator clips"*. J. Phys. Chem. B, 2002. **106**: p. 6740-7.

37. Reimers, J.R., Hall, L.E., Crossley, M.J., and Hush, N.S., *Rigid fused oligoporphyrins as potential versatile molecular wires.* J. Phys. Chem. A, 1999. **103**: p. 4385 - 4397.

38. Grigoriev, A., *Molecular Alligator Clips - A study of metal-molecule contacts for molecular electronics*, 2004, Chalmers University of Technology, Goteborg, Sweeden, PhD thesis in Dept of Microtechnology and Nanoscience

39. Hermann, B.A., Scherer, L.J., Housecroft, C.E., and Constable, E.C., *Self-Organized Monolayers: A Route to Conformational Switching and Read-Out of Functional Supramolecular Assemblies by Scanning Probe Methods.* Advanced Funcional Materials, 2006. **16**: p. 221-235.

40. Chen, F., Li, X., Hihath, J., Huang, Z., and Tao, N.J., *Effect of anchoring groups on single-molecule conductance: comparative study of thiol-, amine-, and carboxylic-acid-terminated molecules.* J American Chemical Society, 2006. **128**: p. 15874 - 15881.

41. Hathaway, J. *Nature's Smallest Shock* ASU Research, Tempe, AZ. 12 Jan 2008; http://researchmag.asu.edu/stories/shock.html.

42. Venkataraman, L., Klare, J.E., Tam, I.W., Nickolls, C., Hybertsen, M.S., and Steigerwald, M.L., *Single Molecule Circuits with Well-Defined Molecular Conductance.* Nano Letters, 2006. **6**(3): p. 458-462.

43. Herrmann, J., Müller, K.-H., Wei, G., Bray, D., Roberts, M., Raguse, B., and Wieczorek, L. *Contact effects in single-molecule conduction.* in *ICONN2006.* 2006. Brisbane.

44. Yu, H.Z., Zhao, J.W., Wang, Y., Q, Cai, S.M., and Liu, Z.F., *Fabricating an azobenzene self-assembled monolayer via step-by-step surface modification of a cysteamine monolayer on gold.* Journal of Electroanalytical Chemistry, 1997. **438**(1-2): p. 221-224.

45. Brolo, A.G., Irish, D.E., Szymanski, G., and Lipkowski, J., *Relationship between SERS Intensity and Both Surface Coverage and Morphology for Pyrazine Adsorbed on a Polycrystalline Gold Electrode.* Langmuir, 1998. **14**(2): p. 517 -527.

46. Cunha, F., Tao, N.J., Wang, X.W., Jin, Q., Duong, B., and D'Agnese, J., *Potential-induced phase transitions in 2,2'-bipyridine and 4,4'-bipyridine monolayers on Au(111) studied by in Situ scanning tunneling microscopy and atomic force microscopy.* Langmuir, 1996. **12**: p. 6410 - 6418.

47. Kim, B.S., Beebe, J.M., Jun, Y., Zhu, X.-Y., and Frisbie, C.D., *Correlation between HOMO Alignment and Contact Resistance in Molecular Junctions: Aromatic Thiols versus Aromatic Isocyanides.* J American Chemical Society; (Communication), 2006. **128**(15): p. 4970-4971.

48. Cunha, F., Jin, Q., Tao, N.J., and Li, C.Z., *Structural Phase Transition in Self-Assembled 1,10 phenanthroline monolayer on Au(111).* Surface Science, 1997. **389**: p. 19-28.

49. Pinheiro, L.S. and Temperini, M.L.A., *Coadsorption of 2-mercaptopyrimidine and 1,10'-phenanthroline on Au(111) as seen by STM.* Surface Science, 1999. **441**: p. 53.

50. Dominguez, O., Echegoyen, L., Cunha, F., and Tao, N., *Self-Assembled Fullerene-Derivative Monolayers on a Gold Substrate Using Phenanthroline-Au Interactions.* Langmuir, 1998. **14**(4): p. 821-824.

51. Yang, D., Bizzotto, D., Lipkowski, J., Pettinger, B., and Mirwald, S., *Electrochemical and second harmonic generation studies of 2,2'-bipyridine adsorption at the Au(111) electrode surface.* J Physical Chemistry, 1994. **98**(28): p. 7083 - 7089.

52.   Noda, H., Minoha, T., Wan, L.-J., and Osawa, M., *Adsorption and ordered phase formation of 2,2'-bipyridine on Au(111): a combined surface-enhanced infrared and STM study.* Journal of Electroanalytical Chemistry, 2000. **481**(1): p. 62 - 68.

53.   Cunha, F. and Tao, N.J., *Surface charge-induced order-disorder transition in am organic monolayer.* Phys. Rev. Lett., 1995. **75**(12): p. 2376 - 2379.

54.   Pinheiro, L.S. and Temperini, M.L.A., *STM study of 2,2':6'2"-terpyridine self-assembly on Au(111).* Surface Science, 2000. **464**(2-3): p. 176 - 182.

55.   Venkataraman, L., Klare, J.E., Nuckolls, C., Hybertsen, M.S., and Steigerwald, M.L., *Dependence of single-molecule junction conductance on molecular conformation.* Nature, 2006. **442**(7105): p. 904-907.

56.   Xu, B.Q., Xiao, X., and Tao, N.J., *Measurements of Single Molecule Electromechanical Properties.* J American Chemical Society, 2003. **125**(52): p. 16164-16165.

57.   Crossley, M.J., Burn, P.L., Langford, S.J., and Prashar, J.K., *Enantioselective recognition of histidine and lysine esters by porphyrin chiral clefts and detection of amino acid conformations in the bound state.* J. Chem. Soc. Chem. Commun., 1995: p. 1925 - 1927.

58.   Kushmerick, J.G., Holt, D.B., Yang, J.C., Naciri, J., Moore, M.H., and Shashidar, R., *Metal-Molecule Contacts and Charge Transports across Monomolecular Monolayers.* Phys. Rev. Lett., 2002. **89**(8): p. 243.

59.   Schull, T.L., Kushmerick, J.G., Petterson, C.H., George, C., Moore, M.H., and Shashidar, R., *Ligand Effects on Charge Transport in Platinum Complexes.* J American Chemical Society, 2003. **125**(11): p. 3202-3.

60.   Reichert, J., Ochs, R., Beckman, D., Weber, H.B., Mayor, M., and Lohneysen, H.V., *Driving Current through Single Organic Molecules.* Phys. Rev. Lett., 2002. **88**(17): p. 176804.

61.   Weber, H.B., Reichert, J., Weigend, F., Ochs, R., Beckman, D., Mayor, M., Alrichs, R., and Lohneysen, H.V., *Electron Transport through Single Conjugated Molecules.* Chemical Physics, 2002. **281**: p. 113-125.

62.   Reed, M.A., Zhou, C., Muller, C.J., Burgin, T.P., and Tour, J.M., *Conductance of a Molecular Junction.* Science, 2001. **294**(5542): p. 252 - 254.

63.   Yaliraki, N., Kemp, S.N., and Ratner, M.A., *The injecting energy at molecule/metal interfaces: Implications for conductance of Molecular Junctions from an ab initio Molecular Description.* J American Chemical Society, 1999. **111**(15): p. 6997-7002.

64.   Binnig, G. and Rohrer, H., *Scanning tunneling microscopy.* Helvetica Physica Acta, 1982. **55**: p. 726-35.

65.   Binnig, G. and Rohrer, H., *Scanning Tunneling Microscopy.* IBM J. Research and Development, 1986. **30**(4): p. 355-369.

66.   Blum, A.S., Yang, J.C., Shashidhar, R., and Ratna B, *Comparing the Conductivity of Molecular wires with The Scanning Tunneling Microscope.* Applied Physics Letters, 2003. **82**(19): p. 3322-3324.

67.   Fan, F.F., Yang, J., Cai, L., Price, D.W., Dirk, S.M., Kosynkin, D.V., Yao, Y., Rawlett, A.M., Tour, J.M., and Bard, A.J., *Charge Transport Through Self-Assembled Monolayers of Compounds of Interest in Molecular Electronics.* J American Chemical Society, 1999. **103**: p. 4006-4010.

68.   Gonzalez, M.T., Wu, S., Huber, R., van der Molen, S.J., Schonenberger, C., and Calame, M., *Electrical Conductance of Molecular Junctions by a Robust Statistical Analysis.* Nano Letters, 2006. **6**(10): p. 2238-2242.

69.   Jang, S.-Y., Reddy, P., Majumdar, A., and Segalman, R.A., *Interpretation of Stochastic Events in Single Molecule Conductance Measurements.* Nano Letters, 2006. **6**(10): p. 2362 -2367.

70.   Leatherman, G., Durantini, E.N., Gust, D., Moore, A.L., Moore, T.A., Stone, S., Zhou, Z., Rez , P., Liu, Y.Z., and Lindsay, S.M., *Carotene as a Molecular Wire: Conducting Atomic Force Microscopy.* J American Chemical Society, 1999. **103**: p. 4006-4010.

71.   Hurst, D.T., Thakrar, U.B., Wells, C.H.J., and Wyer, J., *An N.M.R. Study of Electron Donor-Electron Acceptor Interaction Between Aromatic Hydrocarbons and Diazines.* Australian Journal of Chemistry, 1989. **42**: p. 1313-9.

72.   Li, X., Hihath, J., Chen, F., Masuda, T., Zang, L., and Tao, N.J., *Thermally activated electron transport in single redox molecules.* J American Chemical Society, 2007. **40**(30).

73.   Zhou, C. *About Self.* Center for Microelectronic Materials and Structures Yale Univ. 29 July 2007; http://www.yale.edu/ee100/chongwu/CHONGWU.HTML.

74.   Molec.com. *Molecular Imaging's PicoPlus Microscope.* Agilent. 18 Jan 2007; http://www.orgchem.ugent.be/fdp/pdf/AFM%20PicoPlus.pdf.

75.   Molec.com. *Molecular Imaging's STM unit.* Agilent. 22 Feb 2007; http://cp.literature.agilent.com/litweb/pdf/5989-5997EN.pdf.

76.   Untiedt, C., Yanson, A.I., Grande, R., Rubio-Bollinger, G., Agrait, N., Viera, S., and van Ruitenbeek, J.M., *Calibration of the length of a chain of single gold atoms.* Phys. Rev. B, 2002. **66**: p. 085418.

77.   Whetten, R.L. and Salisbury, B.E. *Quantum Conductance.* Georgia Institute of Technology, Atlanta, Georgia. 29 July 2007; http://www.physics.gatech.edu/research/whetten/rec_results/quantum_cond.html.

78.   Kang, B.K., Aratani, N., Lim, J.K., Kim, D., Osuka, A., and Yoo, K.-H., *Electrical transport properties and their reproducibility for linear porphyrin arrays.* Materials Science and Engineering C, 2005. **26**: p. 1023-1027.

79.   Wohlthat, S., *Conductance of various organic molecules - Personal Communication*, 2008, (Sydney University).

80.   Hu, Y., Zhu, Y., Gao, H., and Guo, H., *Conductance of an Ensemble of Molecular Wires: A Statistical Analysis.* Phys. Rev. Lett., 2005. **95**: p. 156803.

81.   Tomfohr, J. and Sankey, O.F., *Simple Estimates of the Electron Transport Properties of Molecules.* Phys. Status Solidi B, 2002. **233**: p. 59-69.

82.   Halimun, H., Mahapatro, A.K., Choi, J., Lodha, S., Janes, D., and Gosh, S., *Device structure for electronic transport through individual molecules using nanoelectrodes.* Applied Physics Letters, 2005. **87**(233509): p. 3.

83.   Xiao, X., Xu, B.Q., and Tao, N.J., *Measurement of Single Molecule Conductance: Benzenedithiol and Benzenedimethanethiol.* Nano Letters, 2004. **4**(2): p. 267-271.

84.   Tsutsui, M., Teramae, Y., Kurokawa, S., and Sakai, A., *High-conductance states of single benzenedithiol molecules.* Applied Physics Letters, 2006. **89**(16): p. 163111.

85.   Tomfohr, J. and Sankey, O.F., *Theoretical analysis of electron transport through organic molecules.* J Chemical Physics, 2004. **120**: p. 1542.

86.   Lang, N.D. and Avouris, P., *Electrical conductance of individual molecules.* Phys. Rev. B, 2001. **64**(12): p. 125323.

87.   Quek, S.Y., Venkataraman, L., Choi, H.J., Louie, S.G., Hybertsen, M.S., and Neaton, J.B., *Amine-gold linked single-molecule junctions: Experiment and theory.* Condensed Matter arXiv:, 2007. **0707**: p. 2091v1.

88.   Ning, J., Li, R., Shen, X., Qian, Z., Hou, S., Rocha, A.R., and Sanvito, S., *First-principles calculation on the zero-bias conductance of a gold/1,4-diaminobenzene/gold molecular junction.* Nanotechnology, 2007. **18**: p. 345206 (6pp).

89.   Fagas, G. and Greer, J.C., *Tunnelling in alkanes anchored to gold electrodes via amine end groups.* arXiv:, 2007. **0706.**: p. 0835v1.

90.   Wohlthat, S., *Conductance of various organic molecules - Personal Communication*, 2007, (Sydney University).

91.   Cheng, W.W., Chen, H., Note, R., Mizuseki, H., and Kawazoe, Y., *Electron transport through molecular wire: effect of isomery.* Physica E, 2005. **25**: p. 643-646.

92.   Csonka, S., Halbritter, A., and Mihály, G., *Pulling gold nanowires with a hydrogen clamp: Strong interactions of hydrogen molecules with gold nanojunctions.* Phys. Rev. B, 2006. **73**(07): p. 075405 (6).

93.   Jelenic, P., Perez, R., Ortega, J., and Flores, F., *Hydrogen dissociation over Au nanowires and the fractional conductance quantum.* Phys. Rev. Lett., 2006. **96**(046): p. 046803.

94.   Rego, L.G.C., Rocha, A.R., Rodrigues, V., and Ugarte, D., *Role of structural evolution in the quantum conductance behaviour of gold nanowires during stretching.* Phys. Rev. B, 2003. **67**(04): p. 045412 (10).

95.   McConnell, H.M., *Intramolecular Charge Transfer in Aromatic Free Radicals* J Chemical Physics, 1961. **35**(2): p. 508-515

96.   Kim, M.-J., Konduri, R., Ye, H., MacDonnell, F.K., Puntoriero, F., Serroni, S., Campagna, S., Holder, T., Kinsel, G., and Rajeshwar, K., *Dinuclear Ruthenium(II) Polypyridyl Complexes Containing Large, Redox-Active, Aromatic Bridging Ligands: Synthesis, Characterization, and Intramolecular Quenching of MLCT Excited States* Inorganic Chemistry, 2002. **41**: p. 2471.

97.   Chiorboli, C., Fracasso, S., Ravaglia, M., Scandola, F., Campagna, S., Wouters, K.L., Konduri, R., and MacDonnell, F.M., *Primary Photoinduced Processes in Bimetallic Dyads with Extended Aromatic Bridges. Tetraazatetrapyridopentacene Complexes of Ruthenium(II) and Osmium(II)* Inorganic Chemistry, 2005. **44**(23): p. 8368.

98.   Hough, W.A., *Synthesis and properties of oligoporphyrins: Studies for use as molecular wires.*, 2003, Sydney University, PhD thesis in School of Chemistry

99.   Crossley, M.J. and Burn, P.L., *An approach to porphyrin-based molecular wires: Synthesis of a Bis(porphyrin)tetraone and its conversion to a Linearly Conjugated Tetrakisporphyrin system.* J. Chem. Soc. Chem. Commun., 1991: p. 1569.

100.   Molec.com. *Liquid Cell*. Agilent. 14 Aug 2007; http://www.molec.com/products_accessories.html#cells.

101.   Li, X., He, J., Hihath, J., Xu, B., Lindsay, S.M., and Tao, N., *Conductance of Single Alkanedithiols: Conduction Mechanism and Effect of Molecule-Electrode Contacts.* J American Chemical Society, 2006. **128**(6): p. 2135 -2141.

102.   Bilic, A., Reimers, J.R., Hush, N.S., Hoft, R.C., and Ford, M.J., *Adsorption of benzene on copper, silver, and gold surfaces.* J. Chem. Theory and Comput., 2006. **2**: p. 1093.

103.   Fantacci, S., de Angelis, F., Wang, J., Bernhard, S., and Selloni, A., *A combined computational and experimental study of polynuclear Ru-TPPZ complexes: insights into the electronic and optical properties of co-ordination polymers.* . J American Chemical Society, 2004. **126**: p. 9715.

104.   Araki, K., de Souza Lima, S., and Winnischofer, H. *Thin Molecular Films of Supramolecular Porphyrins*. in *Anais da Academia Brasileira de Ciências* 2000. Rio de Janeiro.

105.   Ito, T., Hamaguchi, T., Nagino, H., Yamaguchi, T., Kido, H., Zavarine, I.S., Richmond, T., Washington, J., and Kubiak, C.P., *Electron Transfer on the Infrared Vibrational Time Scale in the Mixed Valence State of 1,4-Pyrazine- and 4,4'-Bipyridine-Bridged Ruthenium Cluster Complexes.* J American Chemical Society, 1999. **121**: p. 4625-32.

106.   McConnell, H.M., Gamble, F.R., and Hoffman, G.M. *Interactions between superconductors and organic molecules*. in *National Academy of Sciences*. 1967.

107.   Caminati, W., Favero, L.B., Favero, P.G., Maris, A., and Melandri, S., *Intermolecular Hydrogen Bonding between Water and Pyrazine.* Angewandte Chemie International Edition, 1998. **37**(6): p. 792 - 795.

108.   Yoon, D.H., Lee, S.B., Yoo, K.-H., J, K., Lim, J.K., Aratani, N., Tsuda, A., Osuka, A., and Kim, D., *Electrical conduction through linear porphyrin arrays.* J American Chemical Society, 2003. **125**: p. 11062-11064.

109.   Kang, B.K., Aratani, N., Lim, J.K., Kim, D., Osuka, A., and Yoo, K.-H., *Length and temperature dependance of electrical conduction through dithiolated porphyrin arrays.* Chemical Physics Letters, 2005. **412**: p. 303-306.

110.   Tagami, K., Tsukada, M., Matsumoto, T., and Kawai, T., *Electronic transport properties of free-based tape-porphyrin molecular wires studied by self-consistent tight-binding calculations.* Phys. Rev. B, 2003. **67**: p. 245324.

111.   Lindsay, S.M. and Ratner, M.A., *Molecular Transport Junctions: Clearing Mists.* Advanced Materials, 2007. **19**(1): p. 23.

112.   Lee, K.H., Suh, Y., Lee, C., Hwang, Y.G., Koo, H.-J., Whangbo, M.-H., and J. Phys. Chem. B 2005, 15322., *Investigation of the scanning tunneling microscopy image, the stacking pattern, and the bias-voltage-dependent structural instability of 1,10'-phenanthroline molecules adsorbed on au(111) in terms of electronic structure calculations.* J. Phys. Chem. B, 2005. **109**(32): p. 15322.

113.   Sugimasa, M., Inukai, J., and Itaya, K., *Adlayer of 1,10-Phenanthroline on Cu(111) in acidic Solution: An in situ STM Study.* J. Electrochemical Soc, 2003. **150**: p. E266.

114.   McDermott, C.A., McDermott, M.T., Green, J.B., and Porter, M.D., *Structural Origins of the Surface Depressions at Alkanethiolate Monolayers on Au(111): a Scanning Tunneling and Atomic Force Microscopic Investigation.* J Physical Chemistry, 1995. **99**: p. 13257-13267.

115.   Zhang, J., Christensen, H.E.M., Ooi, B.L., and Ulstrup, J., *In situ STM Imaging and Direct Electrochemistry of Pyrococcus furiosus Ferredoxin Assembled on Thiolate-Modified Au(111) Surfaces.* Langmuir, 2004. **20**(23): p. 10200-10207.

116.   Pinheiro, L.S. and Temperini, M.L.A., *Coadsorption of 2-mercaptopyrimidine and 2,2'-bipyridine on Au(111) studied by scanning tunneling microscopy.* Surface Science, 1999. **441**: p. 45-52.

117.   Lipkowski, J. and Stolberg, L., *Molecular adsorption at gold and silver electrodes. ,* in *Adsorption of molecules at metal electrodes*, P.N. Ross, Editor. 1992, Vch, New York: New York. p. pp171.

118.   Bilic, A., Reimers, J.R., Hush, N.S., and Hafner, J., *Adsorption of ammonia on the gold (111) surface.* J Chemical Physics, 2002. **116**: p. 8981-7.

119.   Hébert, P., Le Rille, A., Zheng, W.Q., and Tadjeddine, A., *Vibrational Spectroscopic Study of the Adsorption of Pyridine at the Au(111)-Electrolyte Interface by In Situ Difference Frequency Generation.* J. Electroanal. Chem, 1998. **447**: p. 5-9.

120.   Kay, B.D., Lykke, K.R., Creighton, J.R., and Ward, S.J., *The influence of adsorbate–absorbate hydrogen bonding in molecular chemisorption: NH3, HF, and H2O on Au(111).* J Chemical Physics, 1989. **91**: p. 5120.

121.   Albrecht, T., Guckian, A., Ulstrup, J., and Vos, J.G., *Transistor-like Behavior of Transition Metal Complexes.* Nano Letters, 2005. **5**(7): p. 1451-1455.

122.   Andersson, K., Malmqvist, P.-Å., and Roos, B.O., *Second-order perturbation theory with a complete active space self-consistent field reference function.* J Chemical Physics, 1992. **96,**: p. 1218.

123.   Amouyal, E., Homsi, A., Chambron, J.C., and Sauvage, J.P., *Synthesis and study of a mixed-ligand ruthenium(II) complex in its ground and excited states: Bis(2,2'-bipyridine)(dipyrido[3,2-a:2',3'-c]phenazine-N^4N^5)ruthenium(II).* J. Chem. Soc. Dalton Trans., 1990: p. 1841-1845.

124. Chi, Q., Zhang, J., Friis, E.P., Andersen, J.E.T., and Ulstrup, J., *Electrochemistry of self-assembled monolayers of the blue copper protein Pseudomonas aeruginosa azurin on Au(111).* Electrochemistry Communications, 1999. **1**(3,4): p. 91-96.

125. Zhang, J., Chi, Q., Nielsen, J.U., Friis, E.P., Andersen, J.E.T., and Ulstrup, J., *Two-Dimensional Cysteine and Cystine Cluster Networks on Au(111) Disclosed by Voltammetry and in Situ Scanning Tunneling Microscopy.* Langmuir, 2000. **16**(18): p. 7229-7237.

126. Chi, Q., Zhang, J., Nielsen, J.U., Friis, E.P., Chorkendorff, I., Canters, G.W., Andersen, J.E.T., and Ulstrup, J., *Molecular Monolayers and Interfacial Electron Transfer of Pseudomonas aeruginosa Azurin on Au(111).* J American Chemical Society, 2000. **122**(17): p. 4047-4055.

127. Kresse, G. and Hafner, J., *Ab initio molecular dynamics for liquid metals'.* Phys. Rev. B, 1993. **47**: p. RC558.

128. Kresse, G. and Furthmüller, J., *Efficiency of ab-initio total energy calculations for metals and semiconductors using a plane-wave basis set.* Computational Materials Science, 1996. **6**: p. 15.

129. Vanderbilt, D., *Soft self-consistent pseudopotentials in a generalized eigenvalues formalism.* Phys. Rev. B, 1990. **41**: p. 7892-7895.

130. Kresse, G. and Hafner, J., *Norm-conserving and ultrasoft pseudopotentials for first-row and transition elements.* J. Phys. Condens. Matter, 1994. **6**: p. 8245.

131. Perdew, J.P. and Wang, Y., *Accurate and simple analytic representation of the electron-gas correlation energy.* Phys. Rev. B, 1992. **45**: p. 13244.

132. Bilic, A., Reimers, J.R., Hofer, W.A., and Hush, N.S., *Adsorption sites of maleic anhydride on Si(100) revisited: inter row versus intra row attachment.* Chemical Physics Letters, 2004. **385**: p. 341-4.

133. Hubbard, A.T., Ed, *The Handbook of Surface Imaging and Visualization* 1995, Boca Raton: CRC Press: Boca Raton.

134. Methfessel, A. and Paxton, A.T., *Special points for Brillouin-zone integrations.* Phys. Rev. B, 1989. **40**: p. 3616.

135. Neugebauer, J. and Scheffler, M., *Adsorbate-substrate and adsorbate-adsorbate interactions of Na and K adlayers on Al(111).* Phys. Rev. B, 1992. **46**(24): p. 16067 - 16080.

136. Frisch, M.J., Trucks, G.W., Schegal, H.B., Scuseria, G.E., Robb, M.A., Cheeseman, J.R., Montgomery, J.A., Vreven, T., Kudin, K.N., Burant, J.C., Millam, J.M., Tomasi, J., Barone, V., Mennuci, B., Cossi, M., Petersson, G.A., Nakatsuji, H., Hada, M., Ehara, M., Toyota, K., Fukuda, R., Hasegawa, J., Ishida, M., Nakajima, T., Honda, Y., Kitao, O., Nakai, H., Klene, M., Li, X., Knox, J.E., Hratchian, H.P., Cross, J.B., Adamo, C., Jaramillo, J., Gomperts, R., Stratmann, R.E., Yazyev, O., Austin, A.J., Cammi, R., Pomelli, C., Ochterski, J.W., Ayala, P.A., Morokuma, K., Voth, G.A., Salvador, P., Dannenberg, J.J., Zakrzewski, V.G., Dapprich, S., Daniels, A.D., Strain, M.C., Farkas, O., Malick, D.K., Rabuck, A.D., Raghavachari, K., Foresman, J.B., Ortiz, J.V., Cui, Q., Baboul, A.G., Clifford, S., Cioslowski, J., Stefanov, B.B., Liu, G., Liashenko, A., Piskorz, P., Komaromi, I., Martin, R.L., Fox, D.J., Keith, T., Al-Laham, M.A., Peng, C.Y., Nanayakkara, A., Challacombe, M., Gill, P.M.W., Johnson, B.G., Chen, W., Wong, M.W., Gonzalez, C., and Pople, J.A., *Gaussian 03, Revision b.02.* 2003, Pittsburgh PA: Gaussian, Inc.

137. Ahlrichs, R., Bär, M., Baron, H.P., and et al, *TURBOLMOLE-4.0.* 1997, University of Karlsruhe: Quantum Chemistry Group.

138. Hehre, W.J., Ditchfield, R., and Pople, J.A., *Self-consistent molecular orbital methods. XII. Further extensions of Gaussian-type basis sets for use in molecular*

orbital studies of organic molecules. J American Chemical Society, 1972. **56**: p. 2257-2261.

139. Andersson, K., Barysz, M., Bernhardsson, A., Blomberg, M.R.A., Cooper, D.L., Fleig, T., Fülscher, M.P., Gagliardi, C.d., Hess, B.A., Karlström, G., Lindh, R., Malmqvist, P.-Å., Neogrády, P., Olsen, J., Roos, B.O., Sadlej, A.J., Schütz, M., Schimmelpfennig, B., Seijo, L., Serrano-Andrés, L., Siegbahn, P.E.M., Stålring, J., Thorsteinsson, T., Veryazov, V., and Widmark, P.-O., *Molcas Version 5*. 2000, Lund: University of Lund.

140. Hay, P.J. and Wadt, W.R., *Abinitio Effective Core Potentials for Molecular Calculations - Potentials for K to Au Including the Outermost Core Orbitals.* J Chemical Physics, 1985. **82**: p. 270-283.

141. Boys, S.F. and Bernardi, F., *The calculation of small molecular interactions by the differences of separate total energies. Some procedures with reduced errors.* Mol. Phys, 1970. **19**(4): p. 553 - 566.

142. Tao, N.J. and Lindsay, S.M., Surface Science Letters, 1992. **274**: p. L546.

143. Esplandiu, M.J., Carot, M.L., Cometto, F.P., Macagno, V.A., and Patrito, E.M., *Electrochemical STM investigation of 1,8-octanedithiol monolayers on Au(111).* Surface Science, 2005. **600**(1): p. 155-172.

144. Cometto, F.P., Paredes-Olivera, P., Macagno, V.A., and Patrito, E.M., *Density Functional Theory Study of the Adsorption of Alkanethiols on Cu(111), Ag(111), and Au(111) in the Low and High Coverage Regimes.* J. Phys. Chem. B, 2005. **109**(46): p. 21737-21748.

145. Lambropoulos, N.A., Reimers, J.R., and Hush, N.S., *Accurate computational methods for gold ligand complexes: application to AuNH$_3$.* J Chemical Physics, 2002. **116**: p. 10277-86.

146. Xi, M., Yang, M.X., Jo, S.K., Bent, B.E., and Stevens, P., *Benzene adsorption on Cu(111): Formation of a stable bilayer.* J Chemical Physics, 1994. **101**(10): p. 9122.

147. Lukes, S., Vollmer, S., Witte, G., and Wöll, C., *Adsorption of acenes on flat and vicinal Cu(111) surfaces: Step induced formation of lateral order* J Chemical Physics, 2001. **114**(22): p. 10123-10130.

148. Rogers, B.L., Shapter, J.G., and Ford, M.J., *Ab Initio Study of Benzene Absorption on the Cu(110) Surface and Simulation of STM Images.* Surface Science, 2004. **548**: p. 29.

149. Wang, Y., Hush, N.S., and Reimers, J.R., *Simulation of the Au(111) (22 x sqrt3) surface reconstruction.* Phys. Rev. B, 2007. **75**: p. 233416-1-4.

150. Kim, Y.-T. and Bard, A.J., *Imaging and Etching of Self-Assembled n-Octadecanethiol Layers on Gold with the Scanning Tunnelling Microscope.* Langmuir, 1992. **8**: p. 1096-1102.

151. Bilic, A., Reimers, J.R., and Hush, N.S., *The structure, energetics, and nature of the chemical bonding of phenylthiol adsorbed on the Au(111) surface: implications for density-functional calculations of molecular-electronic conduction.* J Chemical Physics, 2005. **122**: p. 094708-1-15.

152. Basch, H., Cohen, R., and Ratner M, A., *Interface Geometry and Molecular Junction Conductance: Geometric Fluctuation and Stochastic Switching.* Nano Letters, 2005. **5**(9): p. 1668-1675.

153. Wackerbarth, H., Marie, R., Grubb, M., Zhang, J., Hansen, A.G., Chorkendorff, I., Christensen, C.B.V., Boisen, A., and Ulstrup, J., *Thiol- and disulfide-modified oligonucleotide monolayer structures on polycrystalline and single-crystal Au(111) surfaces.* J. Solid State Electrochemistry, 2004. **8**(7): p. 474-481.

154.   Darling, S.B., Rosenbaum, A.W., Wang, Y., and Sibener, S.J., *"Coexistence of the (23×√3) Au(111) Reconstruction and a Striped Phase Self-Assembled Monolayer"*. Langmuir, 2002. **18**(20): p. 7462-7468.

155.   Kondoh, H., Iwasaki, M., Shimada, T., Amemiya, K., Yokoyama, T., and Ohta, T., *Adsorption of Tholates to Singly Coordinated Sites on Au(111) Evidenced by Photoelectron Diffraction*. Phys. Rev. Lett., 2003. **90**(6): p. 066102-1-4.

156.   Roper, M.G., Skegg, M.P., Fisher, C.J., Lee, J.J., Dhanak, V.R., Woodruff, D.P., and Jones, R.G., *Atop adsorption site of sulphur head groups in gold-thiolate self-assembled monolayers*. Chemical Physics Letters, 2004. **389**(1-3): p. 87-91.

157.   Molina, L.M. and Hammer, B., *Thoretical study of thiol-induced reconstructions on the Au(111) surface*. Chemical Physics Letters, 2002. **360**: p. 264-271.

158.   Wang, Y., Reimers, J.R., and Hush, N.S., *alleviate reconstruction*. J American Chemical Society, 2007. **submitted JA0743442**.

159.   McNaught, A.D., Wilkinson, A., Nic, M., Jirat, J., Kosata, B., and Jenkins, A., *IUPAC. Compendium of Chemical Terminology, 2nd ed. (the "Gold Book")*. 1997, Blackwell Scientific Publications: Oxford.

160.   Batista, R.J.C., Ordejon, P., Chacham, H., and Artacho, E., *Resistive and rectifying effects of pulling gold atoms at thiol-gold nano-contacts*. Condensed Matter arXiv:, 2006: p. 0609558 v1.

161.   Grigoriev, A., Skoldberg, J., and Wendin, G., *Critical Roles of metal-molecule contact in electron transport through molecular-wire junctions*. Phys. Rev. B, 2006. **74**: p. 045401.

162.   Haiss, W., Nickolls, C., van Zalingre, H., Higgins, S., Bethell, D., and Schiffrin, D.J., *Measurement of single molecule conductivity using the spontaneous formation of molecular wires*. Phys. Chem. Chem. Phys, 2004. **2004**(6): p. 4330-4337.

163.   Romaner, L., Heimel, G., Gruber, M., Bredas, J.-L., and Zojer, E., *Stretching and breaking of a molecular junction*. small, 2006. **2**(12): p. 1468-1475.

164.   Vericat, C., Vela, M.E., Benitez, G.A., Gago, J.A.M., Torrelles, X., and Salvarezza, R.C., *Surface Characterisation of sulfur and Alkanethiol self-assembled monolayers on Au(111)*. J. Phys. Chem.: Condensed Matter, 2006. **18**: p. R867-R900.

165.   Gilman, Y., Allen, P.B., and Hybertsen, M.S., *Density-functional study of adsorption of isocyanides on the gold (111) surface*. Condensed Matter arXiv:, 2006. **0411320**(v2): p. 0411320.

166.   Wang, Y., Hush, N.S., and Reimers, J.R., *Formation of gold-methanethiyl self-assembled monolayers*. Phys. Rev. B, 2007. **75**(23): p. 233416.

167.   Yu, M., Bovet, N., Satterley, C., Bengio, S., Lovelock, K.R.J., Milligan, P.K., Jones, R.G., Woodruff, D.P., and Dhanak, V.R., *True nature of an archetypical self-assembly system: mobile Au-thiolate species on Au(111)*. Phys. Rev. Lett., 2006. **97**: p. 166102.

168.   Maksymovych, P., Sorescu, D.C., and Yates, J.T.J., *Gold-adatom-mediated bonding in self-assembled short chain alkanethiolate species on the Au(111) surface*. Phys. Rev. Lett., 2006. **97**: p. 146103.

169.   Müller, K.-H., *Effect of the atomic configuration of gold electrodes on the electrical conduction of alkanedithiol molecules*. Phys. Rev. B, 2006. **73**: p. 045403.

170.   Wohlthat, S., Pauly, F., and Reimers, J.R., *The conduction properties of α,ω-diaminoalkanes and hydrazine bridging gold electrodes*. Chemical Physics Letters (article in press, accepted), 2008.

171.   Poncharal, P., Berger, C., Yi, Y., Wang, Z.L., and de Heer, W.A., *Room Temperature Ballistic Conduction in Carbon Nanotubes*. J. Phys. Chem. B, 2002. **106**(47): p. 12104 - 12118.

172.   Andersson, K., Blomberg, M.R.A., Fülscher, M.P., Karlstöm, G., Lundh, R.,
        Malmqvist, P.-A., Neogrády, P., Olsen, J., Roos, B.O., Sadlej, A.J., and et al,
        MOLCAS Version 5. 2002, Lund, Sweden: Lund University.

END

(blank page)

Chapter 7 APPENDICES

7-0 Appendices

The following sections include data, images, tables and figures which would detract from the narrative of the thesis if included in their relevant sections, nevertheless add somewhat to the body of work, or are necessary for some reason, or give fuller explanation.

7-1 APPENDIX 1: Plan and design of laboratory.

The following plans are referred to in Section 1.3.2 on page 1-20 above.

The author's plan and sketches used in designing the *nanoPrep Lab* at Sydney University are presented below in Figure Appendix-1-67 and Figure Appendix-1-68:
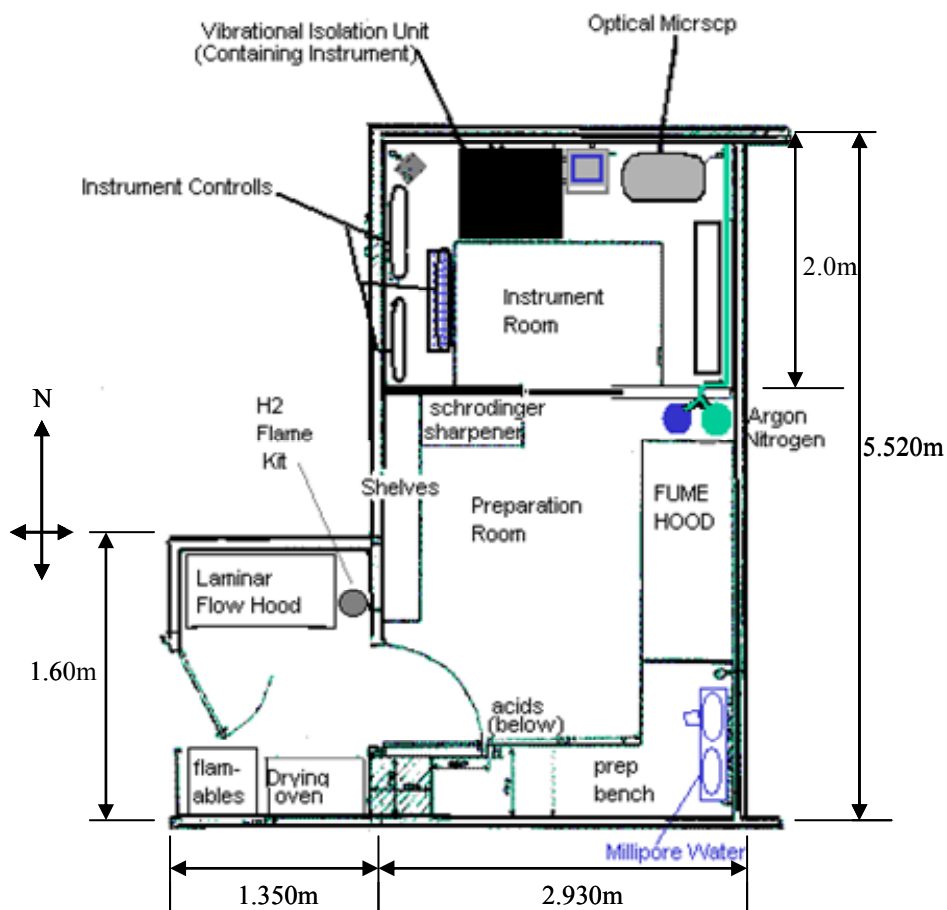
Figure Appendix-1-67: Plan view of the design of the *nanoPrep Lab* at Sydney University.
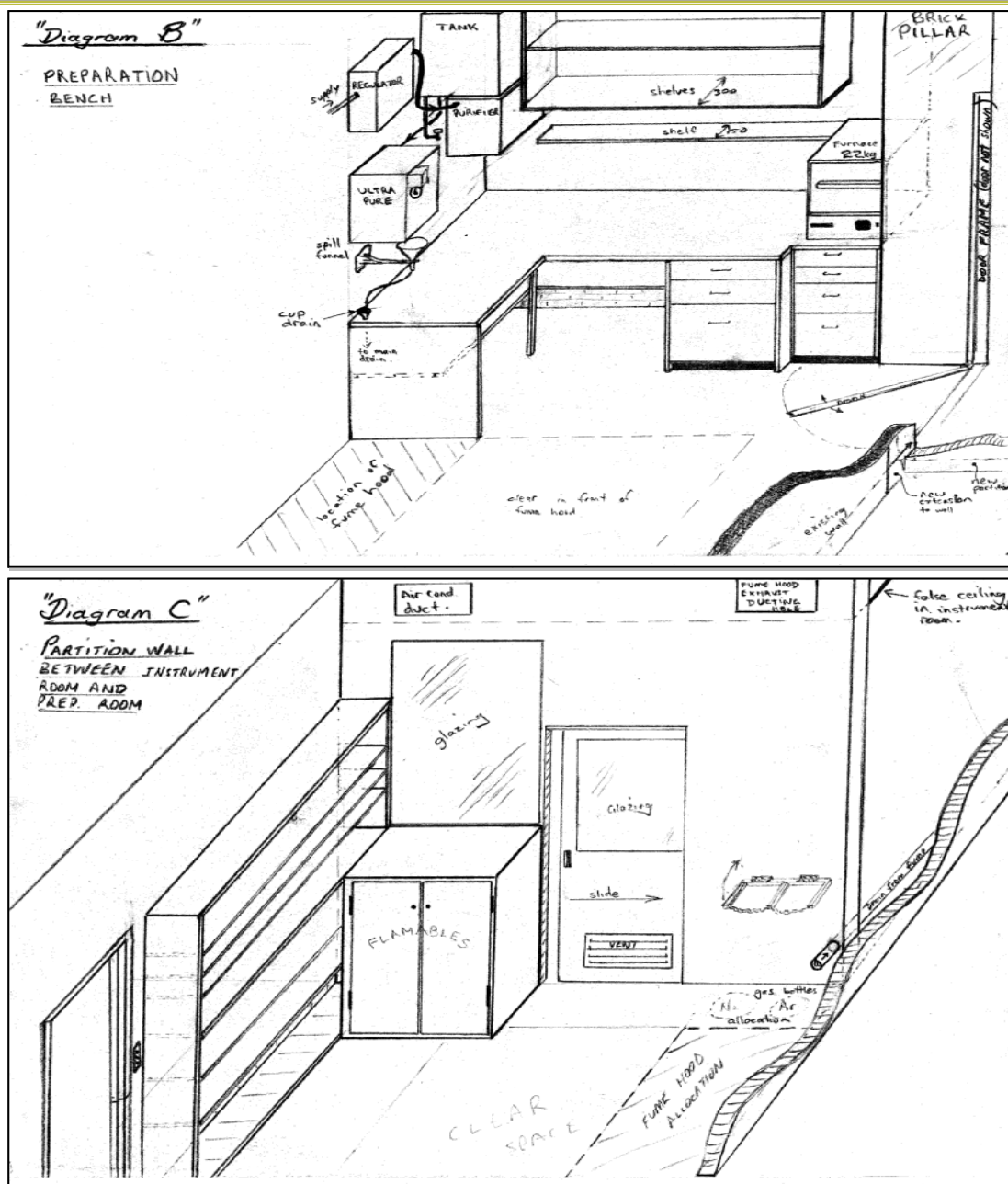
Figure Appendix-1-68: Two sketches of the interior of the *nanoPrep Lab* design showing the preparation area looking south (upper) and looking north (lower), drawn as a guide to construction.

7-2 APPENDIX 2: Supporting Information for Chapter 2

7.2.1 Additional histograms for pyrazine

Pyrazine in phenyloctane – All *Group B* by analysis *Method 1*.
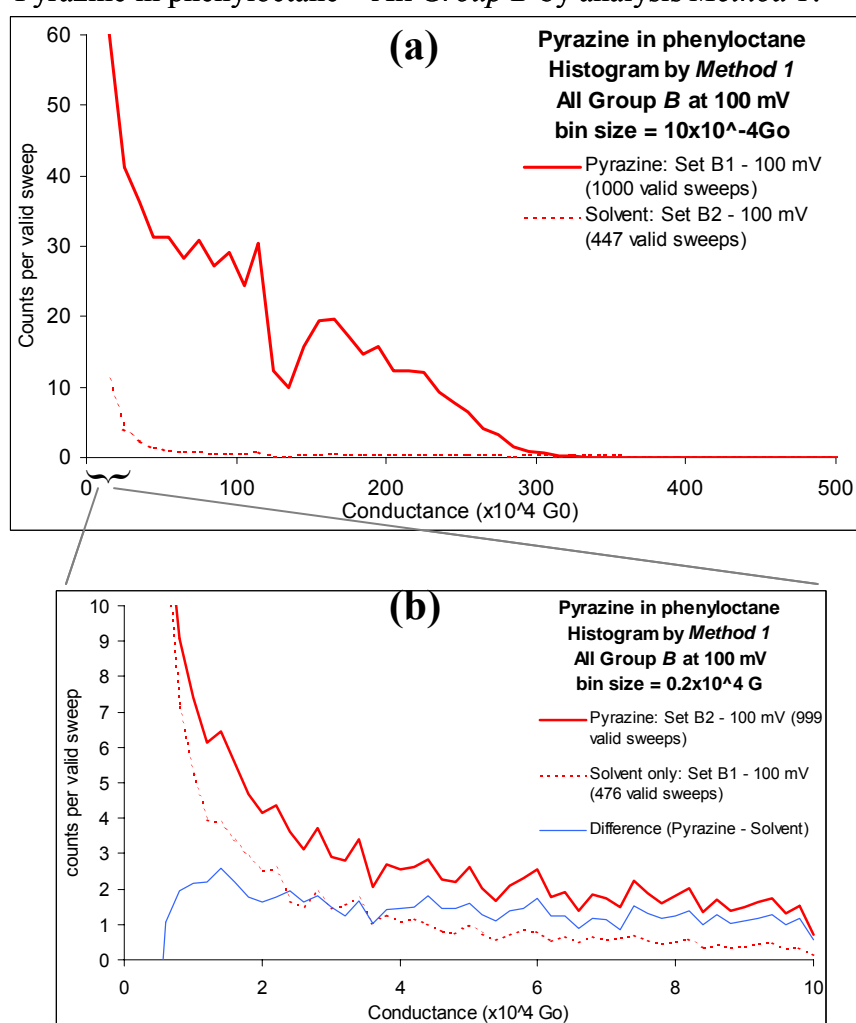
Figure Appendix 2-69: Pyrazine, *Group B*, Analysis *Method 1*. **(a)** High Range (bin size = 10 x 10^{-4} G_0); **(b)** Low Range (bin size = 0.2 x 10^{-4} G_0). Both graphs show pyrazine and solvent histograms, and Graph (b) also shows the difference between the two. For the range from 0.6 to 300 x 10^{-4} G_0 the pyrazine count is greater than the solvent count. The solvent is *phenyloctane*.

Pyrazine in phenyloctane – All *Group C* by analysis *Method 1*.
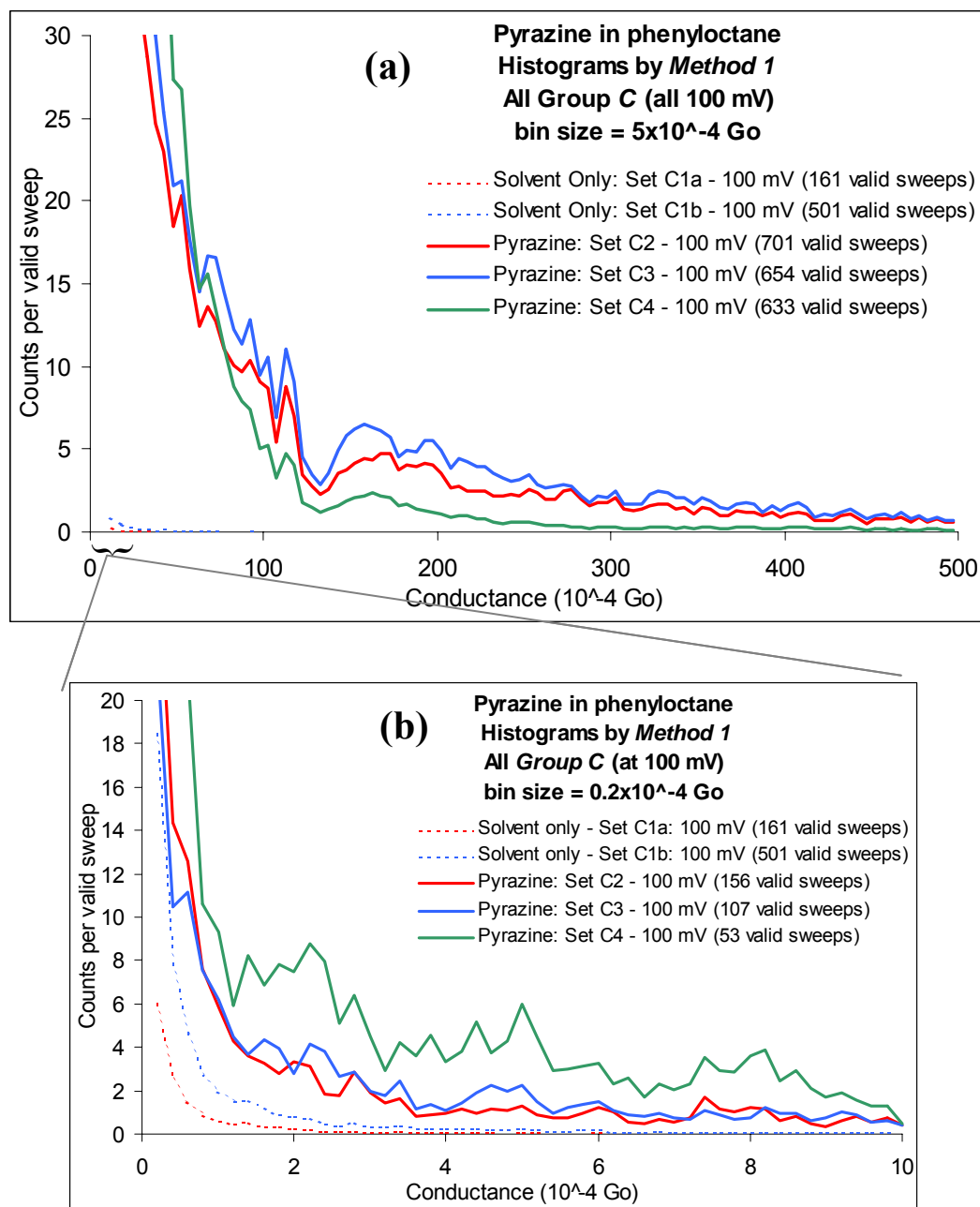
Figure Appendix-2-70: Pyrazine, *Group C*, Analysis *Method 1*. **(a)** High Range (bin size = 5 x 10^{-4} G_0); **(b)** Low Range (bin size = 0.2 x 10^{-4} G_0). Both graphs show pyrazine and solvent histograms. For the range from approximately 0.4 to more than 500 x 10^{-4} G_0 the pyrazine count is greater than the solvent count. The solvent is *phenyloctane*.

Pyrazine in toluene – All *Group D* by analysis *Method 1*.
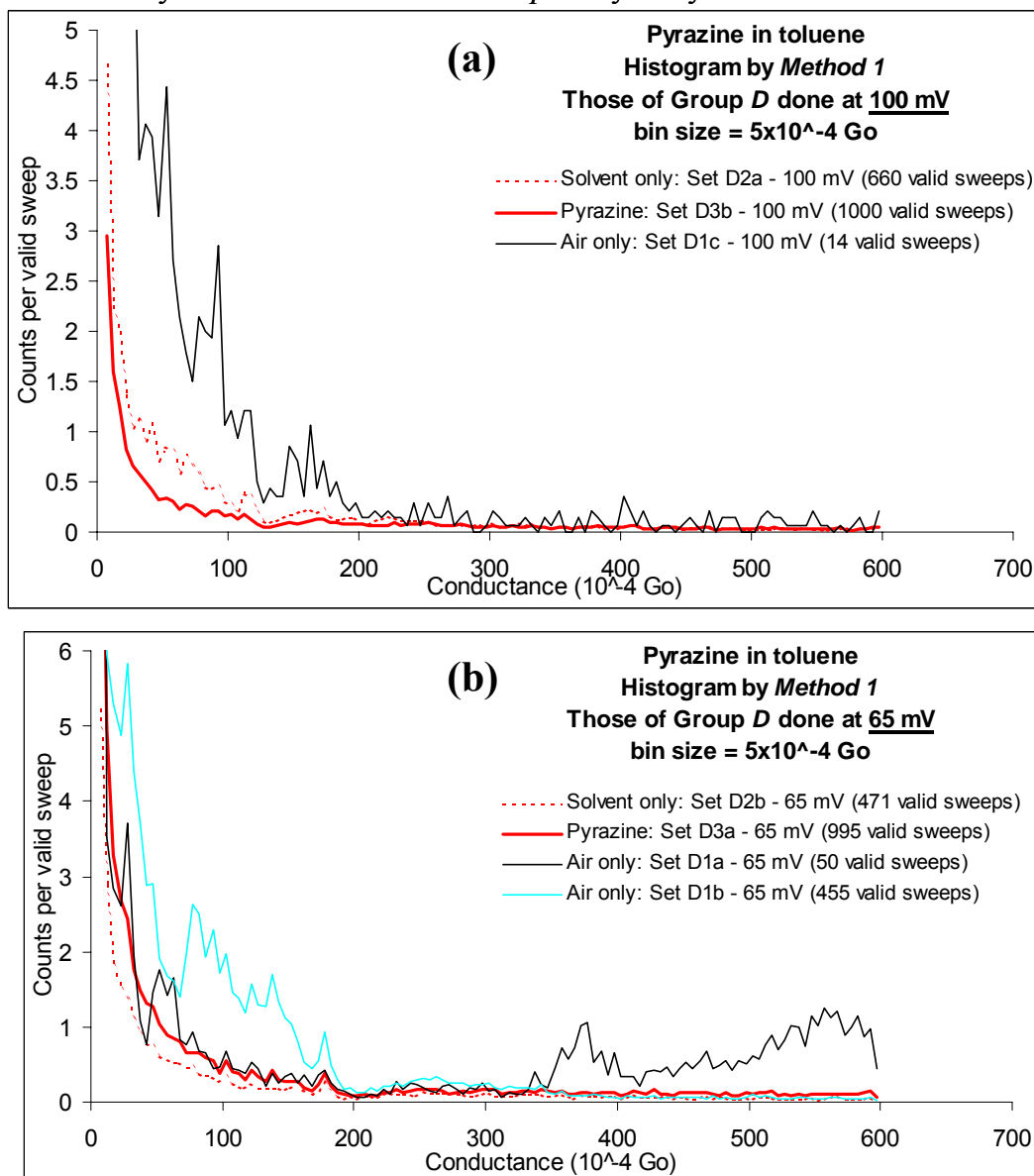
Figure Appendix-2-71: Pyrazine, *Group D*, Analysis *Method 1*. **(a)** Sets done at 100 mV; **(b)** Sets done at 65 mV. Both graphs examine a high range (bin size = 5 x 10^{-4} G_0) and show pyrazine, solvent and air histograms. There is no significant difference between the air, solvent and pyrazine sets of sweeps over the whole conductance range at both voltages (the two "Air only" sets which appear to differ have small data sets: *Set D1c* with 14 sweeps and *Set D1a* with 50 sweeps). A lower range has not been shown (as in other pyrazine groups) however the results are similar: air, solvent and pyrazine histograms do not differ significantly. The solvent is *toluene*.

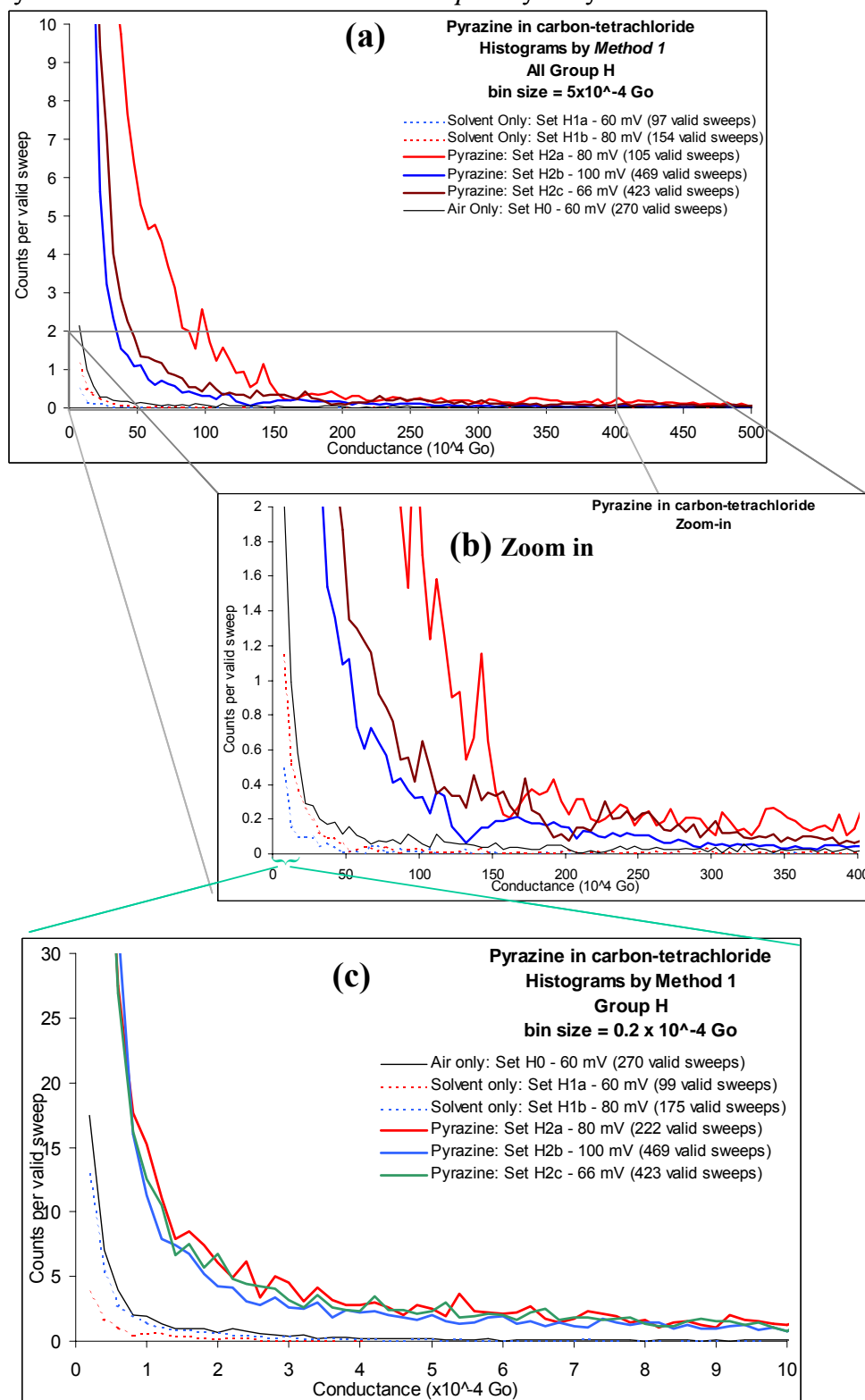Pyrazine in toluene – All *Group E* by analysis *Method 1*.
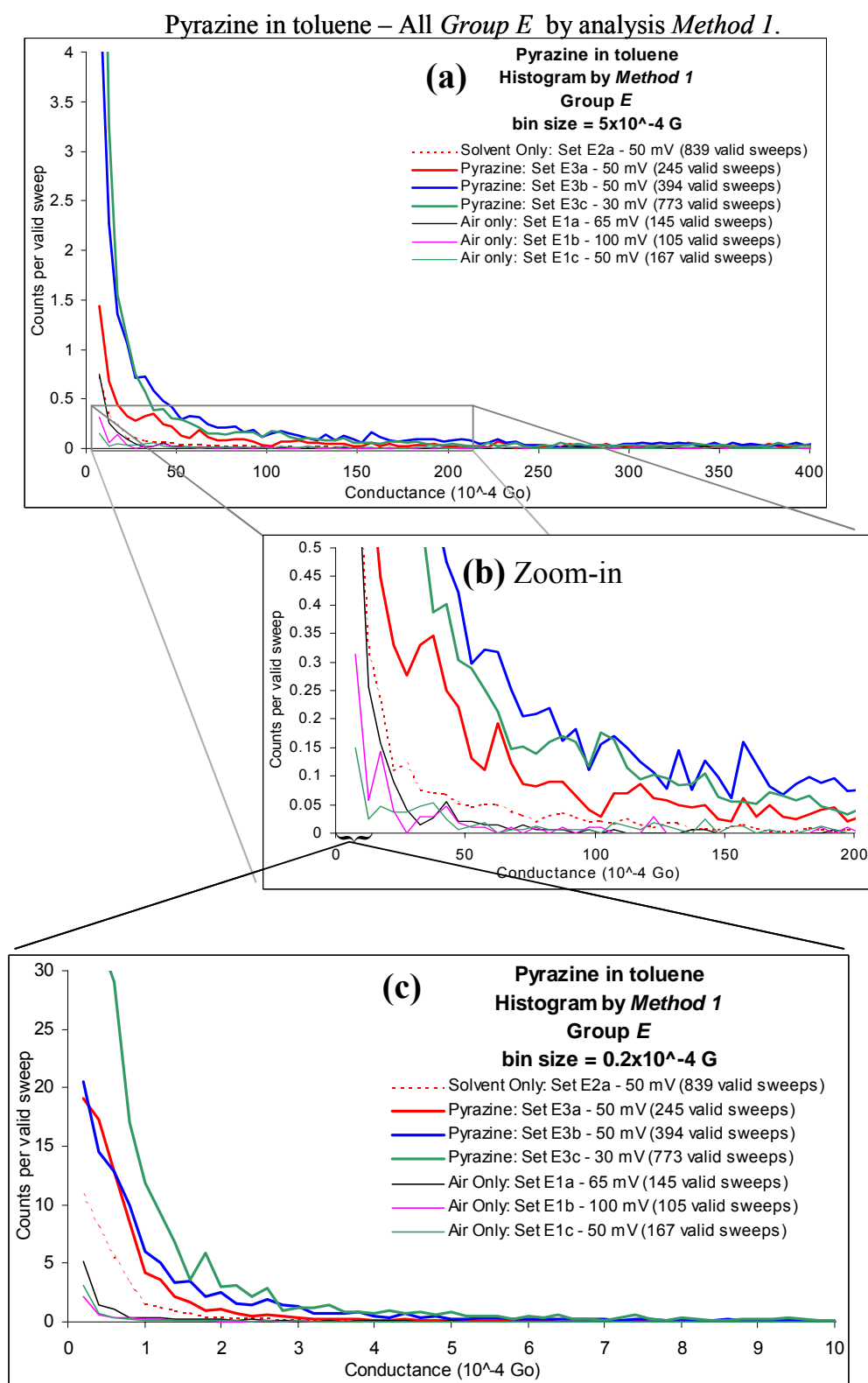
Figure Appendix-2-72: Pyrazine, *Group E,* Analysis *Method 1*. **(a)** All Sets (bin size = 5 x 10^{-4} G_0); **(b)** Zoom-in of graph (a); **(c)** All Sets, lower conductance range (bin size = 0.2 x 10^{-4} G_0). All 3 graphs show pyrazine, solvent and air histograms. Pyrazine histograms have a slightly higher count that the solvent histogram, which is slightly higher again than the air histograms over almost the entire conductance range shown (regardless of voltage). The solvent is *toluene*.

Pyrazine in aqueous solution – All *Group G* by analysis *Method 1*.
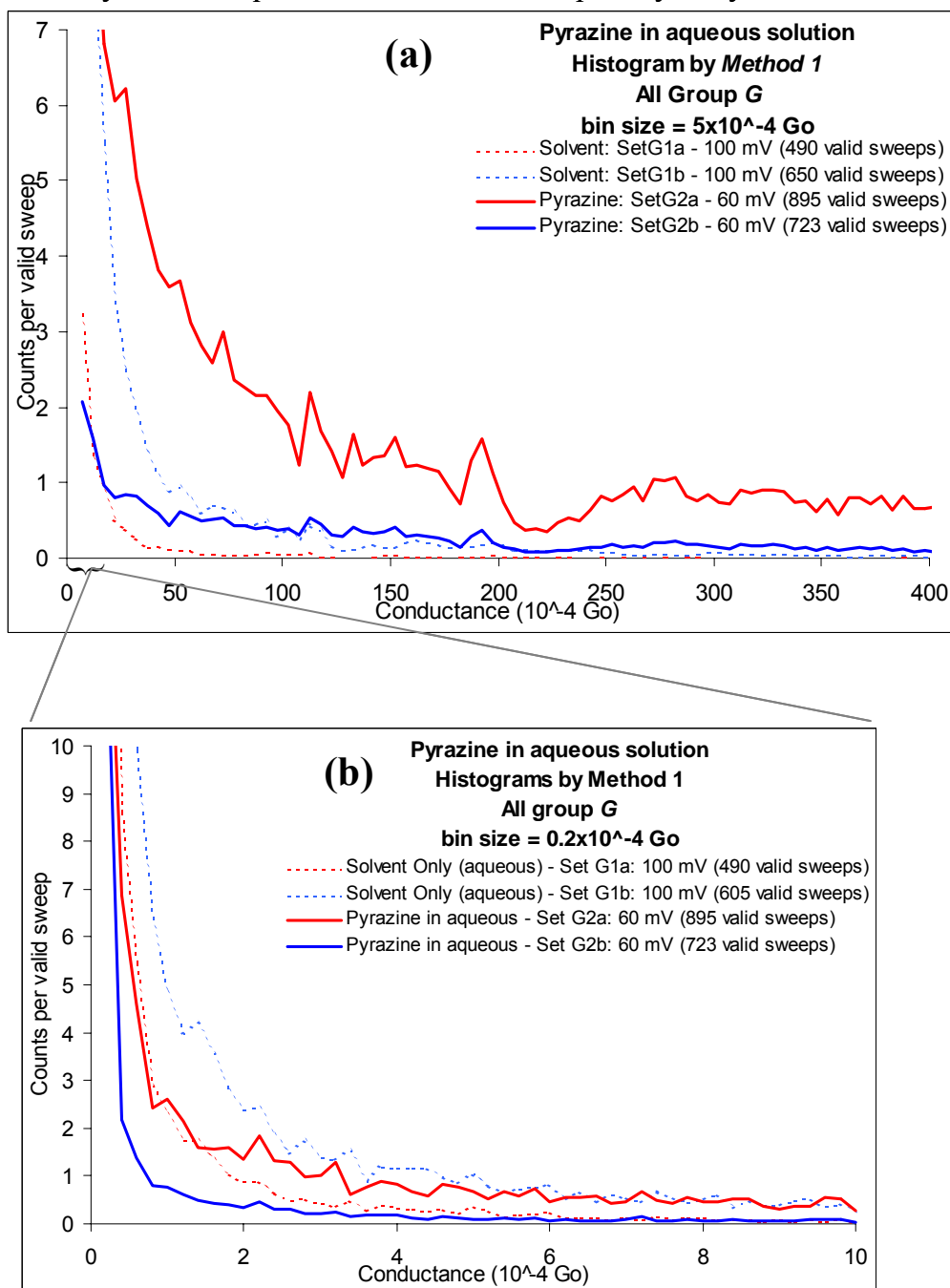
Figure Appendix-2-73: Pyrazine, *Group G*, Analysis *Method 1*. **(a)** *All Sets* (bin size = 5 x 10^{-4} G_0); **(b)** *All Sets*, lower conductance range (bin size = 0.2 x 10^{-4} G_0). Both graphs show pyrazine (at 60 mV) and solvent (at 100 mV) histograms. Only one of the pyrazine histograms shows a significant difference to the solvent histograms: *Set G2a* has a higher count than both solvent sets for conductance values above 30x10^{-4} G_0. Pyrazine *Set G2b* is similar to both solvent sets over the same range. In the lower conductance ranges, Graph (b), there is no significant difference between the pyrazine and the solvent sets. The solvent is *20mM Sodiumperchlorate in pure "Millipore" water.*

Pyrazine in carbon-tetrachloride – All *Group H* by analysis *Method 1*.

Figure Appendix-2-74: Pyrazine, *Group H*, Analysis *Method 1*. **(a)** All Sets (bin size = 5 x 10^{-4} G_0); **(b)** Zoom-in of graph (a); **(c)** All Sets, lower conductance range (bin size = 0.2 x 10^{-4} G_0). All 3 graphs show pyrazine, solvent and air histograms. Pyrazine histograms have a higher count that the solvent and air histograms over almost the entire conductance range shown (regardless of voltage). The solvent is *carbontetrachloride.*

PYRAZINE IN PHENYLOCTANE EXPERIMENTS AT CSIRO

(a) All *Group K* with <u>gain=5</u> in gold conduction range, by analysis *Method 1*.
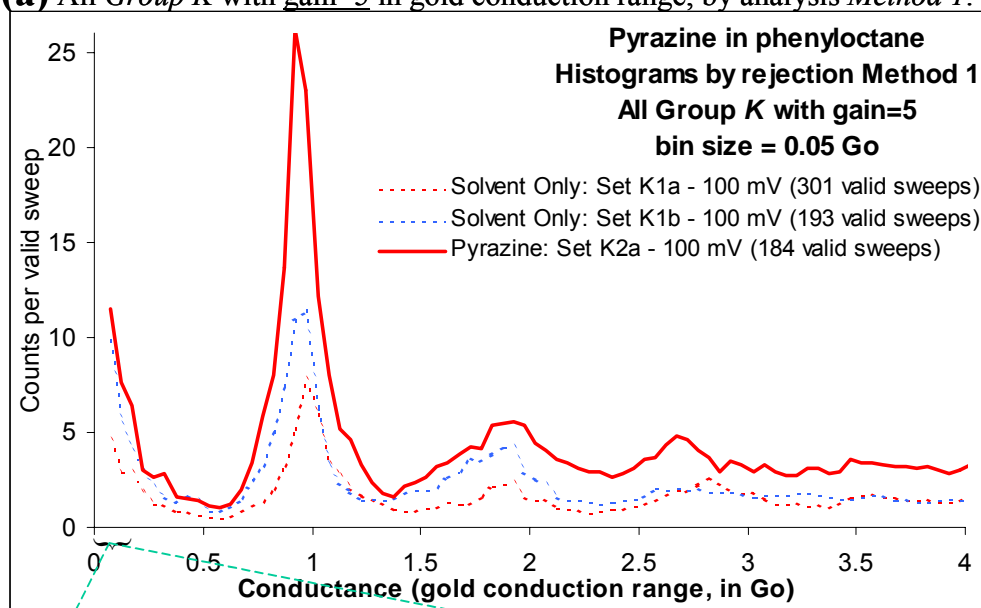
(b) All *Group K* with <u>gain=7</u>, by analysis *Method 1*.

(range of next graph)
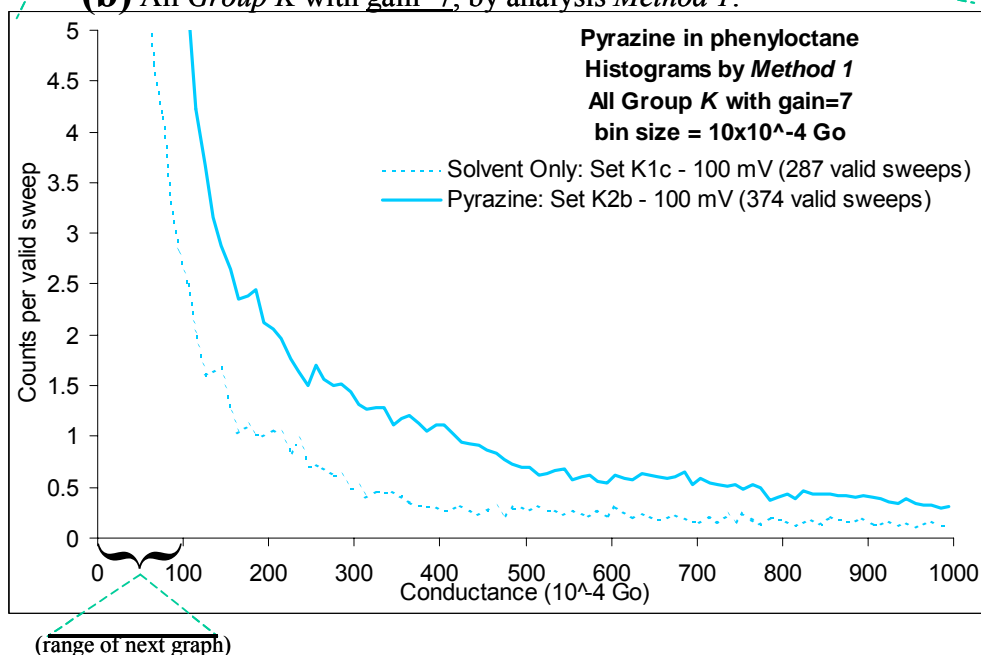
Figure Appendix-2-75: Pyrazine, *Group K*, Analysis *Method 1*.
(a) Sets with gain=5, *Sets K1a and K1b* (solvent) and *Set K2a* (pyrazine). The pyrazine histogram has significantly higher count than the solvent sets around 1.0, 1.8 and 2.7 G_0, and by comparison is similar at other values.

(b) Sets with gain=7, *Set K1c* (solvent) and *Set K2b* (pyrazine). The pyrazine histogram has a higher count than solvent set for all conductance values in the range, particularly below 400 x 10^{-4} G_0.
NOTE: The two graphs do not overlap, they are of different data sets. The solvent is *phenyloctane*.

PYRAZINE IN PHENYLOCTANE EXPERIMENTS AT CSIRO

(a) All *Group K* with <u>gain=8</u>, by analysis *Method 1*.
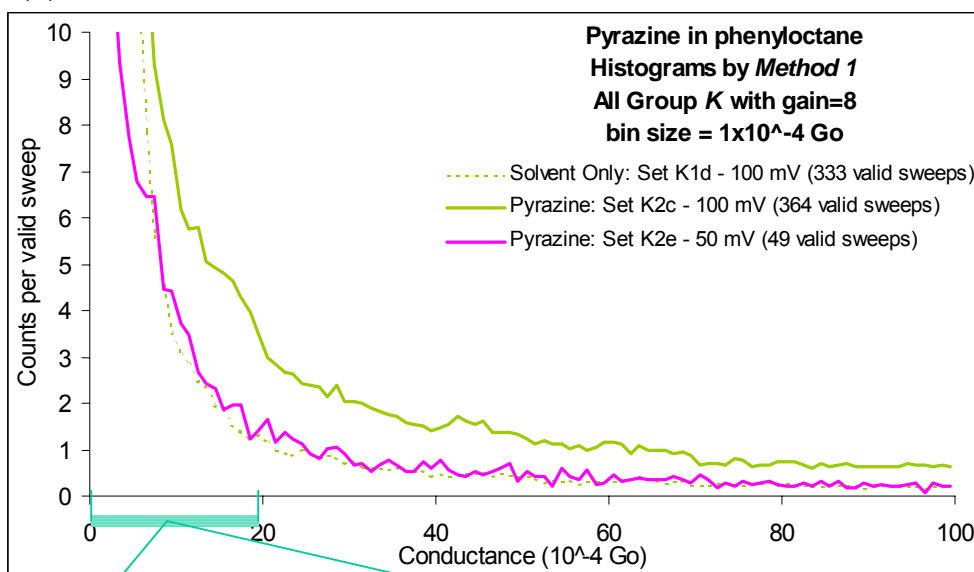
(b) All *Group K* with <u>gain=9</u>, by analysis *Method 1*.
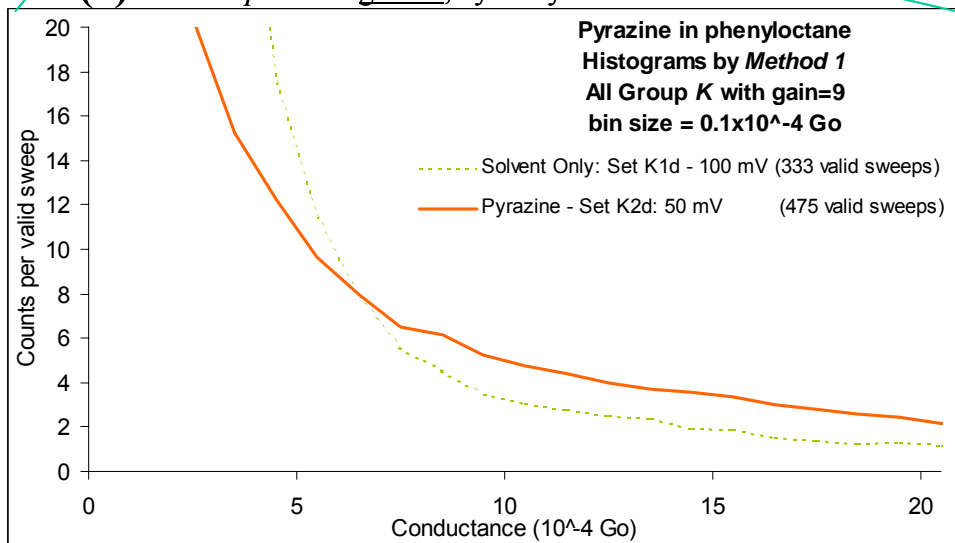

Figure Appendix-2-76: Pyrazine, *Group K*, Analysis *Method 1*.
(a) Sets with gain=8, *Set K1d* (solvent) and *Sets K2c and K2e* (pyrazine). The pyrazine histogram constructed at 100 mV has significantly higher counts than the solvent set from approximately 10×10^{-4} G_0 upwards. The pyrazine histogram constructed at 65 mV is not significantly different than the 100 mV solvent histogram.
(b) Set with gain=9, *Set K2d* (pyrazine) (Note: For comparison purposes the graph also shows the extension of *Set K1d* solvent only, which has gain=8) The pyrazine histogram has no peaks but significantly higher counts than the solvent set from approximately 15×10^{-4} G_0 upwards.
NOTE: The graphs do not overlap, they are of different data sets. The solvent is *phenyloctane*.

7.2.2   Additional histograms for bis-appended porphyrin

All break-junction experiments on bis-appended porphyrins were conducted at CSIRO, where a linear amplifier was used with a pre-set gain to select the appropriate current range (see Section 2.3.1.2). Each of the following five pages show histograms generated by analysis *Methods 1* and *2*. NOTE: For histograms constructed by analysis *Method 2*, "counts per valid sweeps" is equal to (counts as per *Method 2*) divided by (number of valid sweeps as per *Method 1*).
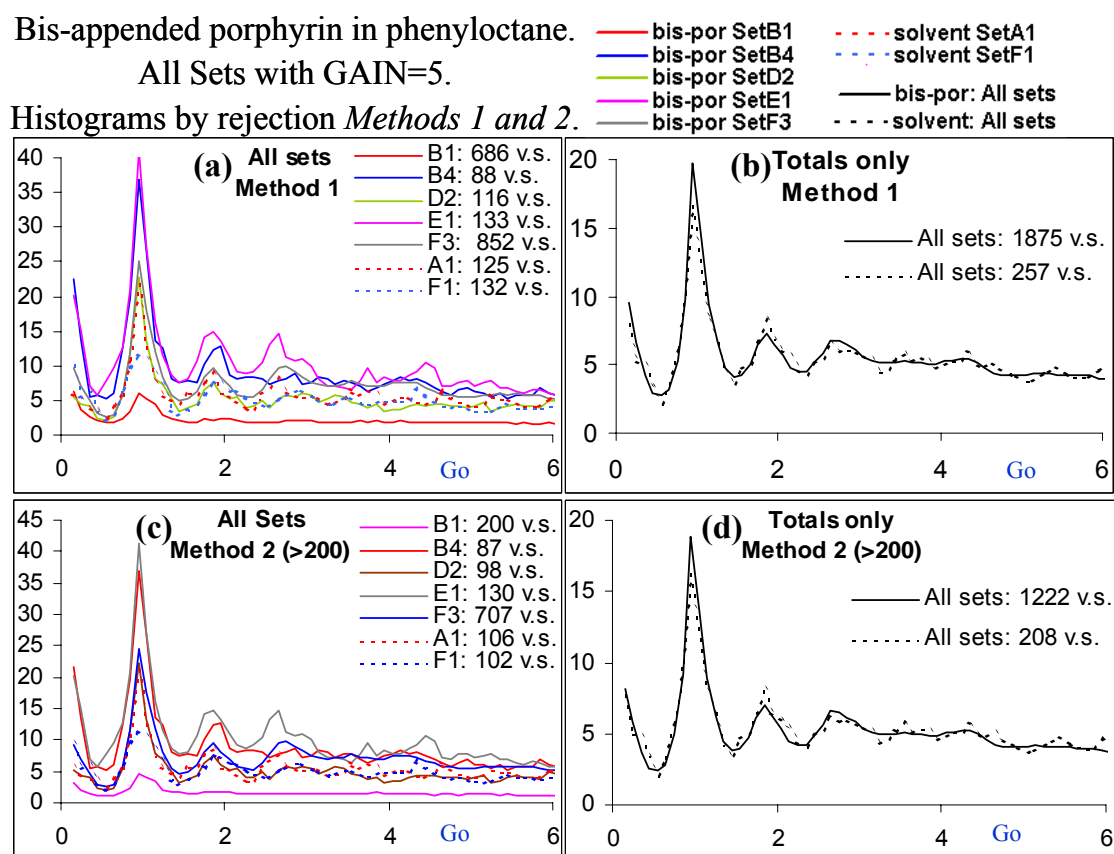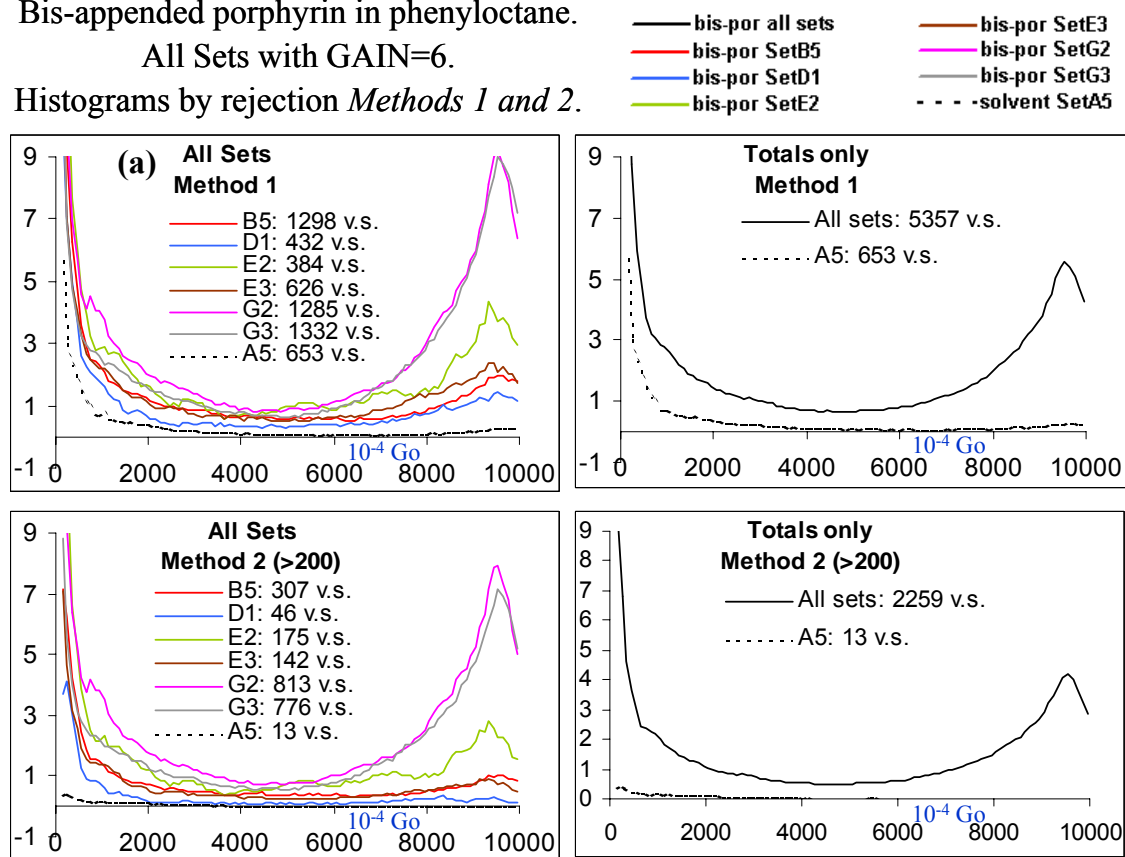

Figure Appendix-2-77: Histograms of bis-appended porphyrin in phenyloctane sets with gain=5 by *Method 1* (upper graphs) and *Method 2* (lower graphs), and showing individual sets (left) and weighted total of individual sets (right). Full lines are bis-por and dotted lines are solvent only. Bias = 100 mV. The vertical axis is counts per valid sweep, the horizontal axis is conductance in **G$_0$**. v.s. = valid sweeps.

Bis-appended porphyrin in phenyloctane.
All Sets with GAIN=6.
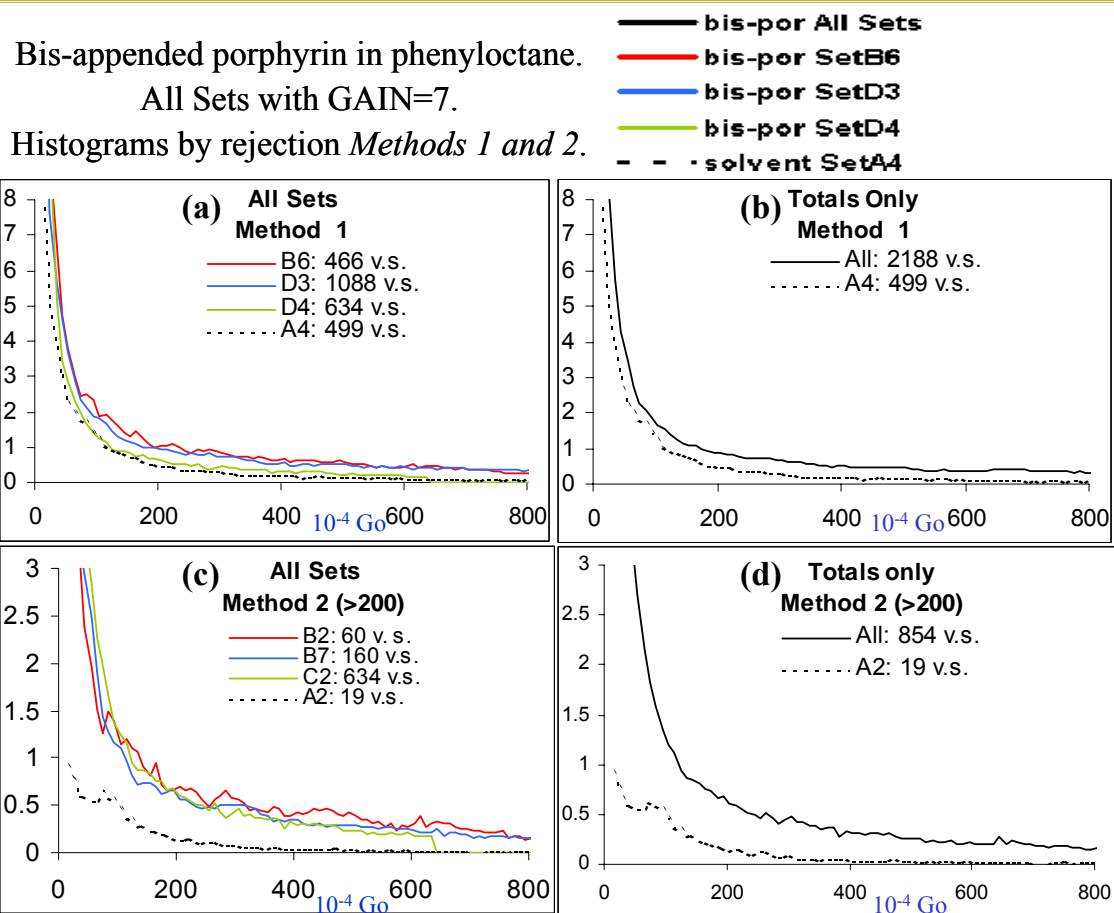Histograms by rejection *Methods 1 and 2*.

Figure Appendix-2-78: Histograms of bis-appended porphyrin in phenyloctane sets with gain=6 by *Method 1* (upper graphs) and *Method 2* (lower graphs), and showing individual sets (left) and weighted total of individual sets (right). Full lines are bis-por and dotted lines are solvent only. Bias = 100 mV. The vertical axis is counts per valid sweep, the horizontal axis is conductance in 10^{-4} G_0. v.s. = valid sweeps.

Bis-appended porphyrin in phenyloctane.
All Sets with GAIN=7.
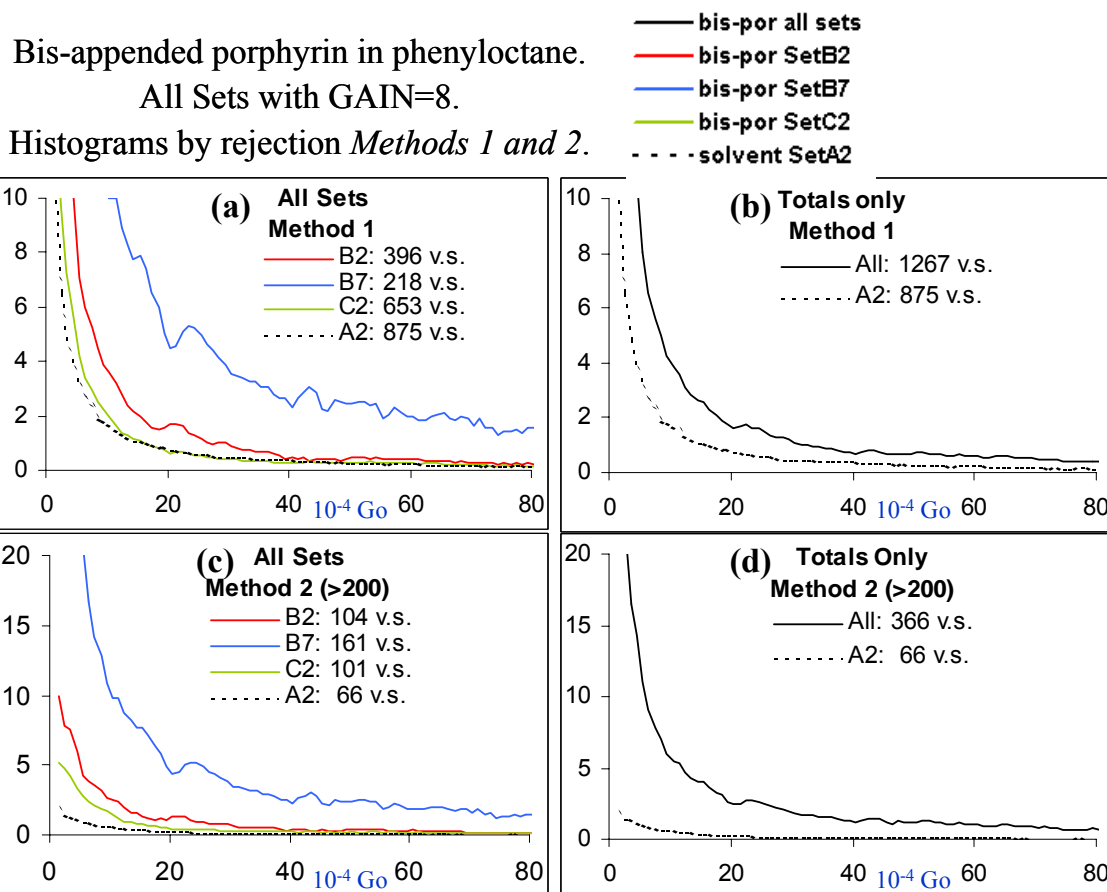Histograms by rejection *Methods 1 and 2*.

Figure Appendix-2-79: Histograms of bis-appended porphyrin in phenyloctane sets with gain=7 by *Method 1* (upper graphs) and *Method 2* (lower graphs), and showing individual sets (left) and weighted total of individual sets (right). Full lines are bis-por and dotted lines are solvent only. Bias = 100 mV. The vertical axis is counts per valid sweep, the horizontal axis is conductance in **$10^{-4} G_0$**. v.s. = valid sweeps.

Bis-appended porphyrin in phenyloctane.
All Sets with GAIN=8.
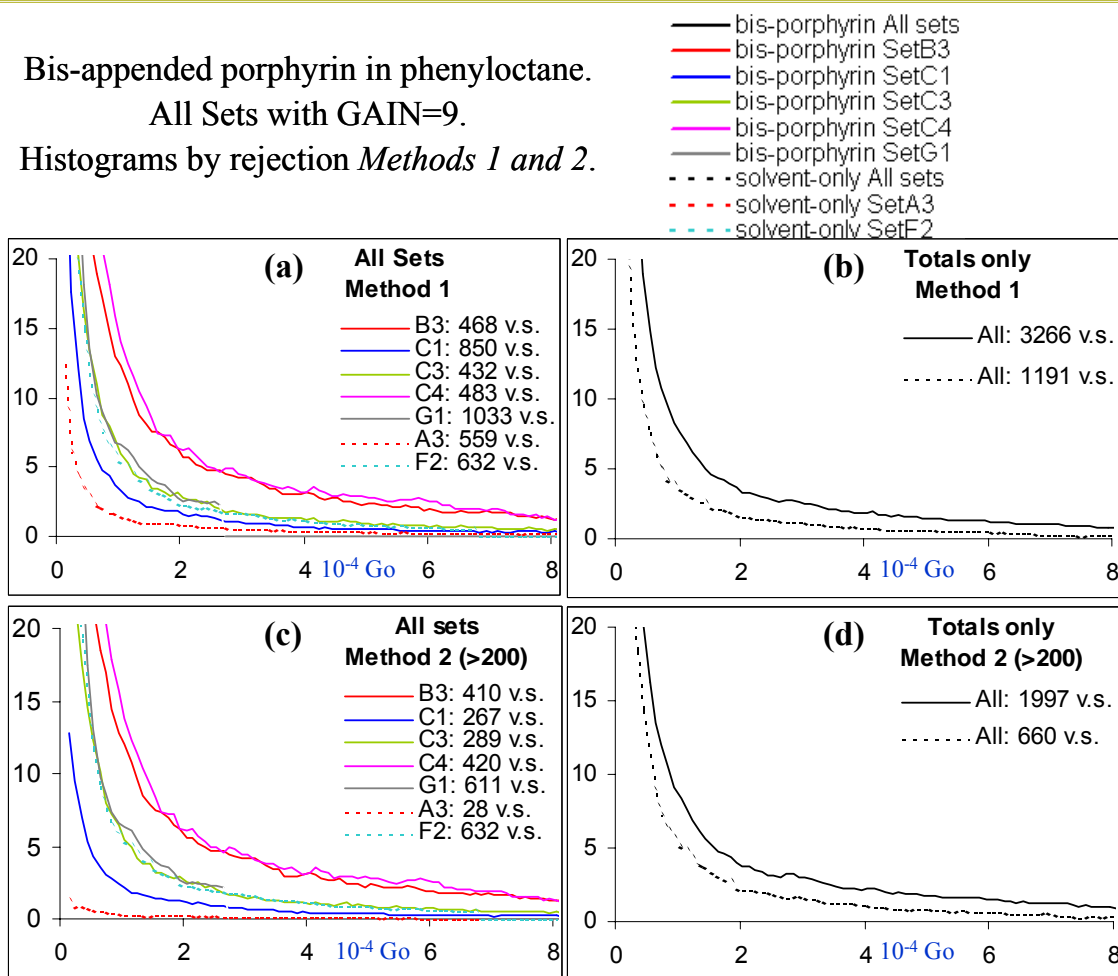Histograms by rejection *Methods 1 and 2*.

Figure Appendix-2-80: Histograms of bis-appended porphyrin in phenyloctane sets with gain=8 by *Method 1* (upper graphs) and *Method 2* (lower graphs), and showing individual sets (left) and weighted total of individual sets (right). Full lines are bis-por and dotted lines are solvent only. Bias = 100 mV. The vertical axis is counts per valid sweep, the horizontal axis is conductance in 10^{-4} **G$_0$**. v.s. = valid sweeps.

Bis-appended porphyrin in phenyloctane.
All Sets with GAIN=9.
Histograms by rejection *Methods 1 and 2*.

Figure Appendix-2-81: Histograms of bis-appended porphyrin in phenyloctane sets with gain=9 by *Method 1* (upper graphs) and *Method 2* (lower graphs), and showing individual sets (left) and weighted total of individual sets (right). Full lines are bis-por and dotted lines are solvent only. Bias = 100 mV. The vertical axis is counts per valid sweep, the horizontal axis is conductance in 10^{-4} G_0. v.s. = valid sweeps.

7-3 APPENDIX 3: Supporting Information for Chapter 3

Further STM images of the bare gold surface and the phenanthroline monolayers formed on it are provided (Sections 7.3.1 to 7.3.3). The images were taken over a 10-hour period, with the images presented in Figure 3-48 being obtained towards the end of this period. The drift of the STM tip reduced continually during this period as the instrument stability increased.

Cyclic voltammograms are presented which help establish the monolayer coverage of 1,10-phenanthroline on gold (Section 7.3.4) and the oxidation potential of gold (Section 7.3.5).

The *Bibliography* allows limited space for each reference. Full versions of certain abbreviated references are shown (Section 7.3.6).

7.3.1   STM images of Au(111).

Figure Appendix-3-82 shows two successive scans of the bare surface, each scan imaged in the opposite direction: the gold ($\sqrt{3} \times 22$) R30° reconstruction is readily identified in these images, and the image drift, even at this early stage of experimentation, is clearly identified. The observed spacing between the reconstruction lines is used to calibrate the instrument.
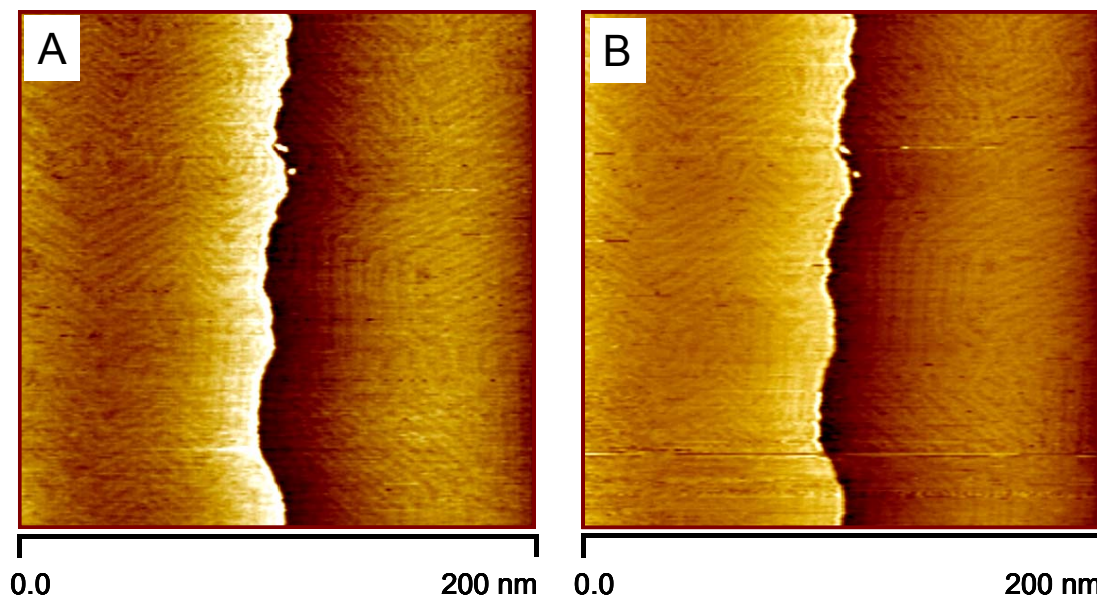
STM images of the bare Au(111) surface.

Figure Appendix-3-82: Two successive current images of the bare Au(111) surface, scanned in alternate directions, obtained in constant-current scanning mode at a set-point current I_t=0.15 nA, nA, V_{bias} = -0.1 V and E_w= -0.6 V vs. SCE.

7.3.2   STM images of phenanthroline on Au(111) *in-situ*.

Soon after addition of the phenanthroline into solution, monolayers appeared on the

surface as short chains of stacked phenanthrolines whose structure evolved rapidly with time

as shown in Figure Appendix-3-83.

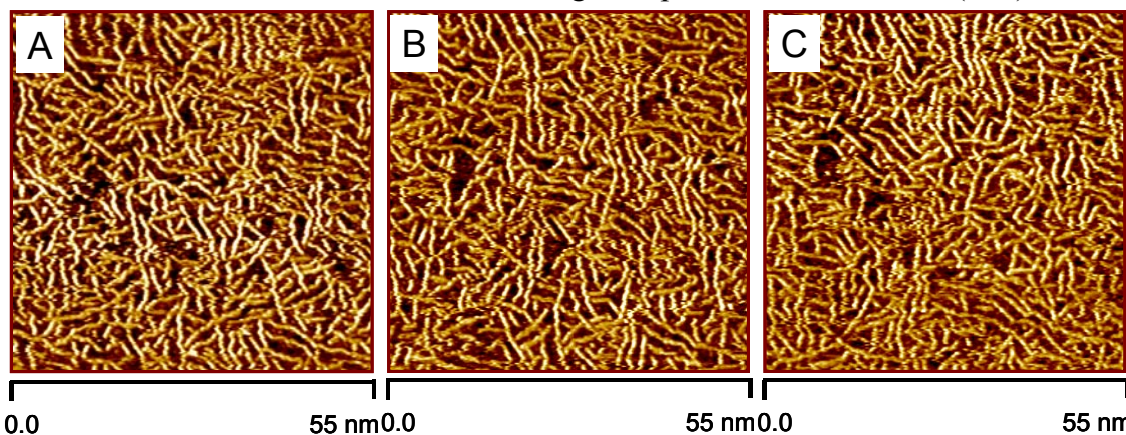Three successive STM current images of phenanthroline on Au(111).

Figure Appendix-3-83: Three successive current images of phenanthroline on Au(111) surface during the early stages of monolayer formation, scanned in alternate directions, obtained in constant-current scanning mode at a set-point current of It = 0.60 nA, Vbias=-0.55 V and Ew = 0.03 V vs. SCE.

However, the long-range order increased gradually, with typical long-time configurations displayed in Figure 3-50. Occasionally, extended regions of high order are seen such as those displayed in Figure Appendix-3-85. High-resolution images indicate a surface coverage of 2.5±0.1 molecules nm^{-2} as expected for a (4 × 4) lattice. The images shown in Figure Appendix-3-85 were obtained using feedback conditions (I = 5.0 and P = 5.0) typical of constant-current STM scanning, but do not achieve the molecular resolution needed to identify the molecular orientation. To obtain the resolution required for this identification, the feedback was reduced (I = 0.6 and P = 1.0) [known as "constant height" mode] to produce the images in Figure Appendix-3-84. Although this reduction results in contamination of the otherwise pure differential current-deviation image, the resolution increased sufficiently to observe the molecular plane and hence allow the full characterization of the structures given in Table 3-16.

Successive STM images of phenanthroline on gold(111)
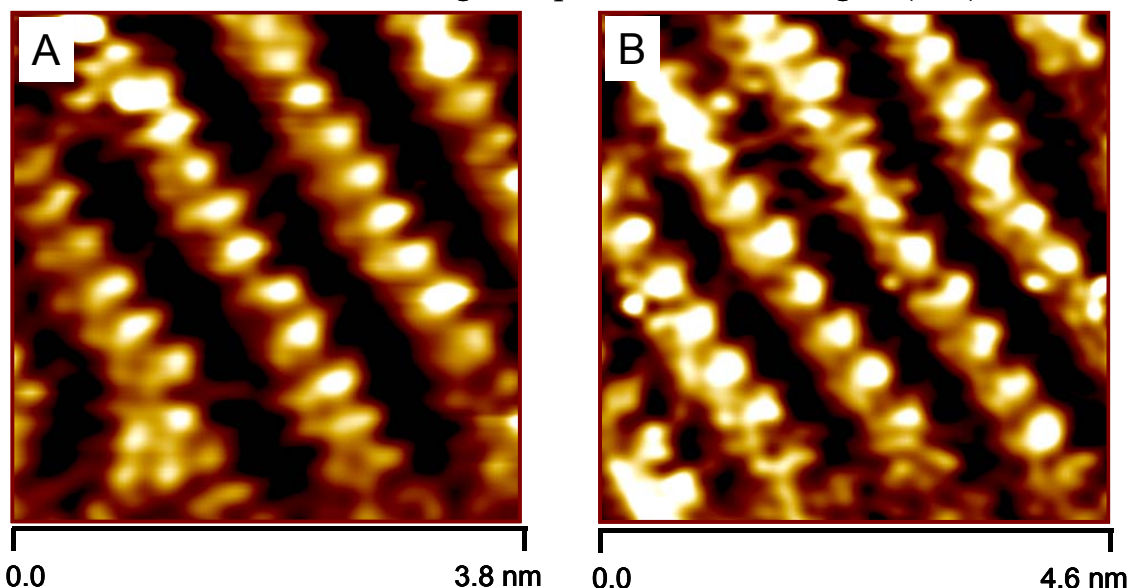

| 0.0 | 3.8 nm | 0.0 | 4.6 nm |

Figure Appendix-3-84: Two successive current images of phenanthroline on gold(111) surface, scanned in alternate directions, obtained in constant-height scanning mode I_t = 0.85 nA, V_{bias} = -0.607 V and E_W = 0.08 V vs. SCE.

Precise definitions of the quantities used in performing the in-situ STM experiments are:

1. V_{bias} = difference in potential between the tip and the working electrode.

2. I_t is set-point tunnelling current from tip to substrate (in these experiments, the substrate is also the working electrode).

3. E_w is the difference in potential between the working electrode and the reference electrode. It has been corrected to be Vs SCE.

4. E_t is the difference in potential between the tip and the reference electrode.

7.3.3   Images depicting long-range order.

Three images of the monolayer formed in-situ are shown in Figure Appendix-3-85 (and superimposed upon each other in Figure Appendix-3-86). The upper of these images is that shown in Fig. 2 while the following images show regions of the surface that overlap in the vertical direction. The blue lines show the boundaries between different regions on the surface, while the number of PHEN molecules per chain in each region (in order 9, 3, 6, 3, 6, 3, 3) is indicated.

STM Scans of overlapping
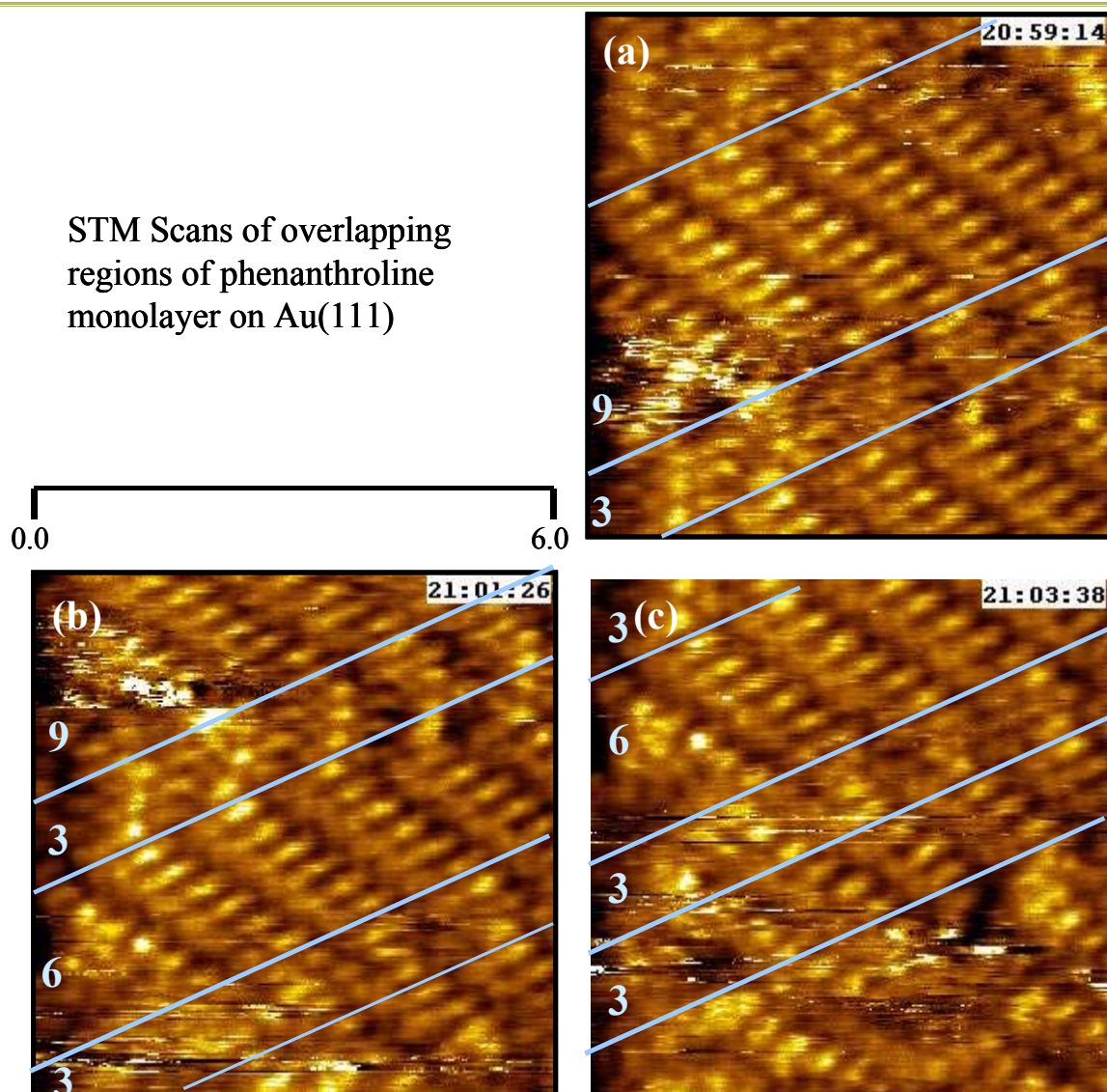regions of phenanthroline
monolayer on Au(111)

Figure Appendix-3-85: Scans of overlapping regions of PHEN on Au(111), each of 6x6 nm. Because of a drift in the downward direction, the instrument images slightly different but overlapping regions. Imaged in aqueous 0.05 M $KClO_4$; tip bias = -0.60 V (vs. the Au(111) substrate), set-point current = 0.85 nA (maximum deviation ± 10%), and sample potential = 0.08 V vs. SCE. The way these images overlap is shown in Figure Appendix-3-86.
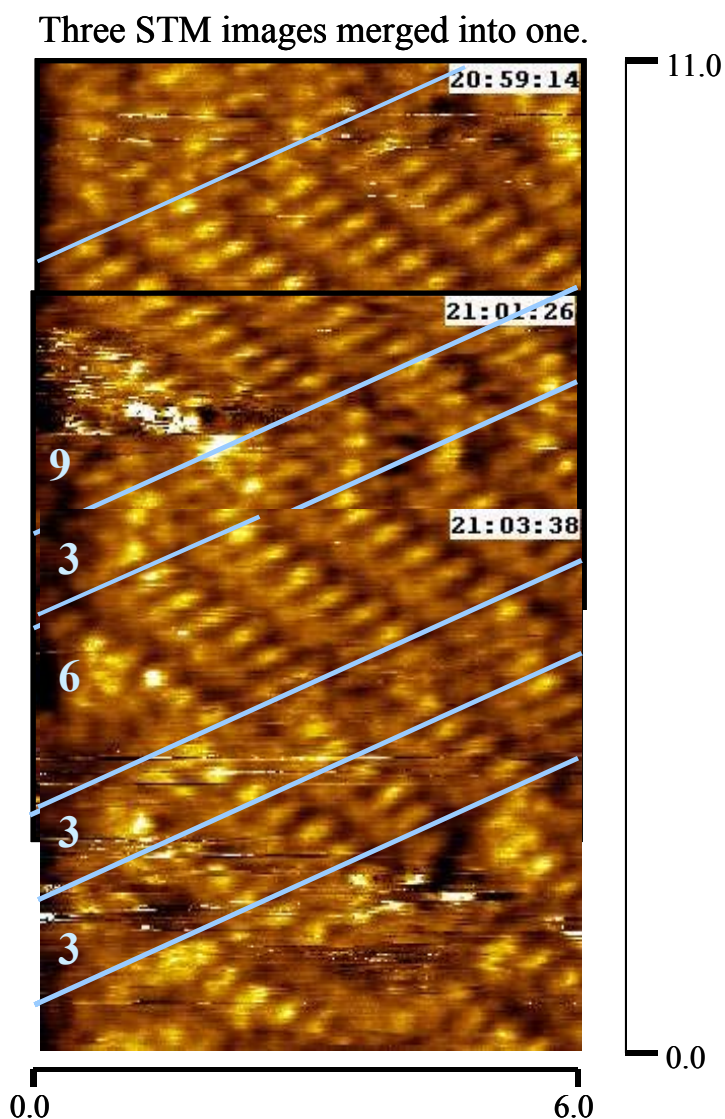
Three STM images merged into one.

Figure Appendix-3-86: The same three images of Figure Appendix-3-85 superimposed on each other where they would overlap, to present a single representation of an extended region of the surface 6x11 nm.

7.3.4   Reductive desorption of the PHEN monolayer.

The results of reductive desorption experiments performed for PHEN on a gold electrode in 0.1M $KClO_4$/water solution are described in Figure Appendix-3-87 and Figure Appendix-3-88. The monolayer was formed by exposing the electrode to a solution of 0.36 mM PHEN in water at pH 6.5. This was then washed with water to remove excess PHEN. Figure Appendix-3-87 shows two cyclic voltammograms taken with a time interval of 1 minute, each consisting of four cyclic sweeps of the potential. For each scan the scan rate

was 5000 mV s^{-1}. The first scan commenced at point A on Figure Appendix-3-87 and reveals the reductive desorption of the PHEN monolayer at point B, -1.15 V. Subsequent cycles of this scan reveal no further reductive desorption current. After standing, the cycles were continued from point D, showing a small change E in the signal at −1.15 V. This first cycle was used as a baseline for the reductive desorption shown at point B, and the differences between the first cycles of the two scans, followed by linear baseline correction, is displayed in Figure 3-49 and used to determine the monolayer coverage.
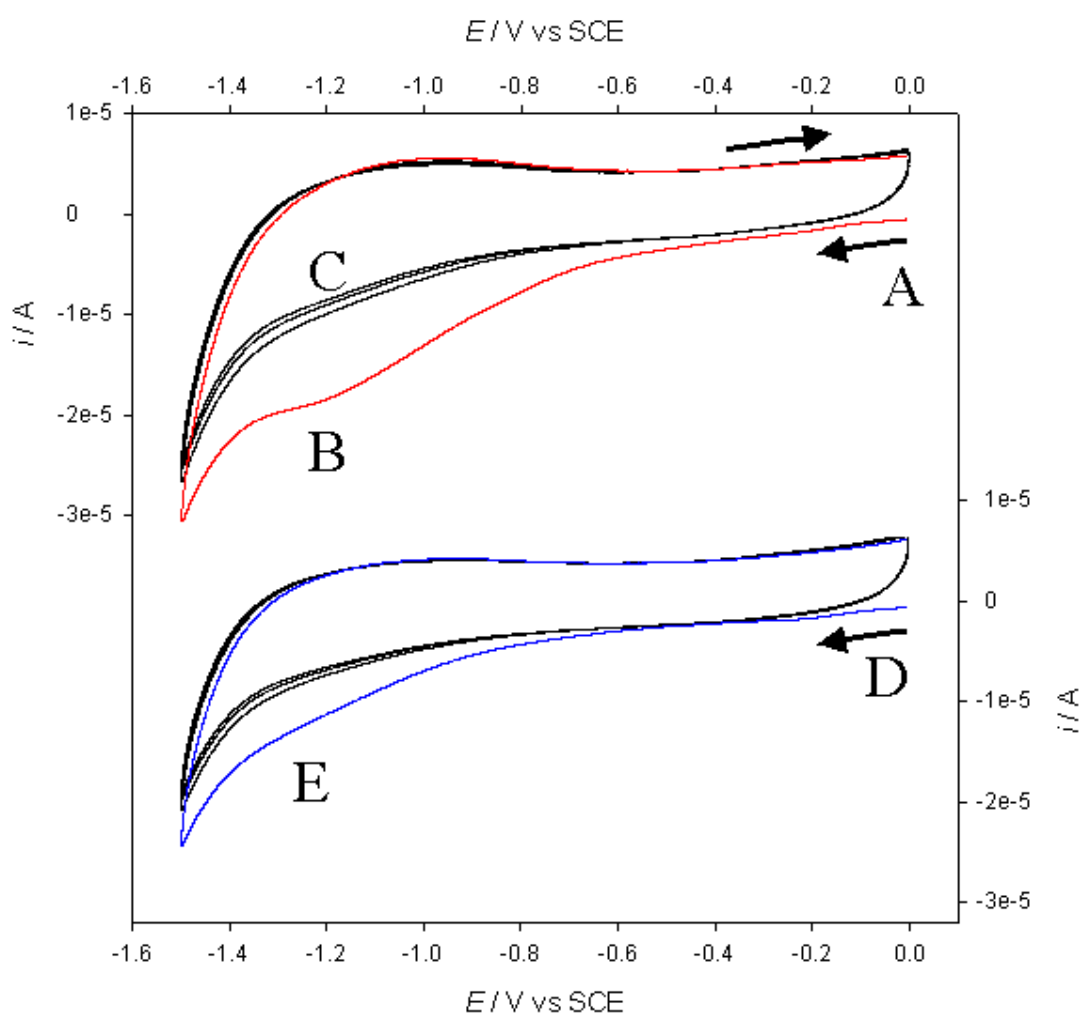

Figure Appendix-3-87: Reductive desorption cyclic voltammetry of PHEN from a gold electrode in 0.1M KClO4/water solution showing 2 scans one minute apart each of 4 cycles The scans start at points A (first scan) and D (second scan), the PHEN layer is removed at stage B.

7.3.5   Oxidation of gold surfaces containing PHEN monolayers.

The stability of a gold electrode in presence of 1,10-phenanthroline was tested by performing a series of electrochemical experiments where the switch potential, E_λ, was gradually shifted further and further into the anodic potential range. 1,10-phenanthroline has the ability of stabilizing oxidized gold atoms and thereby lower the potential needed for gold oxidation. From Figure Appendix-3-88 it can however be seen that no current flow i.e. no oxidation of gold is observed as long as the applied potential does not exceed ca. 0.9V.
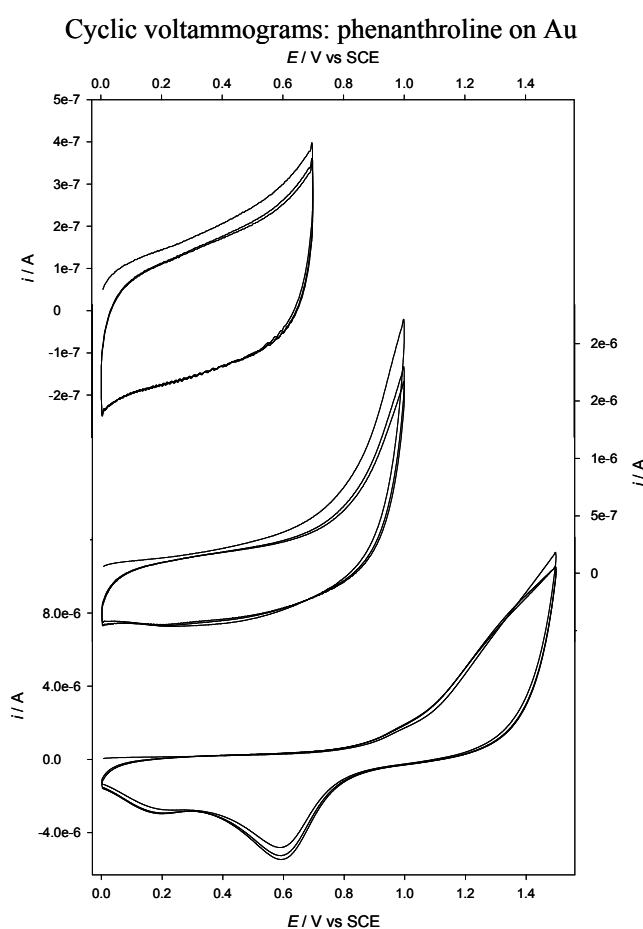

Figure Appendix-3-88: Cyclic voltammograms depicting the response of a gold electrode subjected to a 1,10-phenanthroline/0.1M KClO4/water solution: Scan rate, ν = 500 mV s^{-1}, switch potentials, E_λ, 0.7 V (top), 1.0 V (middle), and 1.3 V (bottom).

7.3.6   Full version of references.

[136]   "Gaussian 03, Revision B.02" Frisch, M. J.; Trucks, G. W.; Schlegel, H. B.; Scuseria, G. E.; Robb, M. A.; Cheeseman, J. R.; Montgomery, J. A.; Vreven, T.; Kudin, K. N.; Burant, J. C.; Millam, J. M.; S., I. S.; Tomasi, J.; Barone, V.; Mennuci, B.; Cossi, M.; G., S.; N., R.; Petersson, G. A.; Nakatsuji, H.; Hada, M.; Ehara, M.; Toyota, K.; Fukuda, R.; Hasegawa, J.; Ishida, M.; Nakajima, T.; Honda, Y.; Kitao, O.; Nakai, H.; Klene, M.; Li, X.; Knox, J. E.; Hratchian, H. P.; Cross, J. B.; Adamo, C.; Jaramillo, J.; Gomperts, R.; Stratmann, R. E.; Yazyev, O.; Austin, A. J.; Cammi, R.; Pomelli, C.; Ochterski, J. W.; Ayala, P. A.; Morokuma, K.; Voth, G. A.; Salvador, P.; Dannenberg, J. J.; Zakrzewski, V. G.; Dapprich, S.; Daniels, A. D.; Strain, M. C.; Farkas, O.; Malick, D. K.; Rabuck, A. D.; Raghavachari, K.; Foresman, J. B.; Ortiz, J. V.; Cui, Q.; Baboul, A. G.; Clifford, S.; Cioslowski, J.; Stefanov, B. B.; Liu, G.; Liashenko, A.; Piskorz, P.; Komaromi, I.; Martin, R. L.; Fox, D. J.; Keith, T.; Al-Laham, M. A.; Peng, C. Y.; Nanayakkara, A.; Challacombe, M.; Gill, P. M. W.; Johnson, B. G.; Chen, W.; Wong, M. W.; Gonzalez, C.; Pople, J. A. *Gaussian 03, Revision B.02*; Gaussian, Inc., Pittsburgh PA, 2003.

[137] "TURBOLMOLE-4.0" Ahlrichs, R.; Bär, M.; Baron, H. P.; Bauernschmitt, R.; Böcker, S.; Ehrig, M.; Eichkorn, K.; Elliot, S.; Haase, F.; Häser, M.; Horn, H.; Huber, C.; Huniar, U.; Kattannek, M.; Kölmel, C.; Kollwitz, M.; Ochsenfeld, C.; Öhm, H.; Schäfer, A.; Schneider, U.; Treutler, O.; von Arnim, M.; Weigend, F.; Weis, P.; Weiss, H. *TURBOLMOLE-4.0*; Quantum Chemistry Group: University of Karlsruhe, 1997.

[172] "Molcas Version 5" Andersson, K.; Barysz, M.; Bernhardsson, A.; Blomberg, M. R. A.; Cooper, D. L.; Fleig, T.; Fülscher, M. P.; Gagliardi, C. d.; Hess, B. A.; Karlström, G.; Lindh, R.; Malmqvist, P.-Å.; Neogrády, P.; Olsen, J.; Roos, B. O.; Sadlej, A. J.; Schütz, M.; Schimmelpfennig, B.; Seijo, L.; Serrano-Andrés, L.; Siegbahn, P. E. M.; Stålring, J.; Thorsteinsson, T.; Veryazov, V.; Widmark, P.-O. *Molcas Version 5*; University of Lund: Lund, 2000.

266 pages   52868 words   284635 Characters

(blank page)